Plug Formation and Dissociation of Mixed Gas Hydrates and Methane Semi-Clathrate Hydrate Stability

A thesis
submitted in partial fulfilment of
the requirements for the degree
of
Doctor of Philosophy
in
Chemical and Process Engineering
by
Thomas John Hughes

UNIVERSITY OF CANTERBURY

2008

ABSTRACT

Gas hydrates are known to form plugs in pipelines. Hydrate plug dissociation times can be predicted using the CSMPlug program. At high methane mole fractions of a methane + ethane mixture the predictions agree with experiments for the relative dissociation times of structure I (sI) and structure II (sII) plugs. At intermediate methane mole fractions the predictions disagree with experiment. Enthalpies of dissociation were measured and predicted with the Clapeyron equation. The enthalpies of dissociation for the methane + ethane hydrates were found to vary significantly with pressure, the composition, and the structure of hydrate. The prediction and experimental would likely agree if this variation in the enthalpy of dissociation was taken in to account.

In doing the plug dissociation studies at high methane mole fraction a discontinuity was observed in the gas evolution rate and X-ray diffraction indicated the possibility of the presence of both sI and sII hydrate structures. A detailed analysis by step-wise modelling utilising the hydrate prediction package CSMGem showed that preferential enclathration could occur. This conclusion was supported by experiment.

Salts such as tetraisopentylammonium fluoride form semi-clathrate hydrates with melting points higher than 30 °C and vacant cavities that can store cages such as methane and hydrogen. The stability of this semi-clathrate hydrate with methane was studied and the dissociation phase boundary was found to be at temperatures of about (25 to 30) K higher than that of methane hydrate at the same pressure.

ACKNOWLEDGEMENTS

Firstly I would like to sincerely thank Professor Ken Marsh, there have been highs and lows during this project, thank you for always supporting and encouraging me, your thirst for knowledge and enthusiasm are an inspiration. I hope you will have more time to enjoy your retirement now.

I would also like to thank Associate Professor John Abrahamson and Professor Alan Mather for supervising me. Thank you for taking the time to show an interest in my work and helping me out when I needed it.

I also wish to express gratitude to Professor E. Dendy Sloan for hosting and supervising me for a period of study at the Center for Hydrate Research at the Colorado School of Mines. It was a great privilege to be in the presence of such a well-renown expert and the knowledge that I gained during my time at CSM was immeasurable helpful in the completion of this work. I would also like to thank Professor Carolyn Koh for her thoughts and suggestions, Simon Davies and Keith Hester for helping me with measurements, and John Boxall for finding somewhere so convenient to stay.

I am also most obliged to Emeritus Professor Ward Robinson and Dr. Jan Wikaira from the Chemistry department for helping me with X-ray diffraction measurements. A thanks also goes to Dr. Marie Squire for collecting my NMR spectra and to Dr. John Smaill from Mechanical Engineering for checking my pressure cell designs.

I have had a great deal of technical assistance during this project and wish to thank all the technical staff for their help. I would particularly like to thank Frank Weerts for the construction of my pressure cells, Mike Lahood, Slywester Zwolinski, and Tim Moore for running electrical tests and diagnostic repairs on the ever unreliable DSC, and Tony Allen for assisting in the set up of data acquisition and computer logging hardware. I would also like to thank Leigh Richardson for the construction of a crate for shipping the DSC and Glenn Wilson for ordering and purchasing parts and materials for my work. Trevor Berry also

deserves a special mention, for always finding the parts and equipment I needed and for teaching me how to use the gas chromatograph.

This work would not have been possible without funding from the Gas Processors Association (GPA); I offer them my appreciation and thanks. I would also like to thank my project's GPA research committee for their patience and understanding.

Finally I wish to thank my family and friends for supporting me throughout this project. I would like to especially thank my parents for bringing me countless cups of tea and coffee during the long process of writing this thesis, amongst other things.

TABLE OF CONTENTS

LIST OF FIGURES

LIST OF TABLES

Chapter 1 INTRODUCTION

1.1 What are clathrate hydrates?

Clathrates are crystalline inclusion compounds in which one group of molecules form a lattice of cages in which other so called "guest" molecules are encaged or enclathrated. Clathrate hydrates are clathrates in which the lattice is constructed from hydrogen bonded water molecules. For a clathrate hydrate to be stable it is essential that guest molecules occupy at least some of the cages. Although strictly speaking clathrate hydrates are non-stoichiometric the near full occupation (90 % or greater) of at least one type or size of cages in the structure is required for stability. Clathrate hydrate formation is favoured by low temperature and high pressure conditions. Clathrate hydrates may be formed from water and gaseous guests such as methane and carbon dioxide or water and liquid guests such as tetrahydrofuran and cyclopentane. Natural gas hydrates refer to clathrate hydrates in which the guest molecules consist of constituents of natural gas.[1,2]

Semi-clathrate hydrates (SCH)[3,4] are clathrates in which water forms a lattice with the help of quaternary ammonium (R_4N^+), quaternary phosphonium (R_4P^+), or tertiary sulfonium (R_3S^+) salts, collectively termed peralkylonium salts, or trialkylamine or trialkylphosphine oxides. In the case of the peralkylonium salts the nitrogen, phosphorus or sulfur atoms as well as the anion (which might commonly be a halide) occupy lattice sites in the structure. In the case of the trialkyl(amine/phosphine) oxide the nitrogen/phosphorus atoms and oxygen atoms occupy lattice sites. The alkyl chains of the SCH former act as guests in some of the cages.[5] The most stable of these SCH form with cations containing the n-butyl or isopentyl alkyl chains.[6] For the peralkylonium salt SCH anions of a similar size to the water molecule such as the fluoride ion tend to result in more stable hydrate phases.[7,8] SCH are stable at atmospheric pressure at temperatures as high as the mid 30 °Cs.[3]

1.2 Structure and stoichiometry of clathrate hydrates

1.2.1 Structure of gas clathrate hydrates

The first documented observation of what would now be recognized as a clathrate hydrate was by Joseph Priestly in 1778.[9] Priestly had cooled an aqueous solution of sulfur dioxide to

approximately -8 °C and he noted "as it melted the ice sank to the bottom of the liquor", what he was in fact observing was sulfur dioxide hydrate (density = 1300 $kg \cdot m^{-3}$,[10] dissociation temperature at atmospheric pressure = 6.8 °C [11]). Humphry Davy later observed in 1811 that "the solution of [chlorine] in water freezes more readily than pure water".[12] A more definitive discovery of clathrate hydrates was made by Michael Faraday under the supervision of Davy in 1823.[13] He studied the solid formed in an aqueous chlorine solution and determined its composition to be $Cl_2 \cdot 10H_2O$. The most pertinent observation made by these early hydrate scientists was the ice-like appearance of clathrate hydrates. Since Faraday's work a wide range of gases of small molecular volume have been observed to form clathrate hydrates, including simple hydrocarbons and noble gases. Clathrate hydrates of liquids with small molecular volumes such as chloroform, tetrahydrofuran and acetone have also been reported. Sloan and Koh[2] tabulate an extensive list of hydrate formers in table 2.5a of their book.

In the early 1940's von Stackelberg and co-workers began X-ray studies of clathrate hydrates.[14] Two unique cubic crystal structures were identified from single crystals, one with a unit cell size of 12 Å and space group of Pm3n from the analysis of a sulfur dioxide hydrate and the other structure "that would appear to have space group [$P4_232$]"[15] from the analysis of a chloroform and hydrogen sulfide double hydrate (see Appendix A for a brief description of crystal systems and space groups). The data from these analyses was lost during World War II and could not be further investigated, nevertheless a hydrogen bonded structure was proposed by von Stackelburg[16] that included voids that could hold gas molecules. This structure however was deemed to be physically unrealistic due to low O-H··O bond distances [(2.42 to 2.6) Å versus 2.76 Å in hexagonal ice] and O-O-O bond angles that deviated greatly from the tetrahedral angle [(61 to 145)° versus the tetrahedral 109.5°]. Claussen[17,18] considered a hydrogen bonded pentagonal dodecahedral as a starting point for considering hydrate structures because the 108° bond angles differed little from the tetrahedral 109.5°. He constructed a cubic cell consisting of 136 water molecules formed from 16 pentagonal dodecahedrals cages, referred to in short hand as 5^{12} cages (where the 5 refers to the pentagonal shape of each face and 12 refers to the number of faces of that shape in the cage), and 8 slightly larger hexakaidecahedrons or $5^{12}6^4$ cages consisting of 12 pentagonal faces and 4 hexagonal faces. This structure was confirmed by von Stackelberg and Müller[19,20] for hydrates they had prepared from larger molecules such as chloroform and ethyl chloride and

their double hydrates with hydrogen sulfide. The space group was confirmed as Fd3m, rather than the originally supposed $P4_232$, with a unit cell size of 17.2 Å. The other structure with a unit cell size of 12 Å was soon also solved almost simultaneously by Claussen[21], Müller and von Stackelberg[22], and Pauling and Marsh.[23] This structure has a unit cell of 46 water molecules composed of two pentagonal dodecahedral cages (5^{12} cages) and six tetrakaidecahedral or $5^{12}6^2$ cages consisting of 12 pentagonal faces and 2 hexagonal faces. These two structures are designated structure I (sI) for the (2×5^{12} cage + $6\times5^{12}6^2$ cage)·$46H_2O$ and 12 Å unit cell hydrate and structure II (sII) for the (16×5^{12} cage + $8\times5^{12}6^4$ cage)·$136H_2O$ and 17 Å unit cell hydrate. These two structures are the most common gas hydrate structures encountered and are shown in Figure 1.1, approximate cage sizes for these structures are shown in Table 1.1. Detailed X-ray studies of the two structures were published in 1965 by McMullan and Jeffrey[24] (sI – ethylene oxide hydrate) and Mak and McMullan[25] (sII – tetrahydrofuran and hydrogen sulphide double hydrate). In 2004 Kirchner et al.[26] published detailed single crystal X-ray analyses for methane sI, propane sII, and several other hydrates. Structure H (sH) hydrates are also shown in Figure 1.1 however these hydrate require a larger approximately spherical molecule such as neohexane as well as a smaller molecule such as methane to be stable and are not encountered in this work.

1.2.2 Occupation of cage by guest molecules and stoichiometry of hydrates

Figure 1.2 from Sloan[27] (modified from von Stackelberg[16]) plots the size of various molecules (mainly natural gas constituents) in terms of their largest van der Waals diameter and labels the structure of hydrates that they form (sI or sII) Table 1.1 includes approximate sizes of the cages that make up sI and sII hydrates. From Figure 1.2 it can been seen that small molecules less than 4.5 Å form sII hydrates by occupancy of the both the small 5^{12} cage and large $5^{12}6^4$ cage, molecules sized between (4.5 and 5.1) Å form sI hydrates with occupancy of both cages (5^{12} and $5^{12}6^2$), molecules sized between (5.1 and 5.8) Å form sI hydrates with occupancy of only the large $5^{12}6^2$ cage and molecules sized between (5.8 and 7.0) Å form sII hydrates with occupancy of the large $5^{12}6^4$ cages only. Molecules greater than 7.0 Å are too large to fit in the cages of sI or sII hydrates although they may form sH with the help of a molecule smaller than 5.2 Å.

Table 1.1 – Approximate cage sizes for structure I and structure II hydrates.[a]

Structure	5^{12} cage size /Å	$5^{12}6^2$ cage size /Å	$5^{12}6^4$ cage size /Å
sI	5.1	5.9	-
sII	5.0	-	6.7

[a] Values calculated from average cavity radius in table 2.1 of Sloan and Koh[2] and the molecular diameter of water taken as 2.8 Å. Note: Lattice parameters and hence cage sizes are a function of temperature, pressure and the guest molecular size,[28] for this reason the values of cage size are approximate.

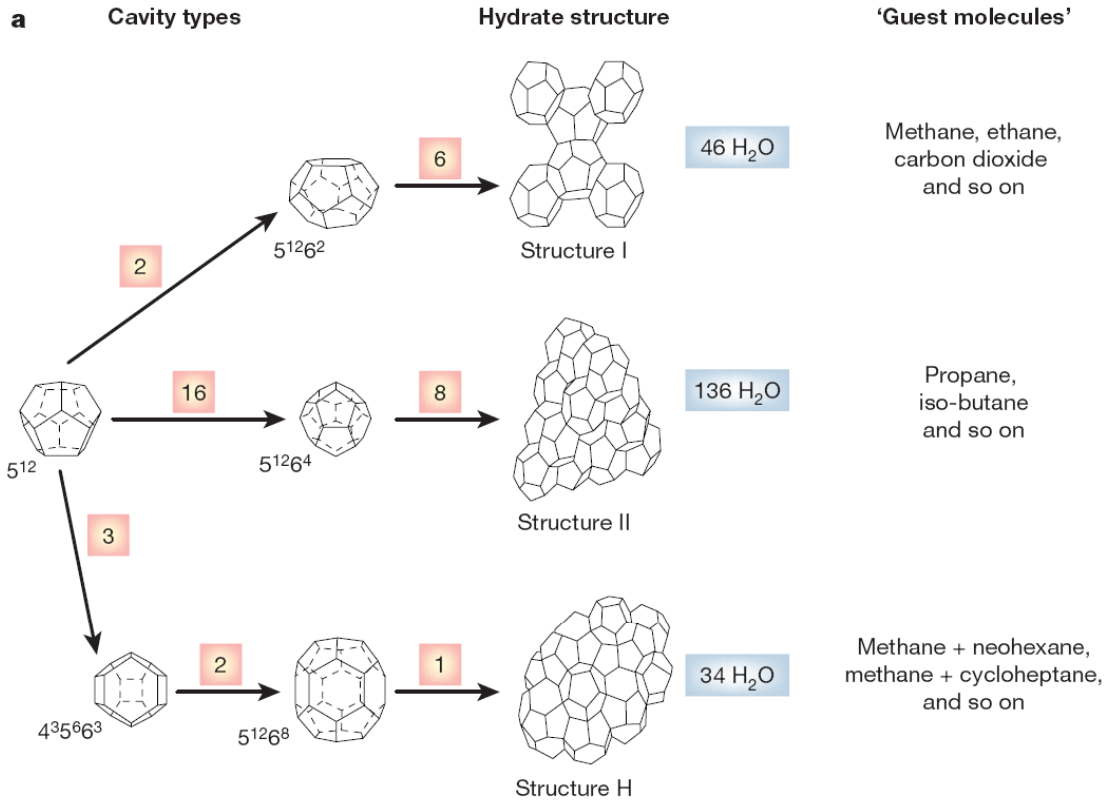

b

Hydrate crystal structure	I		II		H		
Cavity	Small	Large	Small	Large	Small	Medium	Large
Description	5^{12}	$5^{12}6^2$	5^{12}	$5^{12}6^4$	5^{12}	$4^3 5^6 6^3$	$5^{12}6^8$
Number of cavities per unit cell	2	6	16	8	3	2	1
Average cavity radius (Å)	3.95	4.33	3.91	4.73	3.91†	4.06†	5.71†
Coordination number*	20	24	20	28	20	20	36
Number of waters per unit cell	46		136		34		

*Number of oxygens at the periphery of each cavity.
†Estimates of structure H cavities from geometric models.

Figure 1.1 – Structures and cage types of clathrate hydrates. (Reproduced from Sloan[27]).

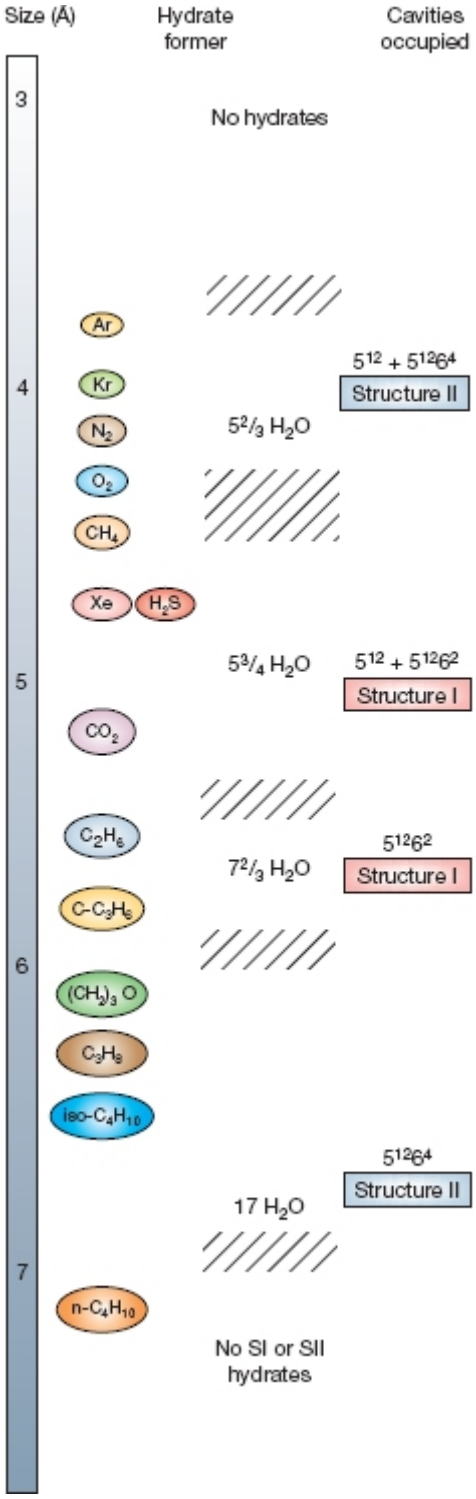

Figure 1.2 – Molecular size (largest van der Waals diameter) of guests versus hydrate cage size ranges. (Reproduced from Sloan[27]; modified from original of von Stackelberg[16]). Perfect hydrate numbers are indicated to the left of the structure. Note: "No Hydrates" label at top at the top is not strictly true, Dyadin et al.[29] showed at very high pressures (exceeding 150 MPa) hydrates of both hydrogen and neon will form. Also von Stackelberg and Meinhold[30] showed that hydrogen can help stabilize an sII chloroethane hydrate, more recently Florusse et al.[31] showed the same effect for a sII tetrahydrofuran hydrate.

1.3 Clathrate hydrate thermodynamic prediction models

1.3.1 The van der Waals and Platteeuw model

Experimentally it is has been shown that clathrate hydrates are non-stoichiometric, sI methane hydrate for example typically has a hydrate number of about 6 versus the perfect stoichiometric value of 5.75 which would result from full occupation of all cages (46 water molecules divided by 8 cages). Sloan and Koh[2] note that "typical occupancies of large cavities are greater than 95 %, while occupancy of small cavities vary widely depending on the guest composition, temperature and pressure". The statistical thermodynamic model of clathrates developed by van der Waals and Platteeuw[32] (also described in detail in Chapter 5 of Sloan and Koh[2] and in Ballard[33]) takes in to account this non-stoichiometry of clathrate hydrates (note: this model is generalized for all clathrate formers however for the purposes of this discussion reference will only be made to clathrate hydrates). The water of the hydrate is considered to be effectively a "solvent" and the guest molecules are considered to be "solutes" allowing for non-occupation of some cages. Details of the derivation of this model will not be considered in detail here however the assumptions upon which the model is based include:

- The guest molecules do not significantly distort the cages, so that the vibrational and electronic modes of the hydrogen bonded hydrate host network are not effected,
- Cages are only occupied by one guest molecule,
- The interactions between enclathrated guest molecules are negligible so that the partition function for the guest molecules is independent of the number and types of guest molecules present,
- Classical statistics are valid (quantum effects do not need to be considered).

The net result of the model is an equation which describes the chemical potential of water in the hydrate lattice, $\mu_{\mathrm{W}}^{\mathrm{H}}$:

$$\mu_{\mathrm{W}}^{\mathrm{H}} = \mu_{\mathrm{W}}^{\beta} + kT\sum_{i} \nu_i \ln\left(1 - \sum_{\mathrm{J}} \theta_{J,i}\right), \tag{1.1}$$

where μ_W^β is the chemical potential of a theoretical empty hydrate lattice, k is Boltzmann's constant, T is the absolute temperature, i is the type of cavity (e.g. a 5^{12} cage), ν_i is the number of type i cavities per water molecule, J is the type of guest molecule and $\theta_{J,i}$ is the fractional occupancy of cavity type i by molecule of type J. The fractional occupancy, $\theta_{J,i}$ is given by the Langmuir isotherm:

$$\theta_{J,i} = \frac{C_{J,i} f_J}{1 + \sum_J C_{J,i} f_J}, \tag{1.2}$$

where $C_{J,i}$ is a Langmuir adsorption constant for the molecule of type J in cavity of type i and f_J is the fugacity of a molecule of type J. It is possible to show (see Sloan and Koh[2] section 5.1.4) that the Langmuir adsorption constant $C_{J,i}$ may be calculated using eq (1.3) if it is assumed that:

- Enclathration does not effect the rotational, vibrational, nuclear or electronic energies, and
- The potential energy of a guest molecule is only a function of its distance from the cavity centre. This means that the cavity in effect is spherically averaged and a symmetric potential function, $\varpi(r)$, can be used, were r is the distance from the centre of the cage.

$$C_{J,i} = \frac{4\pi}{kT} \int_0^R \exp\left[-\varpi(r)/kT\right] r^2 \mathrm{d}r \tag{1.3}$$

The upper integral limit of eq (1.3), R, represents the free cavity radius (which is the average cavity radius minus the radius of the water molecule). A Kihara potential is typically used to generate the spherically symmetric potential function. The pair potentials are averaged between the guest molecule and each water molecules of the cage. Kihara parameters are fitted to the hydrate formation properties for each component.

1.3.2 CSMGem's van der Waals and Platteeuw method

A more recent approach by Ballard[33] replaces the average cage radius idea utilised in eq (1.3) with a more accurate "multilayered" cage approach whereby the radii of each water molecule in the hydrate cage is considered. When this approach is used equation (1.3) is replaced by:

$$C_{J,m} = \frac{4\pi}{kT}\int_0^{R_1 - a_J} \exp\left[\sum_n \varpi_{J,n}(r)/kT\right] r^2 \mathrm{d}r\,, \tag{1.4}$$

"where the summation is over all shells (n) in cage m and a_J is the hard core radius subtracted from R to avoid singularities",[2] R_1 represents the smallest shell in cage m.

Equation (1.4) has been used in the statistical thermodynamic prediction package, CSMGem (Colorado School of Mines Gibbs Energy Minimisation)[34] developed by Ballard[33] that has been used in this thesis (note: a CD containing CSMGem is included with the latest edition of Sloan and Koh[2]). Parameter optimization for CSMGem incorporated spectroscopic data (the X-ray diffraction data of Huo[28], the NMR spectroscopy of Kini[35] and the Raman spectroscopy of Subramanian[36] and Jager[37]) as well as P,T hydrate phase data.[33] Sloan and Koh[2] note "the crucial change introduced in CSMGem is to make the radii of each shell functions of temperature, pressure and composition. As the lattice expands or compressed, the cages also expand or compress. The radii of the shells are assumed to be a linear function of the cubic hydrate lattice parameter". CSMGem also incorporates a Gibbs free energy minimisation routine which allows calculation of phases present at any T and P (whether hydrates are present or not).[2] Fugacity models for other phases involved in hydrate formation (including aqueous, ice, vapour and liquid hydrocarbon) are detailed by Ballard.[33] The accuracy of the predictions that CSMGem makes is covered in section 5.1.8 of Sloan and Koh.[2]

1.3.3 Ab initio methods

Recently *ab initio* methods have been applied to predict the interaction energies of molecules and atoms within hydrates. Sloan and Koh[2] (section 5.1.9) provide a review of these methods.

1.4 Areas of hydrate interest

There are 5 main areas of hydrate research interest to both the oil and gas industry and scientists and engineers. They include:

- Flow assurance,

- Safety,
- Energy recovery,
- Storage and transportation, and
- Climate change.

Each of these areas is discussed briefly below. A more detailed review to these areas can be found in Sloan and Koh.[2] "Hydrate Engineering" by Sloan[38] contains lessons learnt in industry concerning flow assurance and safety from numerous case studies.

1.4.1 Flow assurance

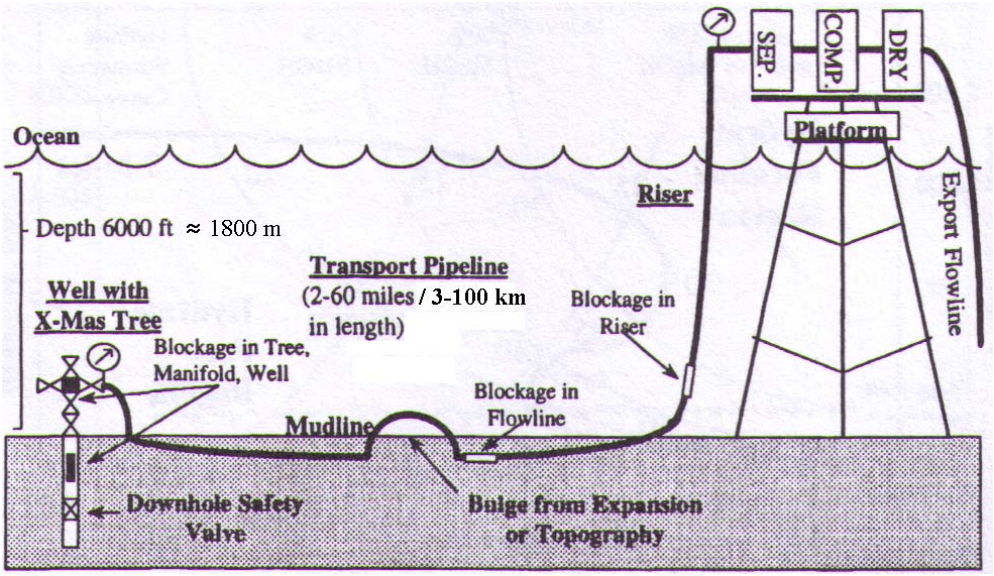

Figure 1.3 – An offshore production facility in deep water showing common hydrate blockage locations. (Reproduced from Sloan[38]).

Since Hammerschmidt[39] discovered in 1934 that gas hydrates rather than ice were causing blockages in natural gas pipelines, hydrates have been a flow assurance concern. Today pipeline hydrate formation is particularly a worry as offshore hydrocarbon recovery moves in to even deeper water. Figure 1.3 from "Hydrate Engineering" by Sloan[38] shows a typical offshore production facility. At the reservoir the pressure is high but the temperature is also high, usually too high for hydrate formation. As the fluids flow along a seafloor and subsea pipelines they begin to cool to the seafloor temperature (approximately 4 °C). In most reservoirs water is produced also with the oil and gas, meaning that hydrate formation is possible. Water dissolved in the gas can begin to condense as the fluids cool, and can collect

at low points in the system as illustrate in Figure 1.3, such as after a high point in the seafloor topography or near the bottom of a riser to the platform. At the platform, water is separated from the oil and gas and the gas is dried. This removes most of the water but some can still remain as part of an oil-water emulsion or dissolved in the gas phase, still allowing for the formation of hydrates. Several strategies for the prevention of hydrate formation are employed, the most common being the use of thermodynamic inhibitors such as methanol or monoethylene glycol. These inhibitors work by shifting the hydrate formation conditions to lower temperatures/higher pressures. Other chemicals can also be used such as kinetic inhibitors which slow the formation of hydrates and anti-agglomerants which inhibit the adhesion of hydrate particles to each other to reduce plug formation. More detail on each of these strategies is included in Sloan[38] and Sloan and Koh.[2]

1.4.2 Safety

Although it is possible in most normal circumstances to avoid hydrate formation, unusual conditions such as start up or shut down can result in the formation of large plugs.[38] To remove these plugs the pressure in the pipeline is usually lowered to drop the pressure below the incipient hydrate formation pressure. Preferably each side of the hydrate is depressurised (two-sided depressurisation) but in many cases it is not possible and a one-sided depressurisation must be performed. One sided depressurisation in particular can lead to very dangerous situations as the pressure gradient across the hydrate plug during the dissociation can cause the plug to dislodge and travel at high speed along the pipeline. In experiments plug speeds have been measured up to 300 $km \cdot h^{-1}$.[38] When a plug moves at such high speed it can cause significant compression on the downstream side and over-pressurise the pipeline causing a blowout. Local heating, be it electrical,[40] or other means can also cause unsafe conditions if not done carefully. The plug ends can contain pressure and cause a pipeline rupture at the source of heat if the hydrate plug is heated in the middle.

1.4.3 Energy recovery

Large natural deposits of hydrates exist both onshore and offshore. These deposits are of potential as an energy reserve and are significant compared to all other fossil fuel deposits. Estimate very widely from $(0.25 \text{ to } 120) \times 10^{15}$ m^3 of methane at STP but even the

conservative estimates are significant.[2] More detail of natural deposits of hydrate and possible extraction techniques such as depressurisation, inhibitor injection and thermal injection are covered in Sloan and Koh.[2]

1.4.4 Storage and transportation

Clathrate hydrates have been shown to be able to store up to 184 m^3 STP of methane per cubic metre of hydrate.[2] They could be used as a storage material for transportation of gas, particularly for the estimated 70 % of natural gas reserves which are considered either too far from an existing pipeline or too small to justify liquefaction plant.[27,41] Research in Japan[42,43] has focused on the shipping technology that would be required. Recently, storage of gases in binary hydrates of tetrahydrofuran (THF) has also been investigated, such as that of THF + hydrogen.[31] Storage of gases in semi-clathrate hydrates, discussed more in the following sections, has also recently been studied.[44-47]

1.4.5 Climate Change

Climate change research on hydrates has focused on theories related to natural methane hydrate dissociation and whether this can explain past climate events.[2] Other environmental research focuses on carbon dioxide sequestration in gas hydrates and on whether it would be possible to extract methane from natural hydrates while simultaneously sequestering carbon dioxide.[48]

1.5 Hydrate plug dissociation

1.5.1 Conceptual view of hydrate dissociation

Knowledge regarding the process of hydrate dissociation is important for both modelling of gas production from natural reserves and the removal of hydrate blockages from pipelines. In the past the conceptual view of hydrate dissociation was that it occurred by axial dissociation (Figure 1.4b) however there is now overwhelming evidence that dissociation occur radially (Figure 1.4a). Peters[49] produced photographic evidence and recently Gupta[50] used X-ray computed tomography (CT) to measure the density of hydrate cores as they dissociated to show that only radial dissociation occurs.

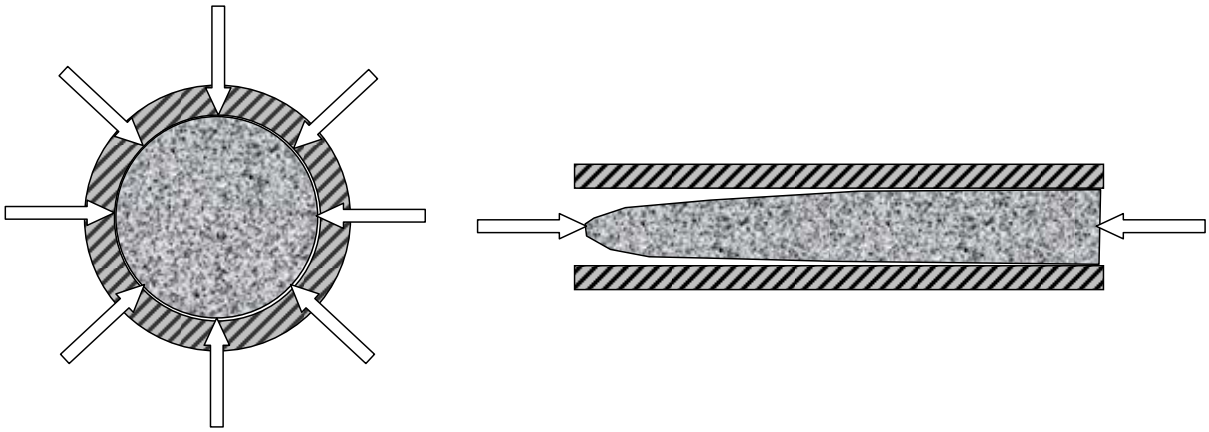

(a) Radial dissociation (b) Axial dissociation

Figure 1.4 – Current radial dissociation picture (a), compared to the old axial dissociation picture (b). (Adapted from Sloan[2]).

1.5.2 Hydrate plug dissociation models

Most hydrate dissociation models such as that of Peters[49] and Nguyen-Hong et al.[51] rely upon heat transfer being the limiting factor in hydrate plug dissociation, some models however also incorporate kinetics. Citing Moridis[52], Hong et al.[53] and Davies et al.[40] Sloan and Koh[2] note: "on the basis of comparisons with experimental data on hydrate dissociation it has been shown by a number of research groups that heat transfer plays the dominant role in hydrate dissipation, rather than intrinsic kinetics". Sloan and Koh further note: "From the extensive experimental and model development work performed at CSM (during a period of over 15 years), it has been demonstrated that a heat transfer controlled model is able to most accurately predict dissociation times (comparing to laboratory experiments) without any adjustable parameters". CSMPlug is the plug dissociation computer program generated out of the initial two-sided dissociation model of Peters,[49] extended by Bollavaram[54] for one-sided dissociation and for electrical heating by Davies et al.[40] The model is based on Fourier's law of heat transfer in cylindrical coordinates and takes in to account hydrate, ice and water phases. The dissociation time of a hydrate plug and accompanying ice plug can be predicted based on the two-moving boundary part of the model.

1.6 Structure and stoichiometry of semi-clathrate hydrates

1.6.1 Cage structure of semi-clathrate hydrates

Semi-clathrate hydrates (SCH) of tetrabutylammonium (TBA) and tetraisopentylammonium (TIPA) quaternary ammonium salts were discovered by Fowler et al. in 1940s.[55] Since that time other SCH have been discovered and structurally analysed by single crystal X-ray crystallography such as those of trialkylsulfonium salts,[56,57] tetraalkylphosphonium[56] and trialkylphosphine oxides.[58] The first series of structural studies of SCH where published by Jeffrey, McMullan and coworkers.[5,57,59-61] In these structures, water lattice sites are replaced by the cation centres and anions and each alkyl chains occupies a larger cage, which may be a tetrakaidecahedral ($5^{12}6^2$), pentakaidecahedral ($5^{12}6^3$) or hexakaidecahedral ($5^{12}6^4$). Small unoccupied dodecahedral (5^{12}) cages are interspaced between some of the large cages. The breaking of the water lattice by the cation centres and anions lead Davidson[11] to introduce the term "semi-clathrate hydrates". Figure 1.5 shows the structure of a tetra-n-butylammonium bromide (TBAB) SCH with a hydrate number of 38 from Shimada et al.[62] The centre of the cation replaces a lattice site and the alkyl chains fill the larger cages as guests. The larger cages in this structure are two tetrakaidecahedrons ($5^{12}6^2$) and two pentakaidecahedrons ($5^{12}6^3$). The smaller dodecahedral (5^{12}) cages are filled with spheres to indicate that they could be filled with suitably sized molecules. Indeed Shimada and coworkers[63] as well as Kamata et al.[64] provided some of the first evidence that unoccupied cages in SCH could enclathrate suitably sized molecules, namely methane, hydrogen sulfide and nitrogen when they showed it was possible to separate these molecules from larger molecules such as ethane, propane and carbon dioxide with tetrabutylammonium bromide SCHs. However McMullan et al.[61] had earlier noted the evolution of gas bubbles from melting tetrabutylammonium fluoride crystals which was shown to be air by gas chromatography. Similar observation of bubbling upon melting of SCH crystals were made by Jeffrey[4] and Davidson.[11] The experiments by Stupin and Stravitnaya had also shown prior to Shimada et al. and Kamata et al. that SCH of tetrabutylammonium bromide and acetate as well as tetrabutylammonium and tetraisopentylammonium phthalates could adsorb sulfur dioxide.[65,66]

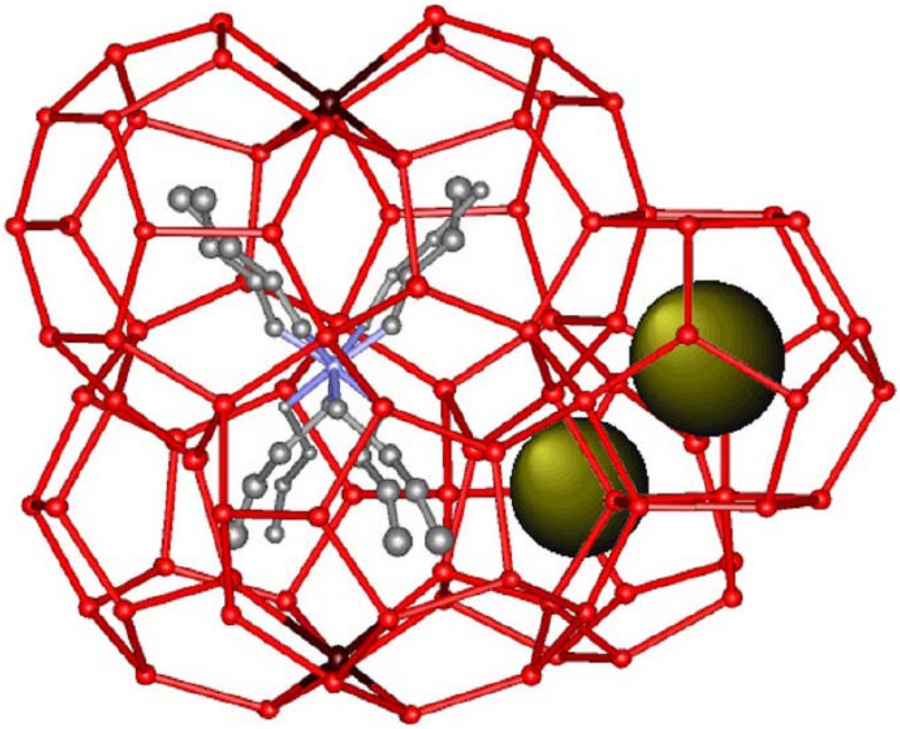

Figure 1.5 – Structure of tetra-n-butylammonium $\cdot 38H_2O$ around the cation showing alkyl chain occupation of larger cages ($2\times5^{12}6^2$ – tetrakaidecahedrons and $2\times5^{12}6^3$ – pentakaidecahedrons), cation centre replacement of water lattice site and small 5^{12} cages that could be occupied with suitably sized molecules (represented by spheres). (Reproduced from Shimada et al.[62]).

1.6.2 Stoichiometry and structure of semi-clathrate hydrates for gas storage

Peralkylonium cations, particularly those with butyl or isopentyl alkyl chains, can form SCH with many different anions and each of these peralkylonium salts may form several different structures of SCH with different hydration numbers (*n*). Many of these salts and the structures that they form are tabulated by Davidson,[11] Dyadin and Udachin[3] and Jeffrey.[4] To maximise the amount of a gas that can be stored per unit mass and/or volume it is important to choose a suitable SCH former and its structure by choosing the hydration number. In general SCH with high hydration numbers have more unoccupied cages per unit mass/volume. Another factor to consider is the stability of the hydrate in terms of it melting or dissociation temperature. An ideal SCH for gas storage would have a relatively larger number of unoccupied cages per unit mass/volume coupled with a higher melting/dissociation temperature. One such SCH with relatively higher numbers of unoccupied cages and a higher melting/dissociation temperature is that of tetraisopentylammonium fluoride (TIPAF) with 38 waters of hydration (abbreviated $TIPAF\cdot38H_2O$). The structure of $TIPAF\cdot38H_2O$ was

determined by X-ray crystallography by Feil and Jeffrey.[5] The structure is identical in cage arrangement to the more recently analysed TBAB·38H_2O SCH determined by Shimada et al.[62] and partially illustrated in Figure 1.5. Figure 1.6 shows a *T*,*w* stability diagram for TIPAF + water (where w_1 is the mass fraction of the salt) reproduced from Lipkowski et al.[67] Lipkowski et al. observed the TIPAF SCH with a hydration number of 38 that Feil and Jeffrey had studied, as well as two other SCH with experimental hydration numbers of 26.8, and 32.7 (these hydration numbers were observed by both Karl Fischer titration for water content and potentiometric titration of tetraphenylborate with an ion-selective electrode for the salt concentration). Interestingly Lipkowski et al. noted that even though the TIPAF·38H_2O structure is metastable to the TIPAF·27H_2O structure for much of the composition range (greater than $w_1 \approx 0.22$) the TIPAF·38H_2O hydrate was "repeatedly observed" indicating it was kinetically favoured. The observation of the stable TIPAF·27H_2O part of the diagram was "only possible when freezing and melting of the mixture of the corresponding composition was repeated many times until the metastable phases disappeared and the mixture had been cooled to (-50 to -60) °C."[67] Crystals of the metastable TIPAF·32H_2O could only be grown "in the absence of any mechanical action or stirring in a [$w_1 \approx 0.22$] solution at [(291.15 to 293.15) K]".[67] "Mechanical disturbance of the solution where [TIPAF·32H_2O] crystals were growing resulted in turbidity and the appearance of many tiny [TIPAF·38H_2O] crystals".[67] A full structural determination of the SCH with an experimental hydration number of 26.8 was also presented by Lipkowski et al.[67] to reveal a structural stoichiometry of TIPAF·27H_2O. In addition the space group for the SCH with experimental hydration number of 32.7 was determined as $P4_2/m$. This space group is the same as that determined for the SCH of tetra-n-butylammonium fluoride (TBAF) with a hydration number of 32.8 whose crystal structure was determined by McMullan and Jeffrey,[61] indicating presumably similar structures. Details of each TIPAF SCH including stoichiometry, crystallography, cage structure, and density are listed in Table 1.2 compiled largely from Lipkowski et al.[67] The geometry of the cages listed in Table 1.2 can be viewed in Figure 1.7.

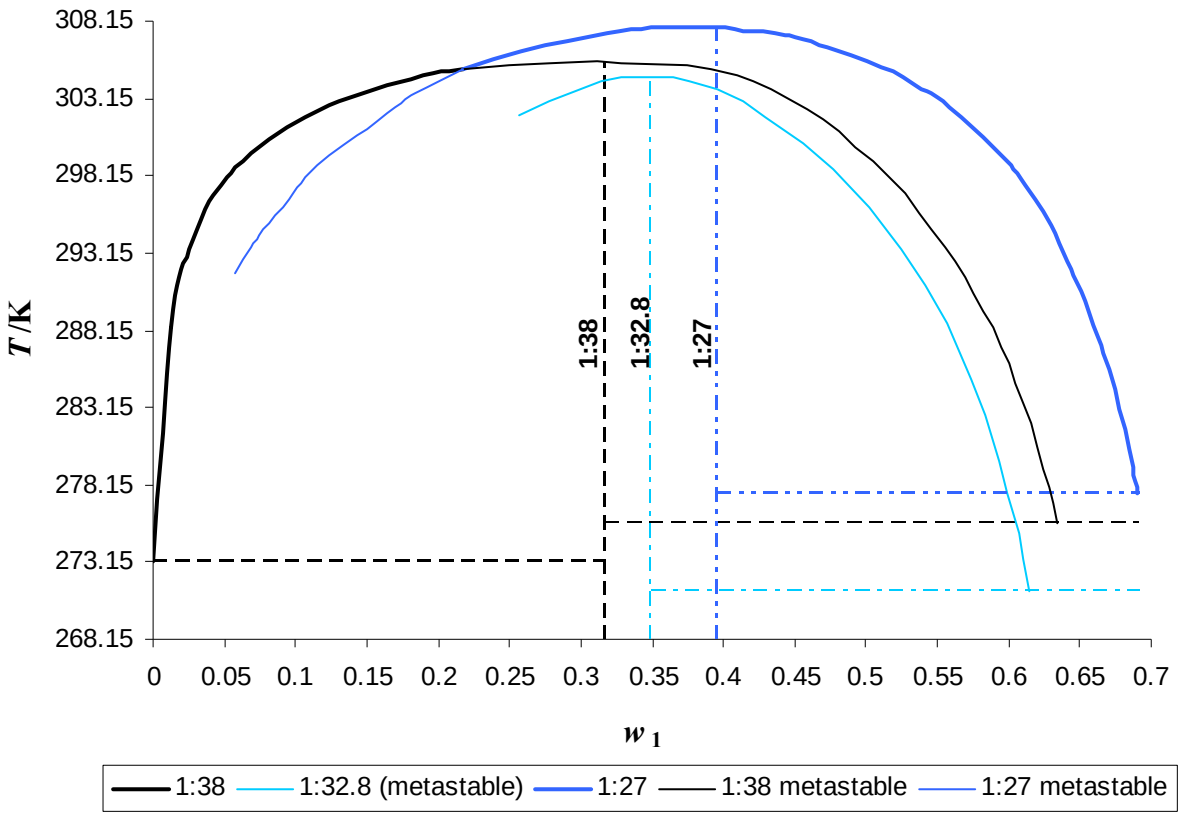

Figure 1.6 – Temperature-mass fraction (T,w) stability diagram for tetraisopentylammonium fluoride (1) + water (2) at atmospheric pressure, composition of semi-clathrate hydrates are represented by the ratios of moles of salt to moles of water, 1:38, 1:32.8 and 1:27. (Reproduced from plotted data of Lipkowski et al.[67]).

Recently experimental *PVT* phase measurements of several SCH + gas combinations have been published. Phase measurements of TBAB aqueous solutions + hydrogen have been made by Hashimoto et al.[46,47] as well as Chapoy et al.[45] (presumably the 1:26 mole ratio TBAB to water) who in addition completed measurements on tetrabutylammonium fluoride (TBAF) aqueous solution (1:28 mole ratio TBAF to water) + hydrogen. Measurements have also been made for carbon dioxide + nitrogen mixtures (as well as the pure gases) and TBAB aqueous solution at four different concentrations by Duc et al.[68] Extensive phase measurements of TBAB aqueous solutions (at various concentrations) with hydrogen, methane, nitrogen, carbon dioxide and a natural gas have been measured by Arjmandi et al.[44]

Table 1.2 – Tetraisopentylammonium fluoride semi-clathrate hydrates: stoichiometry, crystallographic details, cage structures and densities.[a]

Hydrate Number		Melting Point	Space Group and Unit Cell Size	Cage Structure (per unit cell)[g]	ρ/g·cm^{-3}	
Struct.	Exptl.				Struct.	Exptl.[h]
27	26.8	307.8 K 34.6 °C	$I4_1/a$ (tetragonal)[d,e] a = 16.894 Å c = 17.111 Å	$16\times4^2 5^9 6^3 7^1$ (salt) $4\times4^4 5^4$ (unoccupied) Z = 4	1.093	1.079
32.8[b]	32.7	304.6 K 31.4 °C	$P4_2/m$ (tetragonal)[d] a = 23.729 Å c = 12.466 Å	$16\times5^{12}6^2$, $4\times5^{12}6^3$ (salt)[b] 10×5^{12} (unoccupied)[b] Z = 5	1.075[b]	1.062
38	38.9	305.6 K 32.4 °C 304.4 K[c] 31.2 °C[c]	Pbmm (orthorhombic)[f] a = 11.88 Å b = 21.53 Å c = 12.70 Å	$4\times5^{12}6^2$, $4\times5^{12}6^3$ (salt) 6×5^{12} (unoccupied) Z = 2	1.025 0.994[f]	1.019 1.02[c]

[a]Data from Lipkowski et al.[67] unless otherwise noted.

[b]Assumed to be similar structure to TBAF·32.8H_2O[61] as they share the same space group and similar unit cell dimensions.

[c]From Feil and Jeffrey.[5]

[d]Unit cell dimensions were measured at -50 °C.

[e]Unit cell dimensions at 0 °C were measured as: a = 16.937 Å, c = 17.161 Å.

[f]Feil and Jeffrey[5] determined the unit cell dimensions at room temperature as: a = 12.08 Å, b = 21.61 Å and c = 12.82 Å.

[g]Denotes cages and whether they are filled by salt alkyl chains or unoccupied, Z = number of molecules of TIPAF per unit cell.

[h]Measured at 0 °C from Lipkowski et al.'s[67] measurements, for Feil and Jeffrey's[5] TIPAF·38H_2O density measurement the temperature was not noted.

This work attempts to find a SCH that maximizes both the stability in terms of melting point and the storage capacity of the structure for methane. Table 1.3 lists calculated potential storage mass fractions and storage densities (mass of methane per volume of methane filled SCH) assuming full occupancy of the unoccupied cages by methane. As well as the three known TIPAF SCH structures the TBAB·38H_2O structure of Shimada et al.[62] is also included

as well as that of tributylphosphine oxide, TBPO·34.5H_2O.[58] The TBAB·38H_2O hydrate has a similar potential storage capacity to TIPAF·38H_2O but a melting point of only 9.9 °C.[69] TBPO·34.5H_2O has a greater storage capacity than TIPAF·38H_2O (mass fractions of 6.3 % and 4.3 % respectively) but has a considerably lower melting point of 7.1 °C compared to over 30 °C for TIPAF·38H_2O. Because of the requirement of a SCH with both a high melting point and a good storage capability TIPAF·38H_2O was selected for *PVT* phase measurements with methane. These measurements are presented in Chapter 5 of this thesis.

Table 1.3 – Potential occupancies for gas storage of methane in semi-clathrate hydrate structures.[a]

SCH	Unoccupied cages per salt molecule	Methane storage potential mass fraction	Density of empty SCH g·cm^{-3}	Density of filled SCH g·cm^{-3}	Methane storage density kg·m^{-3}
TIPAF·38H_2O	3	4.6 %	1.019	1.068	48.9
TIPAF·32.8H_2O	2	3.4 %	1.062	1.100	37.5
TIPAF·27H_2O[b]	1	2.0 %	1.079	1.101	21.5
TBAB·38H_2O[c]	3	4.6 %	1.045	1.095	49.9
$(C_4H_9)_3PO$·34.5H_2O[d]	3.5	6.3 %	0.97	1.03	64.5

[a]Structural information and densities from Lipkowski et al.[67] and Feil and Jeffrey[5] except where otherwise noted.

[b]Assumes that one molecule of methane can occupy the 4^45^4 cage of this structure. It has been estimated however in Appendix B that the 4^45^4 cage has a mean free diameter of about 3.9 Å and probably would be too small to enclathrate methane molecules especially when the non-spherical nature of the cage is considered.

[c]Data for this SCH from Shimada et al.[62] note: cage structure same as TIPAF·38H_2O see Table 1.2, space group of Pmma, unit cell size of a = 21.060 Å, b = 12.643 Å, c = 12.018 Å, Z = 2, melting point = 9.9 °C (originally from Oyama et al.[69])

[d]Data for this SCH from Alekseev et al.,[58] note: cage structure $4\times5^{12}6^4$, $4\times5^{12}6^3$, $4\times5^{12}6^4$, 14×5^{12} (where the 5^{12} cages are unoccupied and the larger cages are filled by alkyl chains), space group of $P2_12_12$, unit cell size of a = 23.479 Å, b = 19.949 Å, c = 12.136 Å, Z = 4, Dyadin and Udachin[3] give melting point of 7.1 °C (Figure 18b of their work).

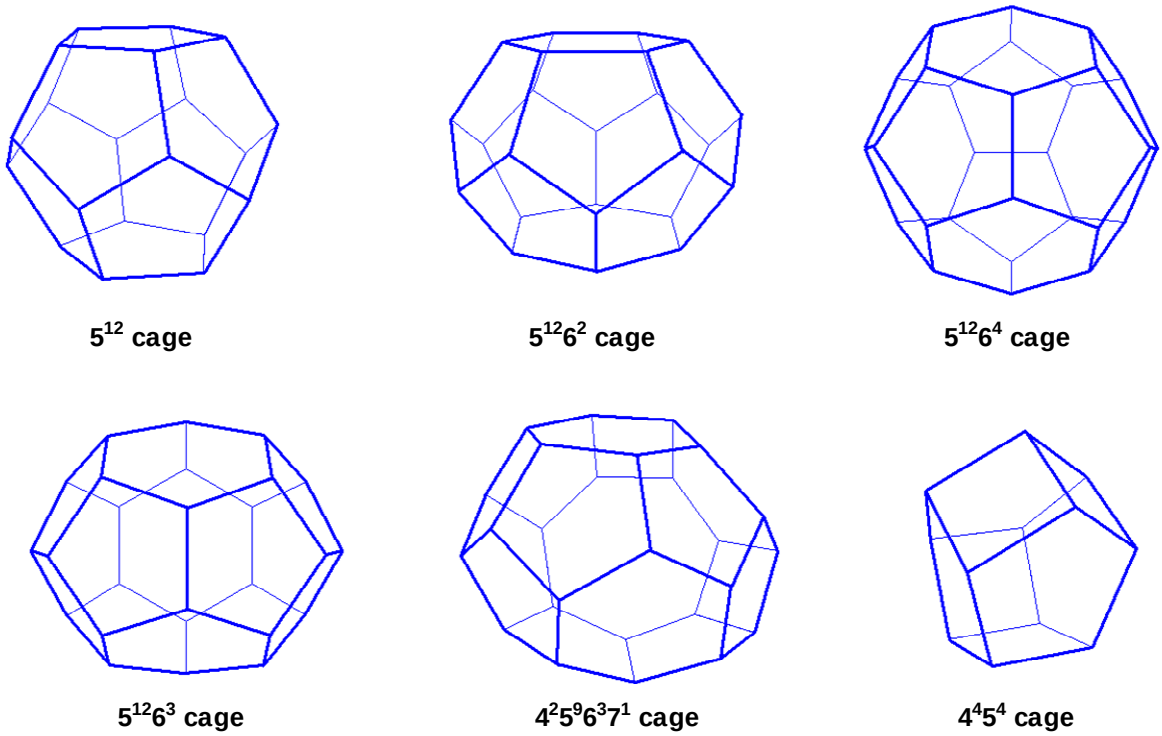

Figure 1.7 – Cages of semi-clathrate hydrate structures; Note: cages not to scale. Cages were produced in ACD Chemsketch 10.[70]

1.7 Aims

There are three major parts to this work:

1. Measurement and interpretation of plug dissociation times and enthalpies of dissociation of structure I (sI) and structure II (sII) gas clathrate hydrates of methane + ethane mixtures,
2. An investigation of preferential enclathration and the associated stripping of a certain component or components during hydrate formation from gas mixtures under typical laboratory conditions and
3. Measurement of the semi-clathrate hydrate (SCH) + aqueous solution + vapour P,T equilibria for the system tetraisopentylammonium fluoride solution (w = 0.315) + methane.

The aims of the first major part of work listed above was to use a processed natural gas (PNG) mixture, that is a natural gas containing methane and low mole fractions of heavier components, to form both sI and sII hydrates and to investigate the dissociation times of plugs

of these hydrates as well as their enthalpies of dissociation by calorimetry. PNGs have been shown to form either a sI or sII hydrate depending on the pressure and temperature of hydrate formation as well as the composition of the gas.[54] Mixtures of methane + ethane have also been shown to form either a sI or sII hydrate depending on the pressure and temperature of hydrate formation as well as the composition of the gas.[71,72] On this basis it was assumed that methane + ethane mixtures were representative of PNGs. CSMPlug, a hydrate plug dissociation prediction program developed by Peters[49] at the Colorado School of Mines, predicts that sII hydrate plugs of PNGs take approximately 30 % longer to dissociate than sI hydrate plugs. An aim of this work was to test this prediction by experimental plug dissociation time measurements. The CSMPlug prediction is based upon a larger dissociation enthalpy for the sII hydrate than the sI hydrate (fixed values are assumed for each hydrate structure, the gas composition and P and T are not taken into account). A further aim of this section of work was to compare the measured enthalpies of dissociation to values predicted from P,T phase data and the Clapeyron equation and to assess whether the enthalpies of dissociation of the sII hydrates were always greater than the sI hydrates.

The second part of this work concerned the modelling of preferential enclathration. Preferential enclathration is defined in this work as the preference of the hydrate phase to enclathrate a certain component or components to a higher mole fraction on a water free basis than in the gas phase. The preferential enclathration of components results in their depletion or stripping from the gas phase. If the gas phase is constantly replenished as in a pipeline or a system with a large mole ratio of gas to water then this preferential enclathration causes little stripping in the gas phase. Typically the laboratory preparation of hydrate plugs involves the supply of only just enough gas to ensure that all the initial ice or water is converted to hydrate (low mole ratio of gas to water). For these typical laboratory systems it was hypothesised that there could be significant stripping of the gas phase due to preferential enclathration. For hydrate formation from methane + ethane mixtures it was also hypothesised that both sI and sII hydrates may form due to a changing composition of the gas phase as hydrate formation proceeded. The aim of this work was to produce stepwise models of the gas phase composition as hydrate formation proceeded from melting ice (a typical laboratory hydrate preparation method) and to validate these models against experimental measurements of the

gas phase composition as hydrate formation proceeded by the same method in a laboratory pressure cell.

The third part of this work focused on *P*,*T* semi-clathrate hydrate (SCH) + aqueous + vapour phase equilibria of tetraisopentylammonium fluoride solution (w = 0.315) + methane. The aim of this work was to investigate the stability of this methane SCH as a function of temperature and pressure and to compare the measurements to published results for the SCH forming system tetrabutylammonium bromide solution (w = 0.30) + methane as well as pure methane sI hydrate.

1.8 Thesis outline

Chapter 2 entitled "Background to Instrumental and Analytical techniques" contain details of each instrumental and analytical technique used in this work, including differential scanning calorimetry (DSC), powder X-ray diffraction, Raman spectroscopy, Karl Fischer titration and NMR spectroscopy. Where appropriate examples of the use of these techniques on gas hydrates or SCHs is presented.

Chapter 3 discusses the fact that processed natural gases, low in components heavier than methane, may form either sI or sII gas hydrates with water depending upon the pressure, temperature and composition. Measurements of the dissociation time of sI and sII hydrate plugs prepared in the laboratory from methane + ethane mixtures are presented and compared to existing models of hydrate dissociation. An important parameter in hydrate dissociation models is the enthalpy of dissociation of the hydrate. Measurements of the enthalpy of dissociation from sII hydrates prepared from methane + ethane mixtures are presented and compared both to the sI dissociation enthalpy of pure methane hydrate as well as predictions of enthalpies of dissociation calculated from the Clapeyron equation. This chapter also includes a literature review of laboratory hydrate plug formation experiments as well as gas hydrate enthalpy of dissociation measurements and predictions using the Clapeyron equation.

Preferential enclathration occurs when a component of a gas mixture is enclathrated in the hydrate phase on a water free basis to a higher mole fraction than in the free gas. This results in the component being stripped from the free gas phase. Composition changes in the gases

may result in the formation of both sI and sII hydrates especially in systems where there is a high mole ratio of water to gas, which are typical laboratory formation conditions. Chapter 4 presents models that consider preferential enclathration and the stripping of the free gas phase for hydrate formations with gas mixtures. These models include a constant volume and a constant pressure model. The constant volume model assumes an initial step pressurization of a cell filled with ice particles. The formation of hydrates occurs by pressure drop when the cell is heating just above ice's melting point. The constant pressure model assumes that the pressure in a cell containing slowly melting ice is maintained by compression of a syringe or piston pump. The constant pressure model is compared to an experiment whereby the composition of the gas was monitored as the hydrate formation proceeded.

In Chapter 5 SCH+Aq+V *P*,*T* equilibria measurements are presented for methane + tetraisopentylammonium fluoride (TIPAF) in solution at a mole ratio of TIPAF·38.3H_2O. TIPAF was selected as the salt to study as it forms a SCH, TIPAF·38H_2O, with a melting point exceeding 30 °C and a relatively high number of unoccupied 5^{12} cages per mole of salt. TIPAF was unavailable commercially and therefore was prepared from triisopentylamine, isopentyl bromide, and silver fluoride. A dilute solution of TIPAF was prepared and crystallised SCH was filtered from the solution and tested for water content by Karl Fischer titration, this confirmed a hydration number of 38.3 for the SCH. This SCH was used in measurements of the *P*,*T* equilibria with methane in a pressure cell. These measurements are compared to similar measurements conducted recently of tetrabutylammonium bromide (TBAB) solution + methane SCH+Aq+V *P*,*T* equilibria.

Chapter 6 presents conclusions and recommendations for all the work encompassed in this thesis as well as potential future work. Following Chapter 6 are references and appendices.

Chapter 2 BACKGROUND TO INSTRUMENTAL AND ANALYTICAL METHODS

In this work a variety of instrumental and analytical techniques have been used and applied to the study of natural gas hydrates formed from methane and ethane gases and tetraalkylammonium salt clathrate hydrates, namely tetraisopentylammonium fluoride clathrates hydrates.

Differential scanning calorimetry (DSC) was used to study the enthalpies of dissociation of (methane + ethane) gas hydrates of different structures (sI and sII). X-ray diffraction and Raman spectroscopy were used to probe the structure of hydrate formed in the experiments and gas liquid chromatography was used to analyse the gas composition of the hydrate phase and gases used to form the hydrates.

Karl Fischer titrations were used to determine the hydration number of tetraisopentylammonium fluoride hydrates formed. Nuclear magnetic resonance was used to asses the purity of this salt that was prepared initially from a tertiary amine and alkyl halide.

2.1 Differential scanning calorimetry

2.1.1 DSC in this work

Differential scanning calorimetry was used in this work to investigate the dissociation enthalpies of sI and sII hydrates prepared from several different mixtures of methane and ethane gases. The DSC used was a MC-DSC 4100 HT from Calorimetry Science Corporation (now part of TA instruments) with a high pressure kit for measurements up to a pressure of 13.8 MPa.

2.1.2 Background to calorimetry

Calorimetry is the science concerned with the measurement of the quantities of heat exchanged. There are many different types of calorimeters available to measure calorimetric or thermal properties and thermal events associated with physical processes and reactions. These methods are discussed in detail in the IUPAC's Experimental Thermodynamics

volumes specifically volume IV entitled "Solution Calorimetry"[73] and Volume VI entitled "Measurement of the Thermodynamic Properties of the Single Phase".[74] This description deals with one of the most important and widely used techniques in calorimetry, differential scanning calorimeter (DSC).

The term differential scanning calorimetry implies that there is a differential signal between a sample and a reference that is monitored while scanning in temperature. There are two main types of DSC techniques, heat flux and power compensated. The DSC used in this work was the heat flux type, so only this type of DSC is considered here, power compensated DSCs are covered in detail by Claudy.[75]

2.1.3 Theory of heat flux differential scanning calorimetry

Heat flux DSC is a modification of the technique of differential thermal analysis (DTA) and was alternatively referred to as quantitative differential thermal analysis (QDTA) when it was initially developed. DTA monitors the temperature difference between a sample and a reference cell as they are heated together, temperature probes (commonly differential thermocouple junctions) are inserted directly into the sample and reference material. A reference material is chosen that has no thermal transitions in the temperature range of interest. A schematic of a DTA apparatus is presented in Figure 2.1. If the sample has a higher heat capacity than the reference the sample temperature will lag the reference temperature and a temperature difference, ΔT, will be observed. This temperature difference will deviate greatly when there is a phase change such as melting (endothermic) or decomposition (exothermic). It would appear that ΔT should be proportional to the difference in heat flow or flux between the sample and reference, however this proportionality is also effected by the thermal conductivity of the sample and reference and the thermal contact resistance between the temperature probe and the materials (important particularly for solid materials). These factors mean that DTA is non-quantitative. In 1955 however Boersma[76] recognized that if the temperature measurement was taken out of direct contact with the material and instead placed in contact with the furnaces that contain the reference and sample crucibles that the temperature difference measured would be proportional to the difference in heat flowing to the sample and reference and that this proportionality would not be dependent on the thermal conductivity or other properties of the sample and/or reference materials.

Boersma's schematic of the sample-holder arrangement is shown in Figure 2.2. Boersma's design was the first heat flow DSC, a heat flow DSC may also be referred to as a heat flux DSC if the base areas of the reference and sample crucibles are identical (which is almost always the case). In modern heat flux DSC the difference in heat flux between the furnace and the sample and reference crucibles may be measured instead of measuring the temperature difference. Thermoelectric devices (TED) are used to measure the heat fluxes. Following the mathematical treatment of Claudy[75] the energy flux (heat flow rate or power, P) exchanged between the furnace and the sample and reference crucibles may be given by eq (2.1).

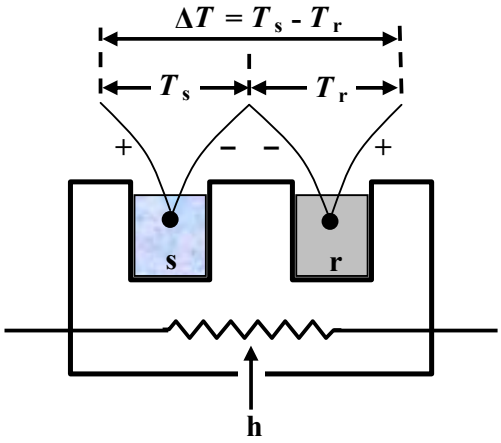

Figure 2.1 – Differential thermal analysis schematic; s = sample, r = reference, h = heat source, T_s = sample temperature, T_r = reference temperature, ΔT = differential thermocouple.

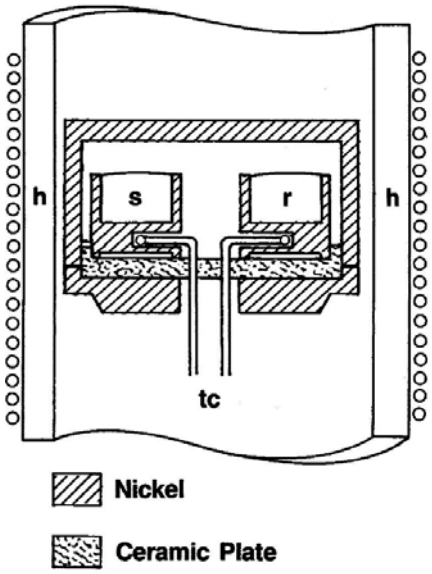

Figure 2.2 – Boersma's original sample holder design); s = sample, r = reference, h = heat source, tc = differential thermocouple. (Reproduced from Mraw[77]).

$$\begin{cases} P^{\mathrm{s}} = \left(C_p^{\mathrm{s}} + C_{p,\mathrm{cr}}^{\mathrm{s}}\right)\left(\mathrm{d}T^{\mathrm{s}}/\mathrm{d}t\right) + \Phi_{\mathrm{tr}}, \\ P^{\mathrm{r}} = \left(C_p^{\mathrm{r}} + C_{p,\mathrm{cr}}^{\mathrm{r}}\right)\left(\mathrm{d}T^{\mathrm{r}}/\mathrm{d}t\right). \end{cases} \tag{2.1}$$

It is assumed that in this equation the sample and reference furnaces are of equal heat capacity. The subscript s refers to the sample (C_p^{s} and $C_{p,\mathrm{cr}}^{\mathrm{s}}$ are the sample and sample crucible heat capacities respectively) and the subscript r refers to the reference (C_p^{r} and $C_{p,\mathrm{cr}}^{\mathrm{r}}$ are the reference and reference crucible heat capacities respectively). The heat flow rate as a result of thermal transformation is represented by Φ_{tr}. If the heating rate of the reference and sample are the same, that is:

$$\frac{\mathrm{d}T^{\mathrm{s}}}{\mathrm{d}t} \approx \frac{\mathrm{d}T^{\mathrm{r}}}{\mathrm{d}t} = \frac{\mathrm{d}T}{\mathrm{d}t}, \tag{2.2}$$

then the calorimetric signal ΔT is given by:

$$\Delta T = k\left(P^{\mathrm{s}} - P^{\mathrm{r}}\right) = \left(C_p^{\mathrm{s}} + C_{p,\mathrm{cr}}^{\mathrm{s}} - C_p^{\mathrm{r}} - C_{p,\mathrm{cr}}^{\mathrm{r}}\right)\frac{\mathrm{d}T}{\mathrm{d}t} + \Phi_{\mathrm{tr}}, \tag{2.3}$$

where k is a calibration factor.

The theory of operation of a heat flux DSC may be further considered by an electrical circuit analogy (for more detail see Appendix C), a circuit diagram is shown in Figure 2.3. The furnace at temperature E transfers heat to the sample and reference at temperatures U^{s} and U^{r} respectively via the thermal resistances R^{s} (between the furnace and sample) and R^{r} (between the furnace and reference) respectively to the sample and reference thermal masses represented by the heat capacities C^{s} and C^{r} respectively. These heat capacities represent the sum of the thermal masses of the crucible, measuring device and sample or reference material. If Kirchhoff's current law is analogously applied to the heat flows in the circuit of Figure 2.3 then eq (2.4) is generated:

$$\begin{cases} C^{\mathrm{s}} \dfrac{\mathrm{d}U^{\mathrm{s}}}{\mathrm{d}t} = \dfrac{E - U^{\mathrm{s}}}{R^{\mathrm{s}}} + \Phi_{\mathrm{tr}} \\ C^{\mathrm{r}} \dfrac{\mathrm{d}U^{\mathrm{r}}}{\mathrm{d}t} = \dfrac{E - U^{\mathrm{r}}}{R^{\mathrm{r}}} \end{cases} \tag{2.4}$$

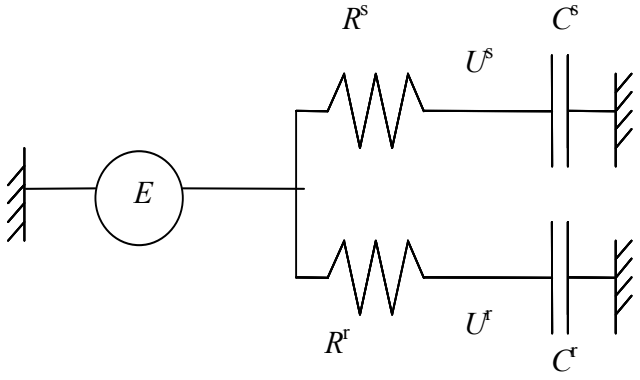

Figure 2.3 – Electrical circuit equivalent of heat flux DSC; E = temperature of the furnace, R^{s} = thermal resistance between the furnace and sample, R^{r} = thermal resistance between the furnace and reference crucible, U^{s} = temperature of the sample, U^{r} = temperature of the reference, C^{s} = heat capacity of the sample and crucible, and C^{r} = heat capacity of the reference and crucible. (Reproduced from Claudy[75] in Goodwin et al.[74]).

The calorimetric signal ΔT is given by:

$$\Delta T = U^{\mathrm{r}} - U^{\mathrm{s}} \tag{2.5}$$

and may be determined by a "symmetric" instrument in which the resistance and heat capacities of the sample and reference are approximately equal:

$$\begin{aligned} R^{\mathrm{s}} &\approx R^{\mathrm{r}} = R, \text{ and} \\ C^{\mathrm{s}} &\approx C^{\mathrm{r}} = C. \end{aligned} \tag{2.6}$$

Combining eqs (2.4). (2.5) and (2.6) leads to:

$$\Phi_{\mathrm{tr}} = \frac{\Delta T}{R} + C \frac{\mathrm{d}\Delta T}{\mathrm{d}t}. \tag{2.7}$$

This arrangement is advantageous because Φ_{tr} is independent of E and for this reason the effect of furnace noise to the calorimetric signal is minimized. However furnace to crucible and intercruciable heat exchange are neglected in this model. The thermoelectric disks measure most of the heat flow but there is also heat flow to the gas flushing the DSC apparatus. Heat transfer to the gas by conduction though can be accounted for by including a thermal resistance in parallel to the other resistors in the analogous electric circuit. The modified circuit diagram to include these effects is shown in Figure 2.4.

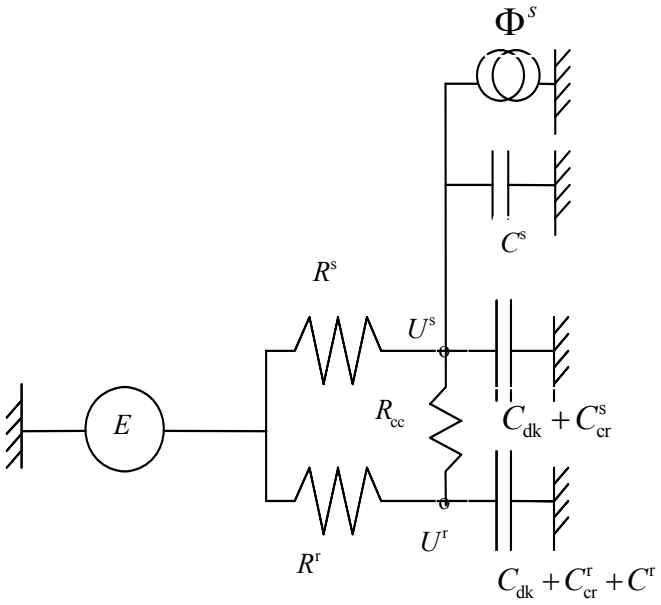

Figure 2.4 – Electrical circuit equivalent of heat flux DSC with coupled cells; E = temperature of the furnace, R^s = thermal resistance between the furnace and sample crucible, R^r = thermal resistance between the furnace and reference crucible, R_{cc} = thermal resistance between the sample and reference crucibles, U^s = temperature of the sample, U^r = temperature of the reference, Φ = heat flux emanating from the sample, C^s = heat capacity of the sample, C_{dk} = heat capacity of the disk, C^s_{cr} = heat capacity of the sample crucible, C^r_{cr} = heat capacity of the reference crucible, and C^r = heat capacity of the reference material. (Reproduced from Claudy[75] in Goodwin et al.[74]).

The equations that lead from Figure 2.4 are given by

$$\left(C^s_{cr} + C_{dk}\right)\frac{dU^s}{dt} = \frac{E - U^s}{R^s} + \Phi_{tr} + \frac{U^r - U^s}{R_{cc}}, \tag{2.8}$$

and

$$\left(C^{\mathrm{r}} + C_{\mathrm{cr}}^{\mathrm{r}} + C_{\mathrm{dk}}\right)\frac{\mathrm{d}U^{\mathrm{r}}}{\mathrm{d}t} = \frac{E - U^{\mathrm{r}}}{R^{\mathrm{r}}} + \frac{U^{\mathrm{s}} - U^{\mathrm{r}}}{R_{\mathrm{cc}}}, \tag{2.9}$$

where $C_{\mathrm{cr}}^{\mathrm{r}}$ and $C_{\mathrm{cr}}^{\mathrm{s}}$ are the heat capacities of the reference and sample crucibles respectively and C_{dk} is the heat capacity of the thermoelectric disk. The thermal resistance between the sample and reference crucibles is represented by R_{cc}.

Solving eqs (2.8) and (2.9) for Φ_{tr} assuming a symmetric calorimeter gives:

$$\Phi_{\mathrm{tr}} = \Delta T\left(\frac{1}{R} + \frac{2}{R_{\mathrm{cc}}}\right) - C\frac{\mathrm{d}\Delta T}{\mathrm{d}t} \tag{2.10}$$

This model only takes in to account first order effects, for a real instrument there may be higher order effects which are included in an expansion of the form:

$$\Phi_{\mathrm{tr}} = k_1\Delta T + k_2\frac{\mathrm{d}\Delta T}{\mathrm{d}t} + k_3\frac{\mathrm{d}^2\Delta T}{\mathrm{d}t^2} + \mathrm{K} \tag{2.11}$$

where the values of the constants k_1, k_2, k_3 etc are determined by calibration.

Other types and methods of DSC such as adiabatic DSC, single cell DSC and temperature modulated DSC are discussed in detail by Claudy.[75]

2.1.4 Phase transition measurement by DSC

When a phase transition is recorded, such as an enthalpy of fusion, by constant scan rate DSC a large peak in the signal from the sample occurs. The signal can be plotted as a differential power versus temperature chart, an example of which is shown in Figure 2.5. When a baseline has been determined, the area between this baseline and the peak is proportional to the enthalpy of transition (strictly speaking a scan with an empty crucible performed at the same scan rate should be conducted first and this signal deducted to remove offset but this

offset is usually smooth and flat over the temperature range of the peak and can be neglected). The specific enthalpy (enthalpy per unit mass) of transition, Δh, is given by:

$$\Delta h = \frac{\int \left[P - P_{\mathrm{b}}(t) \right] \mathrm{d}t}{m_{sam}}, \tag{2.12}$$

where P is the differential power signal, P_{b} is the peak baseline (this may be a constant value or a linear or polynomial function) and m_{sam} is the sample mass. At a constant scan rate, K_{scan} (= dT/dt) the integration of eq (2.12) can alternatively be conducted with respect to temperature:

$$\Delta h = \frac{\int \left[P - P_{\mathrm{b}}(T) \right] \mathrm{d}T}{m_{\mathrm{sam}} K_{\mathrm{scan}}}. \tag{2.13}$$

It is important to note that the DSC will require calibration; calibration is commonly achieved by matching calibration constant to produce the heat capacity of a standard material (described briefly in the next section) however it is good practice to check the calibration of the DSC with a compound with a well known value of Δh such as ice, other substances may also be used.[78]

The temperature of the transition is strictly the point that the peak begins to rise from the baseline however this is difficult to determine and is considered to be non-reproducible. The extrapolated onset temperature of transition, labelled T_{tr} is however considered reproducible. As the temperature is not measured in the sample the true temperature of the sample will lag that of the monitored temperature. This means that the true temperature of the transition will deviate from the value of T_{tr}. The true transitional temperature can be more accurately estimated by repeating measurements at two or more different scan rates and extrapolating to the condition of a scan rate of zero where the temperature lag between the monitored and true sample should be zero.

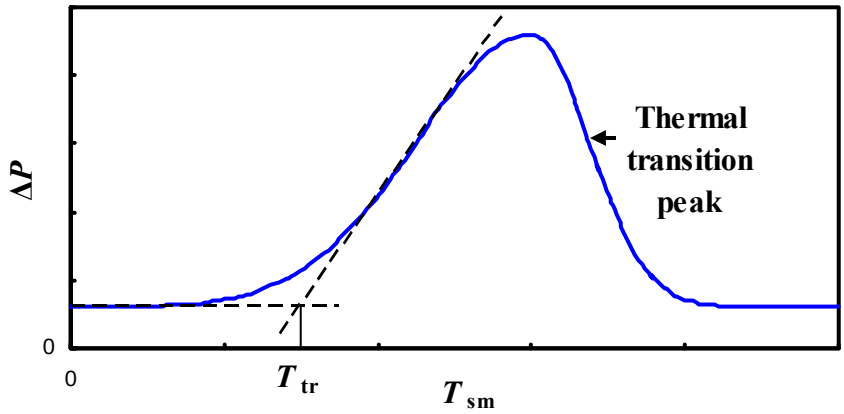

Figure 2.5 – DSC recorded thermal transition peak of differential power (ΔP) versus monitored sample temperature (T_{sm}); T_{tr} = extrapolated onset temperature of transition.

Heat capacities may also be measured by DSC, however no heat capacities were measured in this work, Mraw[77] provides a summary of the methods for measuring heat capacities, particularly for solid samples.

2.1.5 Instrument in this work

The calorimeter used in this work was a heat flux DSC model MC-DSC 4100 HT from Calorimetry Sciences Corporation (now part of TA instruments). The design of the instrument obtained from the user's manual is shown in Figure 2.6. This DSC uses a cascade of TEDs or Peltier modules to heat and cool the furnace.

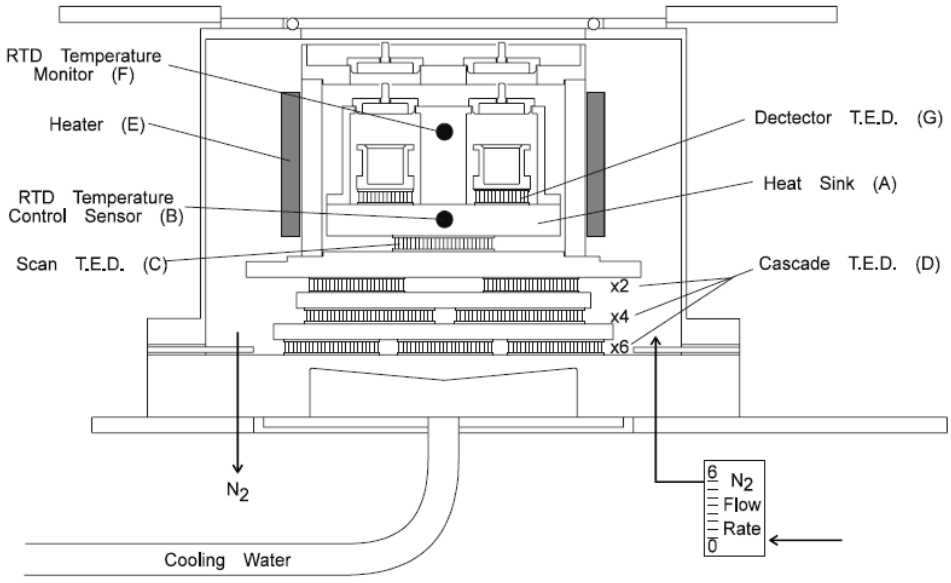

Figure 2.6 – Calscorp MC-DSC 4100 HT DSC measuring unit; RTD = Resistance temperature detector, T.E.D = Thermoelectric device. (Reproduced from user's manual[79]).

2.2 X-ray diffraction

2.2.1 X-ray diffraction in this work

Although there are several methods which can reveal gas hydrate structures the most robust method of structural detection is X-ray crystallography or X-ray diffraction. In this work X-ray diffraction was used to determine the presence of sI and sII in hydrates formed from mixtures of methane and ethane + water. The patterns identified were indexed against available patterns generated from single crystal analyses from the literature.

2.2.2 X-ray diffraction background

Building on the Nobel prize winning work of Roentgen who discovered X-rays in 1895[80] and von Laue who was able to show that crystal can diffract X-rays,[81] William L. Bragg a student studying physics at Cambridge University worked out a simple law relating the observed angles of X-ray diffraction and the interatomic spacings in crystals. He discussed his work with his father, who was also a physicist, William H. Bragg. W.H. Bragg developed an X-ray spectrometer at the University of Leeds that allowed many different types of crystals to be analysed. Father and son received the 1915 Nobel Prize in physics for their work.[82]

2.2.3 Bragg's law

W.L Bragg postulated that as X-rays are very penetrating that they would only be partially reflected from each layer of atoms in a crystal. For some angles of incidence, θ, the reflected beams are in phase and a beam is observed as in Figure 2.7 (a). For other angles of incidence the reflected beams are out of phase and there is a net cancellation and no observed beam. For maximum intensity the waves must be perfectly in phase and their path differences from successive layers of atoms must be an integer number, n, of wavelengths, λ. For a separation in layers of atoms of d (sometimes referred to as a d-value) this path difference is equal to $2d\sin\theta$, this is the path difference illustrated in Figure 2.8 between rays 1 and 2. This relationship is known as Bragg's law:

$$n\lambda = 2d\sin\theta\,. \tag{2.14}$$

From the information collected from a single crystal from scattering from a range of different crystal orientations with respect to the X-ray beam it is possible to precisely work out the complete crystal structure (for more detail of this see Ladd and Palmer[83]), however a pattern may also be recorded for a powdered solid in which there are many small crystals randomly orientated with respect to each other, this is referred to as powder X-ray diffraction. Rather than a series of spots (called Laue spots) a series of rings or diffraction circles are recorded. Each of these diffraction circles corresponds to a cone of scattered radiation, called a Debye-Scherrer cone, which emanates from the sample. The angle between the beam axis and the diffraction circle is 2θ, this along with the wavelength of the X-ray source allows the calculation of a d-value. Often the powder diffraction data is presented as a diffractogram, which plot the intensity of the scattered X-rays as a function of 2θ or d-value. A diffractogram of hexagonal ice, sI hydrate and sII hydrate is shown in Figure 2.9. While technically it is possible to determine the crystal structure from powder X-ray diffraction data using the method of Rietvald analysis,[84] it is much simpler to compare and index the experimental data against literature patterns or d-values for known crystal structures if they are available. A number of large databases exist such as the Cambridge Structural Database[85] and the Powder Diffraction File of the International Centre for Diffraction Data.[86] With software such as Powdercell[87] it is also possible to predict a powder pattern from literature single crystal data. In Figure 2.9 the literature data of Owston[88] for hexagonal ice and Kirchner et al.[26] for sI (methane) hydrate and sII (methane + ethanol + propane) hydrate have been used with Powdercell to generate the pattern.

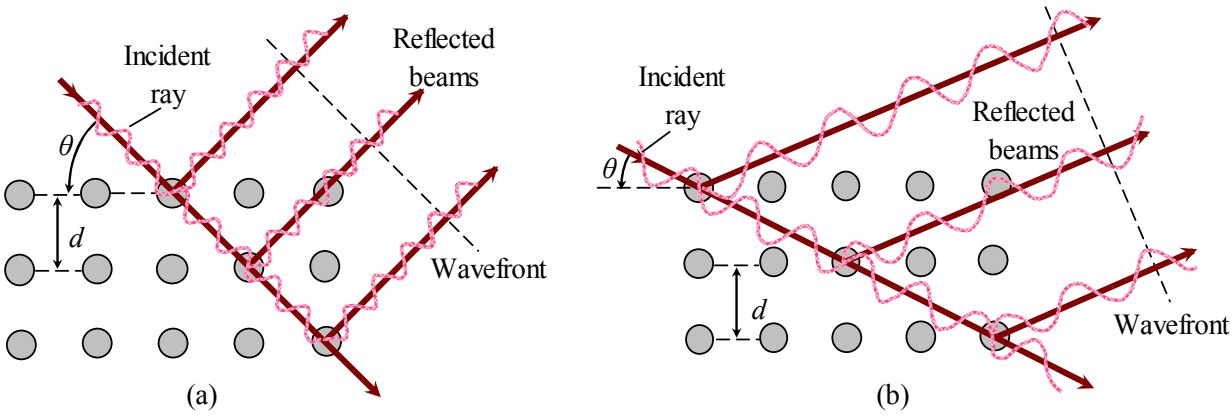

Figure 2.7 – Reflection of X-rays from successive layers of atoms in a crystal. (a) The reflected waves are exactly in phase a reinforce each other. (b) the reflected waves are out of phase and cancel out, d = interatomic spacing, θ = incident angle of X-ray. (Modified from Jones and Childers[89]).

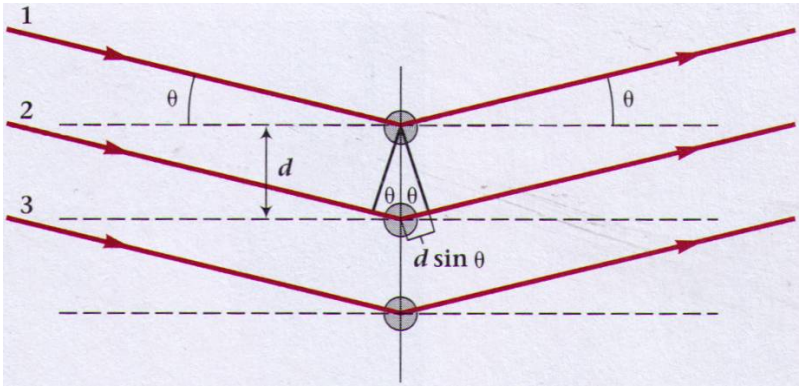

Figure 2.8 – Illustration of diffraction paths difference, maxima occur at angle where 2dsinθ is an integer multiple of wavelengths. (Reproduced from Jones and Childers[89]).

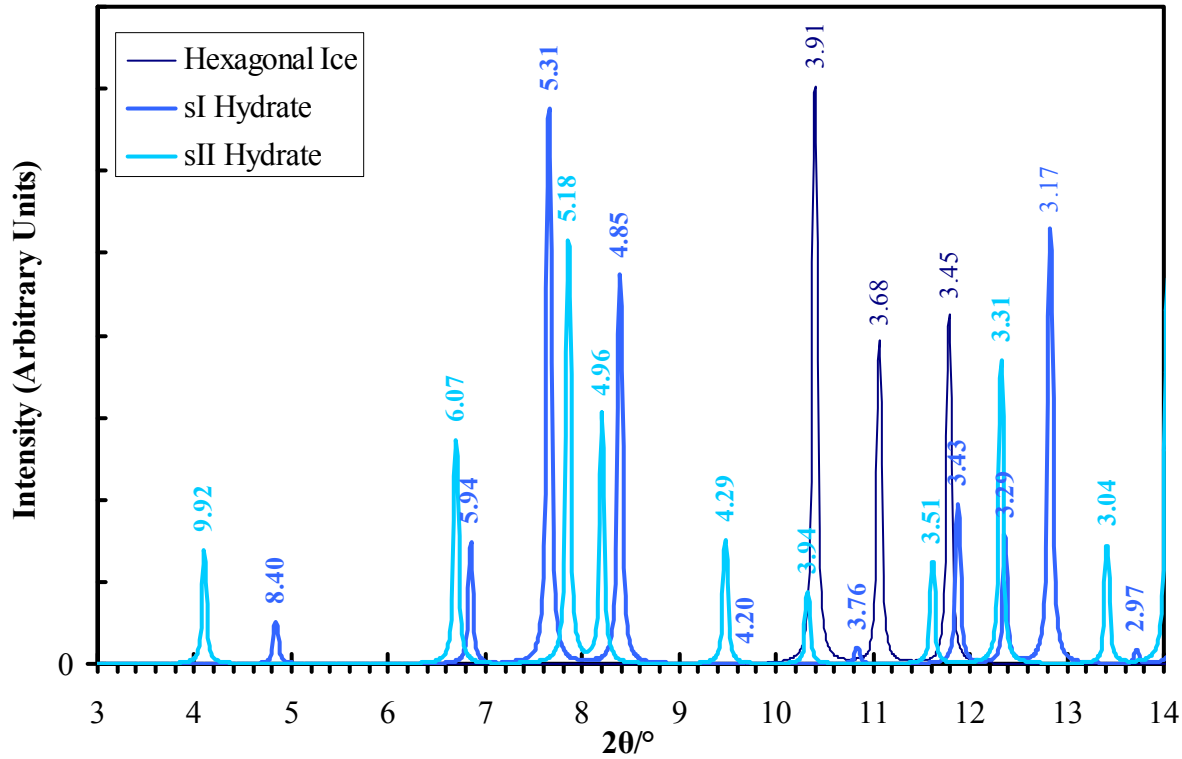

Figure 2.9 – X-ray diffractogram for hexagonal ice, sI hydrate and sII hydrate; d-values in Ångströms are listed above the peaks, data generated using PowderCell[87] using the data of Owston[88] for hexagonal ice and Kirchner et al.[26] for sI hydrate (methane hydrate) and sII hydrate (methane + ethanol + propane), λ = 0.70903165 Å.

2.2.4 X-ray diffraction instrumentation

The basic components of instrumentation for X-ray diffraction collection are an X-ray source (usually an X-ray tube) and a detector. These component are illustrated in Figure 2.10, this figure shows one of many possible layouts which may or may not include a beam stop (which stops non-diffracted X-ray radiation reaching the detector). Not shown in Figure 2.10 is a goniometer, on which the sample would usually sit to allow the sample to be rotated to a precise angular position. The detector in most instruments can also be rotated.

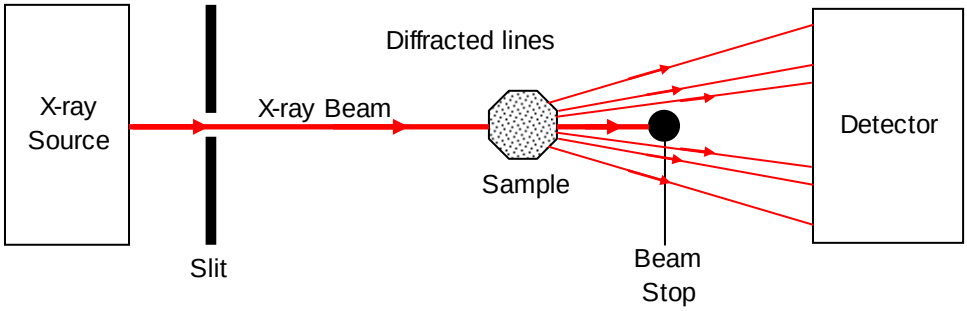

Figure 2.10 – An example of X-ray diffraction instrumentation.

2.2.5 X-ray detectors

The earliest detector used was a photographic plate and photographic film. In modern instruments charge-coupled devices (CCD) are used as detectors. More information on the theory behind the operation of CCD may be found in Skoog et al.[90] The main advantage of the CCD is that the information is digitized and can be quickly analysed by computer.

2.2.6 X-ray diffraction instrument in this work

X-ray diffraction performed in this work used the Bruker Smart CCD area-detector diffractometer with a Mo Kα X-ray source in the Chemistry department of the University of Canterbury. Although this instrument is usually used to collect single crystal X-ray diffraction data but it can be used to collect powder diffraction data if the 360 ° phi drive and scan function is used. This produces an image of diffraction circles from which d-values can be obtained.

2.3 Raman spectroscopy

In 1928 the Indian physicist Chandrasekhara Venkata Raman observed that a small fraction of light scattered by molecules undergoes a shift in wavelength/frequency. Raman noted that the shift depended on the chemical structure and was awarded the 1930 Nobel prize in Physics for his discovery.[91]

2.3.1 Raman and Rayleigh scattering

When the vast majority of light encounters a molecule it scatters elastically, with no change in frequency, this is referred to as Rayleigh scattering, however in a very small fraction of interactions (approximately 1 in 10 million) the molecule will either absorb or release some energy during the scattering, this is referred to as Raman scattering. In Raman Stokes scattering the scattered frequency is less than that of the incident radiation, so the molecule has gained energy from the photon or conversely the photon has lost energy to the molecule. In Raman Anti-Stokes Scattering the scattered frequency is greater than that of the incident radiation, so the molecule has lost energy to the photon or conversely the photon has gained energy from the molecule. Rayleigh and both Stokes and Anti-Stokes Raman scattering are illustrated in Figure 2.11.

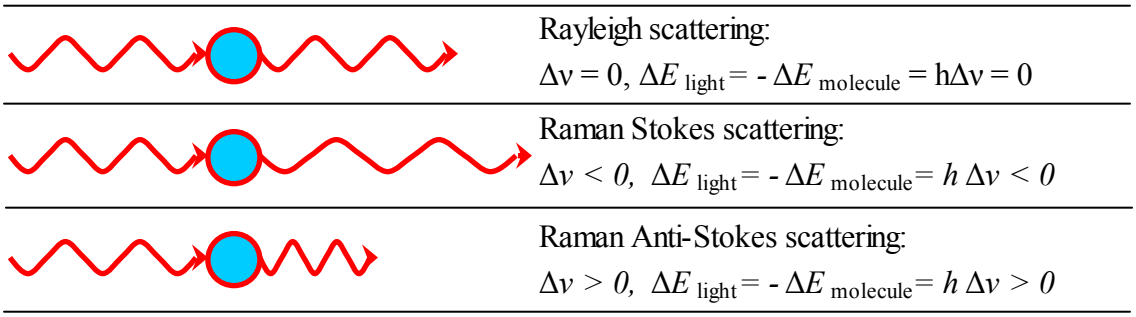

Figure 2.11 – Light encountering a molecule by Rayleigh and Raman scattering; ν = frequency of photon/ray of light, $\Delta\nu$ = difference between scattered light frequency and incident light frequency, h = Planck's constant, ΔE_{light} = difference in energy between the incident and scattered photon, $\Delta E_{molecule} = -\Delta E_{light}$ = energy gained by molecule during scattering process.

2.3.2 Mechanism of Raman and Rayleigh scattering

In Raman spectroscopy the frequency of light is usually well away from the absorption peaks of the molecule being probed. Figure 2.12 (adapted from Skoog et al.[90]) shows qualitatively

each type of scattering on an energy diagram. The upward arrows show the energy of the incident photon that is absorbed by the molecule and the downwards arrow shows the energy of the scattered photon released by the molecule. The process of absorption is not quantized in terms of the molecule's energy levels, the molecule absorbs the energy of the photon, $h\nu_0$ (where h is Planck's constant and ν_0 is the incident photon frequency), and is raised in energy to a virtual state between the ground and first electronic state. In the middle third of Figure 2.12 the elastic process of Rayleigh scattering is represented, the energy of the incident photon $h\nu_0$, is equal to the energy of the scattered photon, $h\nu_s$ (where ν_s is the scattered photon frequency). Two different Rayleigh scattering possibilities are illustrated, one on the left in which the molecule is in the ground vibrational state and returns to the ground vibration state, and one on the right where the molecule is in the first vibrational state and returns to the first vibrational state. Generally the number of molecules in the non-ground vibrational states at room temperature is small so most of the Rayleigh scattering will usually occur by the process illustrated on the left hand side. Raman Stokes scattering is shown in the left third of Figure 2.12, in this process the molecule is raised in energy from the ground vibrational state but returns to the first vibration state, overall the molecule loses energy to the photon in the amount equal to the difference in energy between the molecule's vibrational energy levels, ΔE. Raman Anti-Stokes scattering is shown in the right third of Figure 2.12, in this process the molecule is initially in the first vibrational level but after scattering drops to the ground vibrational state, a net loss of energy from the molecule to the scattered photon by the amount ΔE. Due to the low number of molecules above the ground vibrational state at room temperature Raman Anti-Stokes scattering is less likely to occur than Raman Stokes scattering, higher temperatures will increases the ratio of Anti-Stokes to Stokes scattering by increasing molecular populations in above ground vibrational states.

2.3.3 The wave model of Raman scattering

The radiation source that is focused on a sample to record its Raman Spectrum can be viewed as an electromagnetic wave rather than a photon. Figure 2.13 shows an electromagnetic wave, the electric field part of the wave and the magnetic field part of the wave travel in the same direction in perpendicular planes. The electric field of electromagnetic radiation, E, can be described by eq (2.15) where E_0 is the amplitude of the radiation, ν_{ex} is the frequency of the radiation and t is time.

$$E = E_0 \cos\left(2\pi \nu_{ex} t\right). \tag{2.15}$$

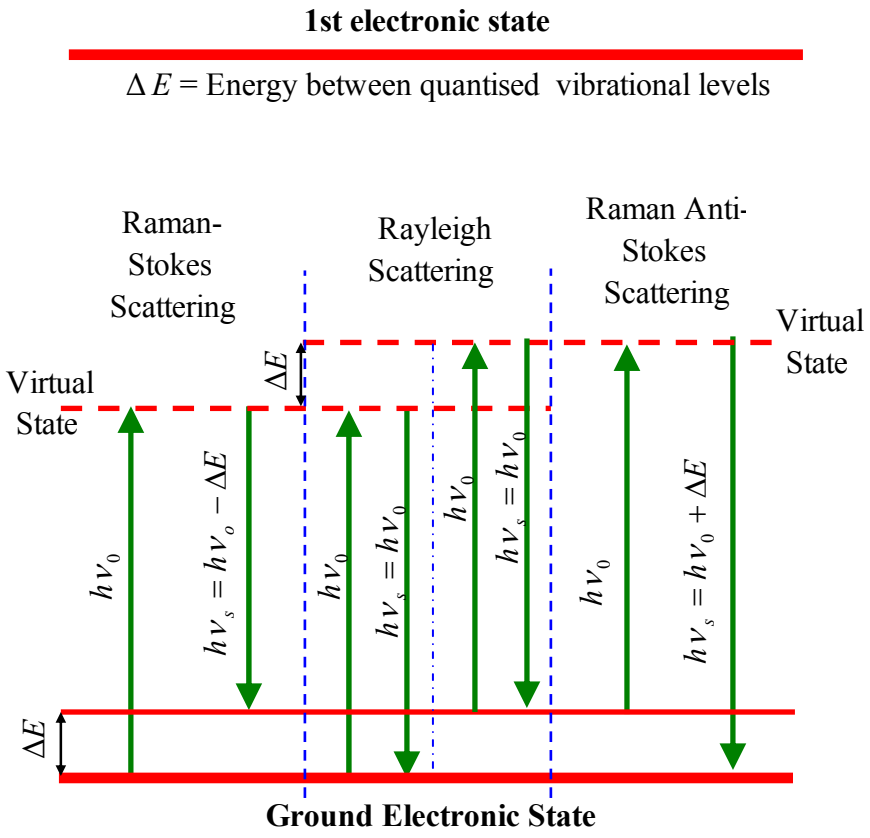

Figure 2.12 – Energy level diagram for Raman and Rayleigh Scattering. (Adapted from Skoog et al.[90]).

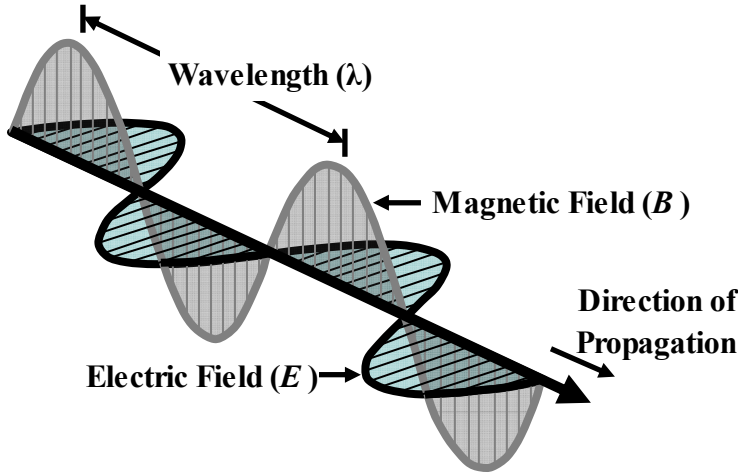

Figure 2.13 – The electromagnetic wave. (Adapted from Skoog et al.[90]).

When the electric field of the wave interacts with the electron cloud of the sample's molecules it induces a dipole moment, *m*, this is described by eq (2.16), where α is the polarizability (a measure of the deformability of the molecule's electron cloud):

$$m = \alpha E = \alpha E_0 \cos\left(2\pi \nu_{ex} t\right). \tag{2.16}$$

To be Raman active the polarizability of the molecule's bond must vary with the bond length. Equation (2.17) describes the change in the polarizability with the bond length, where *r* is the bond length, r_{eq} is the equilibrium bond length and α_0 is the polarizability when the bond length is at is equilibrium length.

$$\alpha = \alpha_0 + \left(r - r_{eq}\right)\frac{\partial \alpha}{\partial r}. \tag{2.17}$$

The bond length varies with the frequency of vibration, ν_{vib} , by eq (2.18), where r_m is the ratio of the maximum bond length to equilibrium bond length:

$$\left(r - r_{eq}\right) = r_m \cos\left(2\pi \nu_{vib} t\right). \tag{2.18}$$

Substituting eq (2.18) into eq (2.17) gives:

$$\alpha = \alpha_0 + \frac{\partial \alpha}{\partial r} r_m \cos\left(2\pi \nu_{vib} t\right). \tag{2.19}$$

Substituting eq (2.19) into eq (2.16) gives:

$$m = \alpha_0 E_0 \cos\left(2\pi \nu_{ex} t\right) + E_0 r_m \frac{\partial \alpha}{\partial r} \cos\left(2\pi \nu_{vib} t\right) \cos\left(2\pi \nu_{ex} t\right). \tag{2.20}$$

By use of the trigonometric identity, eq (2.21), eq (2.20) can be rearranged to yield eq (2.22).

$$\cos\left(x\right)\cos\left(y\right) = \left[\cos\left(x+y\right) + \cos\left(x-y\right)\right]/2, \tag{2.21}$$

$$m = \alpha_0 E_0 \cos\left(2\pi \nu_{ex} t\right) + \frac{E_0 r_m}{2} \frac{\partial \alpha}{\partial r} \cos\left[2\pi\left(\nu_{ex} - \nu_{vib}\right)t\right] + \frac{E_0 r_m}{2} \frac{\partial \alpha}{\partial r} \cos\left[2\pi\left(\nu_{ex} + \nu_{vib}\right)t\right]. \quad (2.22)$$

The first term on the right hand side of eq (2.22) describes Rayleigh scattering, the second Raman Stokes scattering and the third Raman Anti-Stokes scattering.

The advantages of Raman as a spectroscopic technique are that it can be used to study solids, liquids, powders, gels, slurries and aqueous solutions. No sample preparation is required and measurements can be taken in situ and through glass. It is also non-destructive. Disadvantages of Raman are that because the Raman scattering is weak an intense light source (laser) and sensitive detectors are required. Raman equipment is also more expensive than Infrared spectroscopic equipment and the molecular fingerprints are not as complete but for the most part they are complimentary techniques. Problems may also arise with fluorescent compounds as they can interfere with Raman spectra.

Further useful information pertaining to the symmetry of the mode of vibration can be obtained by depolarization, this is discussed in detail in Skoog et al.[90]

2.3.4 Raman instrumentation

Instrumentation required for collecting Raman spectra include a laser source, sample illumination system and a spectrophotometer to measure the intensities of the scattered radiation. The laser system and sample illumination system are described briefly further below, more information on them and spectrophotometers can be found in Skoog et al.[90]

The intensity of Raman scattering is proportional to the fourth power of the frequency of the excitation source ($I \propto v_0^4$), so it is advantageous to use a high intensity light source, for this reason lasers are used as the source. A list of common frequencies is listed in Table 18-1 of Skoog et al.[90] Low frequency (long wavelengths) on the other hand are better for samples where there may be fluorescent interference or photodecomposition.

There are many possible layouts of the sample illumination system,[90] a particularly useful one that allows for in situ studies is a fibre optic system. Fibre optic sample illumination systems have been used for the study of gas hydrates in situ by focussing the laser beam through a fibre optic cable through high strength glass tube or window directly on to the hydrate phase in a pressurised cell.[36] A fibre optic sample illumination system is shown in Figure 2.14. A microscopic objective lens is used to focus the laser beam onto the end of the fibre optic bundle which carries the radiation to the sample. The fibre option bundle probe also contains collection fibres which transport the scattered radiation to the monochromator slit.

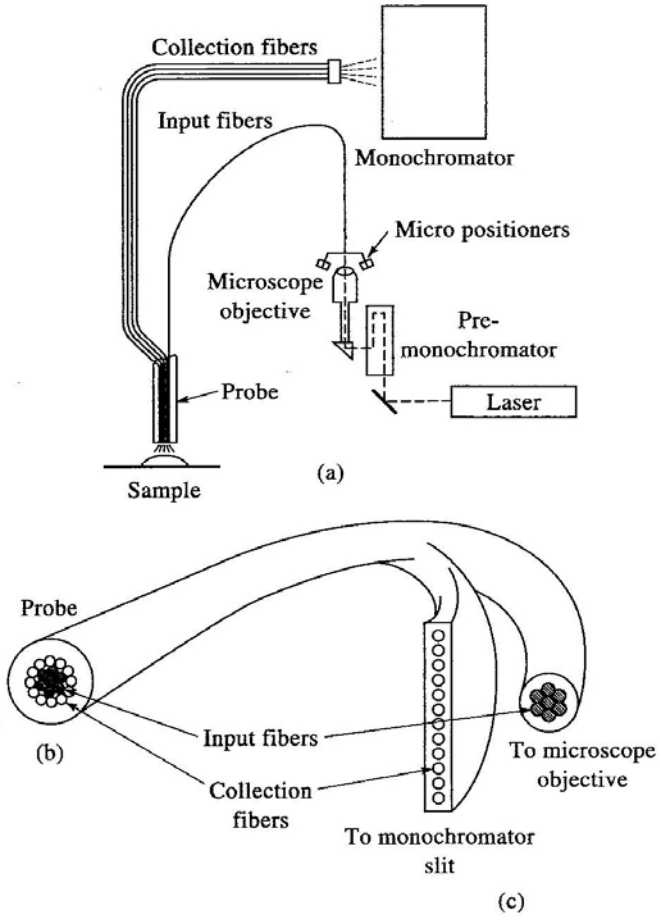

Figure 2.14 – Fibre optic sample illumination system; (a) Schematic of system, (b) Probe showing fibre bundle containing input and collection fibres (c) Collection fibre linearly arranged to enter monochromator slot. (Reproduced from Skoog et al.[90]).

2.3.5 Raman spectroscopy of gas hydrates

When molecules of methane or ethane are enclathrated in the cages of a hydrate the vibrational frequencies are slightly shifted. These slight shifts vary for the different sizes of

cage. These shifts have been studied in detail for methane by Sum et al.[92] and for methane + ethane by Subramanian et al.[36,71,72,93,94] Figure 2.15 from Subramanian et al.[72] shows the Raman wavenumber shifts in the C-H region of methane for hydrates prepared from mixtures of methane + ethane gas. Although it is clear that there are differences in the Raman shifts for methane in the small and large cages between sI and sII, the most easily obvious feature to distinguish between the structures is the ratio of peak intensities. In the sI hydrates the peak for the large $5^{12}6^2$ cage (for which there are 6 per unit cell) is considerably greater in intensity than the peak for the small 5^{12} cage (for which there are 2 per unit cell). In the sII hydrates the situation is reversed, with a larger peak for methane in the small cages rather than the large cages, this is because there are more small 5^{12} cages (16 per unit cell) than large $5^{12}6^4$ cages (8 per unit cell).

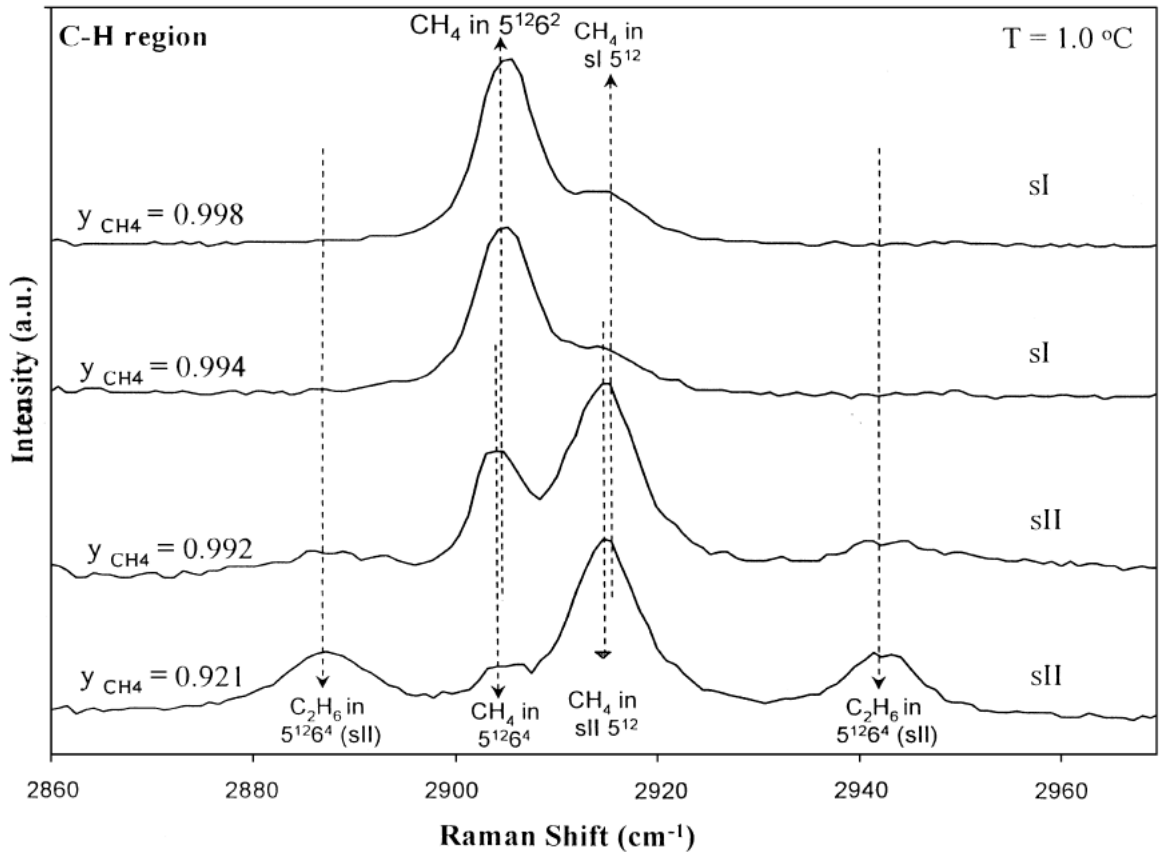

Figure 2.15 – Raman spectra in the C-H region for hydrates formed from methane + ethane gas mixtures showing the slight differences in Raman shifts for enclathrated molecules in sI and sII hydrates. (Reproduced from Subramanian et al.[72]).

Raman spectroscopy in this work was used as a method to identify the structure of a methane + ethane gas hydrates as either sI or sII. The instrument used was a Renishaw Inc. MK III of the Chemical Engineering department at the Colorado School of Mines. This instrument has a 30 mW Argon laser (λ = 514.53 nm) and a 50 μm diameter fibre optic cable that transports the light to a probe. A 20X objective lens is used to focus the laser beam. Back-scattered light is collected by the probe and transported via collection fibres of the cable before passing through a 2400 groove/mm diffraction grating to distribute the scattered light into its component wavelengths. A charged coupled device (CCD) is used to record the spectra. Calibration of the instrument was performed using the emission lines of Neon to give a spectral accuracy of 0.3 cm^{-1}, while the spectral resolution is 4.5 cm^{-1}.

Raman spectroscopy was used in this work to determine if hydrates formed from a mixture of methane + ethane gas were of sI or sII. This is presented in Chapter 3.

2.4 Gas liquid chromatography

Gas liquid chromatography (GLC), sometimes simply referred to as Gas Chromatography (GC), is a method of chromatographic separation for analytical purposes. The mobile phase is a gas that is non-reactive with the sample, usually helium or nitrogen, the stationary phase is a microscopic layer of liquid or polymer bound to an inert solid support inside a metal, glass or ceramic column. This feasibility of this method of chromatography was suggested by Martin and Synge[95] in 1941, a GLC however was not built until about 10 years by James and Martin.[96,97] Martin and Synge received the 1952 Chemistry Nobel prize for the development of partition chromatography.[98]

2.4.1 Basic principles of GLC

If a sample of multiple components is introduced abruptly in to the carrier gas, each component will distribute itself between the mobile carrier gas phase and the stationary phase of liquid or polymer bound to an inert solid. Depending on the affinity of the sample components for the stationary phase the components will be swept through the column in a definite time, called the retention time. Other factors that affect the retention time include the flow rate of carrier gas and the column temperature. The column temperature for most

instruments is adjusted between ambient and about (300 to 400) °C depending upon the volatility of the sample components. All sample components must be volatile over this temperature range for GLC to be a suitable technique.

Figure 2.17 shows a typical schematic of a GLC with a thermal conductivity detector (TCD). The carrier gas flow pressure can be adjusted at the pressure regulator and the flow rate through the column can be adjusted by a flow controller before the flow meter. The sample is injected at an injection point. Before the injection point the flow is split with some of the carrier gas flowing directly to the detector (note this split may not be needed for all types of detectors). The remaining carrier gas and sample mixture flows through the column where the separation takes place. The gas stream out of the column then heads to the detector. In Figure 2.16 a TCD schematic is shown, TCDs are a very common and versatile detector. The TCD works on the basis that at a constant electrical power an electrically heated resistor's temperature and hence resistance is dependent upon the thermal conductivity of the gas surrounding it. The detector's heated resistor elements may be platinum, gold or tungsten wire or semiconductor thermistors. Two pairs of elements are employed. One pair lie in the sample + carrier gas stream (labelled sample in Figure 2.16) and the other pair lie in the pure carrier gas or reference stream. The resistance of the element pairs are compared by placing them in a Wheatstone bridge circuit. When a sample is eluting the thermal conductivity of the sample stream will be different to that of the pure carrier gas or reference stream and the Wheatstone bridge will become imbalanced and will output a current. When no sample is being eluted the Wheatstone bridge will be in balanced and there will be no output current. Another popular detector is a flame ionization detector (FID), which employs a hydrogen-air flame that pyrolyzes most organic material to produce ions, the ions are then collected on metallic plates connected to a sensitive ammeter that records the signal. A disadvantage of FIDs however is that they can only detect flammable compounds whereas TCDs can detect non-flammable compounds like water. There are several other types of basic detectors including atomic emission detectors (AED) and thermionic detectors. GLCs have also been coupled with mass spectrometers and infrared spectrometers as detectors. More information on these alternative detectors may be found in Skoog et al.[90]

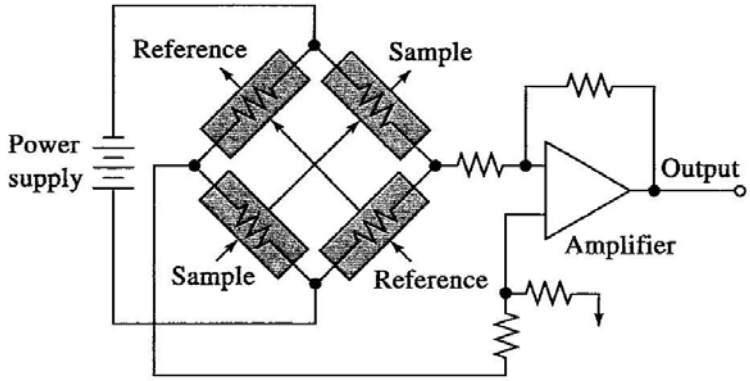

Figure 2.16 – TCD detector, an arrangement of two sample detector and two reference detector cells. (Reproduced from Skoog et al.[90]).

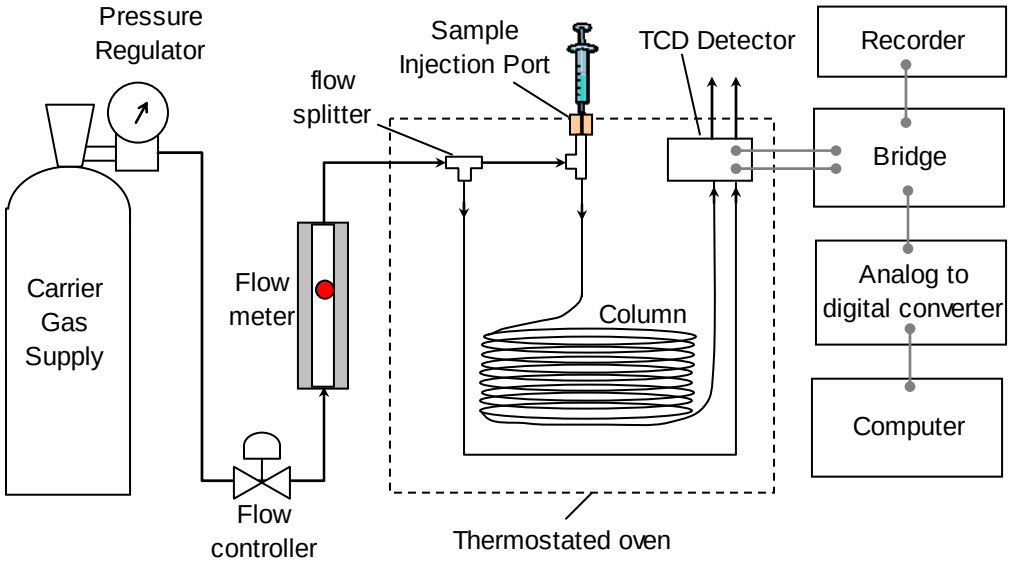

Figure 2.17 – Schematic of a gas chromatograph with a thermal conductivity detector.

2.4.2 Resolution

The resolution is a measure of the separation of two peaks and is defined as the difference in the retention times, t_R, of the two compounds (1 and 2) divided by the average of their extrapolated peak widths, t_{w1} and t_{w2}:

$$R = 2\left(\frac{t_{R2} - t_{R1}}{t_{w1} + t_{w2}}\right). \tag{2.23}$$

Figure 2.18 shows two peaks each with a different retention time (t_{R1} and t_{R2}) and their extrapolated peak widths.

If R is greater than about 1.5 then there is base line separation (0.1 % overlap at $R = 1.5$), if $R = 0.75$ then there is about 4.4 % overlap and if $R = 0.5$ then there is about 16 % overlap. The composition of a mixture is calculated based on the relative areas under the peaks with the application of appropriate calibration factors specific to the detector, if there are overlapping peaks it is impossible to accurately determine the composition of a mixture.

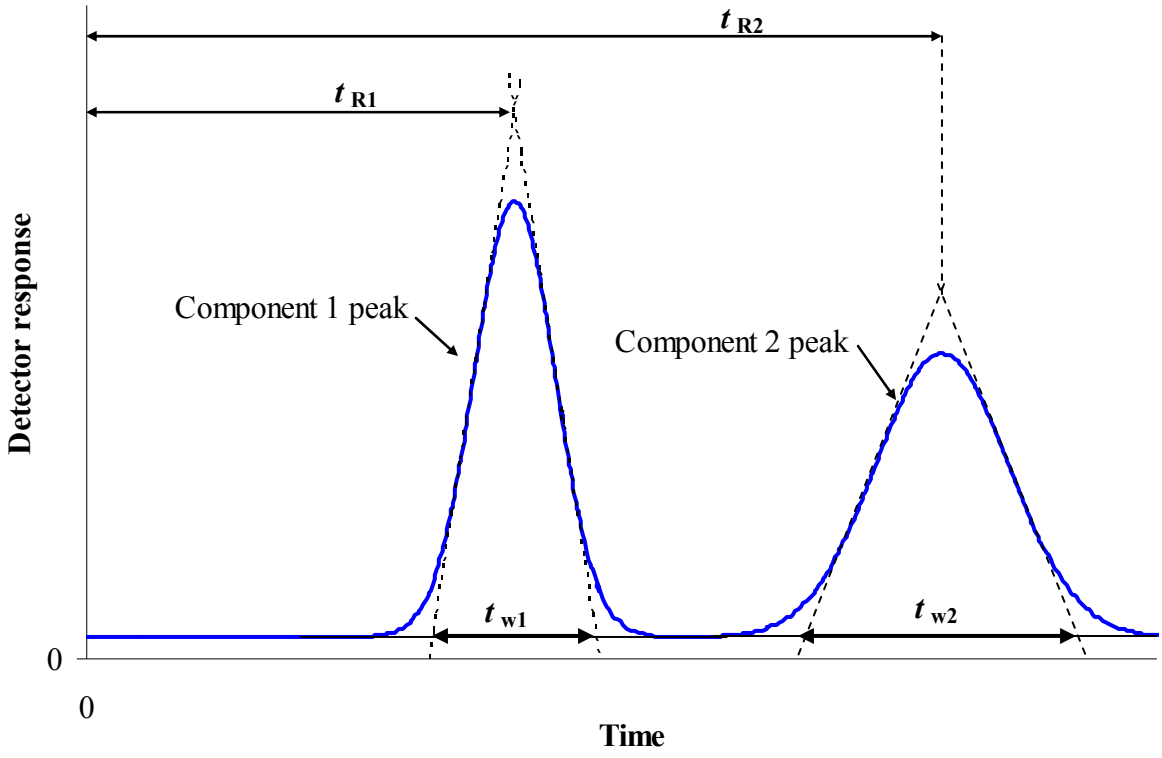

Figure 2.18 – Chromatogram showing the retention times and the extrapolated base widths of two components.

2.4.3 Gas chromatography in this work

Gas chromatography in this work was used to analyse the composition of the gas enclathrated in methane + ethane hydrates by dissociating small lumps of hydrate. It was also used to check the composition of gas mixtures that were prepared in-situ in the ISCO pump. This work is described in Chapter 4.

2.5 Karl Fischer titration

In this work Karl Fischer titrations were used to measure the number of waters of crystallization or hydrate number for the tetraalkylammonium salts. These results and measured values are presented and discussed in Chapter 5.

Karl Fischer (KF) titration is an analytical titration method used to determine water content. The method was developed by the German chemist Karl Fischer in 1935 when he realised it was possible to use Bunsen's reaction of iodine and sulfur dioxide (normally conducted in an aqueous medium) for water determination in non-aqueous systems by using excess sulfur dioxide.[99] Fischer used a primary alcohol, methanol, and pyridine, a base, as the buffering agent. Today the alcohol is still often methanol but also common is 2-(2-ethoxyethoxy)-ethanol (also called diethylene glycol ethyl ether – DEGEE). The base used is most commonly pyridine-free (as pyridine is a carcinogen) and tends to contain imidazole or primary amines. The KF reaction is described by eqs (2.24) and (2.25):

$$\underset{\text{alcohol}}{ROH} + SO_2 + \underset{\text{base}}{R'N} \rightarrow \underset{\text{alkylsulfite}}{[R'NH]SO_3R}, \qquad (2.24)$$

$$[R'NH]SO_3R + H_2O + I_2 + 2R'N \rightarrow \underset{\text{alkylsulfate}}{[R'NH]SO_4R} + 2\underset{\text{hydroiodic acid salt}}{[R'NH]I}. \qquad (2.25)$$

The KF titration method works upon the concentration of iodine. Iodine reacts with a 1:1 stoichiometry with water, once all the water has been consumed the excess iodine is detected potentiometrically by the titrator's indicator electrode (typically a double pin platinum electrode) and this signifies the end point. The amount of water in the sample can be calculated from the concentration of iodine in the KF reagent and the amount of KF reagent consumed during the titration.

2.5.1 Karl Fischer titrators

A Karl Fischer titration can be performed by a volumetric or coulometric method.[100] Generally the volumetric method is best for water mass fractions from 1×10^{-4} to 1.0 whereas

the coulometric technique is best for water mass fractions in the 1×10^{-6} to 0.05 range. In the past manual titrations where commonplace however automatic titrators are widely used today. In this work a volumetric KF titrator was used so only the volumetric method is described, a discussion of the coulometric method may be found in Wieland.[100]

2.5.2 Volumetric KF titrations

In volumetric KF titrations iodine is added mechanically from the titrator's burette in to the titration cell and the amount of water is determined by the volume of KF titrant consumed. There are two common KF reagent systems. In one component volumetric KF titrations all the chemicals for KF are contained in one reagent. The reagent contains an alcohol in which iodine, sulfur dioxide and the base are all soluble. Methanol is commonly used as the working solution in the titration cell where the sample is introduced. In two component KF volumetric titrations the titrant only contains iodine and methanol while the working solution in the titration cell contains the other KF reactants. The advantages of the two component method are quicker titration times and better long term stability of the reagents.

2.6 Nuclear magnetic resonance

Although nuclear magnetic resonance (NMR) has been used in studies of natural gas hydrates (see Sloan[2] and references therein) as well as tetraalkylammonium semi-clathrate hydrates,[101] for this work NMR was used to evaluate the purity of tetraisopentylammonium salts that where prepared from triisopentylamine and isopentyl bromide. The following is an introduction to the principles of NMR and give examples related to amines and tetraalkylammonium salts.

2.6.1 Background and basic principles of NMR

Molecular theory and experimental observations reveal that all energy changes within atoms or molecules are quantized. By irradiating atoms or molecules with photons of energy equal to these quantized energy level differences a transition to a higher energy level can be initiated. Felix Bloch and Edward Purcell first detected the phenomenon of nuclear magnetic resonance (NMR) in 1946 and shared the Nobel prize for Physics in 1952 for this discovery.[102]

Protons, neutrons and electrons all possess the property of spin. Spin is quantized and is represented by spin quantum numbers which come in multiples of ½ and can be positive or negative. In the nucleus of an atom nucleons fill orbitals similar to the way that electrons fill orbitals. Orbitals are full when the number of nucleons is equal to 2, 8, 20, 28, 50, 82 and 126. As the orbitals fill, nucleons pair up (like electrons) and their spin can pair up and cancel out. For nuclei to be NMR active they must have a non-zero nuclear spin quantum number. For the purposes of proton NMR it is important to note that the nuclear spin quantum number of ^{1}H is ½ (1 unpaired proton) and for this purpose further discussion is limited to nuclear spin quantum numbers of ½, particularly ^{1}H. As the proton spins it gives rise to a magnetic field in the same way that a magnetic field is created when electricity passes through a coil of wire. This field is oriented along the axis of spin creating a magnetic moment vector along this axis. The proton can be thought of as a tiny magnet with north and south poles. In the absence of a magnetic field the magnetic moment vectors are orientated randomly however when placed in an external magnetic field the protons can align in one of two ways of states; the lower energy state where a proton aligns in the N-S-N-S orientation or the higher energy state where the alignment is N-N-S-S. Each state is represented by a different magnetic quantum number, m, the lower energy state by $m = +\frac{1}{2}$ and the higher energy state by $m = -\frac{1}{2}$. From quantum considerations the potential energy of a nucleus in each of these quantum states is given by:

$$E = -\frac{\gamma m h}{2\pi} B_0 . \tag{2.26}$$

The magnetic field strength is represented by B_0, h is Planck's constant (6.626×10^{-34} J·s), and γ is the gyromagnetic ratio, a constant for different nuclei (the ratio of magnetic moment to angular momentum of the spinning nuclei, for ^{1}H, γ = 268 MHz·T^{-1}). For the lower energy state ($m = +\frac{1}{2}$):

$$E_{+1/2} = -\frac{\gamma h}{4\pi} B_0 . \tag{2.27}$$

For the higher energy state ($m = -\frac{1}{2}$):

$$E_{-1/2} = +\frac{\gamma h}{4\pi} B_0 . \tag{2.28}$$

The difference in energy between the two states is given by:

$$\Delta E = \frac{\gamma h}{2\pi} B_0 . \tag{2.29}$$

This energy difference is plotted against magnetic field strength below in Figure 2.19.

By equating eq (2.29) with $\Delta E = h\nu_0$ it is possible to find the frequency (ν_0) of radiation or a photon that will bring about a transition between the energy levels:

$$\nu_0 = \frac{\gamma B_0}{2\pi} . \tag{2.30}$$

This explains the size of the energy levels but not how the energy is absorbed. When protons are subjected to a magnetic field they begin to precess much like a gyroscope precesses in the gravitational field of earth. The axis of nuclear spin traces out a cone shape, as shown in Figure 2.20. The angular frequency of the rotation of the axis of nuclear spin about the axis of precession is called the frequency of precession. If nuclei in the lower energy state are irradiated with photons of frequency equal to this frequency of precession the nuclei will absorb the energy of the photon and flip orientation to the higher energy state. The term "resonance" is used to describe the absorption of a photon by the precessing nuclei and the associated flip of nuclear spin state.

2.6.2 Shielding and the chemical shift

In isolation, protons would produce the same resonance signal regardless of the applied magnetic field strength and/or source of radiation. Hydrogen nuclei in molecules however are affected by their local environment. They are surrounded by electrons which too posses spin and create local magnetic fields that are significant at the molecular level. Thus the hydrogen nuclei are "shielded" by the local magnetic field, B_{local}, and the effective magnetic field, $B_{\text{effective}}$, that is experience by the hydrogen nuclei is expressed by:

$$B_{\text{effective}} = B_{\text{applied}} - B_{\text{local}} \,. \tag{2.31}$$

From this equation it becomes clear that the larger the shielding the stronger the applied field (B_{applied}) will need to be to resonate the hydrogen nuclei. It is also possible that the local environment will "deshield" the nuclei so that a lower field strength will resonate the proton. The electronegativity of nearby atoms will effect the shielding too. The differences in shielding/deshielding strength allows the identification of specific hydrogen atoms in molecules.

As different NMR instruments have different magnetic field strengths a way of describing resonances that was independent of magnetic field strength was desirable. This was accomplished by defining a reference resonant frequency, ν_{ref}, and comparing the fractional deviation of the measured resonant frequency, ν, from this reference resonant frequency in parts per million (ppm), this property is defined as the chemical shift, δ:

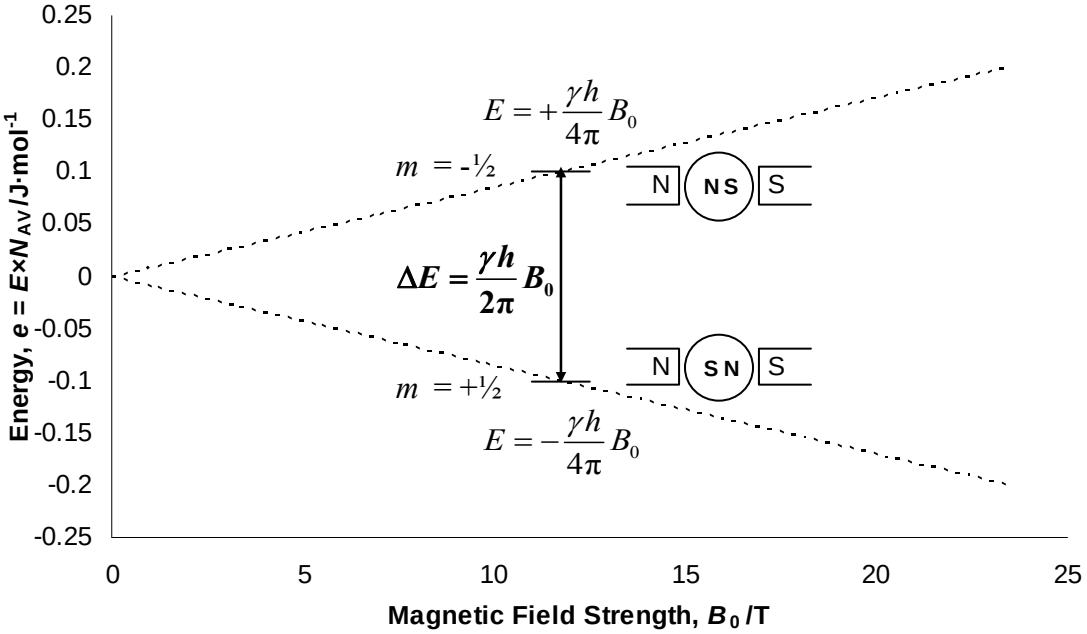

Figure 2.19 – NMR energy levels for a hydrogen nuclei (proton).

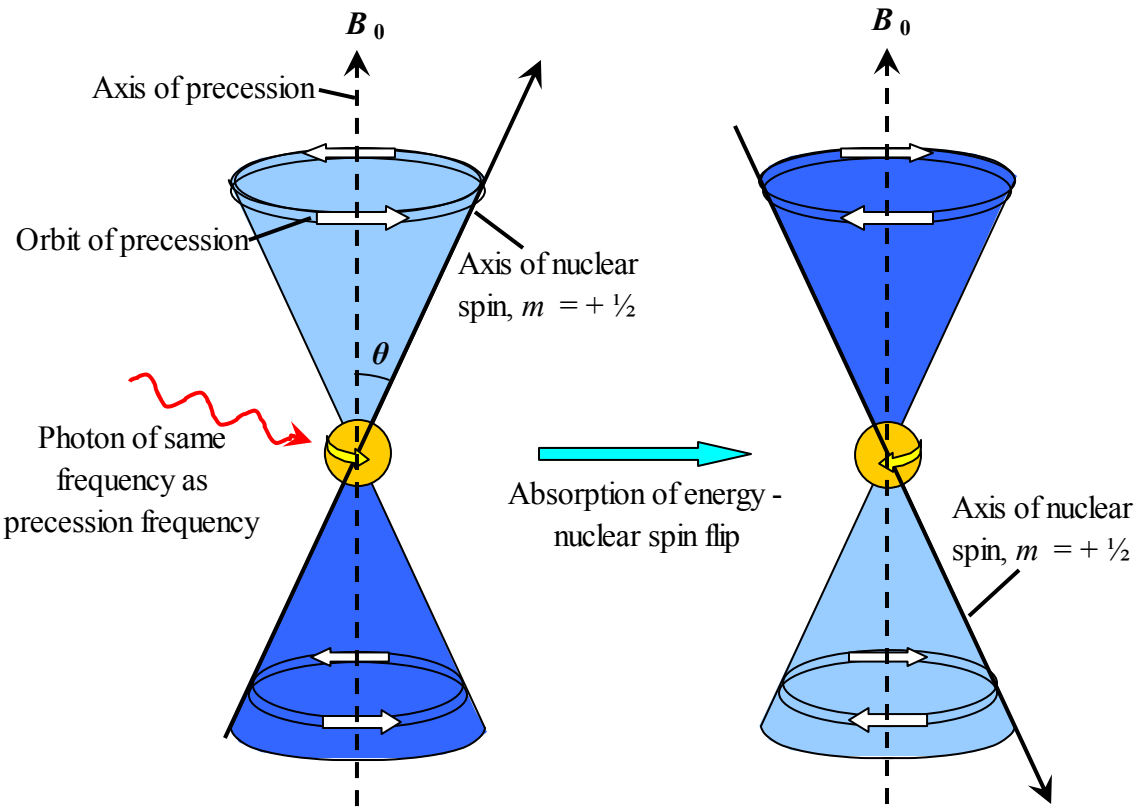

Figure 2.20 - Precession of a spinning nucleus in a magnetic field showing the absorption of a photon at the frequency of precession and the association nuclear spin flip. (Adapted from Brown[103]).

$$\delta = \frac{\nu - \nu_{ref}}{\nu_{ref}} \times 10^6 \ (ppm). \tag{2.32}$$

Tetramethylsilane (TMS) is the universally accepted reference molecule. It was chosen as it soluble and is non-reactive in most organic solvents, and because of the low electronegativity of silicon the hydrogen nuclei are more shielded than in most other organic compounds. Another advantage is that because of molecular symmetry of TMS the hydrogen nuclei are all in the same local environment and all resonate at the same frequency. TMS is also used as the reference molecule for ^{13}C-NMR as ^{13}C resonances can be compared to those of the carbon molecules in TMS.

2.6.3 Instrumentation for NMR

All NMR spectrometers include the same basic components; a powerful magnet, a radio frequency generator, a radio frequency detector and a sample tube. Figure 2.21 illustrates these basic components.

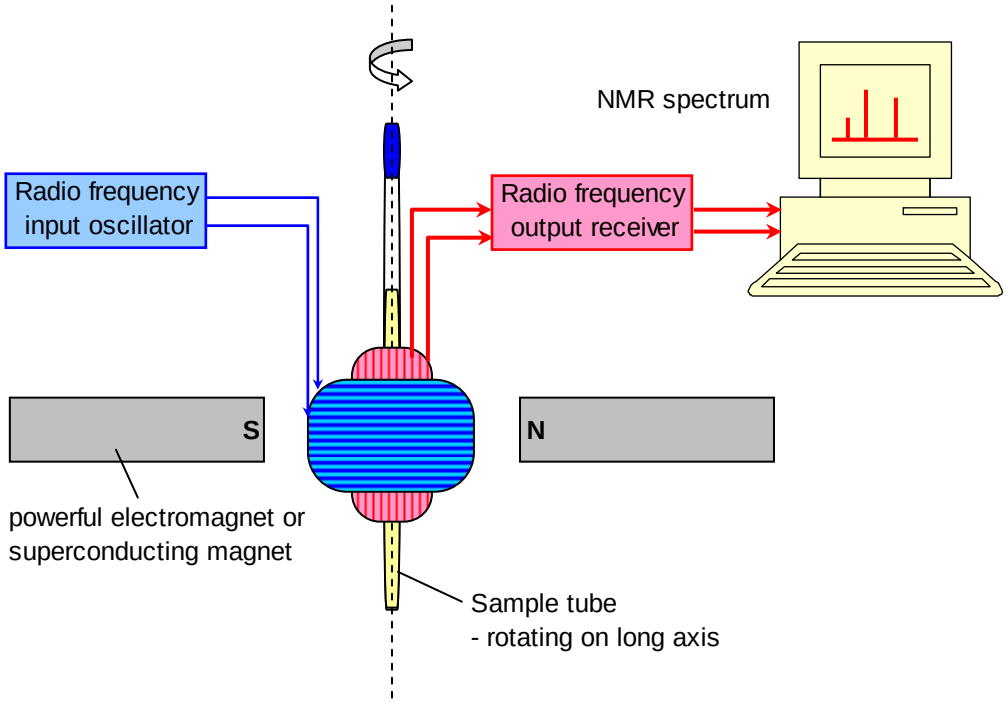

Figure 2.21 – Basic components of NMR spectrometers. (Adapted from Brown[103]).

Samples are dissolved in a deuterated solvent or a solvent that lacks hydrogen atoms, this is usually deuterochloroform ($CDCl_3$) or deuterated dimethyl sulfoxide (DMSO-d_6), but other deuterated solvents are not uncommon such as deuterated water (D_2O) or deuterated methanol (CD_3OD). The sample is placed in a sealed glass tube and placed in the NMR instrument between the poles of the magnet and surrounded by the radio frequency generator/receiver. The sample is rotated to ensure that all the solution experiences a homogenous applied field.

There are two types of NMR spectrometers that can determine resonant frequencies. Earlier instruments are referred to as continuous wave (CW) and used a "field sweep" method whereby a constant radio frequency source is used and the magnetic field is varied to resonate each hydrogen or set of hydrogens in there different local environments. The time required to collect a spectrum by CW is typically (2 to 5) min. The modern technique for collecting NMR spectra is Fourier Transform NMR (FT-NMR). The magnetic field is held constant and a short pulse (less than 10 μs) of radio frequency (100 to 1000) MHz flips the nuclear spin of all of the hydrogen nuclei simultaneously. The process whereby the nuclei return to their equilibrium state produces a sine wave at the frequency of the resonant signal. The intensity of the signal decays with time and drops to zero as the particular nuclei resonating at this

frequency reach their equilibrium state. This information is collected by computer and a Fourier transform is applied that converts the intensity signals from a time-basis to a frequency basis. The process of recording the spectra is typically 2 seconds or less. An advantage of this technique is that a large number of repeated spectra can be recorded and summed to give a time averaged spectra, this reduces noise while enhancing the spectra. It is important to note however that some decay times can however be up 1 min and if the time between sweeps is too short meaningless data will be obtained.

2.6.4 Peak areas

The area of NMR spectra peaks are proportional to the number of hydrogen nuclei resonating at that particular frequency, thus spectra are integrated to yield peak areas. This helps in identifying the number of hydrogen atoms in each equivalent chemical environment.

2.6.5 NMR of amines and ammonium salts

Table 2.1 lists the chemical shifts important for tertiary amine and quaternary ammonium salt analysis. A more complete table including many other groups is available in Brown.[103]

Although the NMR spectra of tetraisopentylammonium ion in deuterated water (D_2O) has been studied by Harmon et al.[104] and is listed in Table 2.2, it was not recorded at a high enough resolution to give clearly individual peaks. For this reason the spectra of a similar ion, the tetrahexylammonium ion is presented in Figure 2.22 as an example. The spectra of the amine from which this salt would be prepared, trihexylamine, is shown in Figure 2.23.

Table 2.1 – Chemical shifts of hydrogen nuclei important for tertiary amine and quaternary ammonium salt analysis.

Type of hydrogen (R = alkyl)	Chemical shift, δ /ppm
$(CH_3)_4Si$	0 (by definition)
R-CH_3	0.8-1[a]
R-CH_2-R	1.2-1.4[a]
R_3CH	1.4-1.7[a]
R_2-N-CH_2-R	2.2-2.6[b]
R_3-N^+-CH_2-R	3.0-3.6[c]

[a] Values from Brown [103]

[b] Range estimated from the NMR spectra of tertiary amines in Sigma Aldrich's online catalogue, tertiary amines used were triethylamine,[105] tripropylamine,[106] and trihexylamine.[107]

[c] Range estimated from values given for tetrabutylammonium iodide,[108] tetraisopentylammonium iodide,[104] tetrahexylammonium hydrogen sulphate,[109] as well as some quaternary ammonium salts derived from cardanol by de Avellar et al.[110]

Table 2.2 – ^{1}H NMR resonances of tetraisopentylammonium iodide in D_2O. (Reproduced from Harmon et al.[104]).

Resonating hydrogen (in bold)	Chemical shift, δ /ppm
$N^+[C\mathbf{H_2}CH_2CH(CH_3)_2]_4$	3.28
$N^+[CH_2C\mathbf{H_2}CH(CH_3)_2]_4$	1.72*
$N^+[CH_2CH_2C\mathbf{H}(CH_3)_2]_4$	1.72*
$N^+[CH_2CH_2CH(C\mathbf{H_3})_2]_4$	1.12

*The peak at this chemical shift could not be distinguished between $N^+[CH_2C\mathbf{H_2}CH(CH_3)_2]_4$ and $N^+[CH_2CH_2C\mathbf{H}(CH_3)_2]_4$ protons

The purity of the prepared tetraisopentylammonium salt was evaluated in this work by estimating the amount of amine impurity present in the salt from the R_2-N-CH_2-R peak in comparison to the salt's R_3-N^+-CH_2-R peak. Other impurities such as solvents and the other reactant, isopentyl bromide, were also searched for in the spectra.

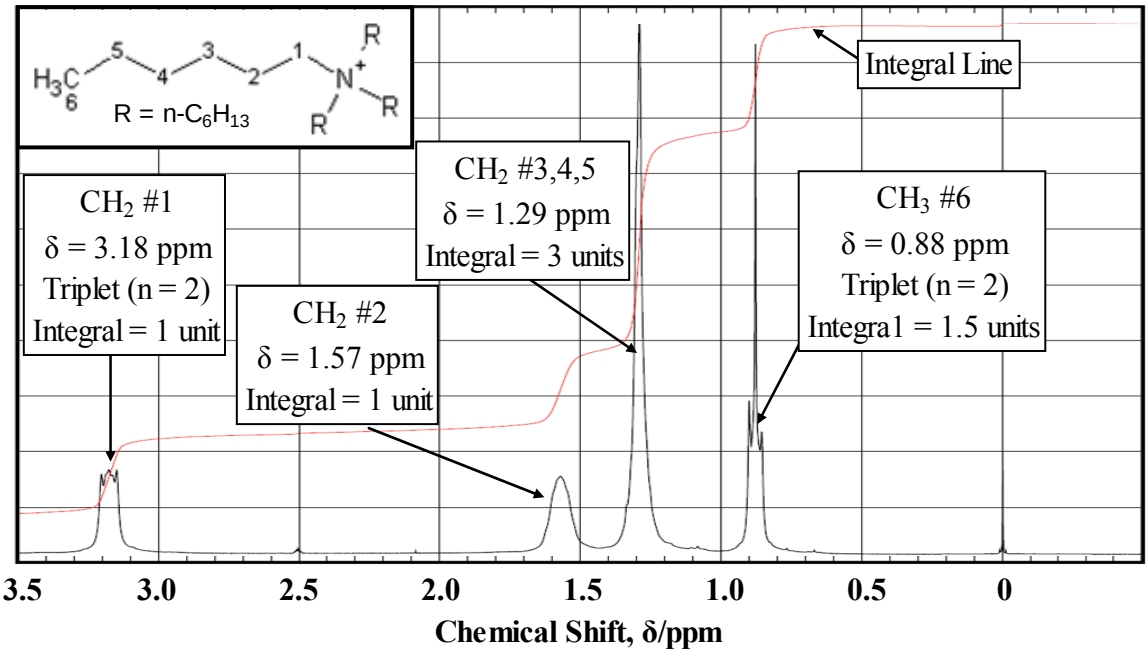

Figure 2.22 – NMR spectra of the tetrahexylammonium ion in DMSO-d_6. (Modified from Sigma Aldrich online catalog[109]).

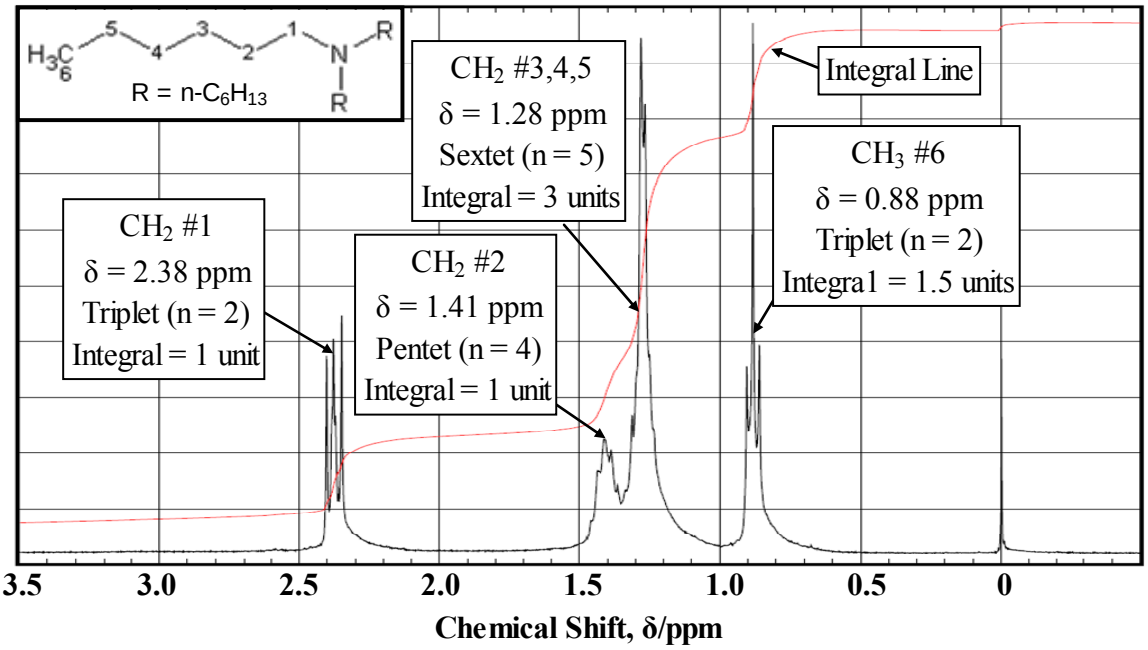

Figure 2.23 – NMR spectra of trihexylamine in $CDCl_3$. (Modified from Sigma Aldrich online catalog[107]).

Chapter 3 PLUG DISSOCIATION TIMES AND ENTHALPIES OF DISSOCIATION OF SI AND SII GAS HYDRATES PREPARED FROM METHANE + ETHANE MIXTURES

3.1 Introduction

Methane rich natural gases, particularly those that are lean in propane and heavier components, may form either a structure I (sI) or structure II (sII) clathrate hydrates in the presence of water. The structure of hydrate is not only dependent on the composition of the gas but also on the pressure-temperature (*P,T*) conditions. A model of two sided depressurization of hydrates developed by Peters[49] suggests that the structure of hydrate has a strong effect on the dissociation time. The model predicts that the dissociation of a sII plug will take approximately 30 % longer than for a sI plug. As hydrate dissociation is endothermic, the dissociated water will often freeze to form an ice plug even when ambient conditions are above 0 °C. Taking this into account the model predicts that removal of a hydrate and ice will take about 20 % longer for the sII plug than the sI plug. The aim of this research was to quantify whether these predictions were correct by calorimetric measurements of enthalpies of dissociation as well as direct plug dissociation time measurements. Mixtures of methane + ethane were used to prepare hydrates of sI and sII. Parts of this section were published in a recent GPA research report.[111]

A literature review is presented discussing methane + ethane hydrates and the fact that despite the pure gases only forming sI hydrates, certain mixtures of the two gases form sII hydrates. Published experimental measurements as well as reasoning on why certain mixtures form sII hydrates are presented. Structure I to structure II transitions of hydrates formed by processed natural gases are also discussed. A review of laboratory hydrate plug formation and the modelling of the dissociation of hydrate plugs then follow. Finally the enthalpy of dissociation of gas hydrates is discussed. Calorimetric measurements as well as the use of the Clapeyron equation for their calculation are reviewed.

Experimental work is then presented. The preparation of methane + ethane mixtures as well as measurements of plug dissociation times, hydrate structure identification by X-ray diffraction and Raman spectroscopy, and calorimetric measurements are included.

Results then follow, firstly *P*,*x* hydrate phase diagrams for methane + ethane mixtures, calculated using the hydrate prediction program CSMGem, at low water to gas mole ratios typical of the conditions in natural gas pipelines are presented. The problem of preferential enclathration is introduced for consideration when preparing hydrate plugs in the laboratory, a calculation algorithm for pressure drop hydrate formations is presented and a calculation is illustrated for a high methane mole fraction mixture of methane + ethane. Methane + ethane *P*,*T* phase diagrams for the mixtures prepared in this work at a high mole ratio of gas to water are then presented. The results of the plug dissociation measurements including the structural analyses of the hydrates formed then follow. Next calorimetric measurements of the enthalpies of dissociation for a sII hydrate formed from a mixture of mole fraction 98.8 % methane + 1.2 % ethane are presented along with Clapeyron calculated enthalpies of dissociation for methane + ethane sI and sII hydrates. Finally CSMGem based predictions of the average guest size in each cage of sI and sII methane + ethane hydrates of a mixture of mole fraction 65.4 % methane + 34.6 % ethane are presented. The results are then considered in the discussion.

3.2 Review of literature

3.2.1 Structure I to Structure II transitions in double guest hydrates

Molecules that are of van der Waals diameter of approximately 6 Å, are of size close to the point in which they are two big to stabilize the $5^{12}6^2$ cage of sI and will instead stabilize the $5^{12}6^4$ cage of sII. Two molecules of about this size, cyclopropane[112] (5.9 Å) and trimethylene oxide[113] (6.1 Å) have been shown to form both sI and sII hydrates depending upon the pressure, temperature and composition. More unusually however certain binary mixtures of hydrate formers that as single guest components form sI hydrates have been shown to form sII double guest hydrates. This effect was first observed in the mid-1950's by von Stackelberg and Jahn[114] who measured sII sized lattice parameters by X-ray diffraction for binary mixtures of H_2S and CH_3Br, COS, and CHF_2CH_3 which each form sI hydrates as single guest

components. In the mid-1990's Hendriks et al.[115] predicted using a van der Waals and Platteeuw based statistical model that certain mixtures of methane + ethane would form sII hydrates despite the fact that the pure gases only form sI at similar temperature and pressure conditions (note: methane has been shown to form both sII and sH hydrates as a single component hydrate at high pressures in excess of 99 MPa,[116,117] Hirai[118] also gives details of other guests that form different hydrate structures at very high pressures). In 2000 Subramanian et al.[72] produced experimental evidence of the formation of sII methane + ethane hydrates from Raman and NMR measurements, indicating at 274.2 K and at liquid water-hydrate-vapour (L_w-H-V) equilibrium conditions that the stable hydrate formed switched from sI to sII at between a methane fraction of (72.2 and 75) % in the vapour. An isothermal (T = 277.6 K) pressure versus composition phase diagram for the system methane + ethane + excess water was generated by Subramanian et al.[71] using a van der Waals and Platteeuw based statistical model and is shown in Figure 3.1. The data generated for this diagram suggests the L_w-H-V equilibrium stable hydrate switches from sII back to sI at a methane mole fraction in the vapour of approximately 99.3 %.

While experimental evidence is clear that two single guest sI hydrate formers can as a mixture form a sII hydrate this does not answer the question why this might occur? Ripmeester suggested a justification as to why two single guest sI former form double guest sII hydrate noting: "that all small structure I guests (those that occupy the 5^{12} cage to a significant extent) when combined with large structure I guests (those that do not occupy the 5^{12} cage) may give structure II hydrate under certain circumstances".[119] Figure 3.2 modified from Ripmeester[119] shows the "complexities of the formation of double hydrates", the combination of two different sized guest can result in sI, sII or sH hydrates.

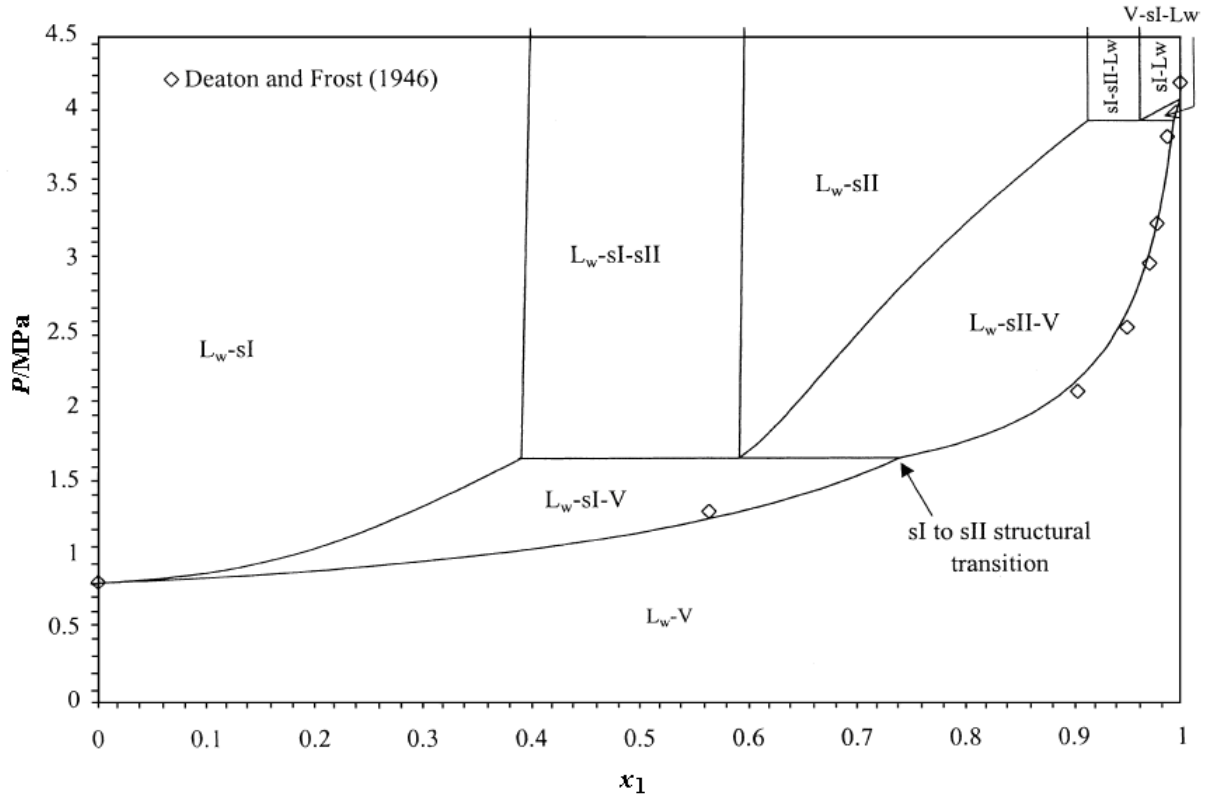

Figure 3.1 – Isothermal (T = 277.6 K) pressure versus composition phase diagram of methane (1) + ethane (2) + excess water; generated using a van der Waals and Platteeuw based statistical model, x_1 is the water free mole fraction of methane, phase labels: L_w = liquid water, V = vapour, sI = structure I hydrate, sII = structure II hydrate, experimental points are from Deaton and Frost.[120] (Modified from Subramanian et al.[71]).

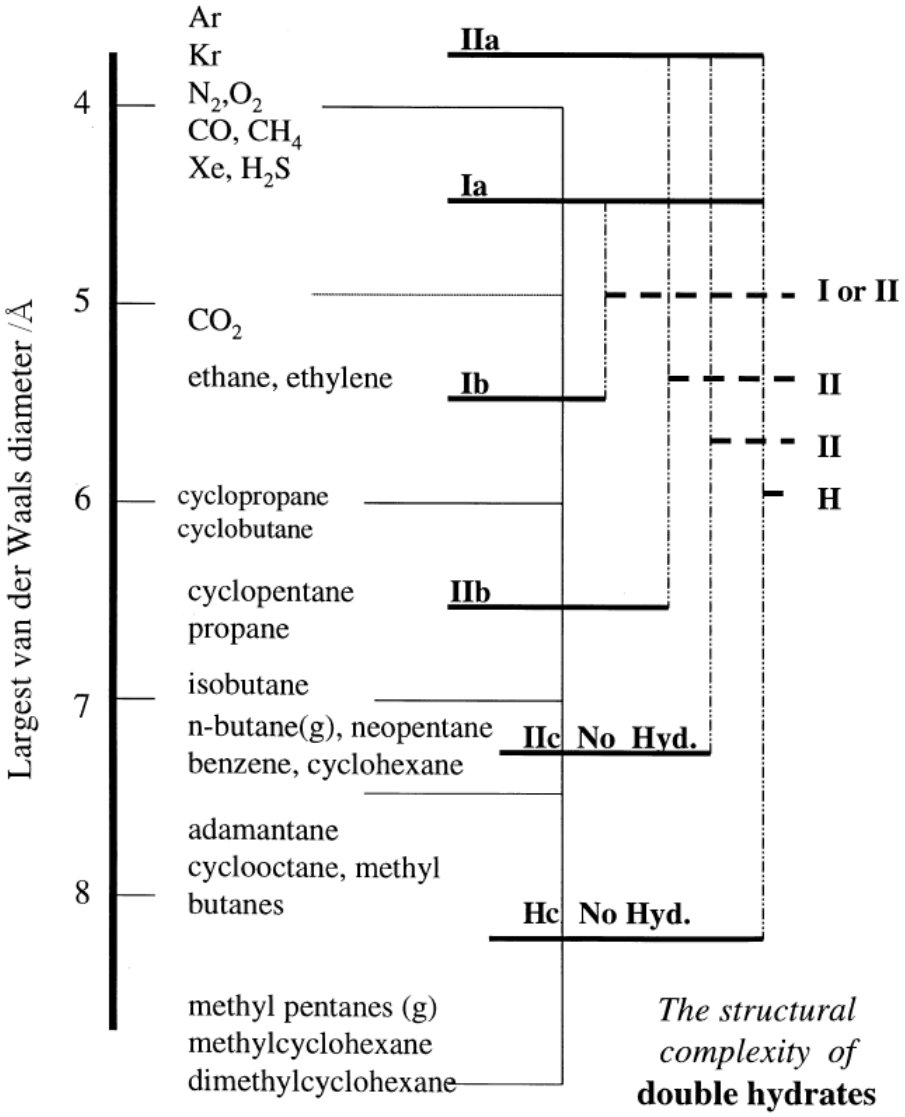

Figure 3.2 – Size-structure classification of single guest component and binary guest component hydrates; potential guest molecules are divided into size ranges a, b and c (i.e. for sII a = occupies 5^{12} cages, b = mostly occupies $5^{12}6^4$ cages and c = too large to occupy either cage). The following combinations are known, although some of the boundaries may not have been firmly established: Ia + Ib →structures I or II; IIa or Ia + IIb → structure II; Ia or IIa +IIc → structure II; and Ia or IIa +Hc → structure H. (Modified from Ripmeester[119]).

Hester[121] and Hester and Sloan[122] studied structural transitions of double guest hydrates using the statistical mechanical model of van der Waals and Platteeuw[32] as modified by Ballard[33] in the program CSMGem (see introduction for a brief description of this model). They note for a single guest hydrate if the guest is too large to fit in the $5^{12}6^2$ cage of sI it will enter the $5^{12}6^4$ cage of sII (if less than about 6.9 Å in van der Waals molecular diameter) and that guests that are too small to stabilize the $5^{12}6^2$ cage will form sII because of the high density of 5^{12} cages. For the purpose of their investigations a "pseudo-methane" molecule was generated with the same water solubility, fugacities, Kihara hard core radius (a), and Kihara potential well depth (ε) as methane but with an adjustable Kihara collision radius (σ). Initial experiments were conducted for a pure pseudo-methane (single value of σ) to establish the single guest Kihara collision radius size limits for sI and sII hydrate formation. These calculations indicated a sI hydrate was the predicted stable form under hydrate forming P,T conditions, for σ values

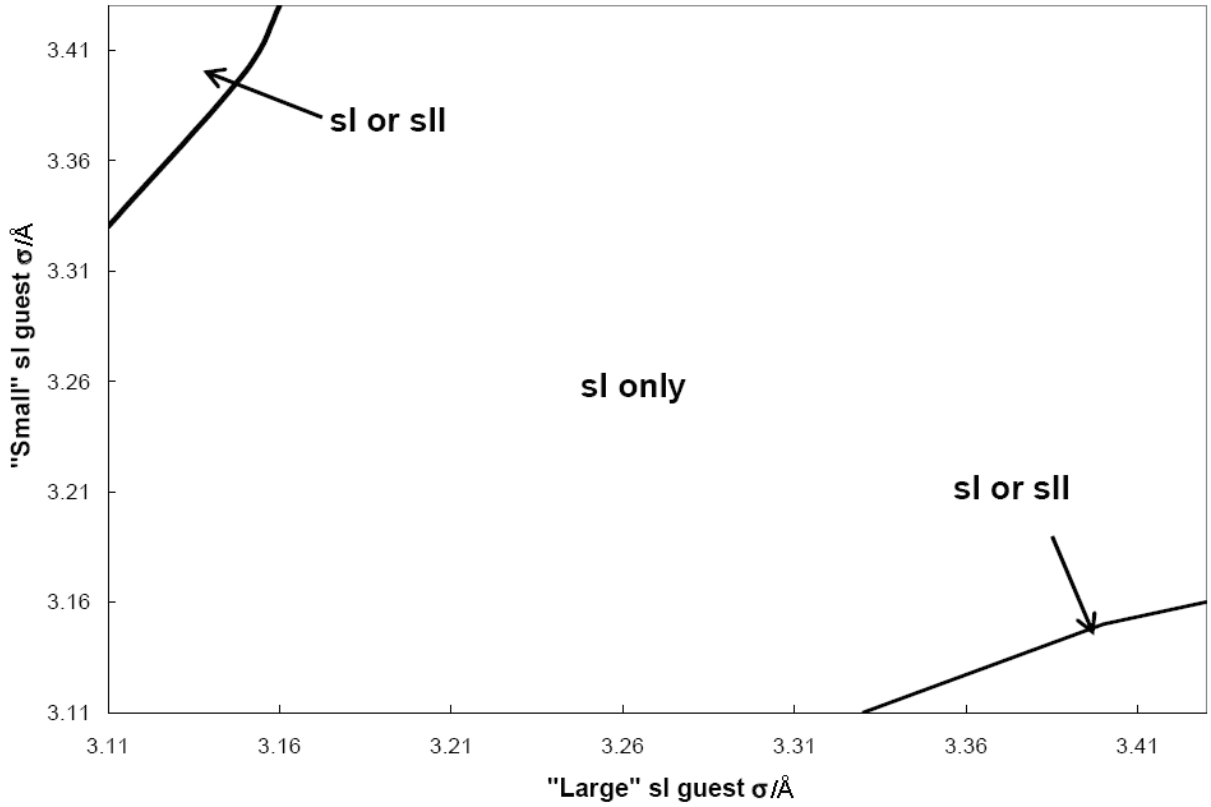

Figure 3.3 – Kihara collision radius (σ) guest size ranges for a mixture of "small" and "large" pseudo-methane molecules showing predicted sII double guest hydrate transitions;, the region of "sI or sII" indicate that at some composition of the mixture "small guest" + "large guest" sII hydrates will form, for the "sI only" region only sI hydrates were predicted for all mixture compositions. (Modified from Hester[121]).

below 3.11 Å, for σ between (3.11 and 3.43) Å sII was the predicted stable hydrate at hydrate forming P,T conditions and for σ above 3.43 Å sII was the predicted stable form at hydrate forming P,T conditions. These calculations provided the size limits for the study of the double guest hydrates. Double guest hydrates were investigated using two pseudo-methane molecules with different values of σ, called the "small guest" and "large guest". The size (σ) of these pseudo-methane molecules was varied between 3.11 Å and 3.43 Å as well as the composition of the mixture of "small guest" + "large guest" to reveal the size combination of "small guest" + "large guest" that could result in a transition to a sII double guest hydrate (note: this transition may only occur at some compositions of "small guest" + "large guest", c.f. Subramanian et al.[72] who showed that for methane + ethane mixtures sII will only form at incipient conditions between a water-free mole fraction of methane of about 0.7 and 0.99). A plot of this data from Hester[121] showing the predicted regions of sI and sI or sII with "large guest" and "small guest" size (σ) is presented as Figure 3.3. Hester[121] also produced a similar diagram for pseudo-hydrogen sulfide molecules. Hester tested these size limit predictions by conducting hydrate structural studies in the systems $CH_4 + C_2H_4$ (confirming the findings of Sugahara et al.[123]) and $Xe + C_2H_6$ by neutron diffraction and Raman spectroscopy to show that only sI hydrate would form in these systems.

3.2.2 Structure I to Structure II transitions in hydrates of natural gases

Structural transitions of the type that occur in the methane + ethane system also occur in certain natural gases. A processed natural gas (PNG) is a natural gas composed of mostly methane, which has had almost all of the heavier and non-combustible components removed. Bollavaram used a PNG of the composition listed in Table 3.1 to form hydrate plugs.[54] In Chapter 5 of Bollavaram's thesis entitled "Structural transitions and plug dissociation" (co-authored with M.D. Jager) P,T conditions for a pipeline flowing this gas were simulated using OLGA® (note: OLGA® is a software package that performs steady state and transient simulations of multiphase flows of oil, water and gas in wells, pipelines and receiving facilities[124]). Pipeline simulations were completed at start-up conditions (low pressure) and design conditions (high pressure). A P,T plot of the hydrate formation boundaries as well as the P,T profiles for the pipeline at design and start-up conditions are shown in Figure 3.4, this figure was adapted from Bollavaram[54] with the hydrate boundaries recalculated in CSMGem (calculated with a gas to water mole ratio of 100:1, Bollavaram had used Infochem

Multiflash® to calculated hydrate boundaries). For the design *P,T* profile the hydrate boundary is crossed at about 293.5 K and 25.12 MPa, sI is the stable structure under these conditions, however the profile also crossed through the thin band where both structures of hydrate are stable (sI + sII + V region) into the sII + V region where sII is the stable hydrate (passing through the sI + V ↔ sI + sII + V line at about 274.5 K and 19.47 MPa and the sII + V ↔ sI + sII + V line at about 273.7 K and 19.10 MPa). For the start-up conditions the *P,T* profile solely crosses in to the sII + V region at approximately 286.6 K and 9.42 MPa. These results show that both composition and the pressure and temperature conditions affect the hydrate structure formed in such processed natural gases.

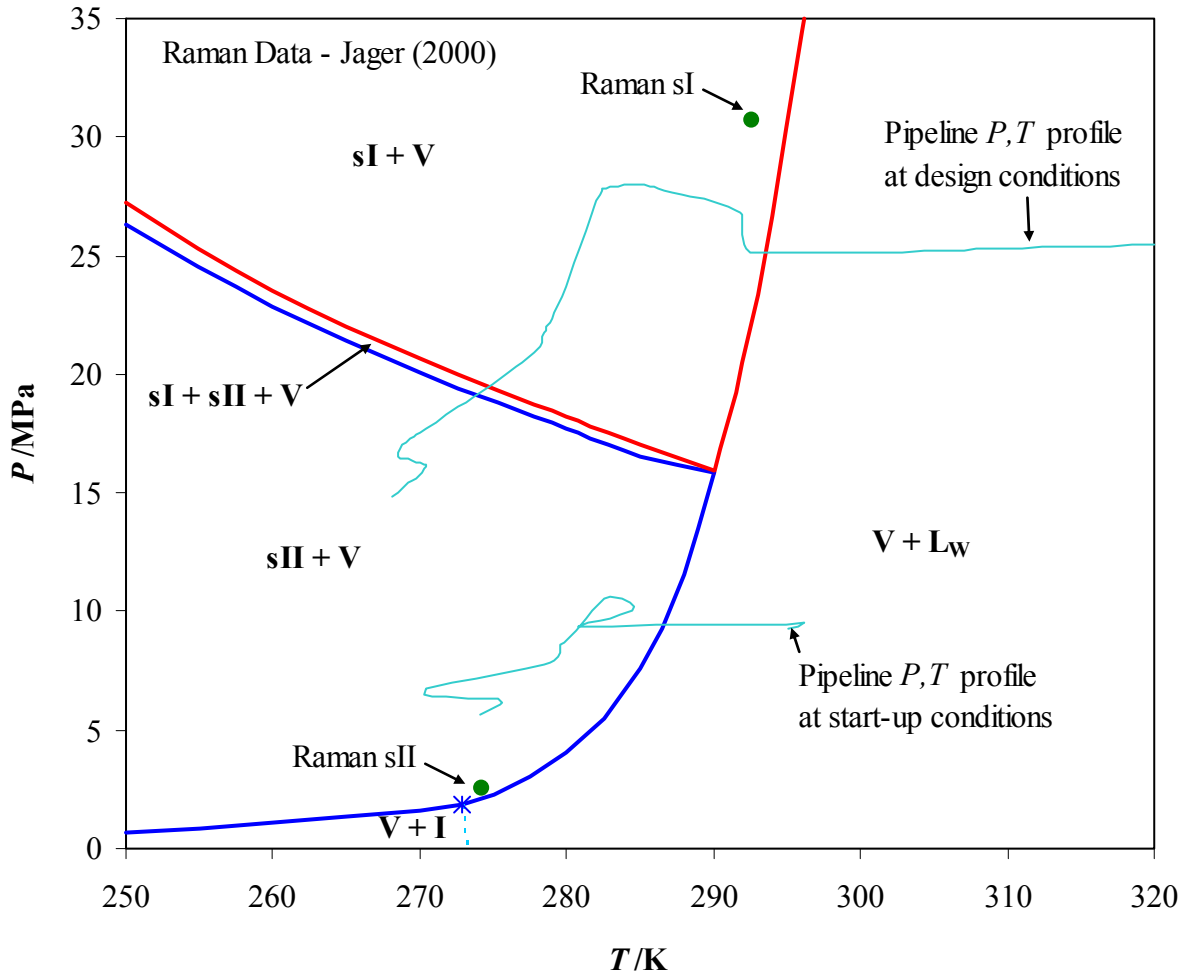

Figure 3.4 – Processed natural gas *P,T* pipeline profiles and hydrate boundaries; V = vapour phase, L_w = liquid water, I = ice, sI = structure I hydrate and sII = structure II hydrate. Hydrate boundaries recalculated in CSMGem using a molar ratio of gas to water of 100:1, Raman structural measurements were completed by Jager. [125] (Adapted from Bollavaram[54]).

Table 3.1 – Processed natural gas composition. (Reproduced from Bollavaram[54]).

Component	Mole Fraction
Methane	0.974788
Ethane	0.009310
Propane	0.001310
n-Butane	0.000271
i-Butane	0.000161
n-Pentane	0.000242
i-Pentane	0.000239
n-Hexane	0.000286
C_7+	0.000163
Nitrogen	0.009230
Carbon dioxide	0.004000

3.2.3 Hydrate plug formation

Peters[49] notes in his thesis entitled "A Study of Hydrate Dissociation in Pipelines by the Method of Two-Sided Depressurization: Experiment and Model" that "the process of making a large, reproducible sample of hydrate proved to be one of the most difficult challenges of the entire project." He found the most reliable method for the preparation of hydrate plugs for dissociation measurements was that developed by Stern et al.[126] Methods of laboratory hydrate formation prior to Stern et al.'s method typically involved rocking, rotating or continuously agitating a pressure vessel of a reaction mixture (see Chapter 6 of Sloan and Koh[2] for a description of such apparatuses). The basis of Stern et al.'s method was the slow, regulated heating of sieved granular ice in a cell pressurized with cold methane gas by the reaction $CH_4(g) + 6H_2O(s \rightarrow l) \rightarrow CH_4 \cdot 6H_2O(s)$, where $H_2O(s \rightarrow l)$ indicates the reaction proceeds as ice melts. A sample cell filled with ice particles between (180 and 250) μm in size was pressurized with cold methane from a second reservoir cell. The initial pressure was chosen so that methane filled the pores between the ice particles in excess of that required for complete conversion of the ice to hydrate. The *P,T* conditions during a hydrate formation are shown in Figure 3.6 (from Stern et al.[126]). The system was heated from a temperature of 250 K reaching the melting point of ice over a period of about 3 h. During this time the pressure increased approximately linearly with increasing temperature. As heating continued beyond the melting point of ice there was no *P,T* discontinuity as there had been in control experiments with Ne + H_2O (Figure 3.6B), indicating persistence of metastable (superheated) ice, but rather a smooth line that began to deviate negatively in pressure (from a linear extrapolation) indicating hydrate formation had begun. The system was then heated over a

period of (7 to 8) h to the close to dissociation conditions of the hydrate [(288 to 289) K and (29.4 ± 0.2) MPa], the extent of reaction could be assessed by comparing the pressure drop linearly extrapolated back to the ice curve (using the initial *P,T* slope of the ice + CH_4 warming) to the final pressure drop, ΔP_r [(1.8 ± 0.1) MPa for these experiments]. Once the reaction was complete the sample was quenched to 77 K while venting the methane and the samples were shown by powder X-ray diffraction (XRD) to contain a mass fraction of ice less than 3 %. Calculations based on the uptake of methane gave a hydrate number of 6.1 ± 0.1. Stern et al. note "the resulting samples were translucent, white, cohesive aggregates with uniformly fine, equant grains of (200 to 350) μm. All 15 samples produced under these conditions displayed consistent and reproducible run history curves, CH_4 uptakes measurements, XRD patterns and physical appearances".[126] Stern et al. also conducted several experiments where the samples were quenched and analysed by XRD before the reaction had reached completion, the *P,T* points at which quenching occurred are shown as A-E on Figure 3.6. The samples quenched at points C ($\Delta P_r = 0.6$) and D ($\Delta P_r = 0.8$) contained (55 ± 5) % and (78 ± 5) % clathrate by mass respectively. The sample quenched at point B ($\Delta P_r = 0.4$) was slowly cooled to 250 K before quenching and showed a *P,T* discontinuity upon cooling indicating some macroscopic melting had occurred. This was further confirmed by the XRD of this sample which showed a clathrate mass fraction of (28 ± 5) %, lower than that predicted of 40 % if no melt was present. Stern et al. noted that this suggests "up to 0.5 ΔP_r, the slow rate of seed ice melting still "outpaces" the rates of clathrate formation. After this period, the rate of clathrate formation essentially keeps pace with incipient melting for the remainder of the 8 h needed for complete reaction under these conditions".[126] Hwang et al.[127] measured the growth under static conditions of methane hydrate on disks of melting ice and observed two stages of formation periods, nucleation and growth. During the initial "nucleation" period the rate of hydrate formation increased, this was followed by the "growth" period where the formation rate decreased until all the ice had reacted. The growth rate of the hydrate was also determined to be a function of the supply of methane to the ice surface and the heat removal rate for the exothermic hydrate formation process. The ice melting on exposed surfaces was considered an endothermic heat sink for hydrate formation and a "template" for hydrate growth. Stern et al. noted that they "generally agree with these interpretations of Hwang et al."[126] they further noted however that the superficial layer of hydrate formed on the surface of the ice particles used in their experiments "not only rate-

limits reaction in the grain interiors, but may also effectively "armour" the grain from nucleating melt and consequently suppress the rate of melting of ice grains. Once such a rind of hydrate has encased an ice grain, the most likely process of continued clathrate formation involves solid-state diffusion of CH_4 gas to the ice core".[126] Peters[49] suggested that the observed rate of hydrate formation is in fact faster than would be expected by solid-state diffusion through an exterior hydrate layer indicating another mechanism. He proposed that "the most reasonable explanation would be the presence of fissures and cracks in the hydrate shell that allowed gas to diffuse through easily".[49] This conceptual mechanism is illustrated in Figure 3.5 from Peters.[49] Peters found the particle size that Stern et al.[128] used of (180 to 250) μm was too small resulting in the ice melting too fast before significant hydrate formation, so ice particles of about 850 μm were used instead. Bollavaram[54] and Ivanic[129] building on the work of Peters found that temperature below the ice point and pressure cycling aided conversion. Ivanic presumed freezing and remelting of ice in the particles helped to create more fissures in the hydrate surface to aid conversion. Hydrate formations by Peters, Bollavaram and Ivanic took longer than those of Stern et al., typically (3 to 4) days, presumably because of the larger ice particle size used.

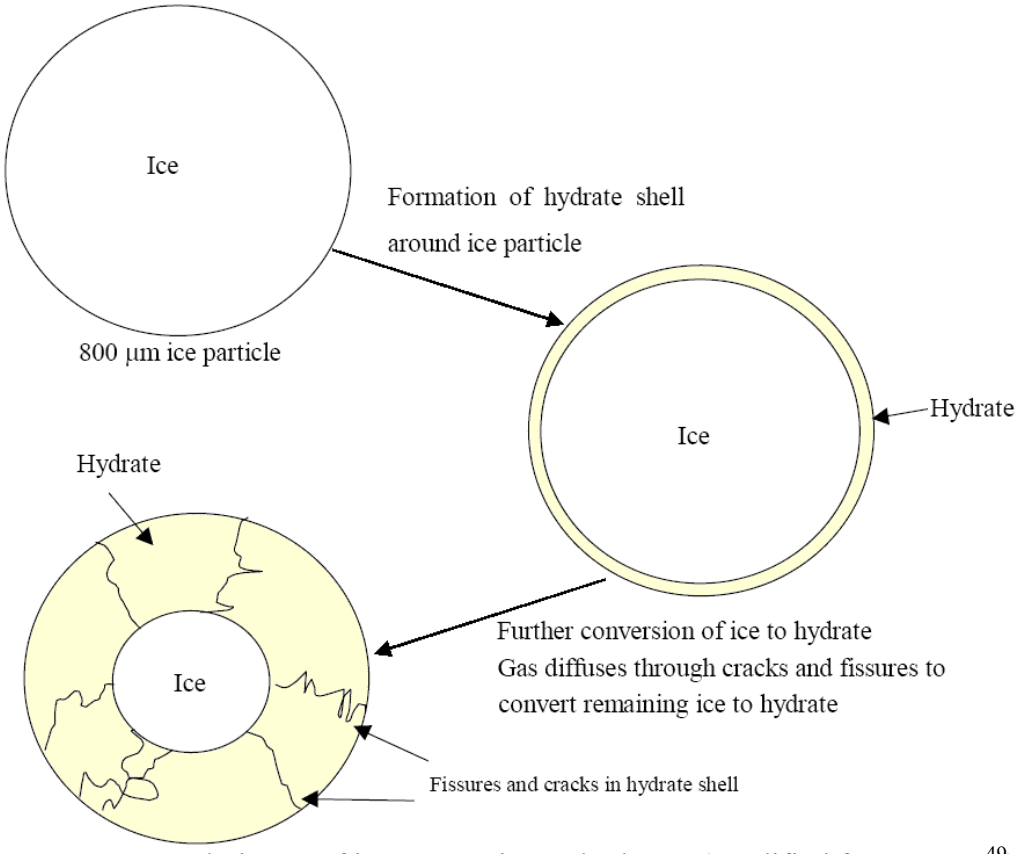

Figure 3.5 – Conceptual picture of ice conversion to hydrate. (Modified from Peters[49]).

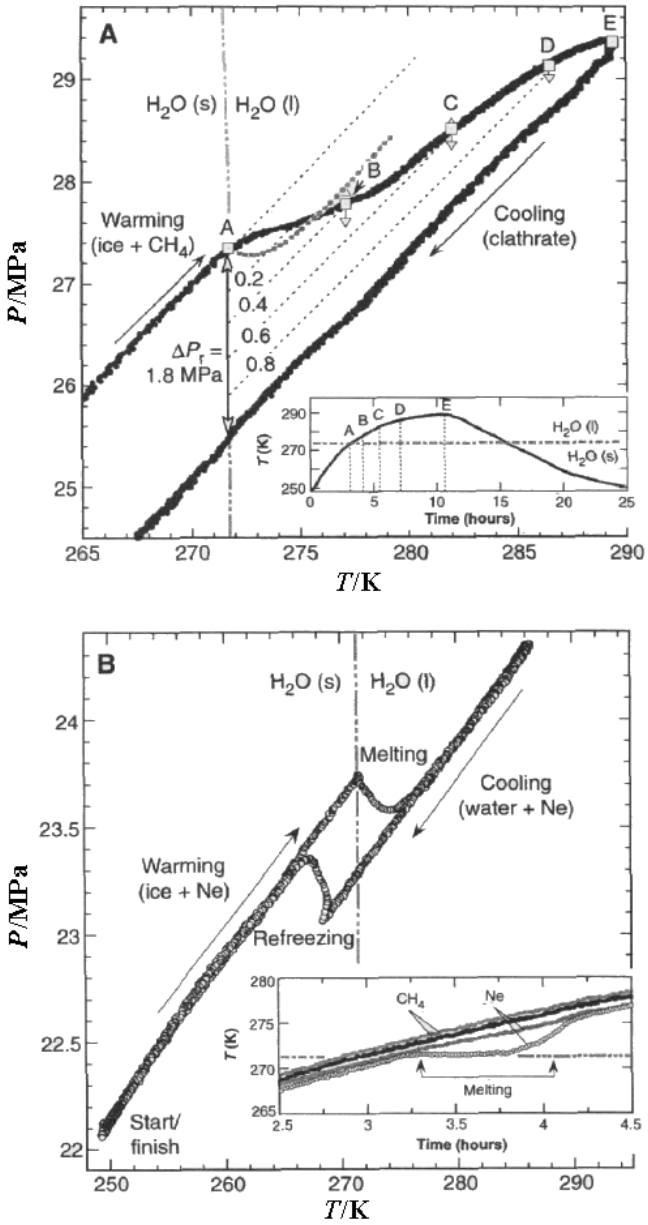

Figure 3.6 – *P,T* conditions during methane hydrate formation of Stern et al.'s method of hydrate plug formation; **A** *P,T* profile during hydrate formation; the near vertical dashed line is the ice melting curve, ΔP_r is the pressure drop for complete reaction, open squares A, B, C, D and E indicate points where reactions were quenched at fractions of ΔP_r of 0, 0.4, 0.6, 0.8 and 1 respectively, the grey dotted curve is a prediction assuming no hydrate formation and melting of all of the ice, triangle and inverted triangles show calculated positions showing no melting and complete melting respectively of all the remaining unreacted ice in each partially reacted sample. The inset shows the temperature-time profile for the full reactions A to E at the *P,T* conditions shown in the main diagram. **B** Control experiment with Neon gas in place of methane showing clear *P,T* discontinuities during heating through the ice melting curve and at refreezing during cooling. The inset shows the temperature-time profile in the region of the ice melting showing the lag of the sample *T* (open circles) compared with the bath *T* (gray trace) due to the endothermic melting of ice. This effect is not observed for the methane hydrate run (sample *T* – black trace, bath *T* – gray line). (Modified from Stern et al.[126]).

3.2.4 Hydrate plug dissociation and modelling

As discussed in Chapter 1 hydrate plugs can form in natural gas or oil pipelines when water is present and the *P*,*T* conditions are within the hydrate forming region (below the hydrate dissociation temperature at a constant pressure, or above the hydrate incipient pressure at a constant temperature). If a hydrate plug does form it has to be removed and the most common method is to lower the pressure below hydrate forming conditions at the temperature of the pipeline. Apart from ensuring that the hydrate dissociation is completed safely, to ensure that the plug does not dislodge and travel at high speed along the pipeline, one of the most important considerations for the operation of the pipeline is the length of time for the dissociation. Although several models such as that of Lysne et al.[130] (also later described by Berge et al.[131]) and Kelkar et al.[132] of the dissociation of hydrates plugs exist, both of these models suffer limitations.

The "one-dimensional steady state"[133] model of Lysne et al[130,131,133] calculated a "propagation velocity of the dissociation boundary"[133] from "the properties of the fluid present, the hydrate phase and wall layers".[133] All the heat from the surroundings was assumed to go into dissociating the hydrate and the formation of ice was not accounted for in the model (note: Peters[49] showed that even if a hydrate was dissociated at a temperature above the ice point due to the endothermic nature of hydrate dissociation ice formation can occur) . The model also required the plug length as an input. An important finding of the model however was that the hydrate porosity, or the void fraction within the hydrate plug (given the symbol ε), had a significant effect on the dissociation time. Lysne[133] had shown in his experimental work on the dissociation of ethane hydrates that hydrates were typically porous (at least 33 %), Lysne hypothesised that due to this porosity there would be pressure communication and as a result of depressurization, if the hydrate dissociation temperature was below ambient, heat would flow radially in from the surroundings. Field experiments reported by Austvik et al.[134] indicate hydrate plugs in real pipelines are also porous.

The model of Kelkar et al.[132] was a one-dimensional transient model based on solving differential equations expressing Fourier's law in rectilinear coordinates assuming semi-infinite media. The advantage of solving assuming semi-infinite media and using rectilinear coordinates rather than radial coordinates was that the equations could be solved exactly

rather than by numerical solution. The dissociation was assumed to be by rapid depressurization and modelled by either a single or double Stefan moving boundary. If the ambient temperature was below 0 °C then only two phases were present, ice and hydrate, with only a single moving boundary. However if the ambient temperature was above the 0 °C but the hydrate dissociation temperature at the pressure selected for dissociation was below 0 °C then three phases were considered present, hydrate, ice and water, resulting in a double moving boundary problem. If the hydrate dissociation temperature at the selected pressure was above 0 °C then only hydrate and water were considered resulting in a single moving boundary. An interesting finding by Kelkar et al.[132] was that due to the high thermal diffusivity, ice aided the rate of dissociation of the hydrate.

Peters[49] model of the two-sided dissociation of hydrate plugs was similar to that of Kelkar et al.[132] except it was expressed and solved in radial coordinates. The model has the following assumptions:

- The hydrate is dissociated due to a step change in pressure on both sides of the plug to a pressure below the hydrate dissociation pressure at the ambient temperature,
- Hydrate and ice are both porous,
- The hydrate dissociation temperature is uniform,
- Radial dissociation dominates over axial dissociation,
- Dissociation is heat transfer controlled and
- Only heat conduction is important.

Solving the equations for radial coordinates required a numerical solution, details of which are not included here (see Peter's thesis[49] for details). The problem could either be a single or double Stefan moving boundary problem, the same as Kelkar et al.'s model. Figure 3.7 shows the phases and temperature gradients for the three phase (hydrate, ice and water) two moving boundary problem. The temperature profiles for this system, with constant wall temperature, according to Fourier's law of heat conduction in radial coordinates are described for $t > 0$ (where t is time) by eqs (3.1) to (3.7), where r_0, r_{F1} and r_{F2} are the radius of the wall, moving boundary between water and ice and moving boundary between the ice and hydrate respectively, T_0 T_W, T_I, T_D and T_M are the wall, water, ice, hydrate dissociation and ice melting point temperatures, α_W and α_I are thermal diffusivity of the water and ice, ρ_W and ρ_I are the density of ice and water, k_W and k_I are the thermal conductivity of water and ice, λ_H

and λ_I are the enthalpy of hydrate dissociation and enthalpy of fusion of ice and ε is the porosity of the hydrate respectively.

For $r_{F1} < r < r_0$:

$$\frac{\partial T_W}{\partial t} = \alpha_W \left(\frac{1}{r} \frac{\partial T_W}{\partial r} + \frac{\partial^2 T_W}{\partial r^2} \right). \tag{3.1}$$

For $r_{F2} < r < r_{F1}$:

$$\frac{\partial T_I}{\partial t} = \alpha_I \left(\frac{1}{r} \frac{\partial T_I}{\partial r} + \frac{\partial^2 T_I}{\partial r^2} \right). \tag{3.2}$$

Eqs (3.1) and (3.2) are subject to the boundary conditions:
at $r = r_0$:

$$T_W = T_0, \tag{3.3}$$

at $r = r_{F1}$:

$$-k_W \frac{\partial T_W}{\partial r} = -k_I \frac{\partial T_I}{\partial r} + (1-\varepsilon) \rho_I \lambda_I \frac{dr_{F1}}{dt}, \tag{3.4}$$

and

$$T_W = T_I = T_M, \tag{3.5}$$

at $r = r_{F2}$:

$$-k_I \frac{\partial T_I}{\partial r} = (1-\varepsilon) \rho_H \lambda_H \frac{dr_{F2}}{dt}, \tag{3.6}$$

and

$$T_I = T_D. \tag{3.7}$$

The boundary conditions of eqs (3.3), (3.5) and (3.7) are due to the pipe wall, water-ice moving boundary and the ice-hydrate moving boundary respectively. Equations (3.4) and (3.6) are heat flow boundary conditions. Equation (3.4) expresses that the heat conducted through the water layer is equal to the heat conducted through the ice layer minus the heat

used to melt the ice to water, whereas eq (3.6) express that the heat conducted though the ice layer is utilised to dissociate the hydrate.

The model solves for the time when the hydrate plug has completely dissociated (time when $r_{F2} = 0$, or when the ice-hydrate moving boundary reaches the centre of the pipe) as well as the time when an ice plug if present is completely melted (time when $r_{F1} = 0$, or when the ice-water moving boundary reached the centre of the pipe).

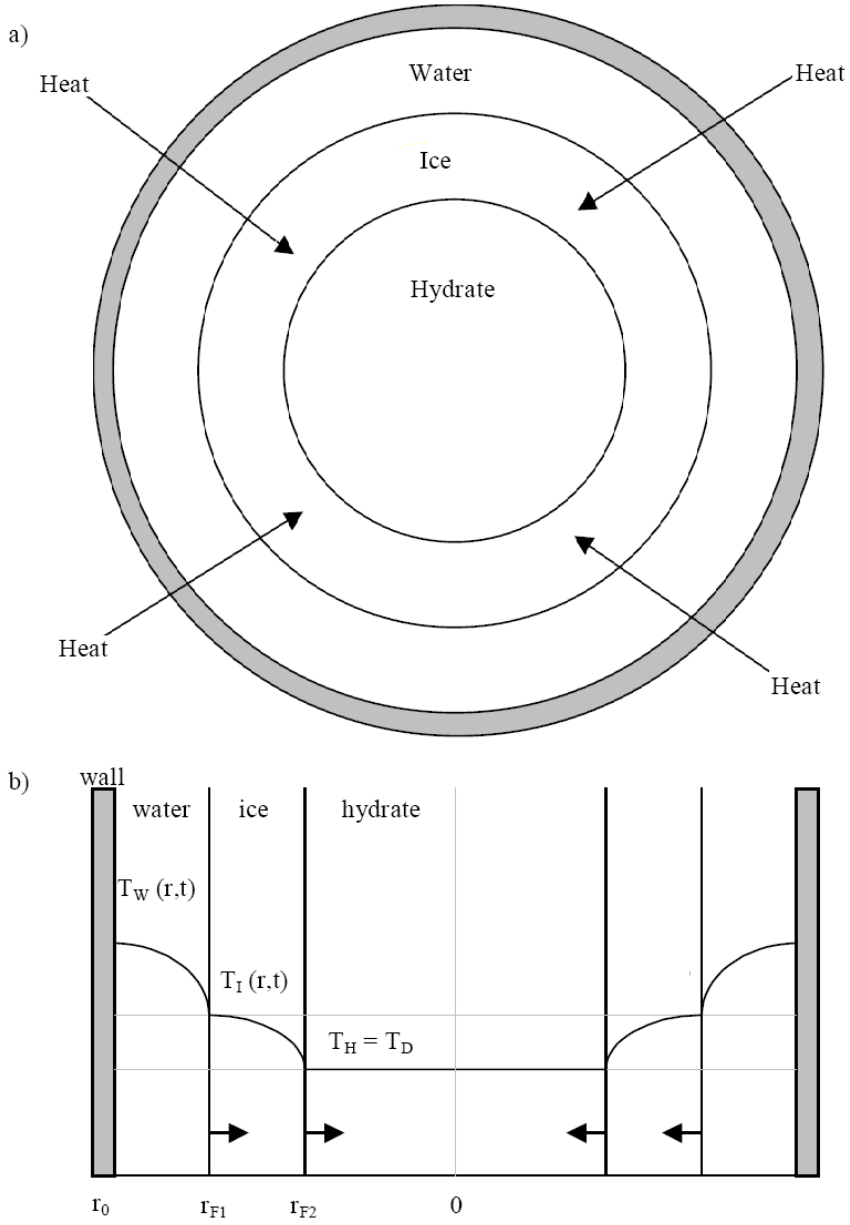

Figure 3.7 – Radial two-sided dissociation of hydrate plug for a double moving boundary including hydrate, ice and water phases. (Modified from Peters[49]).

The model of Peters[49] has been extended by Bollavaram[54] for one-sided dissociations (a safety simulator was also included that considers whether the plug will dislodge from the pipe walls) and by Davies et al.[40] for electrical heating of the pipe (replaces the boundary condition of constant wall temperature with a constant heat flux at the wall). These models are included in the plug dissociation calculation program CSMPlug (where CSM stands for Colorado School of Mines), this program is included with Sloan and Koh.[2] Sloan and Koh note that CSMPlug provides an order of magnitude (or higher) prediction of hydrate dissociation times under field conditions which is acceptable to the industrial setting. It is important to note that the CSMPlug model assumes fixed values of the enthalpies of dissociation, $\Delta_{dis}H$, for sI and sII hydrates (for sI $\Delta_{dis}H = 460.24$ kJ·kg^{-1} and for sII $\Delta_{dis}H = 640.15$ kJ·kg^{-1}).[40]

Peters[49] in his thesis compared measurements of hydrate dissociation with his model. The experimental apparatus he used for dissociations is shown in Figure 3.8. The reactor was a cylindrical stainless steel cell with threaded end caps, a length of 203 mm (8 in.), an internal diameter of 47.6 mm (1 ⅞ in), and an external diameter of 54.0 mm (2 ⅛ in). The reactor also contained 6 thermowells, containing thermocouples, spaced along the length of the cell, that measured the centreline temperature. A data acquisition system monitored the thermowell thermocouple temperatures, as well as the bath temperature and system pressure. In summary, the dissociation measurements were made by first venting excess gas pressure via valves (V4 to V7) (to either atmospheric pressure or a pressure set using pressure relief valves), then the gas emanating from the dissociating hydrate was bubbled through an inverted graduated cylinder filled with water. The flow rate of gas was monitored by the rate at which gas displaced the water in the inverted cylinder. The flow rate of the gas was integrated with time to yield the cumulative volume of gas released with time. This volume was then in turn converted to moles and plotted against time. Figure 3.9 is an example plot from Peters.[49] It shows the experimental and model prediction of the cumulative moles of gas released with time from a methane sI plug.

An approximate solution of a model for the estimation of hydrate plug dissociation times has recently been published by Nguyen-Hong et al.[51]:

$$t_D = \frac{r_0^2}{k_L}\left[\frac{0.335\Delta_{dis}H\rho_H(1-\varepsilon)}{(T_w - T_m)} + 0.09\rho_L c_{pL}\right], \tag{3.8}$$

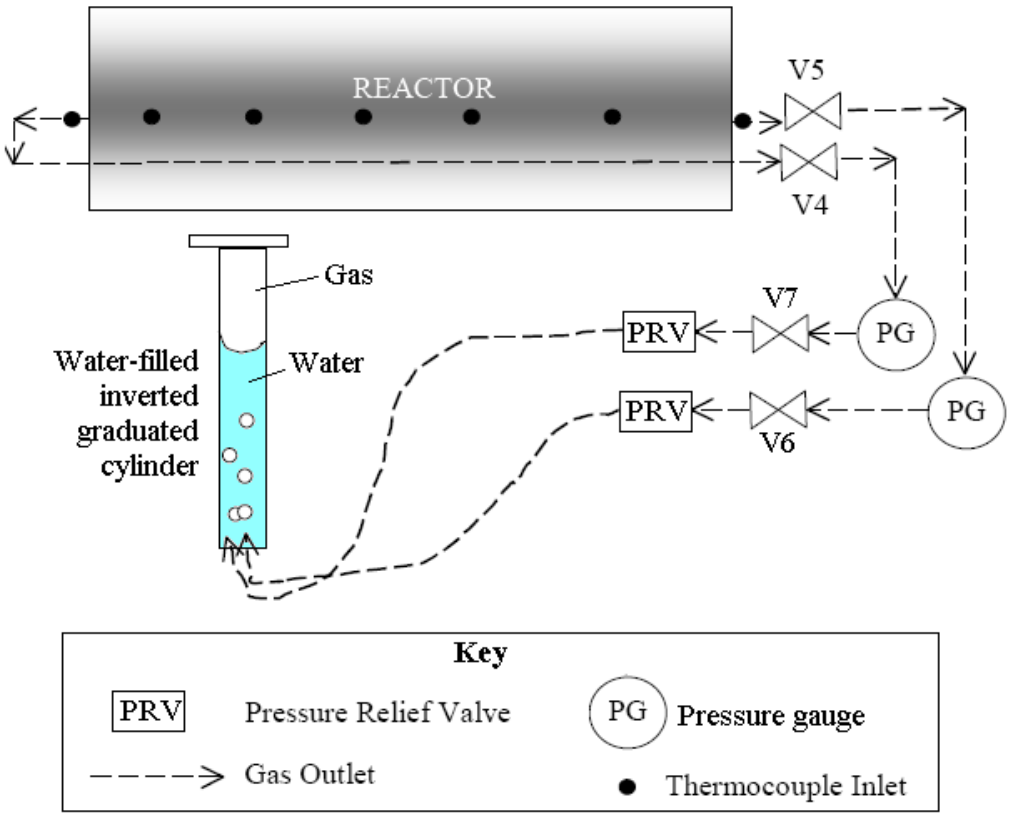

Figure 3.8 – Peters experimental apparatus for hydrate dissociation. (Modified from Peters[49]).

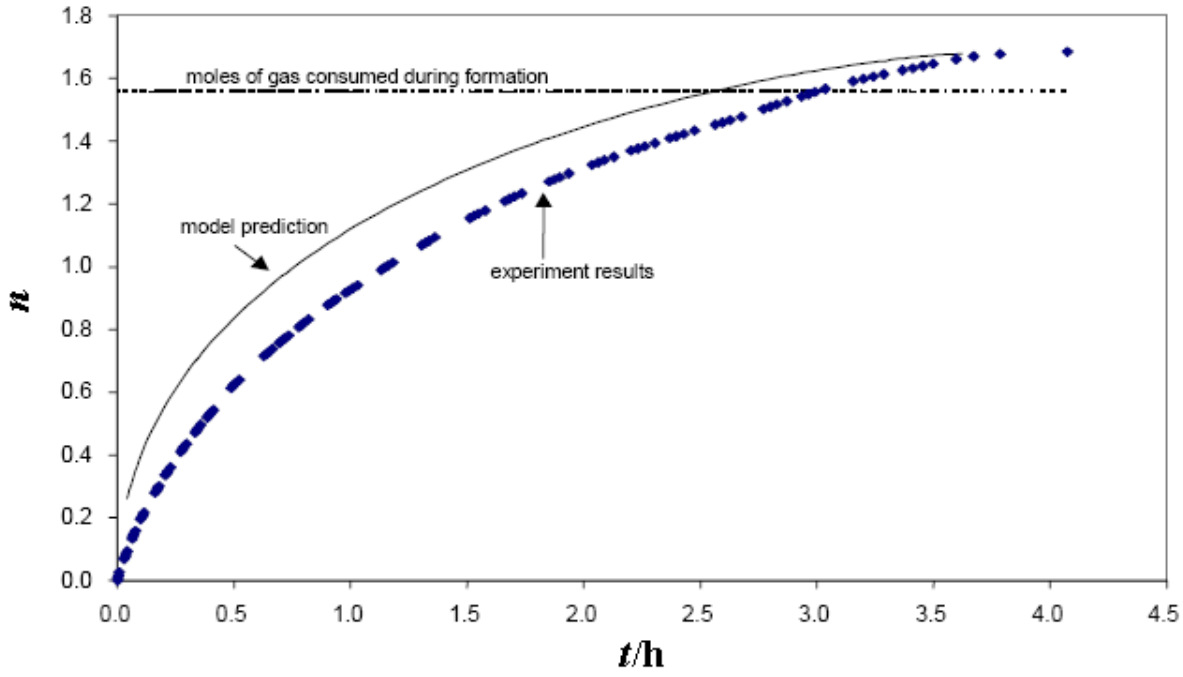

Figure 3.9 – Experimental and model prediction of cumulative moles of gas released, *n*, versus time, *t*, for a methane sI hydrate prepared by Peters. (Modified from Peters[49]).

where the t_D is the dissociation time, r_0 is the internal radius of the pipeline, k is the thermal conductivity, $\Delta_{dis}H$ is the enthalpy of dissociation of the hydrate, ρ is the density, ε is the plug porosity (void fraction that can be occupied by gas), T_W the internal pipe wall temperature, T_m is the dissociation temperature of the hydrate and c_p is the specific heat capacity, the subscripts L and H refer to the liquid and hydrate phase respectively. The model assumes the depressurisation of the plug is slow so that no ice is formed. The model was shown to be valid for plug porosities between 0.3 and 0.9 with an average error of about 4 % for dissociation temperatures (T_m) between 273.15 K and 277.15 K.

3.2.5 Enthalpies of dissociation of gas hydrates

The dissociation of a gas hydrate is described by eqs (3.9) and (3.10). Generally if the dissociation conditions are above the ice point (on the liquid side of the water melting line) the hydrate will dissociate in to gas and aqueous phases (eq (3.9)) whereas if the dissociation conditions are below the ice point the hydrate will dissociate in to gas and ice phases. For a single guest hydrate dissociated above the ice point under idealised conditions where the guest is considered insoluble in water and no water is present in the vapour phase then eq (3.11) describes the stoichiometry of the dissociation, similarly eq (3.12) describes the dissociation below the ice point. In these equations G represents the guest molecule (for example CH_4) and n represent the hydrate number or the number of moles of water per mole of guest in the hydrate.

$$\text{Hydrate} \rightarrow \text{Aqueous Solution} + \text{Vapour} \tag{3.9}$$

$$\text{Hydrate} \rightarrow \text{Ice} + \text{Vapour} \tag{3.10}$$

$$\text{G}\cdot n\text{H}_2\text{O(s)} \rightarrow \text{G}\left(\text{g}\right) + n\text{H}_2\text{O(l)} \tag{3.11}$$

$$\text{G}\cdot n\text{H}_2\text{O(s)} \rightarrow \text{G}\left(\text{g}\right) + n\text{H}_2\text{O(s)} \tag{3.12}$$

The enthalpy of dissociation is the amount of energy at constant pressure required to dissociate the hydrate by either of the reactions given by eqs. (3.9) or (3.10). This enthalpy

may be experimentally measured by calorimetry or may be calculated from *P,T* phase data using the Clapeyron equation.[2]

The enthalpy of many natural gas components have been measured by calorimetry as well as several mixtures. Values of the enthalpies of dissociation for single guest component hydrates are listed in Table 3.2. Handa at the National Research Council of Canada measured dissociation enthalpies for several single guest hydrates of natural gas components namely methane, ethane, propane and isobutane using a Tian-Calvet heat flow calorimeter at low temperatures.[135] Samples of hydrate were prepared outside of the calorimeter from powdered ice and gas in a rolling rod mill and stored in liquid nitrogen until use. The hydrates were loaded in to a sample calorimeter cell that was cooled in a liquid nitrogen bath, in turn the cell was loaded into the calorimeter that was precooled to 78 K. Enthalpies of dissociation were measured at temperatures between (160 and 210) K for methane, (190 to 250) K for ethane, (210 to 260) K for propane and (230 to 260) K for isobutane. The temperature at which dissociation occurred was varied by adjusting the pressure of the gas in the calorimeter cell. Heat capacities of the methane, ethane and propane hydrates were also measured between (85 and 270) K (note: 260 K was the maximum measurement temperature for the ethane and propane hydrates). Handa presented a method of calculating the hydrate dissociation enthalpy at standard *P,T* conditions of 0.1013 MPa and 273.15 K.[136] He used this method to calculate the enthalpies of dissociation of hydrate at both the H+I+V (hydrate + ice + vapour) and H+L_W+V (hydrate + aqueous solution + vapour) points at these standard conditions for the methane, ethane and propane hydrate. Handa also presented measurements for two naturally occurring hydrates, a sI sample from the Mid America Trench off Guatemala and a sII sample from the Green Canyon area of the northern Gulf of Mexico.[137]

Several other authors have also reported calorimetric measurements of enthalpies of dissociation. Lievois et al.[138] published measurements of the enthalpy of dissociation of methane hydrate at 278.15 K and 283.15 K using a pressurised heat flux Calvet calorimeter. Isothermal dissociation measurements were taken at nearly constant pressure by slowly expanding the available volume using a high pressure pump. Rueff et al.[139] measured the enthalpy of dissociation of methane hydrate by differential scanning calorimetry (Perkins-Elmer DSC-2) at 285 K. Rueff et al. also lists measurements of the enthalpy of dissociation

of carbon dioxide published by Nagayev et al.[140] and references measurements on natural gas hydrates by Cherskii et al.[141] Kang et al.[142] measured the enthalpies of dissociation for methane, carbon dioxide as well as nitrogen hydrate using an isothermal microcalorimeter (a modified Calorimetry Sciences Corporation 4400 IMC). The enthalpies were measured at 273.65 K and the dissociation of the hydrates was initiated by rapid depressurisation to a gas reservoir at close to atmospheric pressure (at the end of the dissociation the pressure was between (0.1 and 0.3) MPa). The enthalpies of dissociation of hydrates prepared from two mixtures of carbon dioxide and nitrogen (of mole fractions 0.17 CO_2 + 0.83 N_2 and 0.70 CO_2 + 0.30 N_2) were also measured. Marsh and Gao[143] prepared hydrates from six synthetic natural gas mixtures inside high pressure cells of a Calorimetry Science Corporation MC-DSC 4100. The high pressure cells contained an inlet and outlet tubing, the inlet tubing reached close to the bottom of the cell and the outlet tubing exited from the top of the cell. The cells were loaded with water, using a high pressure syringe pump the gas was flowed through the cells at a slow constant flow rate. The DSC was then initially scanned down to -20 °C to convert the water in to ice and then slowly cycled between -1 °C and +2 °C at 1 $K \cdot h^{-1}$ a number of times. The final stage of hydrate formation involved heating the cells to 2 °C below their predicted hydrate dissociation temperature and holding the cells at that temperature for a period of 6 h. The DSC was cooled to -20 °C to convert any remaining water to ice and was then a scanned from -5 °C to 8 °C above the dissociation temperature at 6 $K \cdot h^{-1}$, during this time the gas flow through the cells was stopped. At 2 °C below the hydrate dissociation temperature the syringe pump volume and pressure were recorded. After hydrate dissociation the DSC was cooled back to that temperature and the pump was reversed to the initially recorded pressure so that the volume and hence moles of gas that had been enclathrated in the hydrate phase could be calculated. During the dissociation process the pressure change was not more than 0.02 MPa so the pressure could be considered constant. Finally the DSC was cooled to -20 °C and another enthalpy of fusion of ice measurements was completed. The peaks of a hydrate dissociation of one of Marsh and Gao's mixtures are shown in Figure 3.10. From the enthalpy of fusion of ice peaks before and after the hydrate dissociation it was possible to calculate the amount of water that had been converted to hydrate by dividing the difference in peaks enthalpies by a value for the enthalpy of fusion of ice of 334.2 $J \cdot g^{-1}$ (6021 $J \cdot mol^{-1}$) measured by Handa.[144] The moles of water in the hydrate was then divided by the moles of gas (from the syringe pump volume difference before and

after hydrate dissociation) to give the hydrate number, *n*. The enthalpy of hydrate dissociation could then be calculated from the dissociation peak.

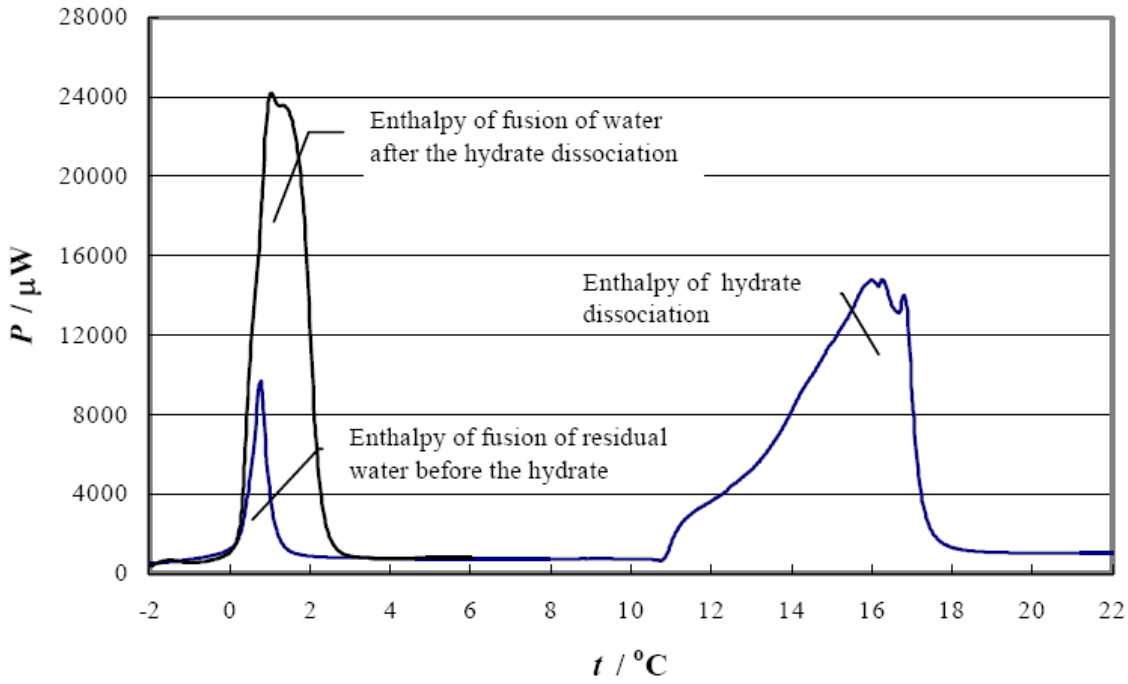

Figure 3.10 – Calorimetric response for enthalpy measurements Marsh and Gao's mixture 3 at 2.07 MPa. (Reproduced from Marsh and Gao.[143]).

Levik[145] made enthalpy of dissociation measurements on hydrate prepared in a laboratory scale flow loop from a mixture containing mole fractions of 92 % methane + 5 % ethane + 3% propane. Measurements were completed in a pressurizable Setaram BT2.15 heat flow calorimeter.

Gupta[50] measured the enthalpies of dissociation of methane hydrate at temperatures between 280.60 K and 291.65 K using a High Pressure Setaram Micro-Differential Scanning Calorimeter VIIa. Hydrate samples were prepared from powdered ice using a method similar to Stern et al.[126] and transferred cryogenically with liquid nitrogen at atmospheric pressure to the DSC sample cell. Heat capacities of the hydrate were also measured.

Rydzy et al.[146] completed measurements of the enthalpies of dissociation of hydrates prepared from pure methane and four different mixtures, two containing methane + carbon dioxide and two containing methane + ethane + propane. Hydrates were prepared in a high pressure cell

from gas and powdered ice. The calorimeter used was a Setaram Calvet DSC 121 that could be cooled with liquid nitrogen. Measurements on the dissociation of hydrates were completed at atmospheric pressure hence the dissociation points were at low temperatures below 273 K and the hydrate dissociated to ice + gas. Interestingly a mixture of mole fractions 98 % methane + 1 % ethane + 1 % propane was demonstrated to have formed a mixture of sI and sII hydrates by both calorimetry (two separate hydrate dissociation peaks were observed) and powder X-ray diffraction.

Table 3.2 – Calorimetric measurements of enthalpies of dissociation for single guest hydrates of natural gas components.

Guest		***T*/K**	***P*/MPa**	***n***	**$\Delta_{dis}H$/kJ·mol^{-1}**	**Reference**
CH_4	H+I+V	273.15	0.101325	6	18.13[a] ± 0.27	Handa[135]
	H+Aq+V	273.15	0.101325	6	54.19[a] ± 0.28	Handa[135]
	H+Aq+V	285[b]	[c]	6.04[d]	54.63[e] ± 0.79	Rueff et al.[139]
	H+Aq+V	278.15	4.217	5.97	57.65 ± 1.50	Lievois et al.[138]
	H+Aq+V	283.15	7.110	5.98	53.24 ± 1.38	Lievois et al.[138]
	H+Aq+V	273.65	0.1 to 0.3	6.38	56.84 ± 0.89	Kang et al.[142]
	H+Aq+V	280.6 to 292.16	5.5 to 19.3	6	54.44[b] ± 1.45	Gupta[50]
C_2H_6	H+I+V	273.15	0.101325	7.67	25.70[a] ± 0.37	Handa[135]
	H+Aq+V	273.15	0.101325	7.67	71.80[a] ± 0.38	Handa[135]
C_3H_8	H+I+V	273.15	0.101325	17.0	27.00[a] ± 0.33	Handa[135]
	H+Aq+V	273.15	0.101325	17.0	129.2[a] ± 0.4	Handa[135]
iC_4H_{10}	H+I+V	273.15	0.101325	17.0	31.07[a] ± 0.20	Handa[135]
	H+Aq+V	273.15	0.101325	17.0	133.2[a] ± 0.3	Handa[135]
CO_2	H+Aq+V	279	[c]	6.00[f]	51.02[e,g]	Nagayev et al.[140 h]
	H+Aq+V	281	[c]	5.82[f]	56.88[e,g]	Nagayev et al.[140 h]
	H+Aq+V	273.65	0.1 to 0.3	7.23	65.22 ± 1.03	Kang et al.[142]
N_2	H+Aq+V	273.65	0.1 to 0.3	5.94	65.81 ± 1.04	Kang et al.[142]

[a] Calculated at standard state of 273.15 K and 0.101325 MPa, see Handa[135] for details, H+Aq+V values calculated used the enthalpy of fusion of ice at 273.15 K.
[b] Averaged value for all measurements.
[c] Not measured or unknown.
[d] Estimated from CSMGem at 285 K.
[e] Calculated from mass specific enthalpy of dissociation.
[f] Estimated from Anderson.[147]
[g] Uncertainty unknown.
[h] Values were listed in Rueff et al.[139]

The calorimetrically measured enthalpies of dissociation for single guest hydrates of natural gas components are listed in Table 3.2. The H+Aq+V enthalpies of dissociation for methane hydrate of Handa,[135] Rueff et al.,[139] Lievois et al.[138] at 283.15 K, and Gupta agree within error

despite being measured at different P,T conditions. The values of Lievois et al.[138] at 278.15 K and Kang et al.[142] are approximately 3 kJ·mol^{-1} higher than the other measurements. The only other single component for which measurements have been conducted by more than one group is that for carbon dioxide. The enthalpies of dissociation of CO_2 hydrate by Nagayev et al.[140] (listed in Rueff et al.[139]) are considerably lower than the measurement by Kang et al.[142] More measurements are needed on system to confirm the value of the enthalpies of dissociation of CO_2 hydrate.

The Clapeyron equation is typically used to calculate the enthalpy of vaporisation from vapour pressure data of a pure component. It expresses the enthalpy of vaporisation, $\Delta_{vap}H$, in terms of the temperature, the change in volume, ΔV, and the vapour pressure P,T slope, dP/dT:

$$\Delta_{vap}H = T\Delta V \frac{\mathrm{d}P}{\mathrm{d}T}. \tag{3.13}$$

As Van der Waals and Platteuw[148] point out the Clapeyron equation "is a direct consequence of the second law of thermodynamics, and as such exact for all univariant equilibria, irrespective of the number of components". As a consequence of this they considered a binary hydrate forming system of water + gas. The points of three phase equilibria along either the H+I+V or H+L_W+V line of such a system are "univariant ones in which the composition of the clathrate varies along the three phase lines". Barrer notes that care should be taken due to the non-stoichiometry of hydrates (n, the hydrate number varies with the P,T conditions), and notes that n should be determined at the same time as the enthalpy of dissociation to ensure that the values does not have "uncertain meaning".[149] Glew suggested that while there are deviations of n from the ideal value required to fill all the cages that generally n varies very little along the hydrate formation lines except for molecules that are approaching the upper limit of the cavity sizes such as ethane, methyl bromide and bromine in sI.[150] Glew also suggested that making all the corrections such as allowing for "phase volume changes, gas imperfections, gas solubility and water saturations" was very important and should be made when "hydrate saturation pressures greater than one atmosphere are involved for example, for argon and methane hydrates".

An alternative expression of the Clapeyron equation can be derived from eq (3.13) if a compressibility factor difference, ΔZ, is defined in terms of the volume change:

$$\Delta Z = \frac{P\Delta V}{RT}, \tag{3.14}$$

and the mathematical relationships $\mathrm{d}P/P = \mathrm{d}\ln P$ and $\mathrm{d}T/T^2 = -\mathrm{d}(1/T)$ are applied:

$$\Delta_{\mathrm{vap}} H = -R\Delta Z \frac{\mathrm{d}\ln P}{\mathrm{d}(1/T)}, \tag{3.15}$$

If the Clapeyron equation is applied for the enthalpy of hydrate dissociation $\Delta_{\mathrm{vap}} H$ is replaced by $\Delta_{\mathrm{dis}} H$. The advantage of this form of the Clapeyron equation is that plots of ln$P$ versus $1/T$ yield linear relationships (constant value of dln$P$/d[$1/T$]) over larger P,T ranges than plots of P versus T. Assuming limited solubility of the vapour in the water and limited vaporisation of water in to the vapour phase (i.e. after dissociation of the hydrate the aqueous phase contains no molecules of the hydrate guest so is pure water and the vapour phase contains no water so the vapour phase is pure guest) ΔV can be calculated by:

$$\Delta V = V_{\mathrm{G}} + nV_{\mathrm{H_2O}} - V_{\mathrm{H}}, \tag{3.16}$$

where V_{H} is the molar volume of the hydrate (defining one mole of hydrate as M·nH$_2$O, i.e. one mole of hydrate has a molar mass that is the sum of the molar mass of M and the molar mass of n water molecules), V_{G} is the molar volume of the gaseous hydrate guest phase, and $V_{\mathrm{H_2O}}$ is the molar volume of the water phase (ice or liquid water). The compressibility factor difference can then be similarly defined as:

$$\Delta Z = Z_{\mathrm{G}} + nZ_{\mathrm{H_2O}} - Z_{\mathrm{H}}, \tag{3.17}$$

by multiplying eq (3.16) by $P/(RT)$. Roberts et al.[151], Barrer and Edge[152] and Skovborg and Rasmussen[153] present similar forms of the Clapeyron equation where the solubility of the guest in the aqueous phase and water content of the vapour are taken in to account, Barrer and Edge also consider a double hydrate composed of a water insoluble liquid guest ($CHCl_3$) and a gaseous guest. Skovborg and Rasmussen note that CO_2 and H_2S have a "somewhat higher solubility" in water than most gas hydrate guest components suggesting it may not be appropriate to make assumption of no solubility of the guest in the aqueous phase.

Sloan and Fleyfel[154] calculated the enthalpies of dissociation for methane, ethane, propane and isobutane hydrates assuming that $\Delta Z = Z_G$ (or $\Delta V = V_G$), from experimental L_W-H-V P,T data (note: when this form is used the Clapeyron equation is referred to as the Clausius-Clapeyron equation). Sloan and Fleyfel[154] compared their calculated values with the calorimetric data of Handa[136], these values are listed in Table 3.3, and show close agreement (the calculated values deviate between (1 and 5)% from the calorimetric measurements).

Sloan and Fleyfel[154] further suggested that to a first approximation for a sI or sII hydrate the size of the guest molecule fixes the enthalpy of dissociation, as the size of the molecule determines which cages are occupied. The initial paper of Sloan and Fleyfel was commented on in a letter to the editor of the journal "Fluid Phase Equilibria" by Skovborg and Rasmussen[153] who critiqued the paper and suggested that Sloan and Fleyfel[154] were incorrect. They deducted a hypothetical empty lattice hydrate dissociation value from Sloan and Fleyfel's enthalpies to magnify the differences in enthalpies of dissociation in terms of the guest molecules contribution and suggested the relationship broke down from their results. However Sloan and Fleyfel[155] noted in a reply to the comments "we concur with their conclusion, but suggest that to ignore "the different amounts of water in the hydrate" would be to ignore the largest portion of the heat of dissociation, i.e. that due to hydrogen bonding" and that Skovborg and Rasmussen's mathematical derivation of hydrate dissociation "suggests a limit to our engineering approximation to explain these phenomena". They also produced a plot to show the slope, $d\ln P/d(1/T)$, as a function of the size of the hydrate guest, shown in Figure 3.11, to emphasize the relationship between the cavity size and the dissociation enthalpy. It was also noted from $\ln P$ versus $1/T$ plots for hydrates of binary gas mixtures of the same components but with different compositions that the data for each

composition could be fit with a line of the same slope indicating similar dissociation enthalpies, sII forming natural gas multicomponent mixtures which contained mole fractions between (65 and 96.5) % methane showed similar results despite great variability in the composition.

Table 3.3 – Comparison of the Clausius-Clapeyron calculated and experimental above ice point enthalpies of dissociation at 273.15 K.*

Hydrate guest component	Calculated[a] $\Delta_{dis}H$/ kJ·mol^{-1}	Calorimetric[b] $\Delta_{dis}H$/ kJ·mol^{-1}
Methane	56.9	54.2
Ethane	71.1	71.8
Propane	126.0	129.2
Isobutane	130.4	133.2

*,[a] From Sloan and Fleyfel.[154]

[b] Handa's[135] calorimetric values for the standard state of 273.15 K and 0.101325 MPa.

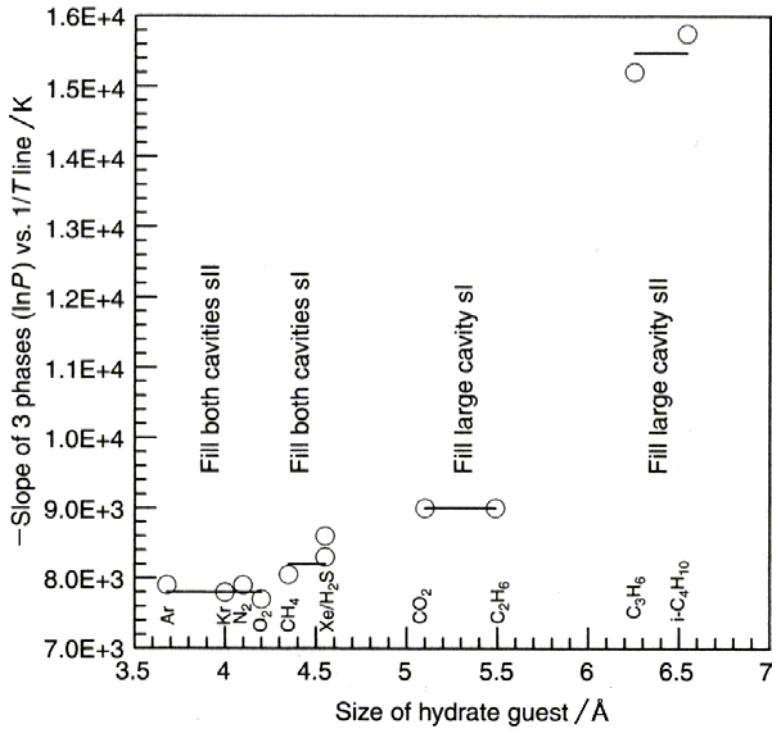

Figure 3.11 – Clapeyron equation slope, -dln$P$/d(1/T), as a function of the hydrate guest size. (Modified from Sloan and Koh[2], originally published by Sloan and Fleyfel[155]).

Recently several papers have been published that attempt to obtain more accurate values of the enthalpy of dissociation of gas hydrates using the Clapeyron equations. Anderson[147] regressed seven sets of carbon dioxide H+Aq+V data to generate a polynomial equation for dP/dT for use in the eq (3.13) form of the Clapeyron equation. A volume difference equation was developed which took into account the solubility of CO_2 in water and the volume of the hydrate phase:

$$\Delta V = \left(1 - \frac{n x_{\mathrm{Aq}}^{\mathrm{CO_2}}}{1 - x_{\mathrm{Aq}}^{\mathrm{CO_2}}}\right) V_{\mathrm{V}} + n V_{\mathrm{Aq}} - V_{\mathrm{H}}, \tag{3.18}$$

where $x_{\mathrm{Aq}}^{\mathrm{CO_2}}$ is the mole fraction of CO_2 in the aqueous phase (see Appendix D for a discussion of the stoichiometry of hydrate dissociation). This equation accounts for the reduction in volume of the vapour phase due to the high solubility of CO_2 in water. The vapour phase molar volume was considered to be pure CO_2 (no water), the aqueous volume was calculated from the molar volume of pure water and the infinite dilution partial molar volume of CO_2 in water, and the hydrate molar volume was calculated from a X-ray diffraction calculated CO_2 hydrate density. Anderson defined dissociation enthalpies based on two equations for above the ice point hydrate dissociations, these were:

$$\mathrm{CO_2 \cdot} n\mathrm{H_2O(s)} \rightarrow \mathrm{CO_2(g)} + n\mathrm{H_2O(l)}, \tag{3.19}$$

and

$$\mathrm{CO_2 \cdot} n\mathrm{H_2O(s)} \rightarrow \left(1 - \frac{n x_{\mathrm{Aq}}^{\mathrm{CO_2}}}{1 - x_{\mathrm{Aq}}^{\mathrm{CO_2}}}\right) \mathrm{CO_2(g)} + n\mathrm{H_2O(l,CO_2\ sat)}. \tag{3.20}$$

As eq (3.19) was referred to as reaction I in Anderson paper the enthalpy of dissociation for this reaction was referred to as ΔH_{I}, similarly eq (3.20) was referred to as reaction IV and is the enthalpy of dissociation for this reaction was referred to as ΔH_{IV}. The connection between these two equations is:

$$n\mathrm{H_2O(l,CO_2\ sat)} \rightarrow n\mathrm{H_2O(l)} + \left(\frac{n x_{\mathrm{Aq}}^{\mathrm{CO_2}}}{1 - x_{\mathrm{Aq}}^{\mathrm{CO_2}}}\right) \mathrm{CO_2(g)}, \tag{3.21}$$

(equation V in Anderson). The enthalpy change of this equation may be found from enthalpy of solution data. By addition of the enthalpies of eqs (3.20) and (3.21) the enthalpy for eq (3.19) is obtained. Values of ΔH_{IV} were calculated using the eq (3.13) form of the Clapeyron equation between (274.15 and 282.15) K. Enthalpies of solution were deduced from these ΔH_{IV} values to calculate ΔH_I values. The ΔH_I values would appear to be a hypothetical enthalpy for the dissociation to pure water and pure CO_2 gas, whereas ΔH_{VI} values should equate to calorimetrically measured enthalpies of dissociation (it should be noted here that if this method was generalised to all guest components, than for guest that are not very soluble in water than $\Delta H_{IV} \approx \Delta H_I$). It is uncertain why Anderson compared ΔH_I values to calorimetrically measured values rather than ΔH_{IV} values (Table 5 of Anderson[147]). The ΔH_I values might be better used to compare enthalpies of dissociation of highly water soluble guests to those of almost insoluble guests.

Unfortunately there are very few calorimetric measurements of the enthalpy of dissociation of CO_2 hydrates to compare to the values Anderson calculated using the Clapeyron equation. Kang et al[142] gave a value of (65.22 ± 1.03) kJ·mol^{-1} (for n = 7.23) at 273.65 K and close to atmospheric pressure. Rueff et al.[139] lists values of the enthalpies of dissociation of 342.98 J·g^{-1} at 279 K and 374.40 J·g^{-1} at 281 K from Nagayev et al.[140], using Anderson's values of n = (6.00 and 5.82) respectively at these temperatures (calculated using eq 15 of Anderson[147]) gives respective values of 51.02 kJ·mol^{-1} and 56.88 kJ·mol^{-1}. The value at 281 K of 56.88 kJ·mol^{-1} is within error of Anderson's calculated value of (55.8 ± 2.4) kJ·mol^{-1} at 281.15 K (ΔH_{IV} value from table 3 of Anderson[147]). Anderson published a similar paper for methane hydrate in which he regressed experimental methane H+Aq+V and H+I+V equilibria P,T data and used the same volume difference correction for the solubility of methane in water as was used for CO_2 hydrate paper.[156] Over the temperature range 274 K to 318 K the calculated enthalpy of dissociation for the methane hydrate changed little. At 273.15 K the calculated value for dissociation of the hydrate to aqueous solution + vapour of (53.5 ± 1.3) kJ·mol^{-1} was within the uncertainty of Handa's[135] calorimetric derived value of (54.19 ± 0.28) kJ·mol^{-1}. For the dissociation to ice + vapour at 273.15 K Anderson calculated a value of (18.01 ± 0.10) kJ·mol^{-1} compared to Handa's calorimetric derived value of (18.13 ± 0.27) kJ·mol^{-1}. Glew[157] performed a similar analysis for methane hydrates (fitting methane hydrate P,T equilibrium data to an equation and calculating ΔV by a method which accounted

for the volume of the hydrate phase, solubility of methane in water and assumed the vapour phase was pure methane free of water), and his values of the enthalpy of dissociation at 273.15 K were (55.36 ± 0.57) kJ·mol^{-1} for dissociation to aqueous solution + vapour and (18.06 ± 0.53) kJ·mol^{-1} for dissociation to ice + vapour (c.f. Handa's values above, uncertainties for these values have been calculated as 95 % confidence intervals based on the standard errors given by Glew[157]).

An another approach is presented by Yoon et al,[158] they appear to calculate values of enthalpies of dissociation that are similar to ΔH_I values of Anderson,[147] that is values to which an enthalpy of solution term has been applied. The derivation of equations in their work is unclear however, Anderson[156] noted they "do not provide enough details to evaluate their results, nor do they quote uncertainties". They compare their calculated values to calorimetric enthalpies of dissociation, no reasons are provided for why ΔH_I type values are better to compare to calorimetric results than ΔH_{IV} type values.

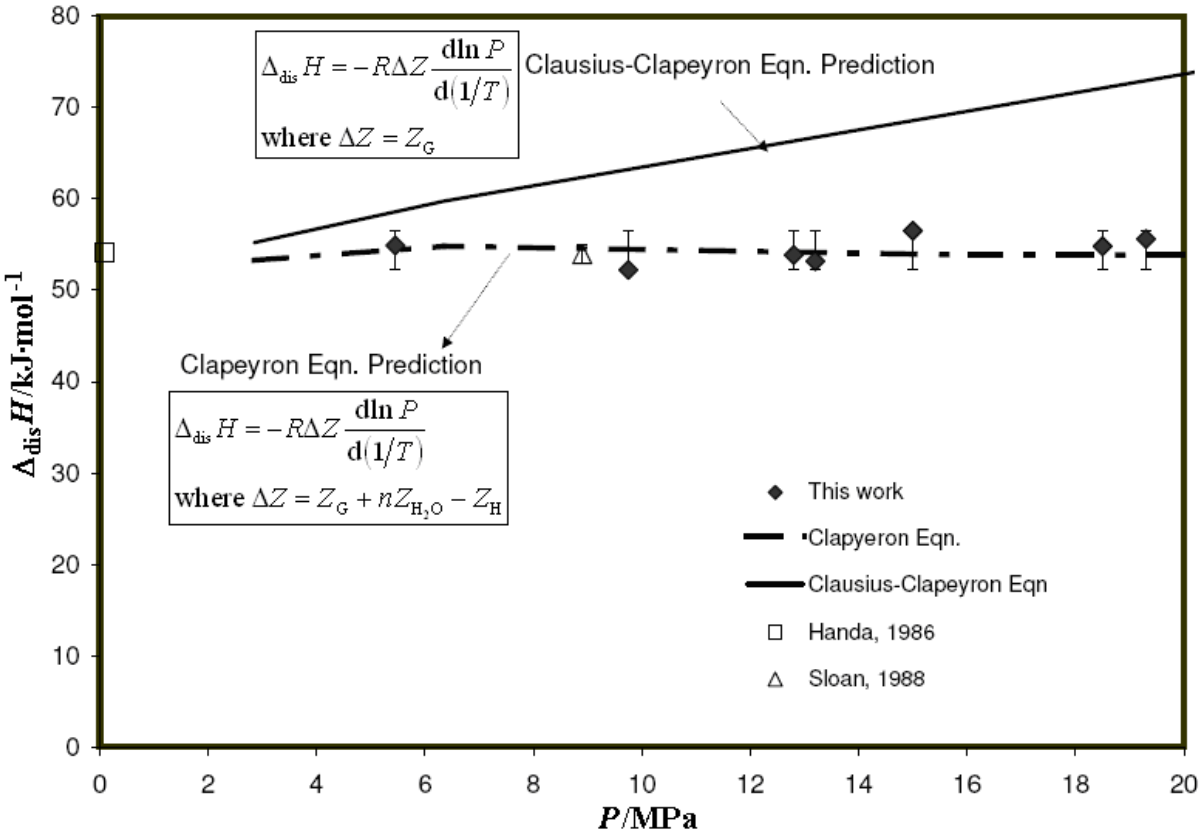

Figure 3.12 – Comparison of experimental enthalpies of dissociation of methane hydrate to those calculated by the Clausius-Clapeyron and the Clapeyron equation. (Modified from Gupta[50]).

Gupta[50] calculated enthalpies of hydrate dissociation for methane hydrates using both the Clausius-Clapeyron equation and the Clapeyron equation accounting for the volume of each phase but approximating the vapour volume with that of pure methane and the aqueous phase volume with that of pure water. These calculated values were plotted against calorimetrically measured values, the revised plot from Gupta[50] is shown as Figure 3.12

3.3 Experimental work

Experiment work described in this chapter involves plug dissociation time measurements and calorimetric measurements. The research was carried out at two schools: The Chemical Engineering Department at the Colorado School of Mines (CSM) in Golden, Colorado and the Chemical and Process Engineering Department at the University of Canterbury (UC) . Plug dissociations were done at the CSM and UC while calorimetry has been completed at UC.

3.3.1 Materials

At CSM the methane and ethane was obtained from Matheson Trigas. The purity of both these gases was 99.99 % and they were used without further purification. Ice used for hydrate formation was prepared from distilled water.

At UC methane was sourced from Linde Gas, U.K Ltd, with a purity of 99.975 %. Ethane was obtained from BOC gases limited and had a purity of 99 %. These gases were used to prepare gas mixtures without further purification. The water used in the calorimeter and to prepare ice from the plug dissociation time measurements was distilled and deionised.

3.3.2 Gas mixture preparation

Gas mixtures were prepared both at CSM and UC. At CSM gas mixtures were prepared using the apparatus shown in Figure 3.13. The lower volatility ethane contained in a 43 L cylinder (8.10 m^3 of ethane at STP when full at 15.7 MPa) was connected to the system first as the pure component cylinder. A small amount of ethane was let into the system (with the mixture gas cylinder valve closed) and Swagelok Snoop® leak detection solution was used to check for leaks at connections. The system lines and aluminium cylinder were then evacuated using a Cenco Megavac vacuum pump powered by a 1725 rpm, 250 W General Electric AC motor

for a period of at least 12 h. The ethane was warmed with heating tape to aid vaporisation as ethane is a liquid at pressures greater than 3.77 MPa at room temperature (20 °C). The ethane cylinder valve was opened to allow ethane to flow into the evacuated aluminium cylinder. No compression of the ethane was required so for this part of the mixture preparation the compressor was not included as part of the system. The flow to the 13.4 L aluminium cylinder, sitting upon a Mettler Toledo SB24001 DeltaRange digital balance, was controlled using a needle valve. The cylinder was tared on the balance after it had been evacuated so that the mass of gas in the cylinder could be directly observed. Once the required mass of ethane had been met the needle valve was closed. The ethane cylinder valve and the aluminium cylinder valve were also closed, then the needle valve was reopened so that the system could be evacuated by the vacuum pump again for a few minutes. Once the vacuuming was complete the final mass of ethane in the cylinder was recorded. The system was then opened to the air just before the vacuum pump and the ethane cylinder was swapped for a cylinder of methane. At this point the compressor was added into the system. The system was closed to the air and evacuated using the vacuum pump for a period of at least 30 min. The methane was initially allowed to flow unaided into the aluminium cylinder until flow slowed significantly, then the compressor was started. The compressor was pneumatic and was run using a cylinder of nitrogen. The needle valve was closed when the required mass of methane had entered the aluminium cylinder. The aluminium cylinder valve was then closed as well as the methane cylinder valve. The needle valve was then reopened and the system evacuated so that the final mass of methane that had entered the cylinder could be obtained. The gases were mixed by thermal convection using a heater plate. The gases were allowed to mix for a period of at least 48 h. During heating the cylinder valve was left open to the relief valve so that if the cylinder was to over-pressurize the gas would be vented instead.

A gas mixture was prepared at a mole fraction of 65.4 % methane + 34.6 % ethane. Table 3.4 shows the masses of each gas added and the level of impurities in the mixture.

Table 3.4 – Methane + Ethane gas mixture mole fractions and purities.

	Methane[a]			Ethane[b]			Impurities	
	Mass[c] g	Moles[c] mol	Mole Fraction[d]	Mass[c] g	Moles[c] mol	Mole Fraction[d]	Moles mol	Mole Fraction[d]
CSM	1344.5	83.813	0.654	1331.0	44.259	0.346	0.013	0.0001
UC1	3515.5	219.11	0.988	82.7	2.72	0.012	0.08	0.0004
UC2	2729.7	170.14	0.53	4500.0	148.15	0.46	1.54	0.005

[a] The mole fraction purity of the methane at CSM was 0.9999 and at UC was 0.99975.
[b] The mole fraction purity of the ethane at CSM was 0.9999 and at UC was 0.99.
[c] Mass values include the impurities, the mole values given are exclusive of impurities (the moles of impurities are listed in the right column).
[d] The error introduced by the uncertainty in the mass (half resolution, ± 0.05 g) results in mole fraction errors lower than the level of impurities

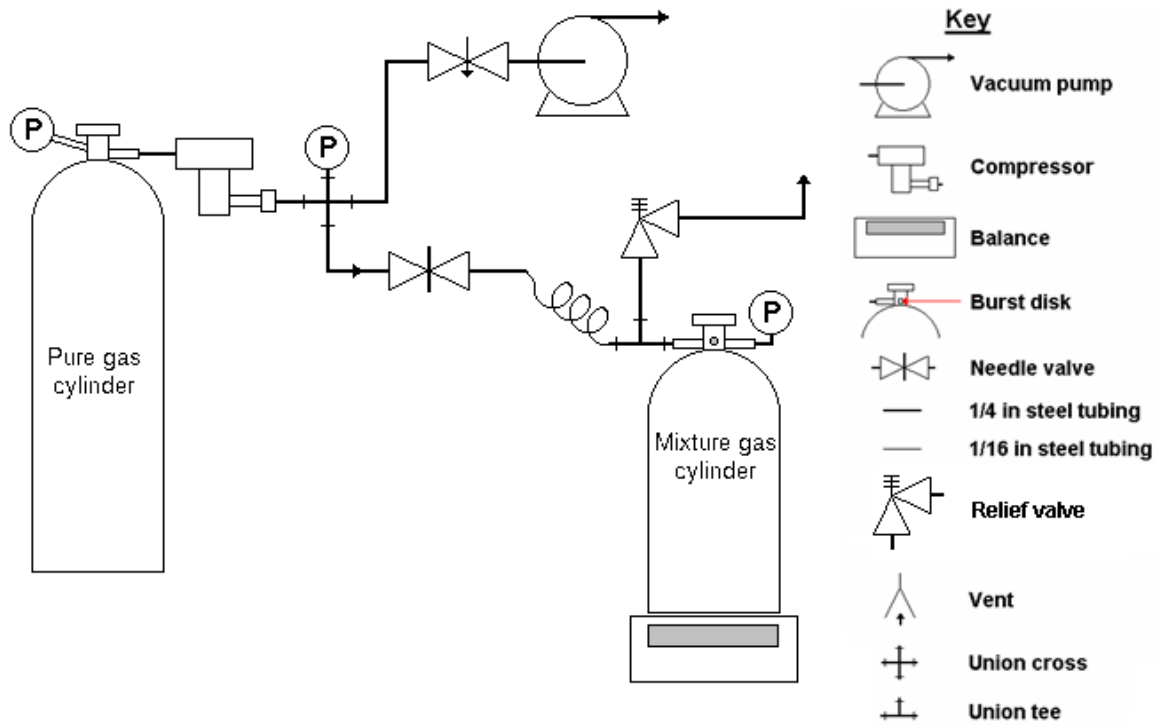

Figure 3.13 – Gas mixture preparation apparatus at CSM.

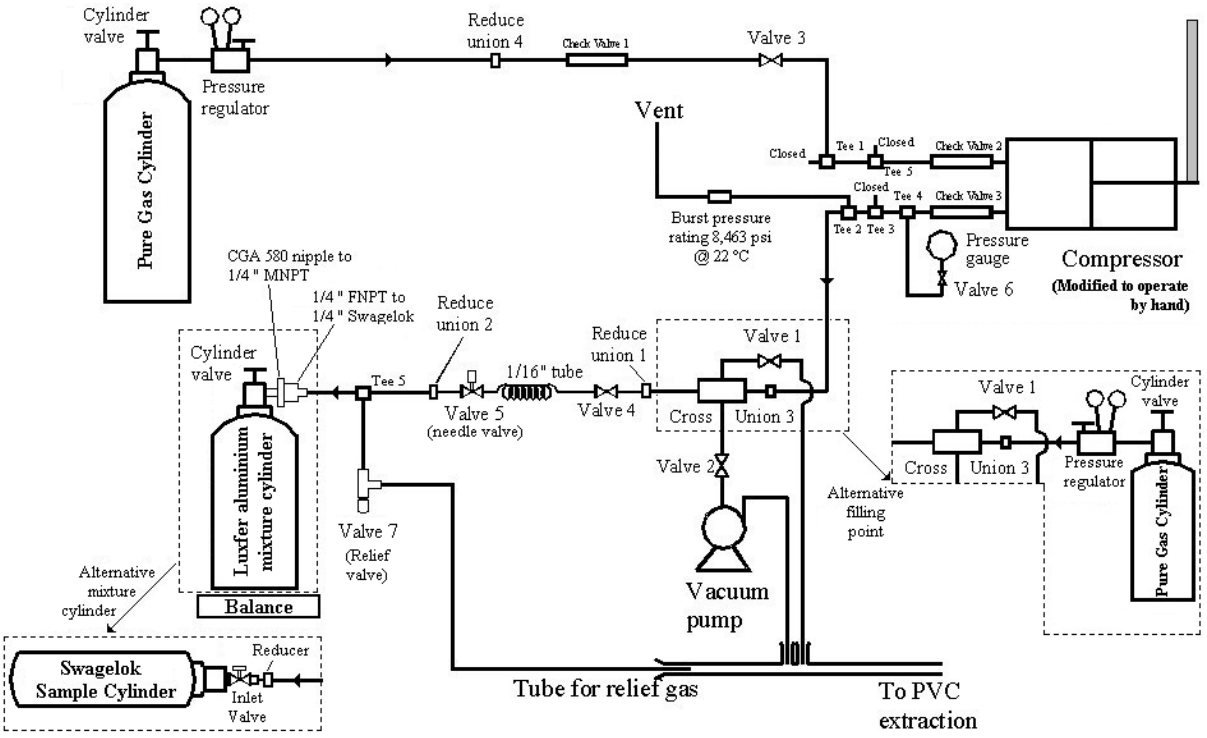

Figure 3.14 – Gas mixture preparation apparatus at the UC.

At the University of Canterbury the gas mixtures were prepared using the apparatus described in Marsh and Gao's work[143] which is shown in Figure 3.14. The electrical motor driven compressor however was modified to operate by hand as this was believed to be safer when compressing flammable gas. This modification involved bolting a 1 m handle on to the slotted lever attached to the compressor's piston. Lower pressure Swagelok valves rated to 17.2 MPa (2500 psi) were also replaced by HiP valves rated to 103 MPa (15,000 psi). Two Luxfer N122 light weight aluminium-magnesium-silicon alloy cylinders were obtained of empty volume of 21.3 L and empty mass of 18.1 kg. Gas mixtures of mole fractions 98.8 % methane + 1.2 % ethane and 53 % methane + 46 % ethane were prepared to a pressure of about 19.0 MPa. The procedure used to fill the cylinders, described below, was similar to the technique used at CSM. The mass of each gas mixed and the level of impurities in the final mixture is shown in Table 3.4.

The relief valves were cracked to 20.7 MPa (3000 psi) using argon, leaks were also checked for by compressing some argon through the system and testing connections with Swagelok Snoop® leak detection liquid. The ethane cylinder was attached at the alternative filling point shown in Figure 3.14. The cylinder to be filled and the lines leading to the ethane cylinder

were evacuated using the vacuum pump for at least two hours. Ethane was then purged into the filling cylinder to a pressure of about 0.2 MPa and vacuuming was repeated. Once vacuuming was complete the balance was tared. The extraction fan was then switched on and the ethane cylinder valve was opened to allow gas to flow into the filling cylinder. The ethane cylinder was insulated with fibre glass wool and heated with a heating cord to encourage vaporization. Once the mass of ethane had reached the required value, as indicated by the force balance, the cylinder valve on the filling cylinder was closed, the heater cord switched off and the ethane cylinder valve was closed. The system lines were then depressurised by slowly opening valve 1 to the extraction system. The ethane cylinder was then disconnected and the methane cylinder attached at the alternative filling point. The lines were then vacuumed for about 30 min. Methane was then introduced to the filling cylinder as described for the ethane (but without heating) until the pressure of the methane dropped to close to that of the filling cylinder. At this point the methane cylinder was detached and reconnected at the pre-compressor filling point (top left Figure 3.14). An undesirable ethane liquid layer will form in the cylinder at room temperature (20 °C) if the final filling density is greater than 86.4 $kg \cdot m^{-3}$ (see Appendix E for a density-temperature diagram for ethane). This was only a concern when preparing the 53 % methane + 46 % ethane mixture. If there is not sufficient mixing the liquid ethane will remain in the liquid phase at a pressure near its vapour pressure (since there is no methane in the liquid). When methane is added at a higher pressure it will mix with the ethane vapour but the volume available for the vapour to fill is reduced by the presence of the liquid ethane, this will result in a higher pressure of the methane + ethane vapour phase than in the final properly mixed single phase mixture. Over-pressurization can occur if this is not considered. For this reason mixing was initiated by disconnecting the partly filled cylinder and inverting it about fifty times. The partly filled cylinder was left to stand for an hour before it was reconnected to the system. The filling was completed by compressing the methane. Firstly the methane cylinder valve was opened, and gas was purged through the lines leading to the compressor. The compressor was then operated for about ten strokes. This methane + air mixture in the lines was slowly vented into the extraction duct by opening valve 1. The lines were purged thrice more to ensure that the methane was sufficiently pure. The valve into the filling cylinder was then opened and methane was compressed into the cylinder until the mass on the balance reached the final

required value. The filling cylinder valve and the methane cylinder valve were then closed and the lines were slowly vented to the extraction duct by opening valve 1.

In situ gas mixtures were prepared in an ISCO pump (model 260D, maximum volume 266 ml, pressure range 0 to 51.4 MPa, pressure uncertainty ± 2 %, flow rate uncertainty ± 0.5 %). The mole fractions of these mixtures were from 80 % to 85 % methane with the balance ethane. Initially the 53 % methane + 46 % ethane mixture cylinder was attached to the system in Figure 3.15 and all valves were shut. Valves 8 to 12 and the cylinder valve were then opened and the regulator was adjusted to the desired pressure. The empty ISCO pump was then set to refill mode and the cylinder was reversed to a calculated volume. This volume was calculated so that the desired gas composition was yielded upon topping the first charge of gas up with pure methane to fill the ISCO pump to its maximum volume (266 ml). Details of the calculations are given in Appendix F.

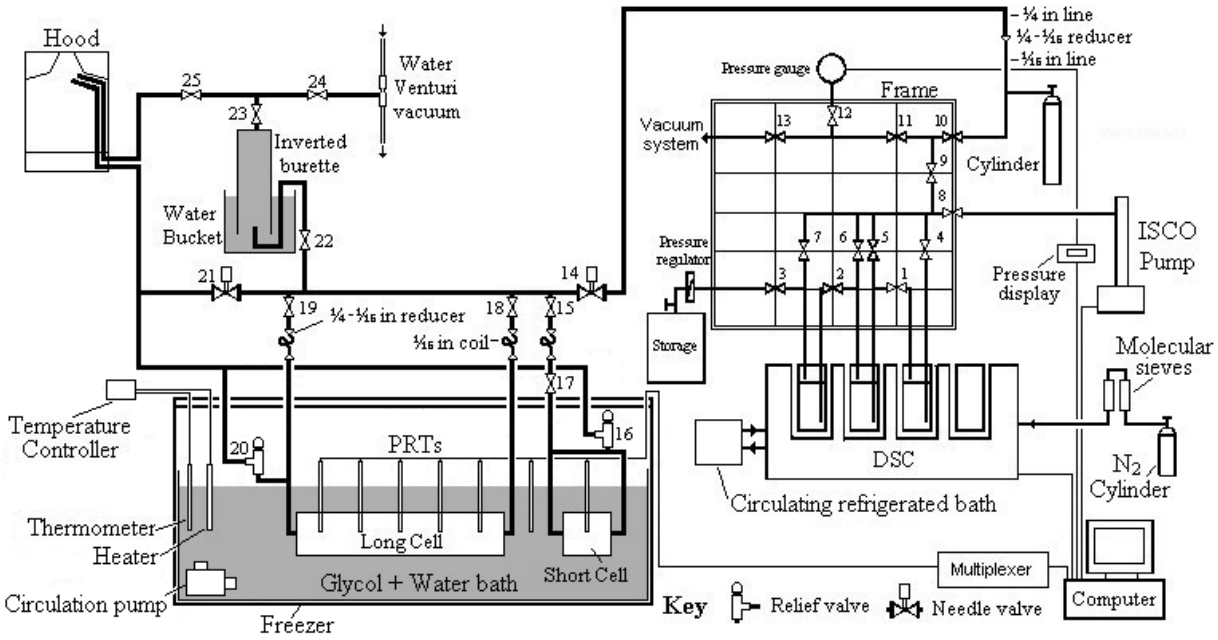

Figure 3.15 – Hydrate dissociation cells and differential scanning calorimeter system.

3.3.3 Plug dissociation studies

A modified Stern and coworker's[126,128] method of hydrate preparation was used to prepare plugs for the dissociation studies. Ice was made in an ice machine or freezer from distilled deionized water. The ice was crushed to small particles using a Hamilton Beach series 936

commercial blender at CSM and a Panasonic model MK-5070P food processor at UC. The ice was sieved to the particle size range (250 to 850) μm in liquid nitrogen cooled sieves to prevent melting. The sieved ice was placed in a thermos flask that was occasionally doused with liquid nitrogen.

At CSM the pressure cell was a 920 mm long pipe with an internal diameter of 25.4 mm giving a total volume of 463 cm^3.[54,159] The cell had external threads at each end with Rocket seal® end caps. The cell had 5 evenly spaced thermocouple probes along its length. A diagram of the cell is shown in Figure 3.16C. At UC a pressure cell made from 1½ in nominal pipe (ID = 34.0 mm, OD = 48.3 mm) of internal length 570 mm and volume 518 cm^3 was used. This cell was sealed with an o-ring compressed by a bolted flange. The cell had 5 temperature wells spaced evenly along its length for platinum resistance thermometers (Omega 100 Ω part number PR-11-2-100-1/16-12-E, ± 0.04 K) and is shown in Figure 3.16A.

The ice loading technique used at CSM and UC were the same. The empty pressure cell was disconnected from its fittings and placed vertically in a vice. The top end cap/flange of the cell was removed and liquid nitrogen was poured directly into the cell to cool it. The cell was considered cool enough when ice crystals covered the outer surface. The ice filled thermos flask was then weighed and the mass recorded. A spoon cooled by immersing it in liquid nitrogen was then used to spoon the ice particles from the thermos into the cell. The cell was occasionally tapped with a mallet especially around the thermowells to make sure no large voids were present in the cell. Once the cell was filled with ice, the thermos was reweighed and the mass of ice determined. The end cap/flange of the cell was then refitted and the cell was reconnected to its fittings and placed in the glycol bath that had been precooled to at least –2 ºC. This minimized the chance of ice melting inside the cell. It was noted that on all occasions the bath would cool further when the cell was placed in it because of the liquid nitrogen cooling of the cell before it was loaded with ice.

The plug formation/dissociation apparatus used at CSM is shown in Figure 3.17. Once the cell was connected, gas was allowed to enter the cell by opening valves V1, V2, V_i1 and V_i2. If the gas cylinder pressure was lower than the desired cell pressure the gas could be compressed using a HiP pressure generator model 87-6-5 hand pump. In this case V1 and V2

would be opened to allow the gas to enter the hand pump and then closed. The gas was compressed by turning the hand pump handle. Once the gas had been compressed the inlet valves V_i1 and V_i2 were opened to allow the gas into the cell. The cell was precooled in the bath to a temperature of -4 °C or lower (typically between -6 °C and -4 °C). When the cell had been charged with gas to the desired pressure the valves between the cylinder and the cell were closed. The temperature of the bath was then increased to just above the melting point of ice (0.1 °C). The pressure began dropping in the cell due to hydrate formation. When the pressure had dropped close to the hydrate formation pressure the bath temperature was dropped to -4 °C or lower and the cell was repressurized. Following the repressurization the bath was heated back up to just above the ice point so that hydrate formation could continue.

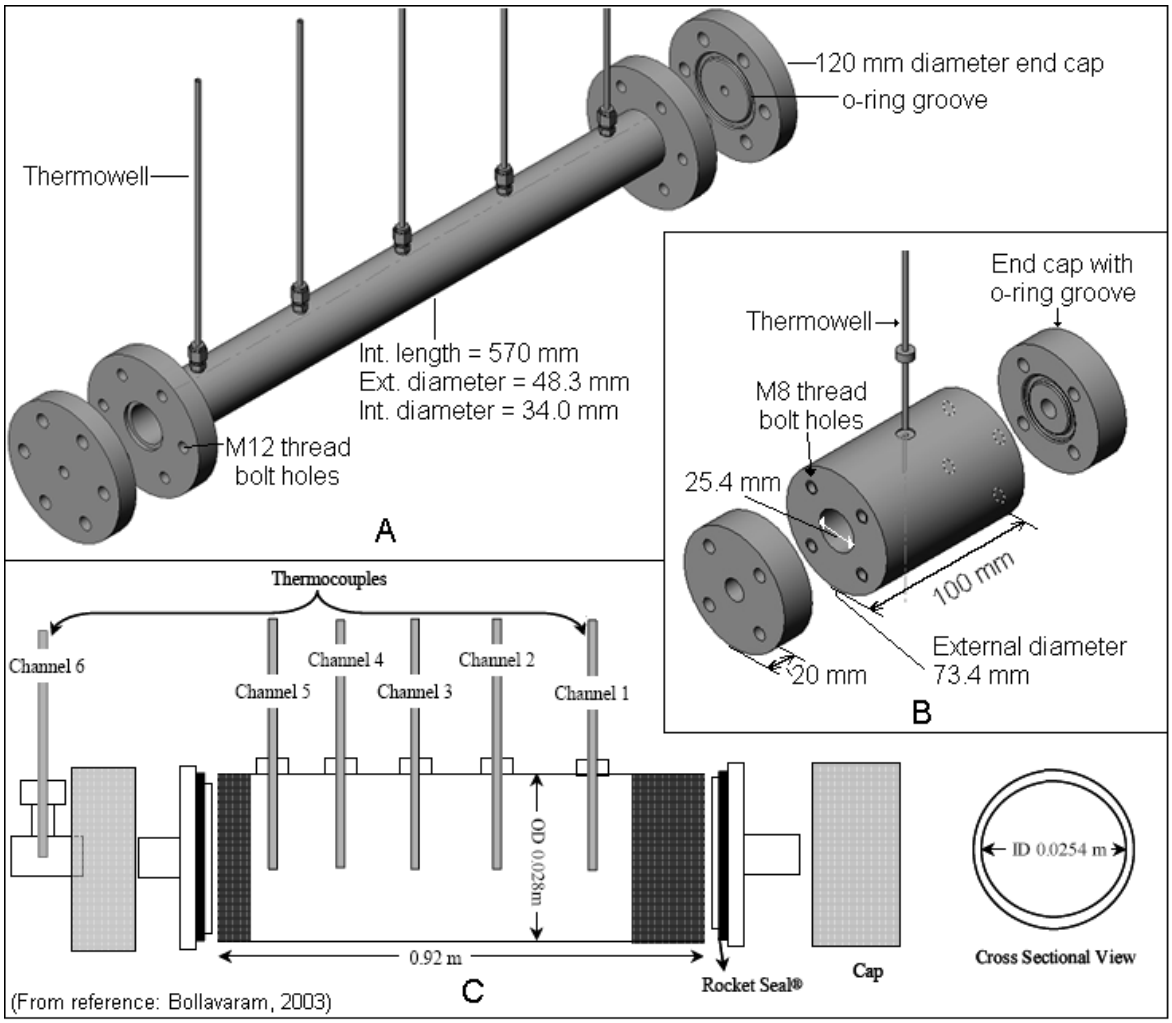

Figure 3.16 – Plug formation/dissociation cells A = long cell (UC), B = short/sample cell (UC), C = CSM cell. (Part C reproduced from Bollavaram[54]).

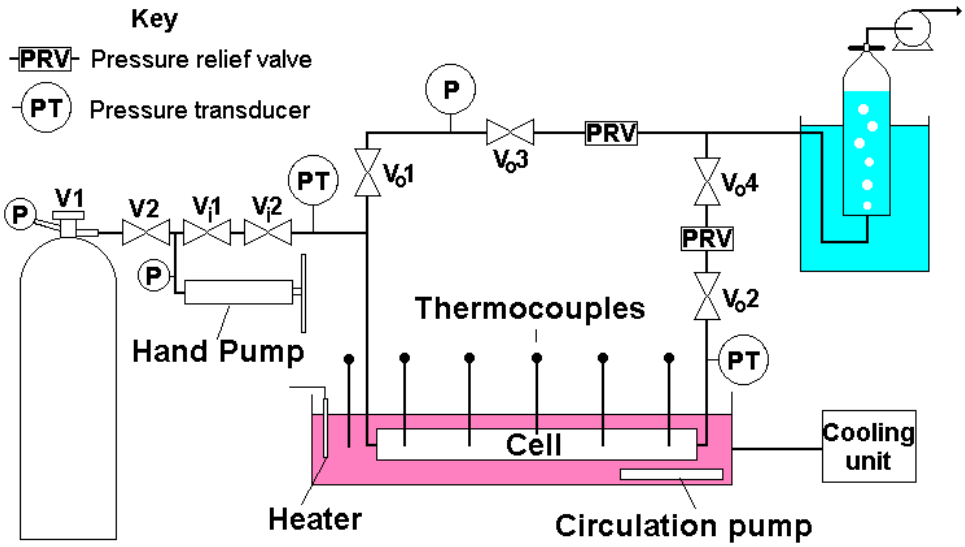

Figure 3.17 – Plug dissociation apparatus at CSM.

The UC plug formation/dissociation apparatus is shown on the left of Figure 3.15. The method of hydrate formation was initially (first two runs) by the pressure drop method as was used at CSM, later formations however were carried out at constant pressure utilizing the ISCO pump's constant pressure mode. Pressure was more accurately read on the Paroscientific pressure gauge (model 9000-6K-101, maximum pressure 41 MPa (6000 psi), pressure uncertainty ± 0.01 %). The ISCO pump was filled by opening the cylinder regulator and valves 8, 9 and 10 (valve numbers refer to valves in Figure 3.15) and running the pump in the refill mode. The pressure was adjusted to approximately the calculated pressure for hydrate formation. The valves to the cells in the glycol + water bath (valves 15, 17, 18 and 19) were then opened and the needle valve (valve 14) was slowly opened to allow gas to flow to the cells. The ethylene glycol + water bath was cooled to -4 °C or lower before pressurization began. The gas flow into the cells was slow to allow the gas to be cooled by the bath. When the cell pressure had equalized with the desired pressure, the cylinder regulator was closed and the ISCO pump was set to pump gas to maintain the desired pressure. The bath temperature was then raised to 0.1 °C to allow hydrate formation to begin. If the ISCO pump ran out of gas, valve 14 was closed and the bath chilled to below the ice point (-4 °C or lower). The regulator was then opened to refill the pump. The cylinder regulator was then closed, valve 14 reopened, and the ISCO pump was again set to pump to maintain constant pressure. The bath temperature was then raised to just above the ice point again.

At UC a short cell was placed in parallel to the long cell. The short cell was constructed with an internal diameter of 25.4 mm, an external diameter of 144.0 mm and a length of 100 mm with a total volume of 51 cm^3 and is shown in Figure 3.16B (note: both the long cell and the short cell were hydraulically pressure tested before they were used for experiments, see Appendix G). Due to the short length of the cell, a thick wall along the entire length of the cell was used rather than flanges with blind M8 threads of 35 mm and bolts sealed the end plates. The purpose of the small cell was not for dissociation studies but to provide samples that could be used for structural analysis and calorimetry, that should have the same structure as the hydrates that were prepared in the long cell under the same formation conditions and then dissociated.

Plug dissociations at both CSM and UC were carried out by the same method. The bath temperature was raised to 4 °C and the system was then rapidly depressurized from both ends of the cell. Gas flow from the hydrate cells was then directed to an inverted graduated burette filled with water. The rate at which the water was displaced by the gas was measured with stopwatches to give the hydrate dissociation rate. This rate was integrated over time and multiplied by the molar density of the gas to give the moles of gas released as a function of time.

3.3.4 Structural identification

Structural analysis of the hydrates was carried out by Raman spectroscopy at CSM and powder X-ray diffraction at UC.

Raman spectroscopy is a technique that measures the vibrational spectra of molecules (see Chapter 2 of this work). Constraining a molecule in a hydrate cage will slightly alter the vibrational spectra of a molecule. The Raman spectrometer at CSM was a Renishaw fibre optic probe with an Argon laser as the excitation source. More detail of the apparatus may be found in the Jager references.[37,125] C-H and C-C vibrational frequencies for ethane in the large cages of structures sI and sII are matched against literature values.[36,71,94]

To obtain samples for the Raman measurements at CSM the pressure cell was cooled in a bath of liquid nitrogen. One end cap was removed and a sample of hydrate was scrapped out with

a cooled spoon. The disadvantage of this technique was that the remainder of the hydrate could not be used for a plug dissociation measurement.

Structural analysis of samples at UC was by powder X-ray diffraction. As the crystal structure of sI and sII hydrates are different they will produce a unique powder X-ray diffraction pattern. Samples for powder X-ray diffraction were obtained from the short cell by disconnecting it from the system before valves 16 and 17 (see Figure 3.15) and immersing it in liquid nitrogen to cool the hydrate below its dissociation temperature at atmospheric pressure. The cell was then opened to the atmosphere with valve 17 and the end flange was removed. Samples were then scrapped out with a cooled spoon into a thermos of liquid nitrogen. One end of a glass capillary (internal diameter = 0.3 mm) held with tweezers was inserted repeatedly into the sample until it was covered with hydrate powder. The capillary was then mounted, with the help of some petroleum jelly, onto the goniometer head of the X-ray diffractometer in place of a mounting pin. The goniometer head was in a stream of nitrogen gas at -180 °C to prevent hydrate dissociation. The X-ray tube (Mo Kα) was then switched on and a pattern was recorded with the Bruker Smart CCD area-detector diffractometer. Usually this instrument is used to collect single crystal X-ray diffraction data but it can, as in this case, also be used to collect powder diffraction data if the 360 ° phi drive and scan function is used.

3.3.5 Calorimetry

The calorimeter used in this work is shown on the right hand side of Figure 3.15. The calorimeter is a Calorimetry Sciences Corporation 4100 multi-cell differential scanning calorimeter (MC-DSC) with a high pressure kit for measurements up to 14.0 MPa. Details of the calorimeter's uncertainties, setabilities and stabilities are shown in Table 3.5. The calorimeter has four cells (one reference cell and 3 measurement cells) of about 1 ml in volume. The MC-DSC's high pressure cells each have two 1/16 in stainless steel tubing connections. The inlet tube extends to near the bottom of the cell whereas the outlet tube runs from the top of the cell.

Table 3.5 – Calorimetry Sciences Corporation MC-DSC 4100 Uncertainties, setabilites and stabilities.

	Uncertainty	Setability	Stability
Temperature	± 0.5 K	± 0.01 K	-
Energy Flux (isothermal mode)	± 0.5 %	-	-
Enthalpy / Heat capacity	± 0.01 $K \cdot h^{-1}$	-	± 0.1 $K \cdot h^{-1}$

Two methods of introducing hydrates in the calorimetry cells for enthalpy of dissociation measurements were utilized. The first method was very similar to that described in Marsh and Gao[143] who used the same calorimeter to measure enthalpies of dissociation of six synthetic natural gases. About (0.15 to 0.3) g of degassed deionized water was added to each of the 3 measurement cells. The water was converted to ice by scanning the DSC down to -20 °C. An enthalpy of fusion of water scan was then conducted by heating at a scan rate of 6 $K \cdot h^{-1}$ from -5 °C to 5 °C.

The enthalpy measured was compared to the reference value of 334.2 $J \cdot g^{-1}$ [144] and the calibration constants adjusted so that measurement matched this value. Hydrates were prepared in the three measurement high pressure cells (see Figure 3.15). Valves 1 to 7 and 14 were closed and valves 8 to 13 opened. The vacuum line was then opened and the system evacuated for about half an hour. Valve 13 was then closed, the cylinder valve was opened and the cylinder regulator adjusted to the desired pressure. The ISCO pump was then reversed to a volume of about 180 ml. The cylinder valve and valve 10 where then shut and the ISCO pump set to constant pressure mode. Valve 4 was gently opened followed by valves 1, 2 and 3 as well as the storage cylinder valve. The TESCOM (model 26-1700) back pressure regulator valve was then carefully adjusted so that the ISCO pump's flow rate was 0.020 $ml \cdot min^{-1}$. This gas flow rate was found to be suitable by Marsh and Gao[143] to prevent hydrate blockages in the tubes. As the gas was bubbling through the cell the calorimeter was set to 0.1 °C. Every (24 to 28) h the calorimeter was cooled to -20 °C to convert the remaining water to ice. The calorimeter was then heated back to -5 °C and then from -5 °C to 3.5 °C at a rate of 6 $K \cdot h^{-1}$ to assess the remaining unconverted water. When the unconverted water peaks became small the enthalpy of dissociation scans, described below, were then made.

Valve 3 was closed and valves 5 to 7 opened. The calorimeter was then cooled to -20 °C for a period of 30 min to convert remaining water to ice. The calorimeter was then heated at it maximum scan rate (120 $K \cdot h^{-1}$ or 2 $K \cdot min^{-1}$) to -5 °C, it was then heated at the lower scan rate of 6 $K \cdot h^{-1}$ (0.1 $K \cdot min^{-1}$) from -5 °C to 3.5 °C to obtain an enthalpy of fusion peak for the unconverted water. The ISCO pump was then stopped as Marsh and Gao[143] reported that gas flow could disturb the calorimetric response. The calorimeter was then set to scan from 5 °C below to 8 °C above the predicted hydrate dissociation temperature (from CSMGem) at 6 $K \cdot h^{-1}$ (0.1 $K \cdot min^{-1}$). Pressure change during hydrate dissociation was not more than 0.022 MPa so the hydrate dissociation could be considered isobaric.

The amount of water in each cell was then measured by an enthalpy of fusion of water scan. The system had to be depressurized first to prevent hydrates reforming when the temperature was lowered below the dissociation temperature. Starting with valves 1 to 8, 10 and 13 closed the system was depressurized by opening valve 10, 14 and 21 and then releasing the pressure to below the hydrate formation pressure at -20 °C, this pressure was typically about 1.0 MPa. The hydrate cells were then depressurized by slowly opening valves 7, then 6, 5, 1, 2 and finally 4. The calorimeter was cooled down to -20 °C to convert the water in the cells to ice then an enthalpy of fusion of ice scan was conducted by heating the calorimeter from -5 °C to 5 °C at a rate of 6 $K \cdot h^{-1}$. This scan enabled the mass of water in each calorimeter cell to be calculated by use of the standard enthalpy of 334.2 $J \cdot g^{-1}$.[144] This mass along with the predissociation mass of unconverted ice allowed calculation of the mass of water associated with the hydrate. This along with a hydrate number predicted using CSMGem allowed the calculation of a dissociation enthalpy. This method of in-calorimeter-cell hydrate formation and dissociation were used to measure the enthalpy of dissociation of a sII hydrate prepared from a gas of mole fractions 98.8 % methane + 1.2 % ethane.

The second method of introducing hydrates into the calorimeter involved cryogenic transfer from the sample cell. The small cell was immersed in liquid nitrogen in a polystyrene container. The cell and contents were allowed to cool to the liquid nitrogen boiling point of -196 °C. At this temperature the hydrate is stable at atmospheric pressure and thus can be stored in a Dewar flask of liquid nitrogen indefinitely.

The transfer technique to the calorimeter involved immersing the bottom of the high pressure calorimetry cells in liquid nitrogen until they had cooled. The top of the cell was not directly contacted with the liquid nitrogen so not to overcool the area around the o-ring seal. A lump of hydrate of suitable size (of approximate radius 5 mm or less) was removed from the storage Dewar flask with cooled tweezers and immediately placed into the calorimeter cell. The calorimeter cell was then sealed and pressurized to a pressure high enough to stabilize the hydrate at about room temperature. The cell was allowed to heat up to room temperature and any atmospheric water that condensed on the outside of the cell was carefully wiped off with a lint free cloth. When the cell reached approximately room temperature it was placed inside the calorimeter. This technique was repeated until all three working cells of the calorimeter contained a sample. The pressure of the calorimeter cell was then slowly adjusted to the desired pressure using the ISCO pump. The hydrate was allowed to equilibrate in the cells for at least 24 h before any measurements were taken.

The hydrate dissociation enthalpy was measured by first conducting an enthalpy of fusion of ice scan. The calorimeter was scanned down to -20 °C to convert any remaining water to ice. The cells where then heated from -5 °C to +5 °C at a scan rate of 6 $K \cdot h^{-1}$. The ISCO pump was then switched off as it had been found to disturb scan results.[143] The enthalpy of dissociation scan was then started from about 5 °C below the expected dissociation temperature to about 8 °C above the predicted dissociation temperature at a scan rate of 6 $K \cdot h^{-1}$. The mass of hydrate was determined as for the other method of hydrate formation in the calorimeter (by a pre-hydrate dissociation ice scan to find the mass of unconverted ice and a post-hydrate dissociation ice scan to find the total amount of ice).

The cryogenic transfer method was used to load hydrate formed in the small cell of the (UC) plug dissociation apparatus from an ISCO pump prepared mixture of mole fraction 80 % methane + 20 % ethane. This plug was formed at a constant pressure of 4 MPa and was structurally analysed as a sII plug by X-ray diffraction. The hydrate phase composition was believed to be similar to that prepared by the flow method in the calorimeter from the gas mixture of mole fraction 98.8 % methane + 1.2 % ethane due to “preferential enclathration” of ethane in the hydrate phase in the high mole ratio of water to gas system of the plug formation cells. Preferential enclathration is a phenomenon where the hydrate phase

selectively enclathrates a certain component or components of a gas mixture to a higher water free mole fraction than in the gas phase. These components can alternatively be viewed as being preferentially stripped by the hydrate from the gas phase. This hydrate was pressurised with the gas mixture of 98.8 % methane + 1.2 % ethane for enthalpy of dissociation measurement in the calorimeter.

3.4 Results

3.4.1 Formation of hydrates from mixtures of methane + ethane mixtures and predicted phase diagrams at high gas to water ratios

Although hydrate *P,x* phase diagrams for methane + ethane hydrates are presented by Subramanian et al.[71,72] these were calculated for a high mole ratio of water to gas. These conditions are not typical of natural gas pipelines, where gas is constantly replenishing its initial composition and there is a high mole ratio of gas to water. For this reason methane + ethane hydrate *P,x* phase diagrams are presented. An isothermal hydrate phase diagram at 273.25 K for the system methane + ethane + water at a mole ratio of gas to water of 100 has been produced using the hydrate phase stability prediction program CSMGem. This diagram is shown as Figure 3.18. It predicts that at incipient pressure conditions a sII hydrate will form between mole fractions of about 71.6 % and 99.5 % methane in the gas mixture.

In a constant volume system the gas in not being constantly replenished with fresh gas at the initial composition, unlike in a pipeline, so preferential enclathration will occur. Preferential enclathration involves a component or components of a gas mixture entering the hydrate phase to a higher mole fraction (on a water free basis) than in the gas phase. Chapter 4 focuses in detail on preferential enclathration, and models are presented that simulate laboratory hydrate formation. An example of constant volume hydrate plug formation illustrating preferential enclathration has been calculated using the algorithm of Figure 4.5 in Chapter 4 for a methane + ethane mixture of mole fractions 98.8 % methane + 1.2 % ethane and is shown in Figure 3.19. At an initial pressure of about 8.2 MPa, at which sII is the favoured hydrate, the model suggests that after a pressure drop of only 0.3 MPa the composition of the gas phase has changed enough to result in the formation of sI hydrate.

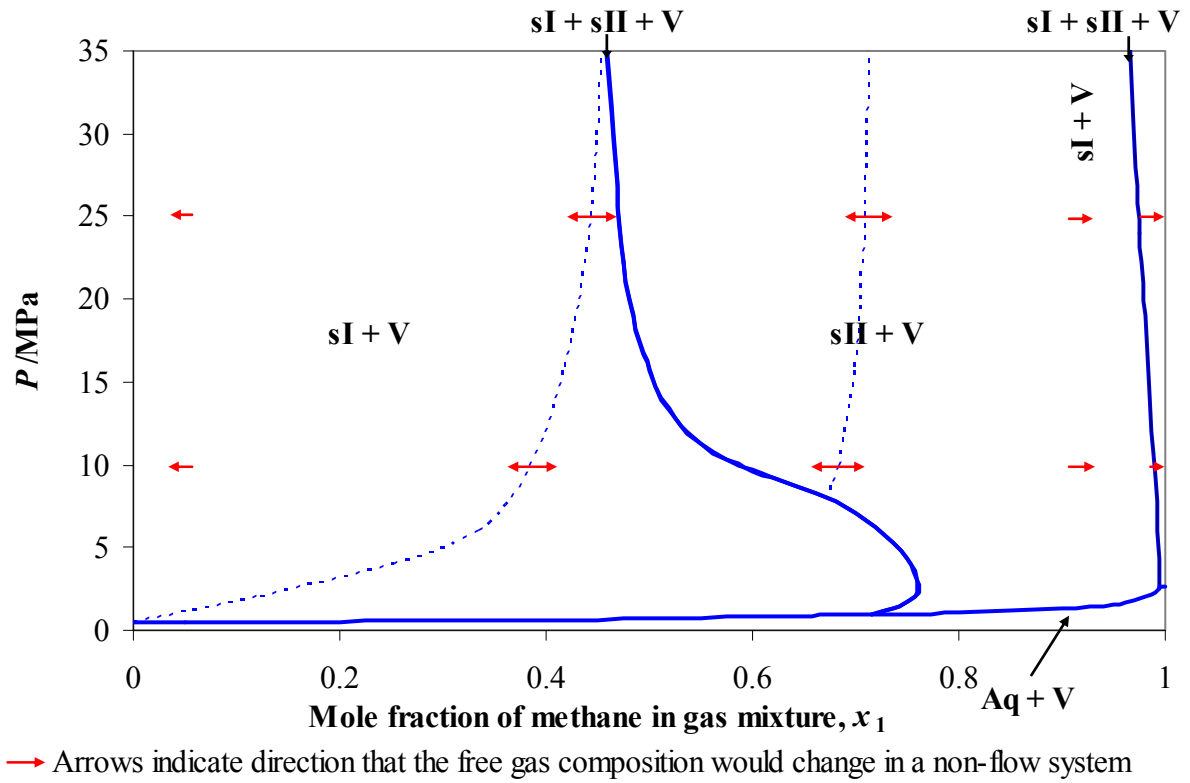

Figure 3.18 – Hydrate phase diagram for methane (1) + ethane (2) system at 273.25 K at high gas to water molar ratio (100 moles of gas to 1 mole of water).

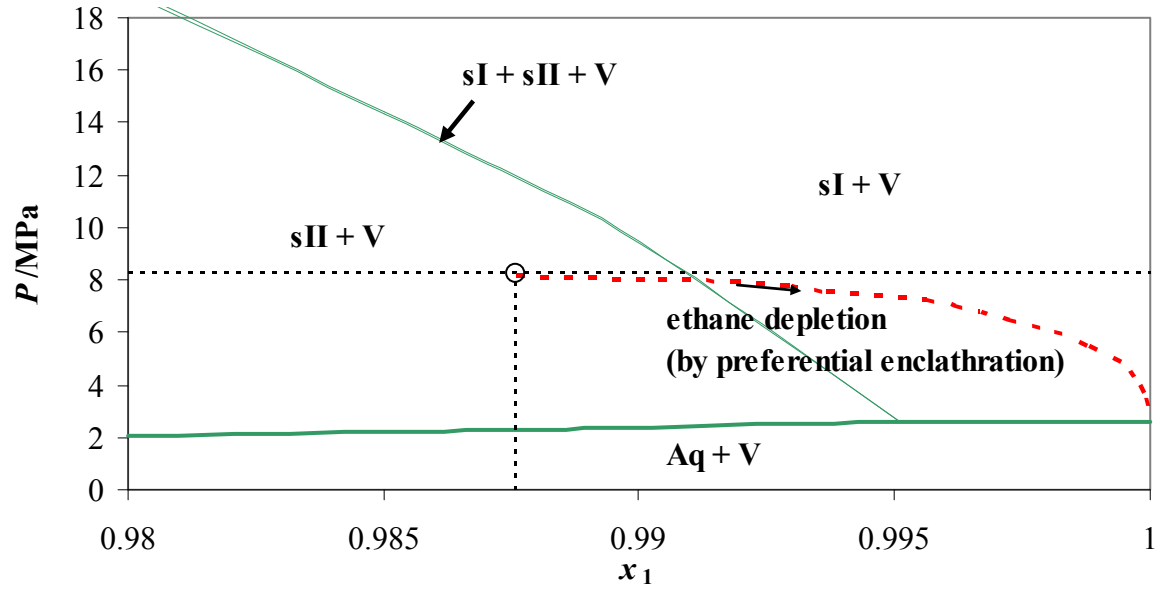

Figure 3.19 – Calculated ethane depletion in the gas phase for a mixture of methane (1) + ethane (2) due to preferential enclathration of ethane in the hydrate for a constant volume hydrate formation at 273.25 K; the gas to water mole ratio used was 1:26, the open circle represents the initial P (8.2 MPa) and initial methane mole fraction of the gas phase, x_1, (98.8 %), the dashed curve plots P and x_1 as hydrate formation proceeds.

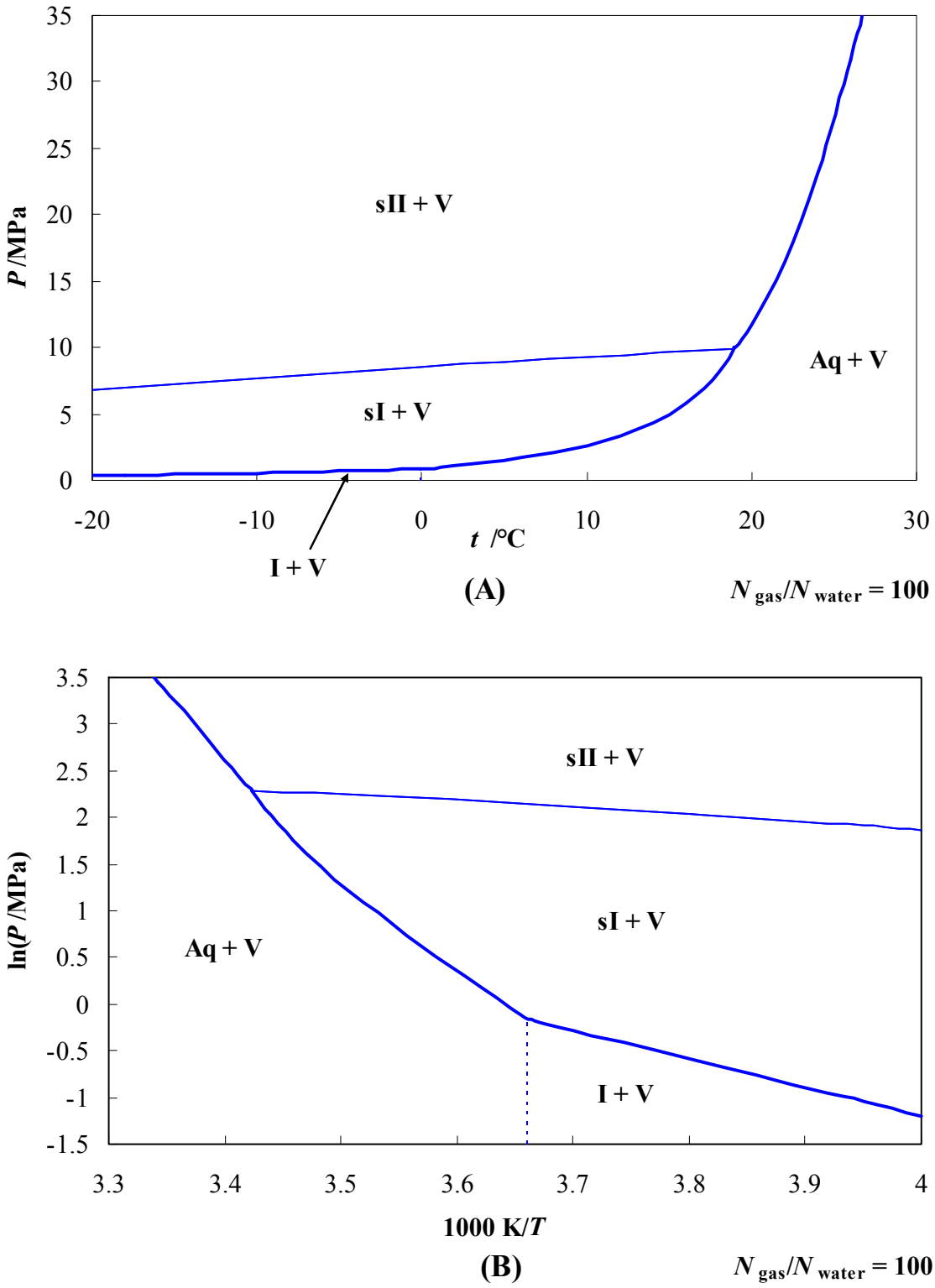

Figure 3.20 – CSMGem *P*,*T* phase diagram for mole fraction 65.4 % methane + 34.6 % ethane mixture at high gas to water ratio (100 moles of gas to 1 mole of water); (A) *P* versus *T* form, (B) ln*P* vs. 1/*T* form.

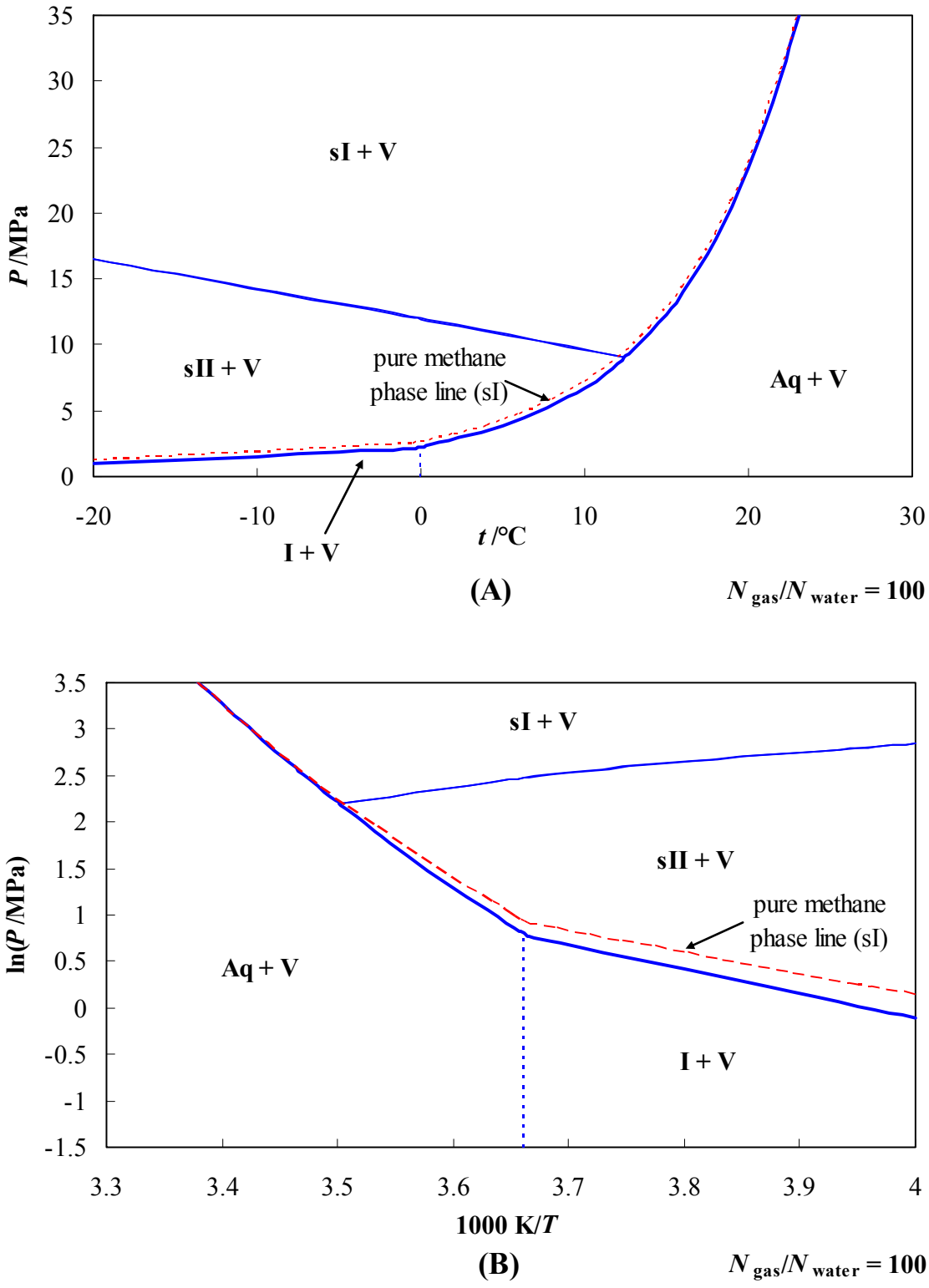

Figure 3.21 – CSMGem *P*,*T* phase diagram for mole fraction 98.8 % methane + 1.2 % ethane mixture at high gas to water ratio (100 moles of gas to 1 mole of water); (A) *P* versus *T* form, (B) ln*P* vs. 1/*T* form.

Figure 3.20 and Figure 3.21 respectively present predicted *P*,*T* phase diagrams calculated using CSMGem at a high gas to water mole ratio of 100 for the methane + ethane gas mixtures prepared in this work with mole fractions of 65.4 % methane + 34.6 % ethane and 98.8 % methane + 1.2 % ethane. Predicted data for the pure methane hydrate boundary is also plotted with the 98.8 % methane + 1.2 % ethane data in Figure 3.21. Further discussion of these diagrams follows later.

3.4.2 Hydrate plug dissociation measurements

Hydrate plug dissociation times were measured for sI and sII hydrates prepared from the gas mixtures with mole fractions of 65.4 % methane + 34.6 % ethane, 98.8 % methane + 1.2 % ethane and in-situ prepared mixtures of about 80 % methane with the balance ethane. The experimental dissociation times have been compared to those of CSMPlug. CSMPlug predicts that sII hydrates will take 20 % longer to dissociate than sI. For the 65.4 % methane + 34.6 % ethane mixture the hydrate formation pressure determined the structure of the plug. At pressures higher than about 9.7 MPa sII hydrates formed whereas at lower pressures sI hydrates may form. Figure 3.24 shows as *P*,*x* phase diagram for methane + ethane at 273.15 K calculated at a mole ratio of gas to water of 100, experimental *P* values and predicted gas phase methane mole fractions, x_1, are plotted for the formation of a sII hydrate plug formed from 65.4 % methane + 34.6 % ethane mole fraction mixture. Experimental measurements of plug dissociation times of hydrates prepared from the 65.4 % methane + 34.6 % ethane do not support the prediction that sII hydrates will take longer to dissociate. Clapeyron equation predictions presented later in this section for hydrates formed from this gas mixture suggest the dissociation enthalpy of sI hydrate is higher than that of sII hydrate, the reverse is true for the 98.8 % methane + 1.2 % ethane mixture. Plug dissociation plots for sI and sII hydrate plugs prepared from this mixture are shown in Figure 3.22 and Figure 3.23 respectively.

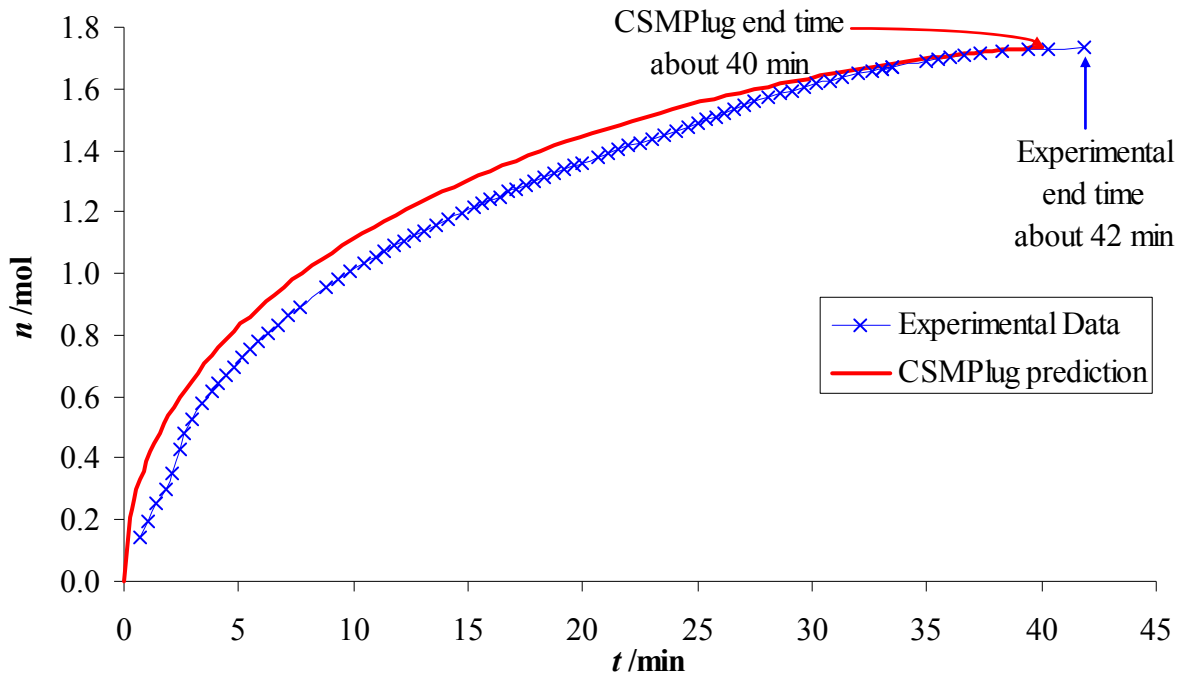

Figure 3.22 – Hydrate plug dissociation plot of mole of gas released, *n*, as a function of time, *t*, for sI hydrate plug prepared from the mixture with mole fractions of 65.4 % methane + 34.6 % ethane.

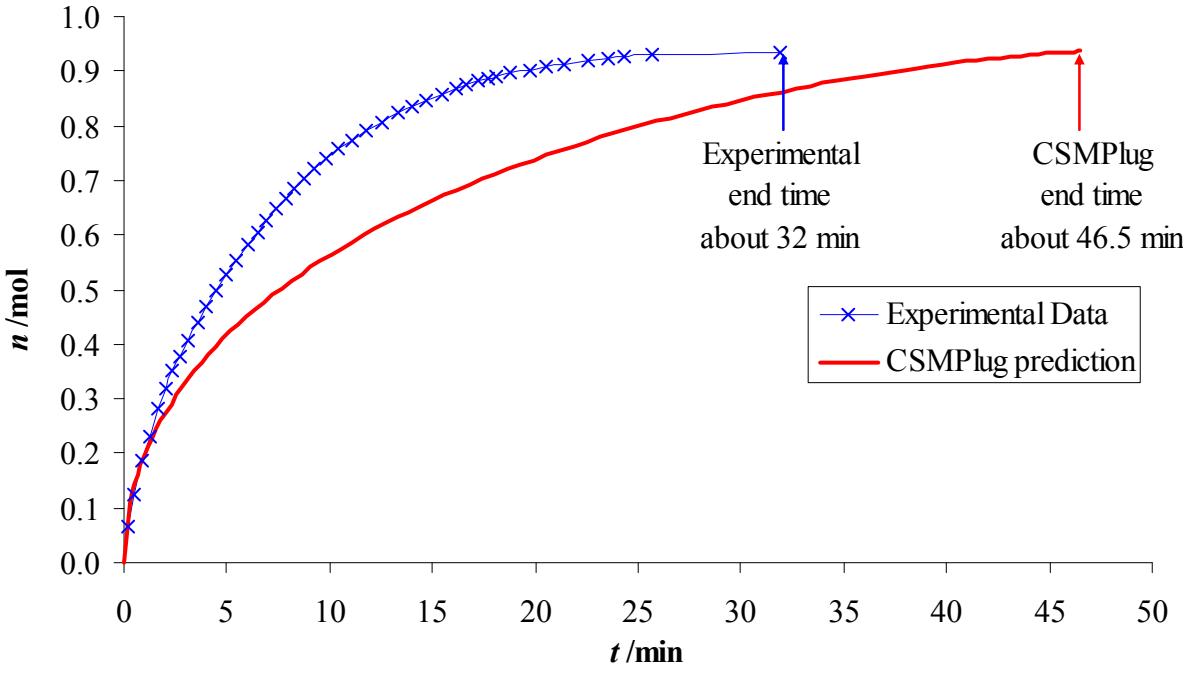

Figure 3.23 – Hydrate plug dissociation plot of mole of gas released, *n*, as a function of time, *t*, for sII hydrate plug prepared from the mixture with mole fractions of 65.4 % methane + 34.6 % ethane.

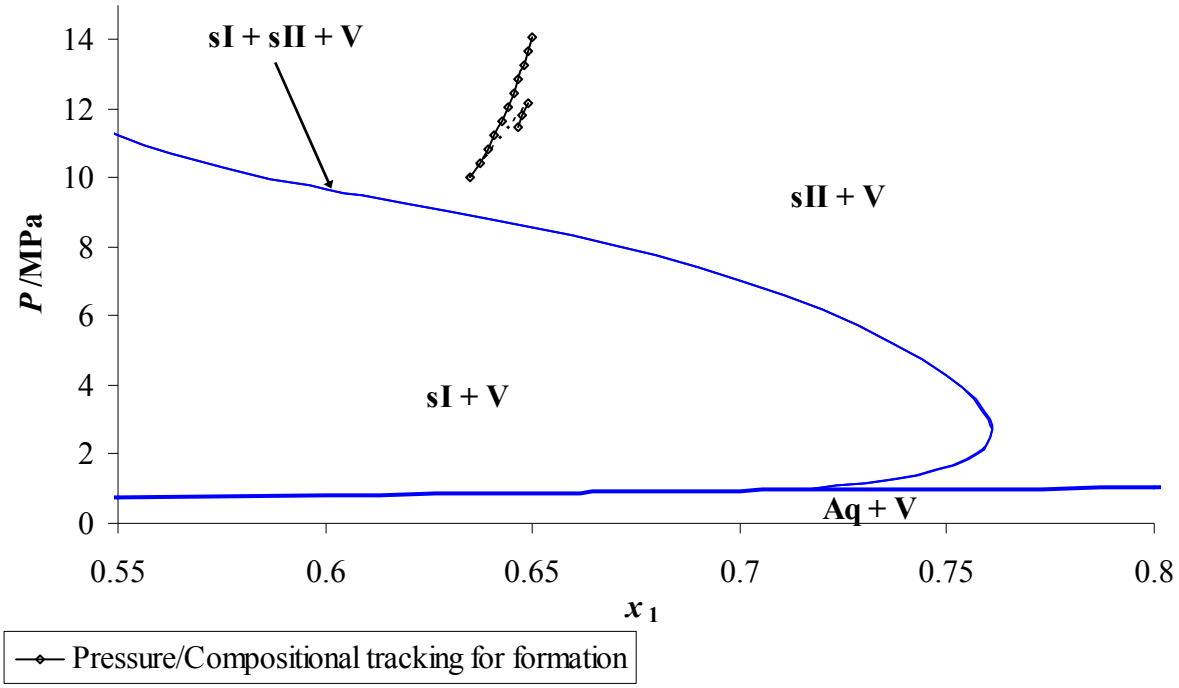

Figure 3.24 – CSMGem predicted P,x phase diagram at 273.25 K for methane (1) + ethane (2) mixtures for x_1 = (0.55 to 0.8) and a high gas to water mole ratio (100:1) showing the experimental formation P and predicted x_1 for the formation of a sII hydrate from a 65.4 % methane + 34.6 % ethane mole fraction gas mixture; the break in the P,x_1 tracking line signifies a repressurization.

Experimental measurements of plug dissociation times for hydrates formed with higher methane content gases indicate that the dissociation time was indeed longer for the sII hydrate than the sI. These results are shown in Table 3.6 and Figure 3.25. Plug structures were confirmed by either Raman spectroscopy (refer to Figure 3.26) or powder X-ray diffraction (refer to Figure 3.27). The dissociation times in Figure 3.25 are plotted against hydrate porosity, ε , which is the gas filled void fraction of the plug. Plugs with low porosities have been shown to take longer to dissociate.[49] The porosity was calculated by deducting from unity the volume of hydrate and ice at the end of a formation experiment divided by the total dissociation cell volume. The volume of hydrate formed was estimated from the mass of ice particles initially loaded in to the cells, the conversion of ice to hydrate and the relative densities of the ice and the hydrate phase predicted using CSMGEM.

A dissociation plot for a hydrate plug prepared from the 98.8 % methane + 1.2 % ethane mixture that appeared to showed evidence of containing both sI and sII hydrate is shown in

Figure 3.28. The overall dissociation time appeared to be controlled by the slower dissociating hydrate (presumed to be sII). Both structures of hydrate may have formed because of preferential enclathration, described in detail in section 3.1, which is a problem for non-flow hydrate formations.

Table 3.6 – Hydrate dissociations of plugs formed to investigate high methane composition structural transition

ε [a]	Exptl. diss. time min	CSM Plug diss. time min	Diff.[b]	Formation method	Predicted structure	XRD detected hydrate	Mole gas comp. Me%:Et%
0.517	70.8	69.6	-2%	*P* drop[c]	sI*	-	99.8:1.2
0.595	70	58.5	-16%	*P* = 14 MPa[d]	sI	sI	99.8:1.2
0.517	78.8	69.6	-12%	*P* = 4 MPa[d]	sI*	-	99.8:1.2
0.483	62	74.4	20%	*P* = 4 MPa[d]	sI*	sI	99.8:1.2
0.538	86.5	92.7	7%	*P* = 4 MPa[d]	sII	sII	80:20
0.545	80.21	91.2	14%	*P* = 4 MPa[d]	sII	sII	80:20
0.462	104.8	108	3%	*P* drop[c]	sII**	-	99.8:1.2

*Could contain up to 5 % sII but due to ethane stripping the majority of this hydrate is sI
** Dissociation appears to be sII dominated (see text and Figure 3.28)
[a] Porosity of the plug, ε, is defined as the void fraction of the plug available for gas to fill.
[b] Percentage difference of CSMPlug predicted dissociation time from experimental value.
[c] Pressure drop method.
[d] Constant pressure method.

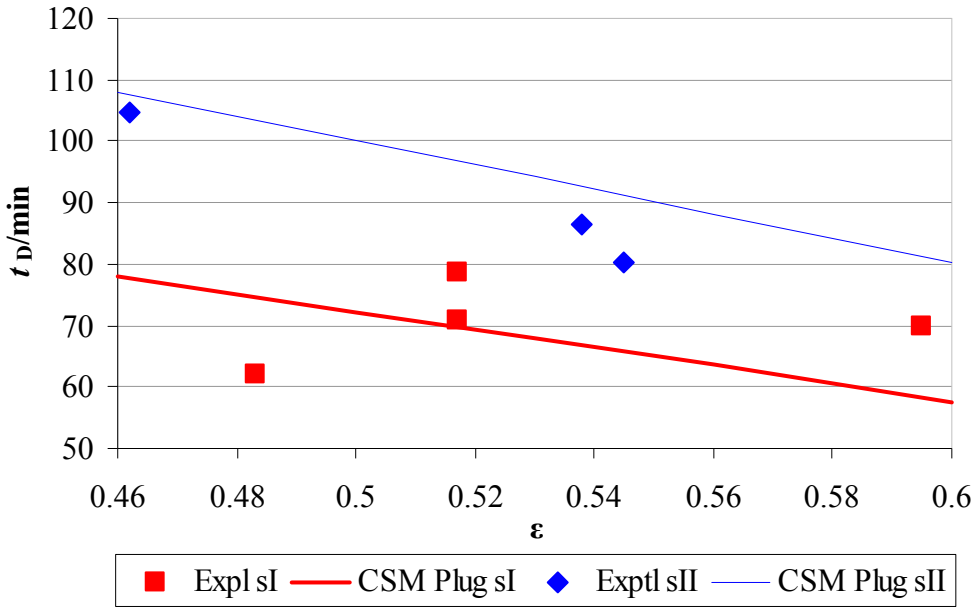

Figure 3.25 – Experimental and predicted hydrate dissociation times, t_D, versus hydrate plug porosity, ε, for plugs prepared and dissociated at the University of Canterbury.

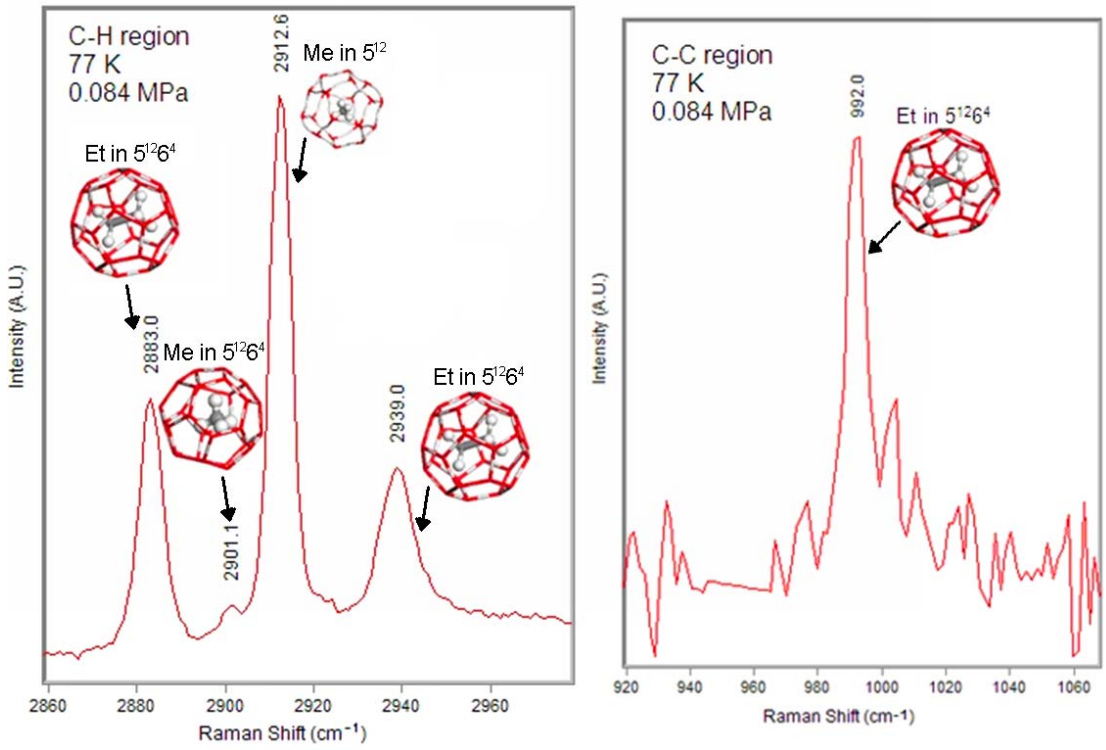

Figure 3.26 – Raman spectra of sII hydrate prepared from 65.4 % methane + 34.6 % ethane mole fraction mixture above 10 MPa (the formation conditions of this hydrate are shown in Figure 3.24).

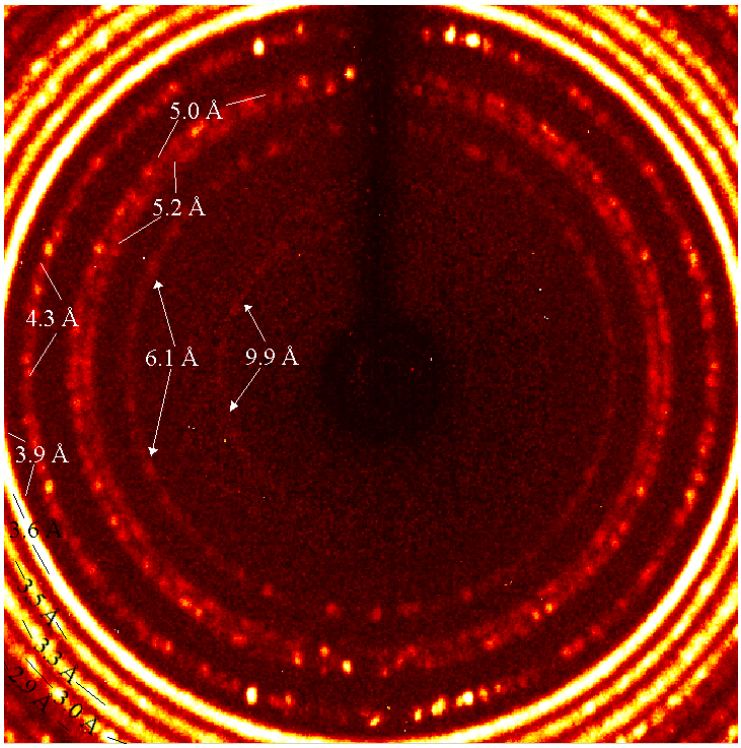

Figure 3.27 – Example X-ray diffraction rings indexing to a sII hydrate; refer to the predicted powder pattern in Chapter 2.

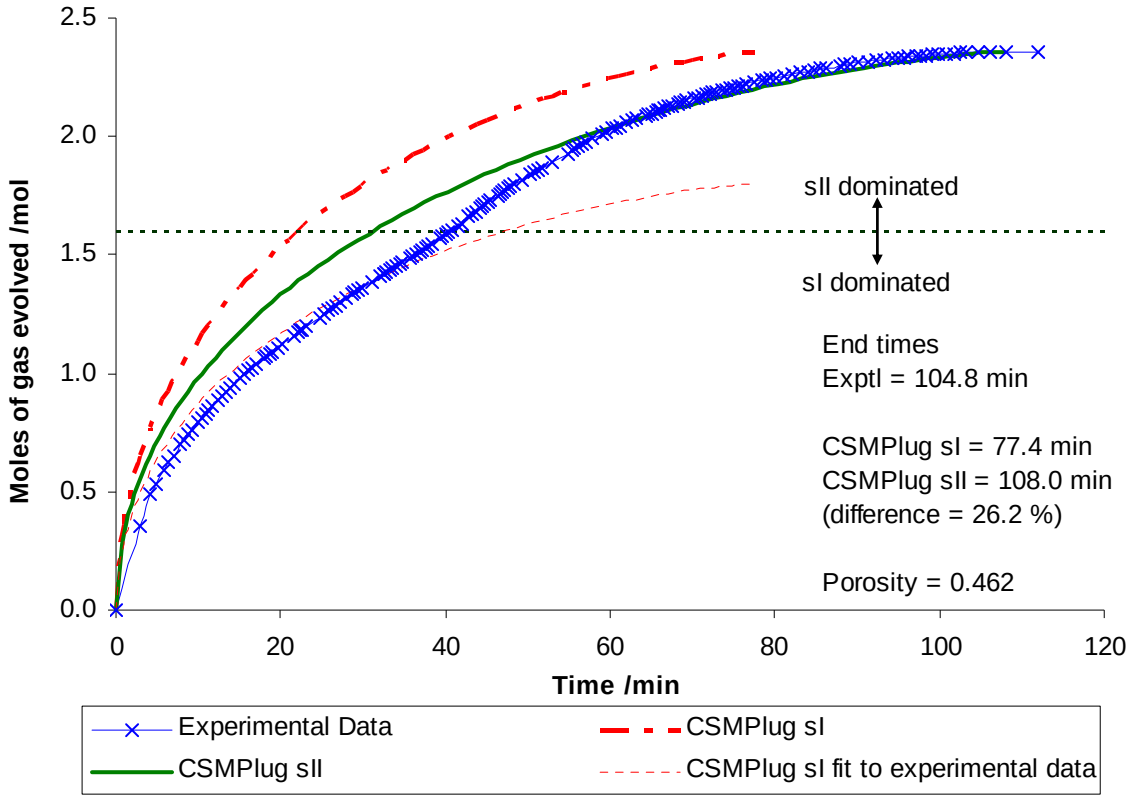

Figure 3.28 – Hydrate dissociation for plug prepared from the 98.8 % methane + 1.2 % ethane mole fraction mixture showing evidence of mixed sI and sII hydrate plug with a sII dominated dissociation time.

3.4.3 Enthalpies of dissociation of sI and sII methane + ethane hydrates

The enthalpies of dissociation of a sII hydrate at 7.03 MPa and 6.92 MPa have been measured by differential scanning calorimetry. The overall conversions for the hydrate dissociated at 7.03 MPa and 6.92 MPa were 64.26 % and 94.16 % respectively. Clapeyron equation [eq (3.15)] predictions, using ΔZ values evaluated from eq (3.17), at these pressures were calculated for comparison. The measurement at 6.92 MPa of (63.15 ± 0.50) kJ·mol^{-1} was within the error of the Clapeyron equation prediction of (62.6 ± 2.8) kJ·mol^{-1}, however the measurement at 7.03 MPa of (66.47 ± 0.50) kJ·mol^{-1} was not within error of the Clapeyron equation prediction of (62.7 ± 2.8) kJ·mol^{-1}. These measurements are tabulated in Table 3.7, the calorimetric scan for the hydrate dissociated at 6.92 MPa is shown in Figure 3.29. Clapeyron equation predictions of the enthalpy of dissociation using phase data from CSMGEM of sI and sII hydrates prepared from the 65.4% methane + 34.6 % ethane mixture, sII hydrates prepared from 98.8 % methane + 1.2 % ethane mixture and pure methane sI hydrates are plotted in Figure 3.30. The experimental measurements are plotted for

comparison. For the Clapeyron equation calculations the gas was assumed to be insoluble in liquid water and the vapour phase was assumed to be water free, eq (3.17) was used to calculate a compressibility difference for use with the eq (3.15) form of the Clapeyron equation. Uncertainties in the enthalpy of dissociation values calculated using the Clapeyron equation (shown as error bars in Figure 3.30) were estimated as approximately 4.5 % from likely errors from the compressibilites (estimated 3 %) and slope d$\ln P$/d(1/T) found from CSMGem (estimated 1.5 %, see Appendix H for comparison of experimentally calculated and CSMGEM calculated d$\ln P$/d(1/T) values). Discussion of these results is presented in section 3.5.3.

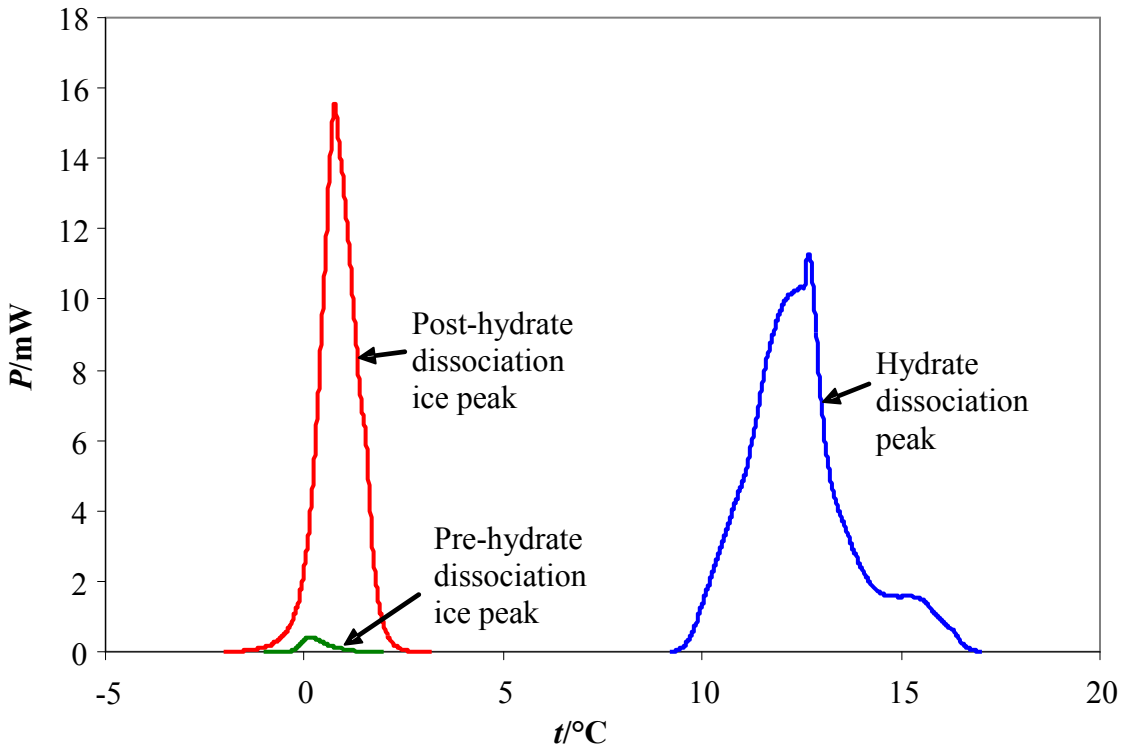

Figure 3.29 – Calorimetry power, P, versus temperature scan for the dissociation of a sII hydrate formed in the short sample cell and dissociated in the 98.8 % methane + 1.2 % ethane gas mixture at 6.92 MPa; note: baselines have been deducted from these peaks.

Table 3.7 – Enthalpy of hydrate dissociation for sII hydrate prepared from 98.8 % Me + 1.2 % Et gas mixture.

P / MPa	$\Delta_{dis}H$ / kJ·mol^{-1}	Hydrate number (n) *	Mass fraction hydrate	Measured Dis. Temp.	CSMGem Dis. Temp.	$\Delta_{dis}H$ Clapeyron CSMGEM / kJ·mol^{-1}
7.03	66.47 ± 0.50	6.09	64.26 %	9.84 °C 282.99 K	10.36 °C 283.51 K	69.7[a] 62.7[b]
6.92	63.15 ± 0.50	6.09	98.16 %	10.22 °C 283.37 K	10.23 °C 283.38 K	69.4[a] 62.6[b]

*Calculated from CSMGEM

[a] Calculated using $\Delta Z = Z_G$,

[b] Calculated using $\Delta Z = Z_G - nZ_{H2O} - Z_H$ (eq (3.17)).

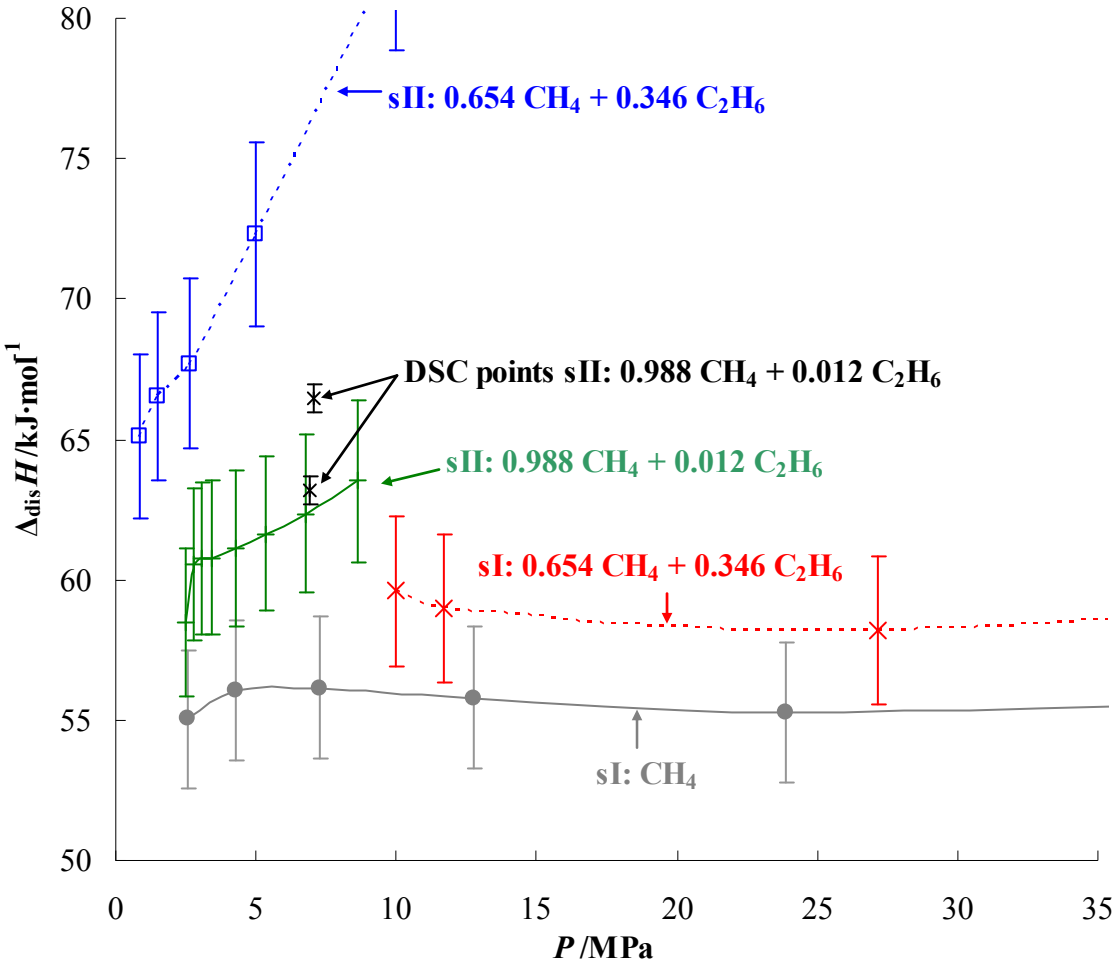

Figure 3.30 – Clapeyron equation enthalpies of dissociation predicted from CSMGem phase data for the mixture of mole fraction 65.4 % methane + 34.6 % ethane sI and sII hydrates, the mixture of mole fraction 98.8 % methane + 1.2 % ethane sII hydrates and methane sI hydrate. Experimental measurements are shown for comparison.

As the plug dissociations were carried out at atmospheric pressure, predictions of the hydrate dissociation enthalpy at atmospheric pressure for sI and sII hydrates for the 65 % methane + 35 % ethane and 98.8 % methane + 1.2 % ethane mixtures have been calculated and tabulated in Table 3.8 (note for the 65.4 % methane + 34.6 % ethane mixture sI is the predicted stable hydrate structure at these conditions and for the 98.8 % methane + 1.2 % ethane mixture sII is the stable hydrate structure, CSMGem however allows calculations on the metastable structure as well, predictions for the metastable structures have also be included).

Table 3.8 – Calculated dissociation enthalpies from CSMGem data for 65 % methane + 35 % ethane and 98.8 % methane + 1.2 % ethane mixtures at atmospheric pressure.

Structure & mole fractions*	**ρ/kg·m^{-3}**	**$\Delta_{dis}H$ /kJ·mol^{-1}**	**Diss. Temp. K**
65 % methane + 35 % ethane mixture:			
sI [(0.2266 CH_4 + 0.7734 C_2H_6)·6.696 H_2O]	968.4	24.45	201.61
sII^m [(0.5533 CH_4 + 0.4467 C_2H_6)·7.702 H_2O]	927.9	22.57	207.64
98.8 % methane + 1.2 % ethane mixture:			
sI^m [(0.8266 CH_4 + 0.1734 C_2H_6)·6.035 H_2O]	946.4	20.86	229.61
sII [(0.7247 CH_4 + 0.2753 C_2H_6)·6.230 H_2O]	942.0	22.14	224.66

* Superscript m denotes metastability of the structure at these conditions.

3.4.4 Predictions of the average guest size in each cage of sI and sII hydrate of the mixture of mole fraction 65.4 % methane + 34.6 % ethane

As discussed in subsection 3.2.5 of this chapter Sloan and Fleyfel[154,155] suggested that larger guests resulted in larger enthalpies of dissociation. For sI and sII hydrates prepared from the 65 % methane + 35 % ethane mixture plots of guest sizes in the small and large cages have been calculated from the fractional cage occupancies predicted using CSMGem and the molecular guest size from Sloan[1] (D_{Me} = 4.36 Å, D_{Et} = 5.5 Å). The plot for sI hydrates is shown in Figure 3.31 and the plot for sII hydrates is shown in Figure 3.32.

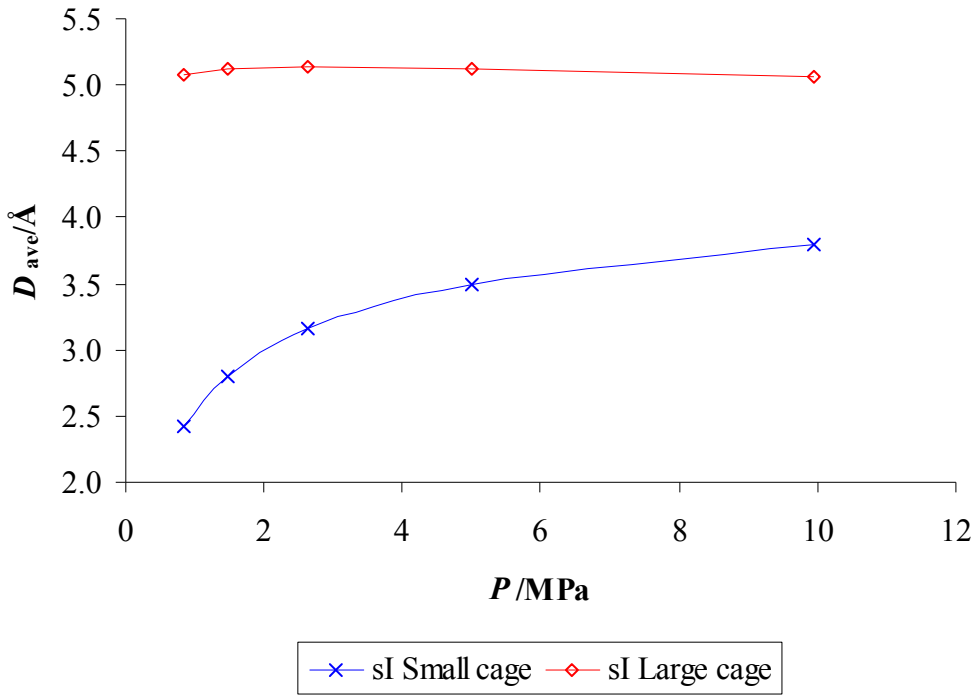

Figure 3.31 – Average guest size, D_{ave}, calculated from CSMGEM fractional cage occupancy and molecular diameters of methane and ethane as a function of pressure for sI hydrate prepared from 65.4 % Me + 34.6 % Et mixture (for a mole ratio of gas to water of 100).

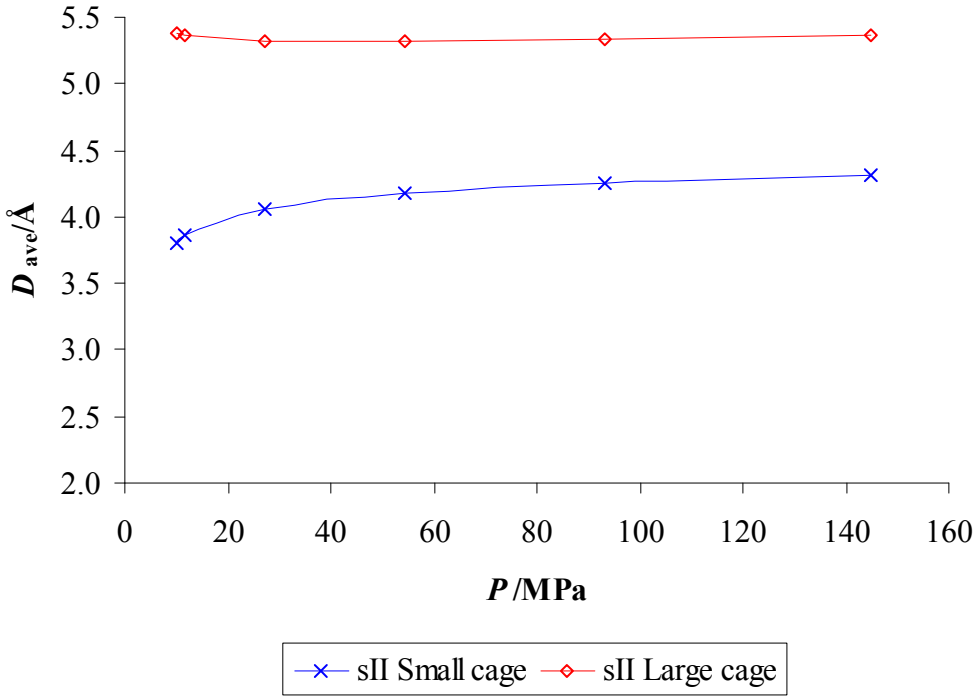

Figure 3.32 – Average guest size, D_{ave}, calculated from CSMGEM fractional cage occupancy and molecular diameters of methane and ethane as a function of pressure for sII hydrate prepared from 65.4 % Me + 34.6 % Et mixture (for a mole ratio of gas to water of 100).

3.5 Discussion of results

3.5.1 Hydrate phase diagrams for the methane + ethane system

Hydrate *P,x* phase diagrams for the methane + ethane system at high gas to water ratio (100 moles of gas to 1 mole of water) have been prepared using CSMGem. These diagrams are representative of conditions in natural gas pipelines unlike earlier published *P,x* phase diagrams.[71,72] CSMGEM has been shown to give pressure predictions of the phase boundaries accurate to ± 7 % and temperature predictions to ± 0.5 ºC for binary gas mixtures with water, better than earlier hydrate prediction programs.[33] A discussion of the features of each diagram particularly with reference to sI/sII transition follows.

Figure 3.18 shows a *P,x* hydrate phase diagram at a temperature of 273.25 K (0.1 ºC) for the methane (1) + ethane (2) system at high gas to water ratio (100 moles of gas to 1 mole of water). The methane mole fraction, x_1, is of the gas phase on a water free basis. At incipient hydrate formation conditions it can be seen that a sI hydrate forms at gas compositions of methane less than 71.6 % and greater than 99.5%. At compositions between 71.6 % and 99.5 % at incipient hydrate formation conditions sII is the favoured form. There are also thin bands of sI + sII + V regions separating the sI + V and the sII + V regions. At higher pressures between (20 and 35) MPa however the sII hydrate forms at mole fractions between about (46 ± 2) mol% methane and (96 ± 2) mol% methane. It can similarly be shown that at constant pressure the hydrate formation conditions will be dependent on temperature.

In constant volume systems, stripping of the gas will most likely occur due to preferential enclathration of either methane or ethane. For example, if 100 moles of 98.8 % methane + 1.2 % ethane gas mixture is contacted with 1 mole of water at 0.1 °C at the incipient hydrate formation pressure of 2.251 MPa a sII hydrate of composition (0.869 CH_4 + 0.131 C_2H_6)·6.455 H_2O is predicted by CSMGEM. It is clear that the hydrate is preferentially enclathrating ethane because the water free ethane content in the hydrate is 13.14 % compared to 1.2 % in the gas phase. For a flow system the gas is constantly replenishing its original composition at the point of hydrate formation but in a constant volume system the gas is being stripped preferentially of specific components. However at certain compositions and *P,T* conditions the mole fraction of the components inside the hydrate is exactly the same as in the

gas phase. For example, a gas mixture of 70 % methane + 30 % ethane at P = 15.77 MPa and T = 273.25 K is predicted to form a sII hydrate of composition (0.700 CH_4 + 0.300 C_2H_6)·5.859 H_2O. The dashed lines on Figure 3.18 represent the P,x conditions at which the hydrate is predicted to enclathrate gas at the same mole fractions as the gas phase composition. It can be shown however that these conditions are unstable. If the gas composition is only slightly perturbed, divergent preferential enclathration will occur. This can be illustrated about the point at 70 % methane + 30 % ethane at P = 15.77 MPa and T = 273.25 K. For a gas mixture of 69 % methane + 31 % ethane at the same pressure and temperature the predicted hydrate has the composition (0.699 CH_4 + 0.301 C_2H_6)·5.860 H_2O. The hydrate has a slight preference for methane in relation to its gas phase percentage and so the gas phase methane composition will begin to drop (or x_1 will decrease with hydrate formation as shown in Figure 3.18). On the other hand for a gas mixture of 71 % methane + 29 % ethane the predicted hydrate composition is (0.702 CH_4 + 0.298 C_2H_6)·5.857 H_2O. The hydrate has a slight preference for ethane in relation to it gas phase percentage and so the gas phase ethane composition will begin to drop (or x_1 will increase with hydrate formation as shown in Figure 3.18). This concept is illustrated in Figure 3.18 with the arrows indicating the direction that the gas phase will be stripped due to preferential enclathration.

Due to gas phase compositional changes during the hydrate formation process in the plug formation cells, conditions that were initially believed would form sII plugs actually formed sI plugs as shown by X-ray diffraction. Figure 3.19 shows the composition stripping calculated for a pressure drop hydrate formation (see Chapter 4 for details of the models used to calculate this stripping). The ethane rapidly becomes depleted due to its preferential enclathration in the hydrate. For this reason gas mixtures containing approximately 80 % methane + 20 % ethane were prepared in situ in the ISCO pump from pure methane and a 53 % methane + 46 % ethane mixture. Due to the stripping in a non-flow system this mixture yielded sII hydrates close to the sI-sII phase boundary. Preferential enclathration is discussed further in the next chapter.

The CSMGEM calculated P,T phase diagrams calculated at a high gas to water mole ratio (100:1) presented for the 65.4 % methane + 34.6 % ethane mixture in Figure 3.20 and for the 98.8 % methane + 1.2 % ethane mixture in Figure 3.21 illustrate some interesting features.

Firstly comparing the *P,T* phase diagram for the 98.8 % methane + 1.2 % ethane mixture to that for Bollavaram's processed natural gas shown in Figure 3.4 both are clearly quite similar. At lower pressure conditions sII hydrate is the stable structure and at high pressures sI is the stable hydrate structure, the sI + sII + V boundary line/region also exhibits a similar negative d*P*/d*T* slope. The *P,T* phase diagram for the 65.4 % methane + 34.6 % ethane mixture on the other hand show some distinct differences with both that of the 98.8 % methane + 1.2 % ethane mixture as well as Bollavaram's processed natural gas. For this mixture sI hydrates are the stable structure at lower hydrate formation pressures (up to 9.1 MPa incipient hydrate formation conditions) and sII hydrates are the stable structure at higher pressures, the opposite to the 98.8 % methane + 1.2 % ethane mixture and Bollavaram's processed natural gas. Also the slope of the sI + sII + V boundary line/region also exhibits an opposite positive d*P*/d*T* slope.

CSMGEM calculated *P,T* phase predictions for pure methane sI hydrate were also plotted on Figure 3.21 of the 98.8 % methane + 1.2 % ethane mixture. The H + Aq + V and H + I + V lines for the sI region of the diagram for the mixture show close alignment with the data for methane sI hydrate. The close alignment in Figure 3.21B suggests very similar dissociation enthalpies for sI hydrates of this mixtures and sI methane hydrates as the Clapeyron equation slope, dln*P*/d(1/*T*), will be similar.

3.5.2 Plug dissociation

Peters[49] model for two-sided hydrate dissociation, the basis for plug dissociation prediction package CSMPlug, suggests that the structure of hydrate has a strong effect on the dissociation time. The model predicts that the dissociation of a sII plug will take approximately 30 % longer than for a sI plug. If the dissociation temperature of the hydrate is below the ice point the dissociated water will often freeze to form an ice plug even when ambient conditions higher than the ice point. Taking this into account the model predicts that removal of a hydrate and ice will take about 20 % longer for the sII plug than the sI plug. Discussion of hydrate plug dissociation times with respect to structure follows.

A hydrate plug dissociation gas evolution plot for a predicted sI plug made from the gas mixture of 65.4 % methane and 34.6 % ethane at CSM is shown in Figure 3.22. The plot

shows that the total time for conversion was about 42 min. CSMPlug predicted a similar dissociation time of 40 min. By comparison of the actual hydrate number to the hydrate number predicted using CSMGEM the conversion to hydrate was calculated to be 100 %.

A hydrate from the 65.4 % methane + 34.6 % ethane mixture was also prepared at higher pressure. Figure 3.24 shows its phase diagram with the formation pressure/composition line. The structure of this hydrate was confirmed by Raman spectrometry. Figure 3.26 shows the vibrational spectra recorded for this hydrate. C-H and C-C vibrational frequencies for ethane in the large cages of structures sI and sII have been compared to literature data at 274 K.[36,71,94] The Raman spectra were taken at 77 K (-196 °C). By comparing the ethane peaks it is possible to observe that the structure is sII (note there is a small shift to lower frequencies due to the lower temperature of measurements). The lower ethane C-H vibration of 2883.0 cm^{-1} at 77 K is comparable to the 2887.3 cm^{-1} peak for sII at 274 K. The higher ethane C-H vibration of 2939.0 cm^{-1} at 77 K is also comparable to the 2942.3 cm^{-1} peak for sII at 274 K.[72] The C-C stretch for the ethane at 77 K is the most comparable however, 992.0 cm^{-1} compared to the 992.9 cm^{-1} peak for sII at 274 K. It appears that this peak changes much less with temperature.

The dissociation plot for the sII hydrate is shown in Figure 3.23. The experimental end time was about 32 min compared to the CSMPlug prediction of 46.5 min. The CSMPlug prediction is about 45 % greater than the experimental time which is larger than all the other differences thus far. The sII forming Qatar gas used in Peters' experiments[49] also yielded a shorter experimental dissociation time than predicted. Peter's sI methane hydrate dissociation showed agreement within about 15 % whereas from the sII the prediction was 120 % longer than the experimental time. Peters suggested that sII dissociation may rely more on kinetic effects. Due to the fact that the sII plug for the 65.4 % methane + 34.6 % ethane mixture had to be formed at a higher pressure than that of the sI plug, its relative stability at atmospheric pressure would be expected to be lower. Estimations of the enthalpy of dissociation by the Clapeyron equation using CSMGem phase data indicate that the dissociation enthalpy is higher for a sI than sII hydrate made from this mixture, whereas the opposite is true for the 98.8 % methane + 1.2 % methane mixture. A plot of the Clapeyron equation enthalpy of dissociation estimates for hydrates formed from pure methane (sI), 65.4 mol% methane + 34.6

mol% ethane (sI and sII) and 98.8 % methane + 1.2 % ethane (sII) with pressure is included as Figure 3.30 (note: more discussion on the Clapeyron equation estimates can be found in section 3.5.3 of this chapter). These experimental results from the lower methane composition structural transition region do not support the prediction that sII hydrates take longer to dissociate. The results of Davies et al.[40] appear at first to somewhat disagree with this result. Davies et al. prepared sII hydrate plugs using a 65 % methane + 35 % ethane mixture and compared the dissociation times to sI hydrate plugs formed with pure methane. They found that the sII plugs took longer to dissociate than the sI plugs. The difference with their measurements however was that they used pure methane to form their sI hydrates instead of the 65 % methane + 35 % ethane mixture. Clapeyron equation calculations of the enthalpies of dissociation using eqs (3.15) and (3.17) shown in Figure 3.30 suggest that the methane sI hydrates have a lower enthalpy of dissociation than sII hydrates prepared from a 65.4 % methane + 34.6 % ethane mixture. However for natural gas systems the more important structural transition region is at the high methane mole fraction transition. In this case the Clapeyron equation calculations suggest that the enthalpy of dissociation of sII 98.8 % methane + 1.2 % ethane hydrate is higher than that of a sI pure methane hydrate. Given that CSMPlug assumes a fixed value of the enthalpy of dissociation of sII hydrate (640 $kJ \cdot kg^{-1}$) which is greater than the fixed value assumed for sI (460.24 $kJ \cdot kg^{-1}$)[40], the method which is used in the model is not in anyway invalidated by the above results. The predictions from CSMPlug however should only be applied to hydrates formed from gas mixtures with high methane mole fractions with the currently assumed values of enthalpies of dissociation.

Seven hydrate plugs were prepared and dissociated to investigate the high methane structural transition region at the University of Canterbury. The sI plugs were prepared from the 98.8 % methane + 1.2 % ethane gas mixture. The sII plugs were prepared from 80 % methane + 20 % ethane mixtures prepared in situ using the ISCO pump. A further hydrate plug prepared by the pressure drop (pressurized to approximately 8 MPa each pressurization) from the 98.8 % methane + 1.2 % ethane mixture showed evidence of containing both sI and sII hydrates. The dissociation plot for this hydrate is shown in Figure 3.28 and appears to show two distinct regions of dissociation. A hydrate formed from this gas at high gas to water ratio is predicted to be sII by CSMGem, however due to non-flow preferential enclathration of the

ethane the gas is likely to be stripped to virtually pure methane and most of the plug was likely sI. Due to this particular plug being the least porous (ε = 0.462) it is hypothesized that gas mixing along the length of the ice/hydrate plug during formation was more highly impeded than for other plugs and gas diffusion would be slower through the plug. This meant that the ends of the plug may have stripped out all the ethane to form sII hydrates before any of the ethane could reach the middle of the plug. This would lead to disks or cylindrical sections of sII hydrate at either end of the plug. If it is assumed as predicted that sI dissociates more quickly the gas evolution curve would be expected to be dominated by evolution from the sI section of the hydrate for the first time period. As gas evolution from the sI section tailed off the sII gas evolution would be at a faster rate than that from the sI section and the sII section would dominate the final dissociation time. This evolution plot would appear to show this behaviour with a distinct change in gas evolution rate at just after 40 min. The hydrate dissociation time for this plug has been assumed to be effectively a sII hydrate dissociation time because it appears that the sII hydrate controls the final time. None of the other plugs prepared from the 98.8 % methane + 1.2 % ethane mixture appeared to show two distinct regions of dissociation.

Figure 3.25 shows a plot of the experimental and the predicted hydrate dissociations times versus the hydrate porosity (the void fraction of the plug). The porosity value is the likely greatest source of experimental-model discrepancy. The porosity was estimated from the mass of ice particles, the volume of the cell and a hydrate density calculated using CSMGem. Although the cell was tapped with a mallet around the thermowells there may have been areas devoid of ice particles. Also as the cell was loaded with ice particles vertically there may have be a segregation of the smaller particles towards the bottom of the cell. These two affects could have caused significant errors in the calculated porosity. The overall conversion of all of the plugs was 97 % or greater. Table 3.6 shows the experimental and CSMPlug predicted dissociation times. The percentage difference the CSMPlug prediction is from the experimental value is also tabulated. The percentage difference of the model prediction from the experimental time for sI plugs spans from -2 % to +20 % giving a mean of – 2.4 %. For the sII plug this difference spans from +3 % to +14 % giving a mean of +8%. The model predicts that the sII plugs will take from 38 % to 40 % longer to dissociate. Applying the two

mean prediction errors to these values gives a time of about 25 % longer for a sII plug than a sI plug.

Structures at the University of Canterbury were analyzed by powder X-ray diffraction using samples from the small sample cell. As sI and sII have unique crystal structures they have unique X-ray diffraction patterns. From the single crystal data of Kirchner et al.[26] using the powder diffraction pattern generation program PowderCell,[87] the collected patterns could be indexed to the correct structure. The predicted pattern of a sI hydrate, sII hydrate and ice is shown in Figure 2.9 of Chapter 2. An example of a pattern collected for a sII hydrate plug is shown in Figure 3.27.

An approximate solution of a model for the estimation of hydrate plug dissociation times has recently been published by Nguyen-Hong et al.[51], see eq (3.8). The model can be used to make an approximate estimation of the difference in dissociation times of plugs of sI and sII. If the ratio of dissociation times for a sII plug versus a sI plug is taken by applying the properties in eq (3.8) (see nomenclature listed after this equation) to both sI and sII and the plugs are assumed to have the same size, porosity and dissociation conditions then:

$$\frac{t_{\mathrm{D,sII}}}{t_{\mathrm{D,sI}}} = \frac{\dfrac{0.335\Delta_{\mathrm{dis}} H_{\mathrm{sII}} \rho_{\mathrm{H,sII}} \left(1-\varepsilon\right)}{\left(T_{\mathrm{w}} - T_{\mathrm{m}}\right)} + 0.09\rho_{\mathrm{L}} Cp_{\mathrm{L}}}{\dfrac{0.335\Delta_{\mathrm{dis}} H_{\mathrm{sI}} \rho_{\mathrm{H,sI}} \left(1-\varepsilon\right)}{\left(T_{\mathrm{w}} - T_{\mathrm{m}}\right)} + 0.09\rho_{\mathrm{L}} Cp_{\mathrm{L}}}, \tag{3.22}$$

where the subscripts sI and sII refer to properties specific for that hydrate structure and $t_{\mathrm{D,sII}}$ and $t_{\mathrm{D,sII}}$ are the dissociation times for hydrate that are similar in all other aspects except structure. For a small $(T_{\mathrm{w}}\text{-}T_{\mathrm{m}})$ of 4 °C or less and for porosities between 0.3 and 0.9:

$$\frac{0.335\Delta_{\mathrm{dis}} H \rho_{\mathrm{H}} \left(1-\varepsilon\right)}{\left(T_{\mathrm{w}} - T_{\mathrm{m}}\right)} >> 0.09\rho_{\mathrm{L}} Cp_{\mathrm{L}}, \tag{3.23}$$

by a factor of about 10 to 60. Applying this to eq (3.22) gives:

$$\frac{t_{D,sII}}{t_{D,sI}} \approx \frac{\Delta_{dis} H_{sII} \rho_{H,sII}}{\Delta_{dis} H_{sI} \rho_{H,sI}}. \quad (3.24)$$

Using the enthalpy of dissociation (437.1 kJ·kg^{-1}) and density (914 kg·m^{-3}) of pure methane sI hydrate given by Nguyen-Hong et al.[51] and the dissociation enthalpy of a sII hydrate formed from a high methane content gas (492 kJ·kg^{-1}) from this work combined with a calculated hydrate density from CSMGem (916 kg·m^{-3}) leads to the prediction that a sII plug will take 13 % longer to dissociate than a sI plug:

$$\frac{t_{D,sII}}{t_{D,sI}} \approx \frac{492 \times 916}{437 \times 914} = 1.13. \quad (3.25)$$

This concurs with the CSMPlug model and the experimental evidence and shows that the dissociation enthalpy is perhaps the most important factor for predicting relative dissociation times of hydrate plugs.

From the plug dissociation enthalpies calculated at atmospheric pressure, listed in Table 3.8, the 65 % methane + 35 % ethane mixture dissociation enthalpies for sI and sII hydrates are 24.45 kJ·mol^{-1} and 22.57 kJ·mol^{-1} (metastable) respectively, using the Nguyen-Hong et al. model the dissociation time of the sI hydrate would be expected to take 13 % longer than the sII hydrate. For the 98.8 % methane + 1.2 % ethane mixture the dissociation enthalpy of sI and sII hydrates are 20.86 kJ·mol^{-1} (metastable) and 22.14 kJ·mol^{-1} respectively, using the Nguyen-Hong et al. model the dissociation time of the sII hydrate would be expected to take 6 % longer than the sI hydrate.

Recently the model for plug dissociation first developed by Peters[49] has been extended to electrical heating in a paper by Davies et al.[40] The model assumes that there is constant heat flow through the wall of the pipe as opposed to a constant wall temperature in the original model of Peters. The electrical heating extension to the model was tested with predictions showing close agreement with experimental measurements. It was also found that electrically heated sII hydrates took longer to dissociate than sI hydrates. It should be noted that for these experiments sII hydrates were prepared from a 65 % methane + 35 % ethane mixture or a

synthetic Qatar gas mixture whereas sI hydrates were prepared from pure methane. From the CSMGem dissociation enthalpy predictions shown in Figure 3.30 it can be seen that dissociation enthalpies of sII hydrates formed from either the 65 % methane + 35 % ethane mixture or the 98.8% methane + 1.2 % ethane mixture are both greater than that of methane sI hydrate. This indicates that the dissociation time of sII hydrates will always be greater than that of a pure methane sI hydrate.

Davies et al. also points out that in the plug dissociation models "the temperature of the hydrate phase was assumed to be constant, with respect to the radius".[40] It is suggested that "this assumption is valid for systems where the pressure does not accumulate significantly which would change the temperature of phase equilibrium (for example a highly porous plug)".[40] As this assumption means no heating or cooling of the hydrate phase, heat capacities of the hydrate are not required for modelling high porosity hydrate plugs but may be more important for accurate predictions with low porosity hydrate plugs more commonly found in systems where oil fills the pores of the hydrate. Davies et al. describe some dissociation experiments where a low viscosity oil was introduced to fill the hydrate pore space of a sI methane hydrate, this resulted in an approximately 10 % longer dissociation time however Davies et al. suggest the extra time required may have just been a result of the heat being consumed to warm the oil, also even though this plug was dissociated by a one-sided dissociation (releasing gas from only one side of the plug) pressure measurements at either end of the cell remained relatively uniform indicating good pressure communication. This perhaps suggests that it is not possible to make a hydrate plug non-porous enough to need heat capacities as dissociation model inputs and indicates that only enthalpies of dissociation of the hydrate are needed like the current model uses.

3.5.3 Calorimetry

Enthalpy of dissociation measurements have been shown by the Nguyen-Hong et al.[51] simplified model to be perhaps the most important determinant of the relative dissociation times of sI and sII hydrate plugs. Measurements of the enthalpy of dissociation of sII hydrate prepared from the 98.8 % methane + 1.2 % methane are discussed below. Calculations of the enthalpy of dissociation from the Clapeyron equation for sI and sII hydrates of both the 65.4 % methane + 34.6 % ethane and 98.8 % methane + 1.2 % ethane mixture are also

discussed. The enthalpy of dissociation is also considered in terms of the average predicted guest size of the each cage of each structure for the 65.4 % methane + 34.6 % ethane mixture.

Measurements of the enthalpy of dissociation of sII hydrate with the 98.8 % methane + 1.2 % ethane gas mixture have been completed using the DSC at a pressure of about 7 MPa. The results of the dissociation enthalpy measurements are recorded in Table 3.7. The first measurement of (66.47 ± 0.50) kJ·mol^{-1} at a pressure of 7.03 MPa was conducted with hydrate formed inside the calorimeter by the method first used by Marsh and Gao.[143] The second measurement of (63.15 ± 0.50) kJ·mol^{-1} at a pressure of 6.92 MPa was made from cryogenically transferred hydrate. The conversion to hydrate for the second measurement was 98.16 % compared to 64.26 % for the first. Higher conversions are usually considered to result in better measurements of the dissociation enthalpy.[143] Figure 3.29 shows the pre-hydrate dissociation ice peak, the hydrate dissociation ice peak as well as the post-hydrate dissociation ice peak for the second measurement. The two different hydrates may have had slightly different hydrate compositions due to their different methods of preparation, this may explain why the 3.32 kJ·mol^{-1} difference in dissociation enthalpies despite the close dissociation pressures.

A comparison of the measured values to predictions of the enthalpy of hydrate dissociation is also given in Table 3.7. The predicted values were calculated from CSMGem *P*,*T* phase stability data and compressibility factors (calculated from molecular masses, mass densities, *P*, *R* and *T*). Calculations using the compressibility factor difference expressed by eq (3.17) as well as $\Delta Z = -Z_G$ where completed using the Clapeyron equation as expressed by eq (3.15). Traditionally it has been assumed that the compressibility factor of the gas, Z_G, is the dominant term (the compressibility factor of the water and the hydrate are assumed negligible) as represented by $\Delta Z = Z_G$. The compressibility difference represented by equation eq (3.17) is equivalent mathematically to the molar volume difference that Anderson[156] used for his study of the enthalpy of dissociation of methane hydrate except it has been assumed that the gases are not soluble in the aqueous phase.

Gupta[50] has recently measured the enthalpy of dissociation of sI methane hydrate up to 20 MPa and found that above about 10 MPa that, unless the water and hydrate phase

compressibility were taken into account, errors in the dissociation enthalpy predicted using the Clapeyron equation would be in the range of (50 to 100) % (see Figure 3.12 taken from Gupta). By comparing Anderson's[156] molar volume differences to the molar volume of pure methane the difference in enthalpies of dissociation from the use of this expression versus using only the gas molar volume can be calculated. Similarly to what Gupta found it can be shown that at 9.88 MPa there is a 30 % difference by using the molar volume difference rather than only the molar volume of the gas ($\Delta V = V_G$). This difference grows almost linearly with pressure, exceeding 100 % (124 %) at 69.68 MPa and higher pressures. The prediction using the eq (3.17) form of ΔZ is only 0.9 % higher than the experimental value for the 98.16 % hydrate compared to a 10 % lower value from $\Delta Z = Z_G$. This suggests that more accurate predictions of enthalpies of hydrate formation can be made using the eq (3.17) ΔZ. Considering the accuracy of the phase prediction data and the compressibility factors as the only sources of error for use in the Clapeyron equation these values are estimated to have an uncertainty of ± 4.5 %.

The hydrate formation enthalpy for pure methane hydrate of 54.19 kJ·mol^{-1} from Handa,[135] is about 18 % lower than the value measured for the sII hydrate. The higher formation enthalpy would suggest that the dissociation time would be longer for the sII hydrate because more energy would be required to dissociate it.

Given that the structural transition is at such a high methane composition it has been assumed that the enthalpy of dissociation for a sI hydrate prepared from a high methane gas mixture would be the same as that of a pure methane sI hydrate. The *P*,*T* phase diagrams shown in Figure 3.21 for the 98.8 % methane + 1.2 % ethane mixture are overlaid with data for methane sI hydrate. The methane hydrate lines and the sI lines for the mixture are very closely aligned, the similar Clapeyron equation slopes (d$\ln P$/d(1/*T*)) in part (B) of the figure indicate very similar dissociation enthalpies given that the small fraction of ethane in the gas and hydrate will have little effect on their compressibility factors.

The Clapeyron equation with *P,T* phase data and compressibilites for each phase (calculated from molar masses, mass densities, *P*, *R* and *T*) from CSMGem predictions was used to estimate the dissociation enthalpy of hydrates prepared from the 65.4 % methane + 34.6 %

ethane mixture (sI and sII), the 98.8 % methane + 1.2 % ethane mixture (sII) and 100 % methane (sI). Error in the values has been estimated at 4.5 % from the error in the *P,T* phase data and compressibilites from CSMGem. The calculated dissociation enthalpies as well as the experimental measurements were plotted with pressure in Figure 3.30. The estimations suggest that for high methane natural gases the dissociation enthalpies for sII hydrates (represented by the 98.8 % methane + 1.2 % ethane mixture sII data) are higher than those of sI hydrates (represented by the pure methane sI hydrate data). The estimation also shows that the case is the opposite for the 65.4 % methane + 35 % ethane hydrates (the sII hydrates have lower dissociation enthalpies than the sI hydrates). For comparison with the plug dissociation time measurements of Davies et al[40] it can be seen that the estimated dissociation enthalpies of the 65.4 % methane + 34.6 % ethane sII hydrates are higher than those of pure methane sI hydrates. Although several authors suggest that the Clapeyron equation can only be used at univariant conditions,[148,150] comparison of the predicted hydrate dissociation enthalpies seem to be within reasonable agreement with the experimental value using the eq (3.17) form of ΔZ, deviating by 0.8 % at 6.92 MPa and 5.9 % at 7.03 MPa. It is also interesting to note that, in comparison that the methane hydrate predictions are almost constant with pressure and are within the range of calorimetric results reported in Table 3.2.

The change in the enthalpy with pressure (and hence temperature), particularly for the sI hydrate formed from the 65 % methane + 35 % ethane mixture, is most likely a result of changing guest size. Sloan and Fleyfel[154,155] first suggested that larger guests resulted in larger enthalpies of dissociation. Plots of the average guest size for the large and small cage versus pressure for the 65 % methane + 35 % ethane sI and sII hydrates are shown in Figure 3.31 and Figure 3.32 respectively. It can be seen that the large cage guest for both hydrates changes little with pressure, however that of the small cage changes more significantly. The small cage average guest size for the sI hydrate increases by about 1.4 Å over a pressure range of about 9 MPa. For the sII hydrate the small cage average guest size only increases very marginally by about 0.5 Å over a pressure range of about 135 MPa. The much larger change in small guest average size in the sI hydrate would appear to give rise to the comparatively much larger change in the calculated dissociation enthalpy with pressure/temperature.

3.5.4 Further calorimetric measurements

Initially more measurements of enthalpies of dissociation of gas hydrates were planned as well as measurement of heat capacities, however due to recurring breakdowns of the DSC used in this work these measurements were not possible. Measurements of the enthalpies of dissociation of sI and sII hydrates formed from the mixture of mole fractions 65.4 % methane + 34.6 % ethane would have been useful as further confirmation of Clapeyron equation predictions presented in this chapter. From the literature review there is a general lack of calorimetrically measured enthalpies of dissociation and heat capacity data for gas hydrates of both pure gases and gas mixtures. Measurements of the enthalpies of dissociation of highly soluble gaseous guests such as CO_2 or H_2S would be particularly useful to investigate assumptions associated with the used of the Clapeyron equation.

Chapter 4 PREFERENTIAL ENCLATHRATION AND GAS PHASE STRIPPING DURING LABORATORY HYDRATE FORMATION FROM GAS MIXTURES

4.1 Introduction

In doing the plug dissociation studies in this work at high methane mole fractions a discontinuity was observed in the gas evolution rate (see Figure 3.28) and X-ray diffraction indicated the possibility of the presence of both sI and sII hydrate structures in some plugs. Forming laboratory hydrate samples that are representative of hydrates encountered industrially for plug dissociation and other studies is important if laboratory results are to be applied to industry. It is of particularly importance in the case of plug dissociation studies that the structure of the hydrate formed is that that was desired (or even in worst case assumed). Typically this is not a problem when preparing a hydrate of a single guest component as most single guests only form one structure of hydrate over a wide range of P,T conditions. For mixtures of gases on the other hand it has been shown that changes in the composition can result in the formation of hydrates of a different structure. One such mixture is methane + ethane, even though both components form sI hydrate as single guests a mixture of the two gases at certain compositions can result in the formation of sII hydrates,[71,72] the stable hydrate structure has also shown to be a function of the composition in multi-component natural gas mixtures (see Chapter 3). Duplication of conditions such as the flow of gas through or around ice or water when forming a hydrate is not always possible in the laboratory, yet the industrial conditions where water or ice contact gas to form hydrate plugs are under flow conditions (or conditions were there is a extremely large mole excess of gas to water). The formation of hydrates in the laboratory are typically carried out under conditions where the gas supplied to the ice or water for the formation to the hydrate is only just in excess of that which is required for complete conversion of ice or water to hydrate.

Although hydrate phase stability predictions packages such as CSMGem can perform simulations and predict conditions where only sI, only sII or a mixture of sI and sII hydrates form under excess water conditions, such as that shown for a mixture of methane + ethane on the isothermal P,x diagram of Figure 3.1, these prediction packages don't explain why (or

why don't) both structures form together. This chapter investigates reasons this may occur; isothermal hydrate formation is considered by numerical mole balance models in a number of steps whereby only a small amount of the water or ice react over a given step to form a hydrate of stoichiometry that is fixed by the conditions at the beginning of the step. The gas phase composition changes during the hydrate formation due to the fact that the gas composition of the hydrate (on a water free basis) is not the same as the initial gas phase. Certain components of the gas phase will be more likely to enter the hydrate phase than others, this is referred to as preferential enclathration in this work. If the composition of the gas phase determines the structure of hydrate formed, like in the methane + ethane system, this preferential enclathration may lead to the formation of more than one structure of hydrate.

There are several laboratory hydrate formation methods/conditions to consider, they include:

1. The constant volume pressure-drop hydrate formation method,
2. The closed-system constant pressure hydrate formation method (e.g. a piston pump maintains constant pressure of initial feed gas), and
3. The open-system constant pressure hydrate formation method (gas pressure is regulated in the system by flow from a cylinder or other supply).

Models of the conditions described by 1 and 2 are considered and experimental results for a mixture of methane + ethane in a system were hydrate was formed at constant pressure by decreasing the system volume with a syringe pump are compared to the relevant model predictions and CSMGem P,T flash calculations.

4.2 Review of literature

4.2.1 The composition of the gas phase and hydrate phase on a water free basis

To the best of this author's knowledge of the literature, no study to date has investigated the laboratory formation of hydrate plugs from melting ice and gas mixtures and considered modelling the gas phase composition as a function of conversion of the water/ice phase to hydrate. It has however, been known for 75 years that the composition of the guest molecules in the hydrate on a water free basis can be considerably different to that of the gas phase used to form the hydrate. Hammerschmidt[39] performed measurements on a hydrate formed from a

pipeline natural gas, he noted that "the composition of this pipeline gas does not vary greatly as shown by frequent analyses over a 2-year period. Typical analyses are given in [Table 4.1]". A section of pipeline containing a hydrate formed from this gas was vented and a sample of hydrate was collected. This hydrate was then dissociated and an analysis was performed of its composition, the results of these measurements are also shown in Table 4.1. Hammerschmidt[39] noted that "both the propane and isobutane are highly concentrated in the sample of pipe line [hydrate]". It is also clear that the methane mole fraction of the hydrate gas is significantly lower than that of the pipeline gas.

Table 4.1 – Mole fractions of each component in Hammerschmidt's pipeline gas and hydrate gas. (Reproduced from Hammerschmidt[39]).

	Pipeline Natural Gas		Hydrate
Date sampled	8/06/1933	28/08/1932	3/01/1933
Methane	0.8250	0.8270	0.5695
Ethane	0.0599	0.0668	0.0566
Propane	0.0326	0.0446	0.2497
n-Butane	0.0049	0.0057	0.0083
Isobutane	0.0030	0.0040	0.0469
Pentanes, plus	0.0007	0.0008	0.0000
Nitrogen	0.0719	0.0511	0.0646
Carbon dioxide	0.0020	0.0000	0.0044

The distribution coefficient method of estimating the hydrate formation conditions of gas mixtures, first suggested by Wilcox et al.[160] and fully developed by Carson and Katz[161] in the 1940's is based upon the fact that at a high gas to water mole ratio the composition of the water free hydrate phase is different to that of the gas phase and a function of temperature and pressure. The vapour to solid distribution coefficient for gas hydrates, K_{vsi}, is defined as:

$$K_{vsi} = y_i / x_{si} \,, \tag{4.1}$$

where y_i is the gas mole fraction of component i and x_i is the hydrate phase mole fraction of component i on a water free basis. From knowledge of K_{vsi} as function of P and T it is possible to estimate the hydrate formation conditions using a method analogous to the K-value method for dew-point calculations in a mixture, that is by fixing either P or T and iterating the other until the sum of mole fractions of components within the hydrate phase is equal to unity:

$$\sum_{i=1}^{n} \frac{y_i}{K_{vsi}} = 1, \tag{4.2}$$

where n is the total number of components in the gas mixture. Carson and Katz[161] set values for the K_{vsi} for methane as a function of P and T and values for other component were derived from two component gas mixtures based on the values of methane (Carson and Katz produced charts of K_{vsi} as a function of P and T for ethane and propane, other authors produced charts for further components, see Sloan and Koh[2] section 4.2.2 for charts, K_{vsi} correlations with T and P and references, note: K_{vsi} were based on methane in mixtures that form sII hydrates). It is clear that because the values of K_{vsi} are functions of temperature and pressure for individual components that hydrate gas compositions on a water free basis can be very different to that of the gas surrounding the hydrate and the success of this method's prediction of hydrate formation P,T conditions is based upon this fact. The absolute average deviation of pressure predictions for a given temperature using the K_{vsi} values has been evaluated from data from 20 natural gases, the deviation was 12.3 % compared to 5.8 % for CSMGem.[2]

The model of van der Waals and Platteeuw[32] described briefly in the introduction calculates the composition of the hydrate based on fractional occupancies calculated from Langmuir adsorption constants derived from statistical thermodynamics. This model provides a way of calculating the hydrate phase composition from the P, T and composition of the gas. CSMGem (developed by Ballard[33]) further allows flash calculations in the hydrate region at pressures higher than the incipient pressure or lower temperatures than the dissociation temperature and hence allows for the calculation of more than an infinitely small amount of the hydrate phase. This means that the effect of the ratio of moles of water to gas can be investigated (note: sometimes however the program does not always converge to a solution at high mole ratios of water to gas).

The separation of gases has even been proposed and investigated, using the fact that the water free gas composition of the hydrate phase is different to that of the gas. Happel et al.[162] studied the separation of methane and nitrogen by the formation of hydrates in a continuous flow reactor. A 1 L high pressure reactor, with jacketed temperature control and a magnetically coupled turbine agitator was used in experiments. The flow rate of gas mixtures

of methane + nitrogen from a cylinder was set using a mass flow controller, the gas were then compressed and contacted with the water in the bottom of the reactor. A purge flow exiting at the top of the reactor was controlled using a back pressure regulator. The system contained an external flow loop, water containing hydrate particles was pumped from the bottom of the reactor and circulated back to the top of the reactor. Samples of hydrate could be collected at a viewing port in a sample loop off this external loop. Gas exiting the reactor as well as the gas from the hydrate was analysed by gas chromatography. The results of this paper are not entirely clear given that the feed composition of the methane + nitrogen mixtures feed in to the system are surprisingly not stated, however several isobaric *T*,*x* plots of the compositions of the purge gas composition and the hydrate gas composition are presented. The maximum mole fraction differences in the composition of the hydrate gas and the purge gas occurred at about 275 K and 7.17 MPa (1040 psi), where the mole fraction of methane in the purge gas was about 0.37 and the mole fraction in the hydrate gas was about 0.75.

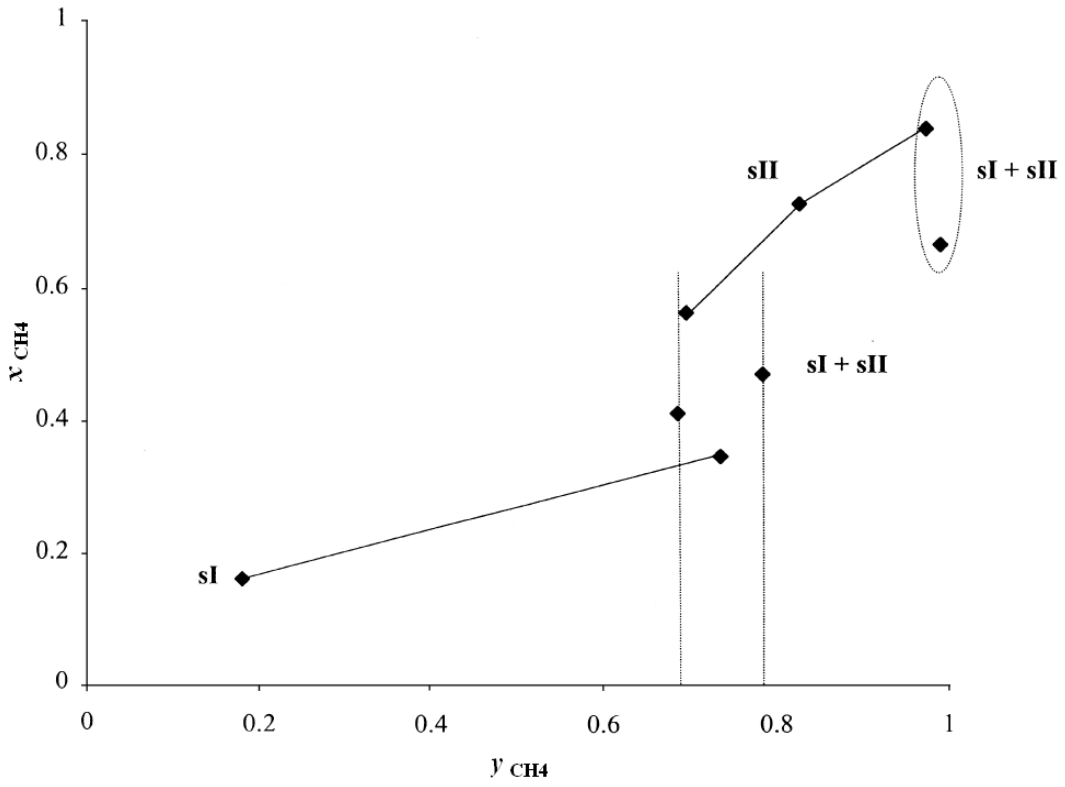

Figure 4.1 – Mole fraction in the hydrate phase on a water free basis of methane, x_{CH4}, as a function of the vapour phase mole fraction of methane, y_{CH4}, used to prepare hydrates from methane + ethane mixtures, compositions were calculated from NMR peak areas or estimated from Raman spectra peaks areas, abrupt changes in the range 0.686-0.784 indicate the stable hydrate structure changes from sI to sII, a similar effect is seen near y_{CH4} =1. (Modified from Subramanian et al.[71]).

Studies of hydrates formed from methane + ethane mixtures by Subramanian et al.[72] and Kini[163] reveal the mole fraction of methane and ethane in the hydrate phase as a function of vapour phase mole fractions used to form the hydrates. The mole fractions of methane and ethane in the vapour phase and the hydrate phases were calculated from NMR peak areas or Raman spectra peak areas (Note: the Raman peak areas could be used to estimate the composition of methane + ethane mixtures as a calibration curve of the ratio of methane to ethane Raman peak areas versus the methane to ethane mole ratio of calibration gases of known mole fractions had been prepared, see Subramanian et al.[72]). A step change was observed in the hydrate phase composition for hydrates prepared from the methane + ethane mixture with a mole fraction of methane in the gas mixture of between 0.7 and 0.8, this is illustrated in Figure 4.1 reproduced from Subramanian et al.[71] The change was attributed to a change in the structure of hydrate formed from the mixture of sI to sII, a similar but opposite change from sII to sI was observed between methane mole fractions in the vapour phase of about (0.97 and 0.99). The upper transition point was determined more accurately by Raman spectroscopy to occur between methane mole fractions in the vapour phase of (0.992 to 0.994). These results showed that the composition of the vapour phase is crucial in the determination of the structure of hydrate that will form.

4.2.2 Notes on metastability

Several authors have conducted experimental studies which have shown that usual sI hydrate formers carbon dioxide[164,165] and methane[166] can transiently form metastable sII crystals. A recent article also showed evidence of formation of both sI and sII hydrate for mixtures of methane + ethane + propane hydrates.[167] In this study hydrates were formed under flow conditions or conditions of a large volume of gas to water. It was determined by the authors that these conditions would result in no or limited changes in the gas composition so that the formation of a different structures due to composition changes in the gas was not a contributing cause. Four different mixtures were investigated with mole fractions between (90.28 and 98.01) % methane, between (0 and 4.95) % ethane and between (0.65 and 4.77) % propane. For all of the mixtures morphological changes were observed when crystals of hydrate formed just below the three phase H + Aq + V line were cooled isobarically to temperatures below the H + Aq + V line of pure methane hydrate. Large euhedral crystal transitioned to a fine crystal foamy mass. A reversal in morphology could be achieved by

reheating above the H + Aq + V line of pure methane hydrate. "Raman spectroscopy and X-ray diffraction data indicated that formation/decomposition of sI methane hydrates was part of this process".[167]

The models in this study do not investigate metastability, the most stable hydrate predicted using CSMGem is assumed to be formed given a composition of gas and the temperature and pressure.

4.3 Models and calculations

4.3.1 The extremes of hydrate formation and preferential enclathration

Consider this thought experiment: A piston maintained at constant temperature contains water and a gas mixture (containing only components that can be enclathrated in hydrate cages) at a ratio to which there is excess water in requirement to fully convert all of a gas mixture to hydrate. If the piston is compressed so the conditions are within the hydrate formation P,T region hydrate will begin to form until the pressure drops to the incipient pressure at the set temperature. However if the mixture is continuously compressed by the piston to maintain the conditions within the hydrate formation region then the gas will continue to combine with remaining water until all the gas is consumed. It is then clear that the hydrate composition on a water free basis on average will be equal to the initial gas mixture composition.

Alternatively the above piston can be considered for a system containing a very small amount of water and a large amount of gas (in mole terms). If such a system is in the hydrate formation P,T region then hydrate formation will occur to consume all the aqueous phase. The hydrate composition under these conditions is defined by the measured K_{vsi} values discussed in the introduction to this section. The hydrate composition on a water free basis can be considerably different to the composition of the gas mixture (note: however under certain conditions the hydrate composition on a water free basis can be the same as that of the gas mixture, see the dashed lines on Figure 3.18 and refer to Section 3.4.1 for further detail).

To form a large hydrate plug in the laboratory ice particles are typically melted just above the ice point temperature in a pressure cell in the presence of a hydrate forming gas above the hydrate formation incipient pressure, this method was developed by Stern et al.[126] and is discussed in detail in Chapter 3 of this work. The amount of gas feed to the known amount of

ice particles in the cell is typically in only a slight excess to that required for complete conversion to hydrate. These conditions of formation lie between those of the two extreme conditions in the paragraphs above, and so the hydrate composition formed will be between theses two limits.

Two sets of formation conditions are considered for modelling in this work (1 and 2 of the list in the introduction). In the method of Stern et al.[126] hydrate formation proceeds by pressure drop of an amount of gas initially charged to the cell. An alternative method is to connect the pressure cell to piston or syringe pump and maintain the pressure of the gas constant during the formation. A further possible formation technique not considered here but that could be potentially modelled by similar techniques is an open system constant pressure hydrate formation in which a gas mixture from a cylinder is regulated in to a pressure cell to maintain constant pressure (i.e. the pressure drop from hydrate formation draws more fresh gas at the initial feed composition from the cylinder in to the pressure cell).

4.3.2 Constant pressure formation preferential enclathration - stripping model for the formation of gas hydrates from ice particles and gas mixtures

Objective: To model the mole fractions of the components in the gas phase and in the hydrate phase (on a water free basis) to assess the stripping of components from the gas phase due to preferential enclathration of selected components in the hydrate phase.

Scope: The scope of this model is a closed system maintained at constant pressure during formation of hydrate. The pressure is kept constant as hydrate formation consumes gas by reducing the system volume using a piston (syringe pump), a diagram of this system is shown below in Figure 4.2.

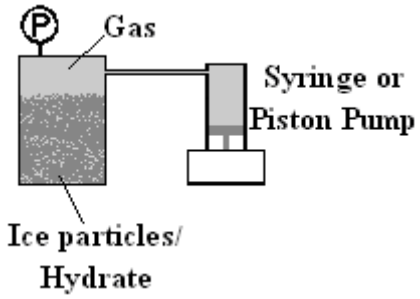

Figure 4.2 – Constant pressure syringe or piston pump formation of hydrate from ice particles.

Assumptions:

- Hydrate formation will only occur when the temperature is above the ice point temperature or in other words the hydrate is not considered to form directly from ice (this assumption was verified experimentally).
- As hydrate formation is controlled by the melting of ice, the gas is considered to be only in contact with a small amount of water at any time.
- For a small fraction of conversion of ice to (water then) hydrate the hydrate being formed is of constant composition (mole fraction of each guest and hydrate number).
- Equilibrium hydrate phase predictions can be used to determine the composition of the hydrate phase.
- The system is well mixed (uniform gas composition).
- Pressure and temperature are uniform over entire system
- Vaporisation of water from the ice is considered negligible.
- The initial ratio of gas to water is great enough to ensure that complete conversion to hydrate can occur.
- Initially values that are assumed to be known include:
    - Mass of ice particles loaded into the cell.
    - The total system volume.
    - The pressure and temperature.
    - The molar density of ice.

Equations:

The equations are based on the conversion of a small amount of the ice to hydrate over a step in the conversion of ice to hydrate, *i* (note: as ice conversion to hydrate proceeds with time, time will progress with *i*, however time is not likely progress linearly with *i*). Note, a notation follows in section 4.3.4.

Firstly the initial values are calculated by eqs (4.3) to (4.9). The moles of ice loaded into the pressure cell, N_0^{ice}, to form hydrate is first considered:

$$N_0^{\text{ice}} = m_0^{\text{ice}} / M^{\text{ice}}, \tag{4.3}$$

where m_0^{ice} is the mass of ice particles loaded in to the cell and M^{ice} is the molar mass of ice (water). The number of moles of water that react with the gas to form hydrates over a small step in the conversion, ΔN^{ice}, is then defined by a small fraction, f, of the initial ice:

$$\Delta N^{\text{ice}} = f N_0^{\text{ice}}. \tag{4.4}$$

The volume of the ice particles loaded in to the cell initially, V_0^{ice}, may be calculated from the initial moles of ice, N_0^{ice}, and the molar density of ice, ρ^{ice}:

$$V_0^{\text{ice}} = N_0^{\text{ice}} / \rho^{\text{ice}}. \tag{4.5}$$

The initial volume of the gas phase, V_0^{g}, can then be calculated assuming the initial total volume of the system, V_0^{tot}, is known:

$$V_0^{\text{g}} = V_0^{\text{tot}} - V_0^{\text{ice}}. \tag{4.6}$$

The initial gas phase density, ρ_0^{g}, may be evaluated assuming knowledge of the composition (mole fractions $y_{j,i}$ of component number j (of a total of J components) in the gas at conversion step i), pressure and temperature. The Refprop equation of state (RefpropEOS)[168] was used in calculations in this work:

$$\rho_0^{\text{g}} = \text{RefpropEOS}\left(P, T, y_{1,0} \ldots y_{J,0}\right). \tag{4.7}$$

The initial number of moles of each gas in the mixture, $N_{j,0}^{\text{g}}$, and the total moles of gas, N_0^{g}, can then be calculated from:

$$N_{j,0}^{\text{g}} = y_{j,0} \rho_0^{\text{g}} V_0^{\text{g}}, \tag{4.8}$$

and

$$N_0^{\mathrm{g}} = \rho_0^{\mathrm{g}} V_0^{\mathrm{g}} = \sum_{j=1}^{J} N_{j,0}^{\mathrm{g}} \,. \tag{4.9}$$

The process of taking a step, i, in the conversion can then be taken (equations (4.3) to (4.9) set up the initial conditions), initially:

$$i = 0 \,, \tag{4.10}$$

so that i+1 in the following calculations will be equal to 1 (end of the first step).

The water to gas ratio, $r_{\text{Ice-Gas},i}$, is then defined as:

$$r_{\text{Ice-Gas},i} = \Delta N^{\text{ice}} \big/ N_i^{\mathrm{g}} \,. \tag{4.11}$$

The composition of the hydrate phase, $\left(x_{1,i}\mathrm{G}_1 + \ldots + x_{J,i}\mathrm{G}_J\right)\cdot n_i \mathrm{H_2O}$ (where $x_{j,i}$ represents the water free mole fraction of component number j of a total of components, and G represents the hydrate guest component, e.g. CH_4), as well as the hydrate density can then be calculated by setting the feed composition for a CSMGem P,T flash calculation, so there is one mole of gas (consisting of $x_{\text{me},i}$ moles of methane and $x_{\text{et},i}$ moles of ethane) to $r_{\text{Ice-Gas}}$ moles of water:

$$\left.\begin{matrix} x_{1,i},\ldots,x_{J,i},n_i \\ \rho_i^{\mathrm{h}} \end{matrix}\right\} = \text{CSMGemPTFlash}\left(T, P, y_{1,i}, \ldots, y_{J,i}, r_{\text{Ice-Gas},i}\right), \tag{4.12}$$

(note: $x_{1,i},\ldots,x_{J,i}$ and n_{i}, have to be calculated from the overall fractions of each guest component and water in the hydrate phase).

The moles of hydrate formed over the step, ΔN_i^{h}, can then be calculated:

$$\Delta N_{i+1}^{\mathrm{h}} = \Delta N^{\mathrm{ice}} / n_i \,, \tag{4.13}$$

where one mole of hydrate is represented by $\left(x_{1,i}\mathrm{G}_1 + \ldots + x_{J,i}\mathrm{G}_J\right)\cdot n_i \mathrm{H_2O}$, where the G_j represent guest component *j* of the hydrate.

The mole of each gas component and the total moles of gas can then be recalculated for the end of the step by considering the composition of the enclathrated gas (on a water free basis):

$$N_{j,i+1}^{\mathrm{g}} = N_{j,i}^{\mathrm{g}} - x_{j,i}\Delta N_i^{\mathrm{h}} \,, \tag{4.14}$$

and

$$N_{i+1}^{\mathrm{g}} = \sum_{j=1}^{J} N_{j,i+1}^{\mathrm{g}} \,. \tag{4.15}$$

The mole fractions of each component in the gas phase can then be calculated at the end of the step:

$$y_{j,i+1} = N_{j,i+1}^{\mathrm{g}} / N_{i+1}^{\mathrm{g}} \,. \tag{4.16}$$

As the number of moles and composition of the gas phase has changed the density of the gas at the end of the step to maintain constant pressure must be recalculated:

$$\rho_{i+1}^{\mathrm{g}} = \mathrm{RefpropEOS}\left(P, T, y_{1,i+1}, \ldots, y_{J,i+1}\right). \tag{4.17}$$

It is then possible to calculate the volume of the gas phase at the end of the step:

$$V_{i+1}^{\mathrm{g}} = N_{i+1}^{\mathrm{g}} / \rho_{i+1}^{\mathrm{g}} \,. \tag{4.18}$$

The volume of ice remaining at the end of the step may then be calculated by:

$$V_{i+1}^{\text{ice}} = V_i^{\text{ice}} - \Delta N^{\text{ice}} \big/ \rho^{\text{ice}}, \tag{4.19}$$

and the volume of the hydrate formed is given by:

$$V_{i+1}^{\text{h}} = V_i^{\text{h}} + N_i^{\text{h}} \big/ \rho_i^{\text{h}}, \tag{4.20}$$

noting that $V_0^{\text{h}} = 0$.

The total volume at the end of the step can then be recalculated by:

$$V_{i+1}^{\text{tot}} = V_{i+1}^{\text{g}} + V_{i+1}^{\text{ice}} + V_{i+1}^{\text{h}}, \tag{4.21}$$

this equation takes in to account the difference in the density between ice and the hydrate.

The volume of gas displaced or pumped out by the piston of the syringe pump over the step is hence:

$$\Delta V_{i+1}^{\text{g}} = V_{i+1}^{\text{tot}} - V_i^{\text{tot}}, \tag{4.22}$$

(taking in to account the volume of ice consumed and volume of hydrate formed).

The moles of ice remaining can then be calculated:

$$N_{i+1}^{\text{ice}} = N_i^{\text{ice}} - \Delta N^{\text{ice}}, \tag{4.23}$$

if this value is equal to zero then all the ice has converted to hydrate and the formation is complete, otherwise a step can be taken in the conversion *i* by setting:

$$i = i + 1, \tag{4.24}$$

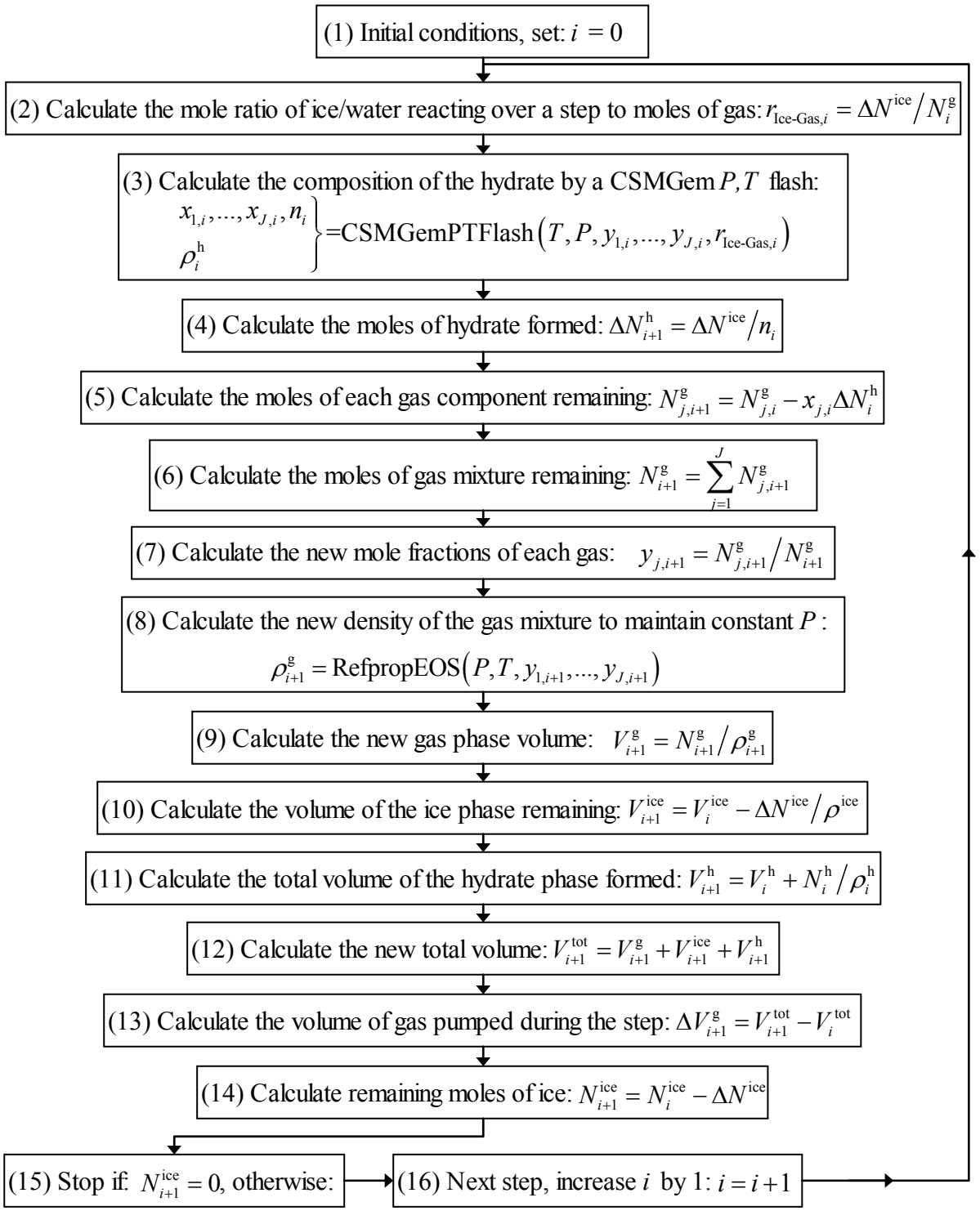

Figure 4.3 – Algorithm for gas phase stripping and preferential enclathration for a constant pressure syringe or piston pump formation of gas hydrate for a gas mixture. Note: Initial conditions (described by eqs (4.3) through to (4.9)) have to be prior calculated to use this algorithm.

this increases the step number by one, and then values can be recalculated by going back to eq (4.11) and following though again to eq (4.24) repeating calculation cycles until $N_{i+1}^{\text{ice}} = 0$. This process is represented in an algorithm shown in Figure 4.3.

4.3.3 Constant volume formation preferential enclathration - stripping model for the formation of gas hydrates from ice particles and gas mixtures

Objective: To model the mole fractions of the components in the gas phase and in the hydrate phase (on a water free basis) to assess the stripping of components from the gas phase due to preferential enclathration of selected components in the hydrate phase.

Scope: The scope of this model is a closed system of constant volume. The pressure is allowed to drop as hydrate formation consumes gas, a diagram of such a system is shown in Figure 4.2.

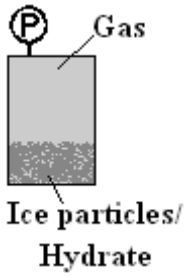

Figure 4.4 – Constant volume system for formation of hydrate from ice particles.

Assumptions:

- Hydrate formation will only occur when the temperature is above the ice point temperature or in other words the hydrate is not considered to form directly from ice (this assumption was verified experimentally).
- As hydrate formation is controlled by the melting of ice, the gas is considered to be only in contact with a small amount of water at any time.
- Equilibrium hydrate phase predictions can be used to determine the composition of the hydrate phase.
- The system is well mixed (uniform gas composition).

- The temperature is uniform over entire system at any step.
- Vaporisation of water from the ice is considered negligible.
- The initial ratio of gas to water is great enough to ensure that complete conversion to hydrate can occur.
- Initially values that are assumed to be known include:
    - Mass of ice particles loaded into the cell.
    - The total system volume.
    - The pressure and temperature.
    - The molar density of ice.

Equations: (a list of notation follows at the end of this section)
To model the constant volume pressure drop formation small steps were taken in the conversion by taking small steps in pressure drop.

The initial part of the model is similar to the constant pressure model of the previous section Firstly the initial amount of ice loaded into the pressure cell to form hydrate is considered. The moles of ice initially loaded in to the cell ($i = 0$), N_0^{ice}, can be calculated by:

$$N_0^{\text{ice}} = m_0^{\text{ice}} / M^{\text{ice}}, \tag{4.25}$$

where m_0^{ice} is the mass of ice particles loaded in to the cell and M^{ice} is the molar mass of ice (water).

The volume of the ice particles loaded in to the cell initially, V_0^{ice}, may be calculated from the initial moles of ice, N_0^{ice}, and the molar density of ice, ρ^{ice}:

$$V_0^{\text{ice}} = N_0^{\text{ice}} / \rho^{\text{ice}} . \tag{4.26}$$

The initial volume of the gas phase, V_0^{g}, can then be calculated assuming the initial total volume of the system, V_0^{tot}, is known:

$$V_0^{\mathrm{g}} = V_0^{\mathrm{tot}} - V_0^{\mathrm{ice}}. \tag{4.27}$$

The initial gas phase density, ρ_0^{g}, may be evaluated assuming knowledge of the composition (mole fractions $y_{j,i}$ of component number j (of a total of J components) in the gas at conversion step i), pressure and temperature. The Refprop equation of state (RefpropEOS)[168] was used in calculations in this work:

$$\rho_0^{\mathrm{g}} = \mathrm{RefpropEOS}\left(P, T, y_{1,0} \ldots y_{J,0}\right). \tag{4.28}$$

The initial number of moles of each gas in the mixture, $N_{j,0}^{\mathrm{g}}$, and the total moles of gas, N_0^{g}, can then be calculated from:

$$N_{j,0}^{\mathrm{g}} = y_{j,0} \rho_0^{\mathrm{g}} V_0^{\mathrm{g}}, \tag{4.29}$$

and

$$N_0^{\mathrm{g}} = \rho_0^{\mathrm{g}} V_0^{\mathrm{g}} = \sum_{j=1}^{J} N_{j,0}^{\mathrm{g}}. \tag{4.30}$$

Unlike the constant pressure model of the previous section, the pressure drop model takes a step in pressure drop rather than conversion of ice to hydrate. The pressure step, ΔP_{step}, can be set by taking a small fraction, X, of the pressure drop, ΔP_{drop}:

$$\Delta P_{\mathrm{step}} = X \Delta P_{\mathrm{drop}} \tag{4.31}$$

Initially the mole ratio of water (ice) consumed to gas, $r_{\text{Ice-Gas}}$, was set at:

$$r_{\text{Ice-Gas},0} = 0.01, \tag{4.32}$$

(however, this value is reiterated).

Equations (4.25) to (4.32) set up the initial conditions, now the first step, *i*, can be taken along the pressure drop data, this is done by setting:

$$i = 0\,, \tag{4.33}$$

so that *i*+1 in the following calculations will be equal to 1 (end of the first step).

A step in the pressure drop is then taken:

$$P_{i+1} = P_i - \Delta P_{\text{step}}\,. \tag{4.34}$$

An estimation of the molar density of the gas at this step is made:

$$\rho^{\text{g}}_{i+1} = \text{RefpropEOS}\left(P_{i+1}, T, y_{1,i} \ldots y_{J,i}\right), \tag{4.35}$$

using the gas phase mole fractions from step *i* (the mole fractions $y_{j,i+1}$ are found by iteration below)

The hydrate phase composition and molar density can be calculated by:

$$\left.\begin{matrix} x_{1,i}, \ldots, x_{J,i}, n_i \\ \rho^{\text{h}}_i \end{matrix}\right\} = \text{CSMGemPTFlash}\left(T, P_i, y_{1,i}, \ldots, y_{J,i}, r_{\text{Ice-Gas},i}\right), \tag{4.36}$$

where P_i is the pressure at step *i*.

The moles of gas that are enclathrated over a step, $\Delta N_{\text{enc},i}$, can be calculated:

$$\Delta N_{\text{enc},i+1} = \left(\rho^{\text{g}}_{i+1} - \rho^{\text{g}}_i\right) V^{\text{g}}_i\,, \tag{4.37}$$

as well as the moles of ice consumed, $\Delta N_{\text{ice},i+1}$:

$$\Delta N_{i+1}^{\text{ice}} = n_i \Delta N_{\text{enc},i+1} . \tag{4.38}$$

The mole ratio of water (ice) consumed to gas, $r_{\text{Ice-Gas}}$, can then be calculated:

$$r_{\text{Ice-Gas},i} = \Delta N_i^{\text{ice}} \big/ N_i^{\text{g}} , \tag{4.39}$$

the hydrate CSMGem flash of eq (4.36) can then be repeated with a more accurate $r_{\text{Ice-Gas}}$ value, eqs (4.37) to (4.39) are then re-evaluated, this calculation loop continues until $r_{\text{Ice-Gas}}$ converges to a constant value.

The moles of each gas mixture component at step i+1 can then be calculated:

$$N_{j,i+1}^{\text{g}} = N_{j,i}^{\text{g}} - x_{j,i}^{\text{h}} \Delta N_{\text{enc},i} . \tag{4.40}$$

The total moles of gas can be found from:

$$N_{i+1}^{\text{g}} = \sum_{j=1}^{J} N_{j,i+1}^{\text{g}} , \tag{4.41}$$

the mole fractions of each component can then be calculated:

$$y_{j,i+1} = N_{j,i+1}^{\text{g}} / N_{i+1}^{\text{g}} . \tag{4.42}$$

As eqs (4.37) to (4.42) have been evaluated from an approximate value of ρ_{i+1}^{g} in eq (4.35), ρ_{i+1}^{g} can be re-evaluated:

$$\rho_{i+1}^{\text{g}} = \text{RefpropEOS}\left(P_{i+1}, T, y_{1,i+1} \ldots y_{J,i+1}\right), \tag{4.43}$$

Then each of eqs (4.37) through to (4.43) (including the loop to calculate $r_{\text{Ice-Gas}}$) can be re-evaluated iteratively until the molar density, ρ^{g}_{i+1} (or mole fractions, $y_{j,i+1}$), doesn't change between iterations.

The moles of ice remaining can then be calculated:

$$N^{\text{ice}}_{i+1} = N^{\text{ice}}_{i} - \Delta N^{\text{ice}}_{i}, \tag{4.44}$$

as well as the total moles of hydrate formed (noting: $N^{\text{h}}_{0} = 0$):

$$N^{\text{h}}_{i+1} = N^{\text{h}}_{i} + \Delta N_{\text{enc},i}. \tag{4.45}$$

The total volume of hydrate formed is calculated from the moles of hydrate formed over the step, the hydrate molar density and the moles present at the previous step (note: $V^{\text{h}}_{0} = 0$):

$$V^{\text{h}}_{i+1} = V^{\text{h}}_{i} + \Delta N_{\text{enc},i} \big/ \rho^{\text{h}}_{i} \tag{4.46}$$

Changes in the volume that the gas phase has to occupy as a result of the difference in density between the hydrate formed and the ice consumed can be accounted for by:

$$V^{\text{g}}_{i+1} = V^{\text{tot}}_{i} - V^{\text{h}}_{i+1} - N^{\text{ice}}_{i+1} \big/ \rho^{\text{ice}}. \tag{4.47}$$

For the purposes of the next step in the calculations the mole ratio of ice consumed to gas for the next step, $r_{\text{Ice-Gas},i+1}$, was set equal to the value for the current set, $r_{\text{Ice-Gas},i}$ as an estimate:

$$r_{\text{Ice-Gas},i+1} = r_{\text{Ice-Gas},i}. \tag{4.48}$$

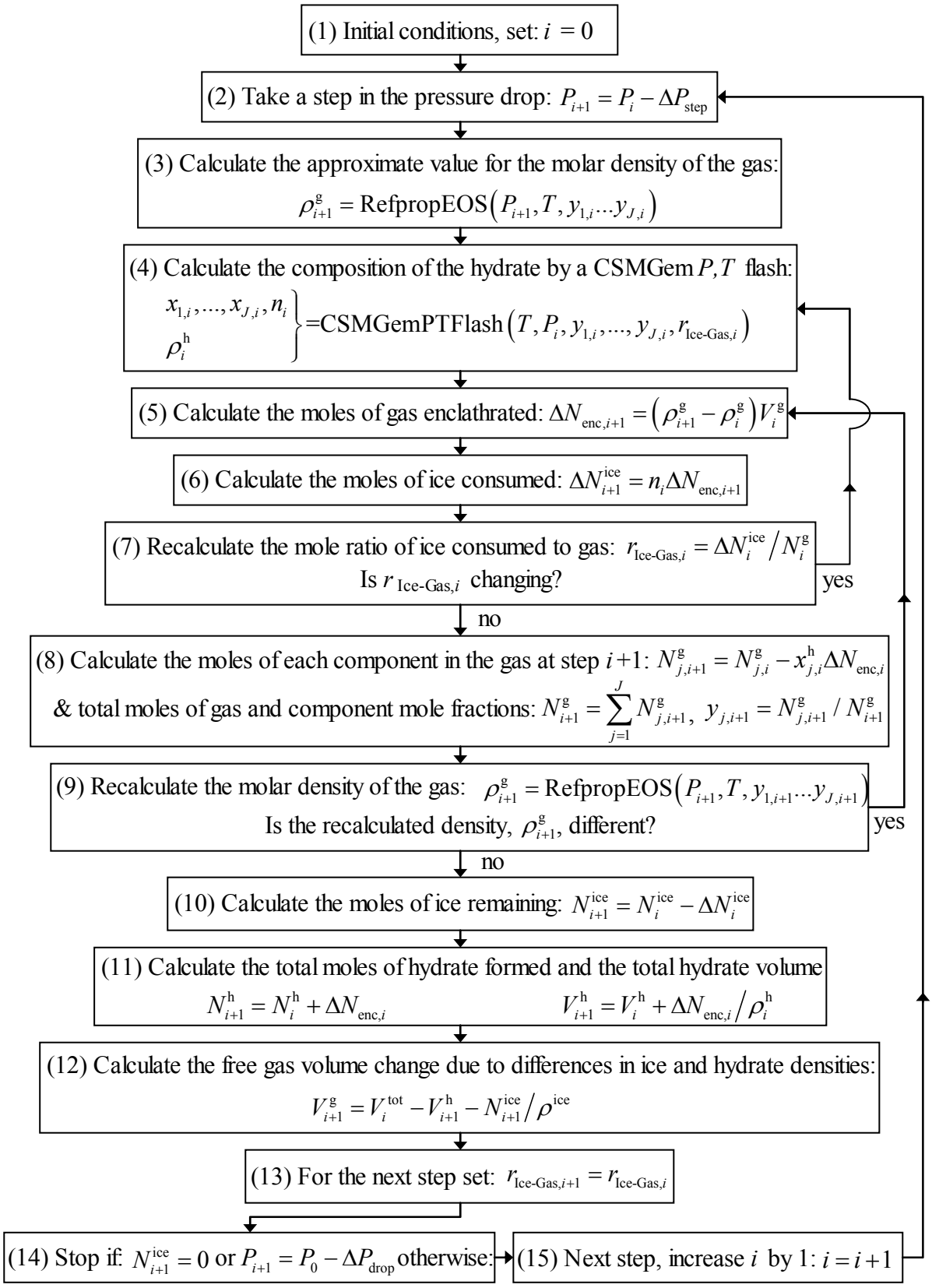

Figure 4.5 – Algorithm for the gas phase stripping and preferential enclathration for a constant volume formation of gas hydrate for a gas mixture. Note: Initial conditions (described by eqs (4.25) through to(4.30)) have to be prior calculated to use this algorithm.

If there is no ice left to convert $\left(N_{i+1}^{\text{ice}} = 0\right)$ or alternatively the full amount of pressure drop $\left(P_{i+1} = P_0 - \Delta P_{\text{drop}}\right)$ has been achieved calculations stop, otherwise a new step in the pressure drop is taken, this is accomplished by taking a step in *i*:

$$i = i + 1 . \tag{4.49}$$

Calculations for the new step begin again at eq (4.34).

The calculations described in eqs (4.34) through to (4.49) are represented in the calculation algorithm of Figure 4.5.

4.3.4 Notation for models

Roman

f	Small fraction in conversion of ice to hydrate (used in constant pressure model).
i	Step counter.
M	Molar mass.
m	Mass.
N	Number of moles of a component or phase.
n	Hydrate number (ratio of moles of water to moles of gas in the hydrate phase).
P	Pressure.
$r_{\text{ice-gas}}$	Mole ratio of ice converted to hydrate over a step to total moles of gas mixture.
T	Temperature
V	Volume of phase.
X	Small fraction of the total pressure drop (used in constant volume model).
x	Hydrate phase mole fraction of a guest component on a water free basis.
y	Gas phase mole fraction.

Greek

ΔN	Changes in moles of a phase or component over a step.
ΔP_{drop}	Total overall pressure drop (used in constant volume model).
ΔP_{step}	Pressure drop step size (used in constant volume model).

ΔV	Changes in the overall volume or volume of a phase over a step.
ρ	Molar density.

Subscripts

0	An initial condition (step 0)
enc	Indicates enclathrated over a step.
i	Property at step i.
J	Total number of components.
j	Component number.

Superscripts

g	Gas phase property.
h	Hydrate phase property/
ice	Ice phase property.
tot	Total overall property.

4.4 Experimental work

Experimental work in this chapter involves the preparation of a gas mixture of methane + ethane for measurements of the gas phase composition during hydrate plug formation and the final hydrate gas composition on a water free basis. During the hydrate plug formation samples of the gas phase were taken and their compositions were measured by gas liquid chromatography (GLC). The gas composition of the final hydrate was also measured by GLC.

4.4.1 Materials

Materials were the same as where used at the University of Canterbury in Chapter 3, methane was sourced from Linde Gas, U.K Ltd, with a purity of 99.975 %. Ethane was obtained from BOC gases limited and had a purity of 99 %. These gases were used to prepare gas mixtures without further purification. The water used to prepare ice for hydrate preparation was distilled and deionised.

4.4.2 Gas mixture preparation

A gas mixture of methane + ethane was prepared in situ in an ISCO 260D syringe pump by the same method as described in section 3.3.2 of Chapter 3. The mole fraction of methane desired for these experiments was 90 % and a mixture of this approximate mole fraction was prepared from pure methane and a mixture of mole fractions 53 % methane + 46 % ethane. The final pressure of this mixture was approximately 7.2 MPa for a syringe pump volume of 266 ml (pump full). Gas chromatography measurements (described in more detail below) indicated mole fractions of (89.7 ± 0.3) % methane and (10.3 ± 0.3) % ethane. The technique of taking a sample of gas is described in detail in the section 4.4.4.

4.4.3 Hydrate preparation

The hydrate preparation method was essentially the same as the constant pressure formation method described in section 3.3.3 of Chapter 3. Sieved ice particles were loaded in to a cell and the cell was then filled with gas and maintained at a constant pressure using a syringe pump during formation (note: all the experimental work of this chapter was completed at the University of Canterbury). The system used was slightly different however and only utilised the short/sample cell of Figure 3.16 described in section 3.3.3. A diagram of the system is shown in Figure 4.6. The total system volume bound by valves (3, 13 and 21) and the cylinder regulator was approximately 330 cm^3, estimated from the volume of the lines, fittings and cell (cell volume = 51 cm^3). The liquid nitrogen cooled cell loaded with 19.3 g of ice particles was place in a Polyscience model 9601 bath preset to 258 K. The cell was then connected via a ¼ in (6.35 mm) Swagelok quick-connect fitting to valve 15. Platinum resistance thermometers, PRT (Omega 100 Ω part number PR-11-2-100-1/16-12-E, ± 0.04 K), were then placed in the cell thermowell and in the bath (these were connected via a multiplexer (a 16 channel analog Intech 2100-A16) to a computer for logging using a data acquisition board (Advantech PCL-812G)). Air was removed from the cell by both vacuuming and purging. Values (3, 8 and 21) were closed (note: some values marked closed in Figure 4.6 remained closed during all these experiments and the ISCO pump was closed off as it was full with the gas mixture), and vacuuming of the cell was initiated by the opening valve 13 to the building vacuum system, this reduced the pressure to about 0.02 MPa. Valve 13 was then closed and the valve 8 (a High Pressure Equipment Co. 15-11-AF1 needle valve) was carefully adjusted to bleed gas in to the system to a final pressure of between about (0.2

and 0.4) MPa. The system was slowly depressurized to atmospheric pressure via valve 21 (a Swagelok SS-1RS4 needle valve). Valves (21 and 8) were then closed and vacuuming was initiated again by opening valve 13 to the building vacuum system. This vacuuming and purging cycle was repeated three times to ensure the removal of air from the system.

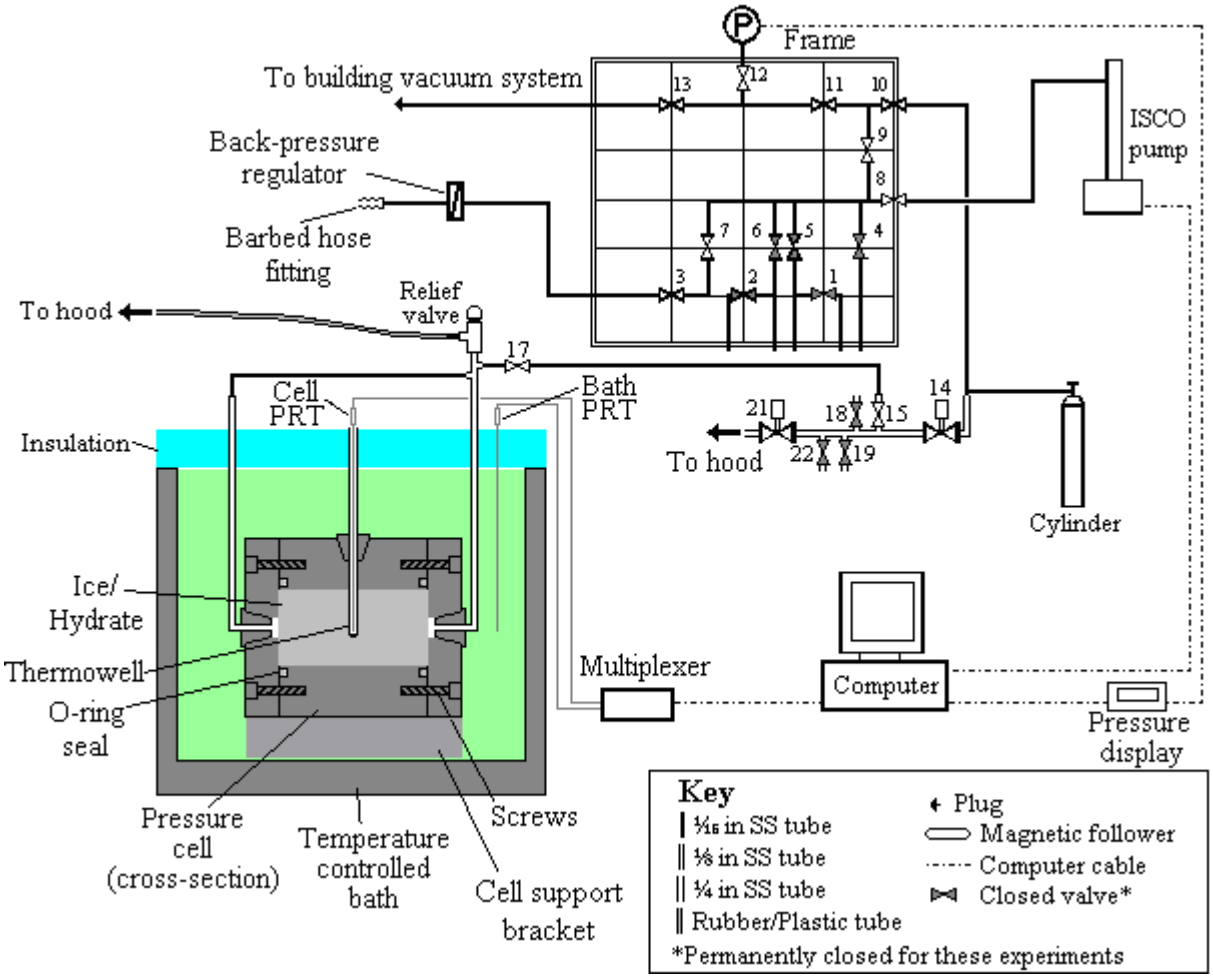

Figure 4.6 – Experimental apparatus for preferential enclathration formation tests at constant P (maintained by ISCO syringe pump). PRT refers to platinum resistance thermometers (not to scale).

Pressurization of the cell then began, valve 8 was gently opened to slowly bleed gas in to the cell. This was to ensure there was sufficient cooling of the gas as it entered the cell so that the temperature in the cell did not rise significantly (the cell was at 258 K in the bath), the temperature in the cell was observed to rise by less than 1 K. When the pressure between the cell side and the ISCO pump had equalised the cell and connections were checked for leaks with Swagelok Snoop leak detection liquid, valve 8 was then fully opened. The pressure

selected for the experiment was 6 MPa and the ISCO pump was set to slowly pump gas (at 0.5 mL·min^{-1}) in to the system until the pressure reached 6 MPa. The ISCO was then set at constant pressure mode to maintain the pressure at 6 MPa. Finally the temperature of the bath was raised to 273.25 K to initiate hydrate formation. Samples of the gas phase were analysed by gas chromatography during the hydrate formation, the method used is described in the following section.

4.4.4 Sampling and gas chromatography measurements during hydrate formation

Samples of the gas phase were collected and were analysed by gas chromatography during the process of hydrate formation. Before taking a sample the cell was cooled to 258 K and a mixing process was initiated using the ISCO pump. The ISCO pump was set to pressurise and depressurise in cycles so that the gas phase composition was homogenous. The pump was set to pressurise up to 8 MPa and then depressurise to 4 MPa (for some of the earlier mixing processes the depressurisation was limited to about 5 MPa due to the maximum volume of the ISCO pump). This cycle was repeated at least four times. The reason for cooling the cell to 258 K was so even if the cell was heated up it would not reach such a temperature to initiate the dissociation of hydrate. The temperature in the cell was monitored and never exceeded 278.5 K, approximately 3 K below the hydrate dissociation temperature at 4 MPa (the hydrate dissociation temperature was calculated conservatively using a gas composition of mole fraction 95 % methane + 5 % ethane as 281.45 K at 4 MPa).

After the mixing process was completed samples were extracted from the system using the back-pressure regulator (abbreviated BPR, Tescom model 26-1700, maximum pressure 41.4 MPa). The knob of the BPR was tightened to so it would only release gas if the pressure was above the maximum pressure for the BPR. Valves (7 and 3) were opened and then valve 7 was shut and the knob of the BPR was slowly adjusted so gas just started to flow. The 25 mL syringe shown in Figure 4.7 was used to collect a sample. Before use the seal of the syringe's diaphragm was lubricated with a few drop of silicone oil. The $\frac{1}{16}$ in stainless steel tubing leading from the BPR was connected to a barbed hose fitting, this was lubricated with some Vaseline. With the 3-way stopcock connected to the syringe as in Figure 4.7 position (1) and

the plunger was pushed fully in to flush out most of the air, and the rubber tubing was then slipped over the barbed hose fitting and the plunger was forced back slowly with the flow of gas from the BPR. When the plunger was near full the stopcock was changed to position (3) and the rubber tubing was quickly removed from the barbed hose fitting. The syringe was then flushed out again by holding the rubber tubing between the finger tips to generate a flow restriction (to prevent inward flow of air) the stopcock was changed to position (1) and the plunger was pressed down steadily. The stopcock was changed to position (3) when the plunger was close to fully pushed-in. A fresh sample of gas was then collected by the method just described. This flushing procedure was repeated at least three times. The BPR knob was then slowly turned to lower pressure until the gas flow was stopped. This was done to bleed the gas from the line leading to the BPR so not to cause contamination for the next measurement.

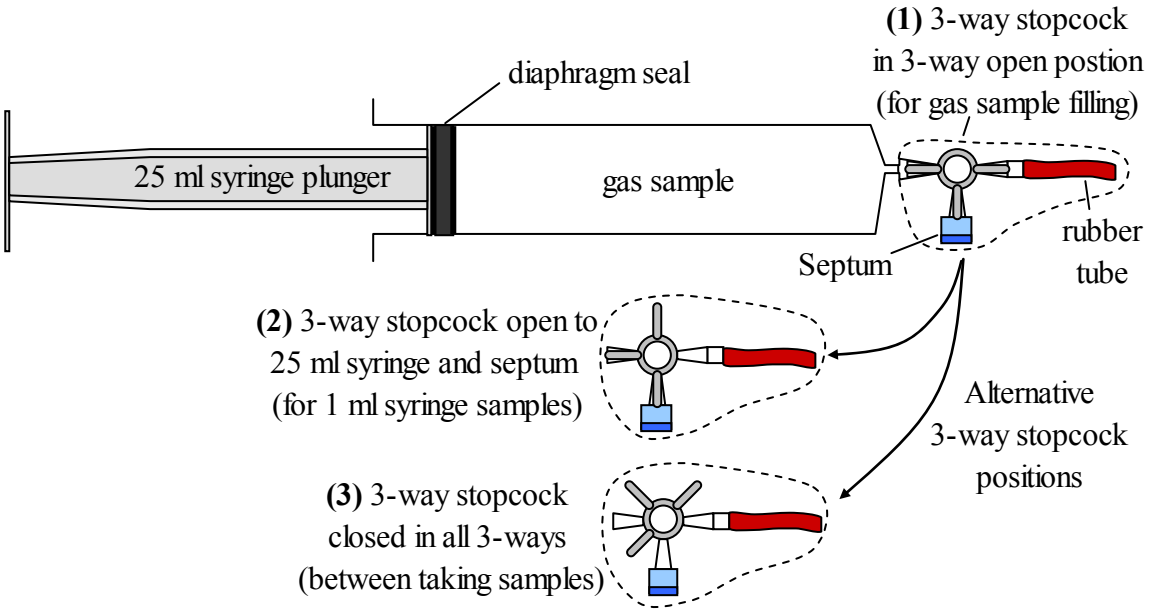

Figure 4.7 – Syringe used to gas samples showing alternative positions of the 3-way stopcock.

The 25 mL syringe was then used to provide samples of approximately 0.3 mL for gas chromatography. These samples were taken from the 25 mL syringe via the 3-way stopcock septum (the stopcock was position (2) of Figure 4.7). The syringe used to extract the samples was a Valco Instruments series A-2 1 mL syringe with a push button valve. The 1 mL syringe was flushed approximately ten times with the gas from the 25 mL syringe, the push button valve was then closed and the needle was removed from the septum.

The sample was then injected into the gas chromatograph. The chromatograph used was a Shimadzu GC-R1A with a RPR-G1 GC-processor and chart recorder. A 1.83 m (6 ft), 6.35 mm (¼ in) O.D Porapak Q packed column was utilized with a TCD detector. The injection and detection temperatures were 423 K and the column temperature was 318 K. The flow rate or helium was set to 25 mL min^{-1}. Experimentally it was impossible to remove all the air from the samples and a small amount was always present, the oxygen and nitrogen peaks were indistinguishable and formed a single air peak. If there was significant air contamination a fresh sample was collected using the 25 mL syringe. Contamination was considered to be too large when the resolution of the air and the methane peak was below 1.5. Typical elution times for air, methane and ethane were about 1.2 min, 1.75 min and 8.9 min respectively. For each 25 mL syringe of gas 6 to 10 injections were completed so that errors in the compositions measured could be estimated.

4.4.5 Hydrate phase measurements and structural identification

When the consumption of gas, indicated by no flow from the ISCO pump (set to pump at constant pressure), had ended the hydrate formation was considered ended and valve (15 and 17) of Figure 4.6 were closed. An $\frac{1}{16}$ in (6.35 mm) Swagelok fitting at valve 15 was then carefully untightened and the gas from this line was bled in to the room (this was only a small volume, less than 15 mL at STP, as the tube diameter was $\frac{1}{16}$ in). The cell was then disconnected from the system and placed in a bath of liquid nitrogen in the hood. The temperature continued to be monitored by the cell PRT (using an extension cable from the multiplexer) and when the temperature inside the cell had dropped to below 180 K valve 17 was opened carefully to depressurise the cell to the hood (under these conditions the hydrate should be stable at atmospheric pressure). Once the cell was completely depressurized the cell was carefully tipped on to one of ends so that the screws and lid of the other end could be removed. The hydrate inside the cell was then quickly scrapped out with a liquid nitrogen cooled spoon and was placed into a Dewar flask also containing liquid nitrogen.

The water free gas composition of the hydrate was measured by dissociating samples of the hydrate within the 25 mL syringe. A lump or several lumps (of perhaps several cm^3) of hydrate from the liquid nitrogen Dewar flask were quickly removed and placed in the 25 mL

syringe that had its plunger removed. The plunger was then reinserted with the stopcock of Figure 4.7 in position (1) and the plunger pushed down as far as possible (even if it meant breaking the lumps of hydrate apart). The rubber hose was held between fingertips initially due to an initial large release of gas assumed to be the vaporisation of the liquid nitrogen. When the hydrate was observed to bubble and fizz the stopcock was changed to position (3) and the syringe plunger was allowed to be pushed back by the pressure of the gas from the dissociating hydrate in the syringe. When the volume of gas was close to 25 mL the stopcock was changed back to position (1) and the gas was expelled by pressing the plunger with fingertip compressing the rubber hose to create a flow restriction. After the gas had been expelled the stopcock was switched back to position (3) and the syringe once again started to be filled with the gas from the dissociating hydrate. This process of expelling the gas when the plunger reached a volume near 25 mL was repeated until all the hydrate had dissociated. However enough gas was left in the syringe to take samples for gas chromatography. The chromatographic method used for these samples was the same as previously described above, although special care was taken due to water in the 25 mL syringe. The syringe was held upside down so that the water drained to the plunger end away from the stopcock and septum where the samples for gas chromatography were removed.

4.4.6 Modelling the experiments

The model presented in section 4.3.2 of this chapter presents somewhat of an ideal model as the temperature of the entire system was assumed to be uniform. This however was not the case experimentally. In the system shown in Figure 4.6 the cell was in a temperature controlled bath and the ISCO syringe pump was at room temperature. The property affected by this difference in temperature was the molar density of the gas in the system. Instead of assuming one temperature for the whole system the density was calculated at the average room temperature during experiments and the cell temperature and the density was volume averaged for the approximate volumes of gas at each temperature. Equations (4.7) and (4.17) were replaced by:

$$\rho_0^{\mathrm{g}} = \mathrm{RefpropEOS}\left(P, T_{\mathrm{cell}}, y_{1,0} \ldots y_{J,0}\right) \frac{V_{\mathrm{cell},0}^{\mathrm{g}}}{V_0^{\mathrm{g}}} + \mathrm{RefpropEOS}\left(P, T_{\mathrm{room}}, y_{1,0} \ldots y_{J,0}\right) \frac{\left(V_0^{\mathrm{g}} - V_{\mathrm{cell},0}^{\mathrm{g}}\right)}{V_0^{\mathrm{g}}}, \tag{4.50}$$

and

$$\rho_{i+1}^{\mathrm{g}} = \mathrm{RefpropEOS}\left(P, T_{\mathrm{cell}}, y_{1,i+1}, \ldots, y_{J,i+1}\right) \frac{V_{\mathrm{cell,i+1}}^{\mathrm{g}}}{V_{\mathrm{i+1}}^{\mathrm{g}}} + \mathrm{RefpropEOS}\left(P, T_{\mathrm{room}}, y_{1,i+1}, \ldots, y_{J,i+1}\right) \frac{\left(V_{\mathrm{i+1}}^{\mathrm{g}} - V_{\mathrm{cell,i+1}}^{\mathrm{g}}\right)}{V_{\mathrm{i+1}}^{\mathrm{g}}}, \tag{4.51}$$

where the initial volume of gas in the cell, $V_{\mathrm{cell},0}^{\mathrm{g}}$, is defined by:

$$V_{\mathrm{cell},0}^{\mathrm{g}} = V_{\mathrm{cell}} - V_0^{\mathrm{ice}}, \tag{4.52}$$

and the volume of gas in the cell at step i+1, $V_{\mathrm{cell,i+1}}^{\mathrm{g}}$, is defined by:

$$V_{\mathrm{cell,i+1}}^{\mathrm{g}} = V_{\mathrm{cell}} - V_{\mathrm{i+1}}^{\mathrm{ice}} - V_{\mathrm{i+1}}^{\mathrm{h}}. \tag{4.53}$$

The average room temperature is represented by T_{room} and the cell temperature is represented by T_{cell}.

To directly compare the experimental results to the model results the model has to take account of the volume of gas removed for the GC samples. These changes were considered by adjustment of the moles of gas in the system. The volume change of the ISCO pump, ΔV_{pump}, was modelled by:

$$\Delta V_{\mathrm{pump}} = V_{\mathrm{pump},0} - \sum_i \Delta V_i, \tag{4.54}$$

where $V_{\mathrm{pump},0}$ represents the initial fill volume of the ISCO pump. The effect of the volume of sample removal in experiments was applied in the model over the step in the conversion when

the modelled ISCO pump volume was the same as the experimental initial ISCO pump volume when the sample was taken experimentally. For steps in the conversion where a sample was removed, eq (4.11) was replaced by:

$$r_{\text{Ice-Gas}} = \Delta N^{\text{ice}} \Big/ \left(N_i^{\text{g}} - \rho_i^{\text{g}} \Delta V_{\text{sam}} \right), \tag{4.55}$$

where ΔV_{sam} is the volume of gas sample removed. The equation for the moles of each component in the gas mixture at the beginning of the next step in the conversion (step i+1) was also adjusted, eq (4.14) was replaced by:

$$N_{j,i+1}^{\text{g}} = N_{j,i}^{\text{g}} - x_{j,i} N_i^{\text{h}} - y_{j,i} \rho_i^{\text{g}} \Delta V_{\text{sam}}, \tag{4.56}$$

for sample removal steps.

4.5 Results and discussion

4.5.1 Hydrate formation

Figure 4.8 shows the experimental ISCO syringe pump volumes, V_{pump}, as well as the cell temperature, T_{cell}, as a function of time. The vertical spikes in the pump volume are due to the mixing process as described in the method (section 4.4.4). The sudden drops in pump volume indicate the removal of samples for gas chromatography measurements The flat period of both temperature and pump volume between about day (4 and 11) was due to a leak in the back pressure regulator (indicated by the larger than normal sample drop in pump volume at about day 4). The leak meant that no samples could be taken until it was repaired so the cell was maintained at 258 K for the time the back pressure regulator was out of service (note: the leak was treated like a sample removal for modelling purposes). It is interesting to note that over this time the ISCO pump volume did not change significantly, indicating the assumption that hydrate did not form directly from ice was correct (note: the sharp deviation at the end of the flat region was the BPR being tested). After about day 15 no further changes in the methane mole fraction was observed by gas chromatography within the error limits estimated by a 95 % student-t confidence interval (error bars in Figure 4.8) and hydrate formation was considered to be complete (note the sharp spike in temperature and pump volume just before

day 20 occurred after the cell had been disconnected and chilled in liquid nitrogen to extract hydrate samples).

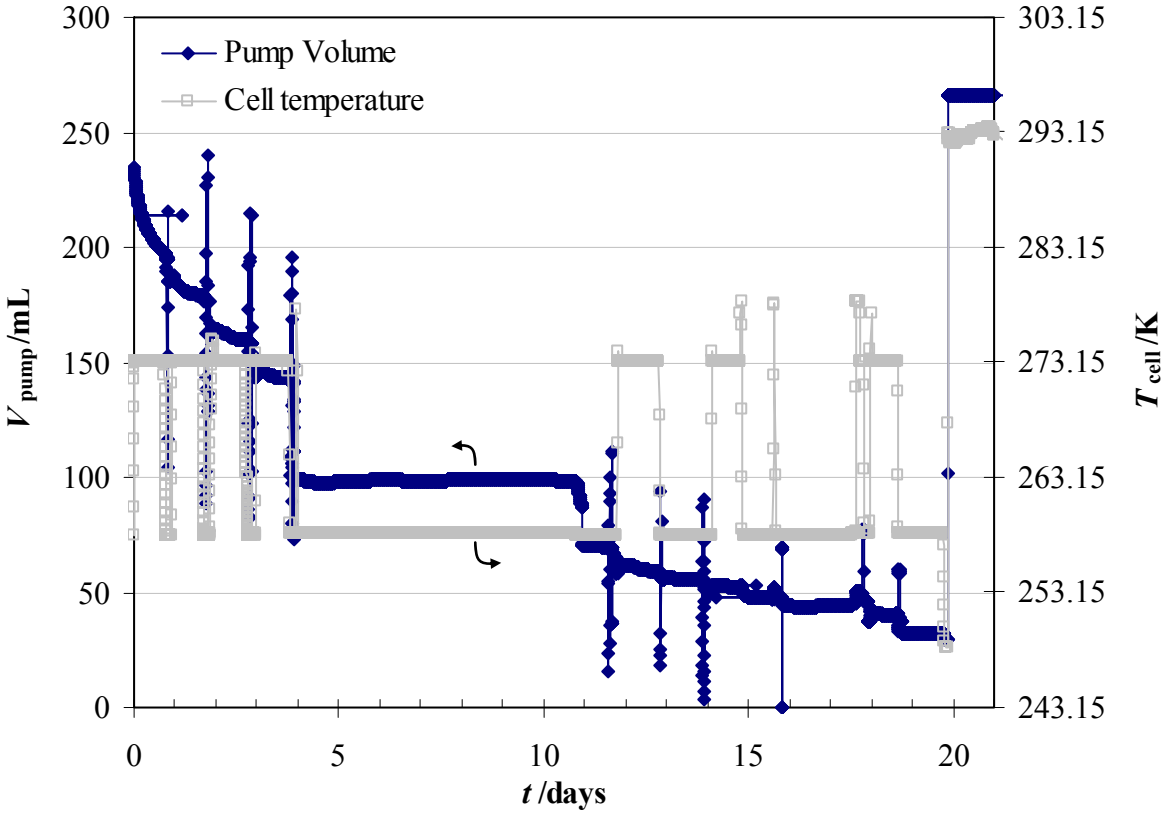

Figure 4.8 – Volume of the ISCO syringe pump and temperature of the cell as a function of time.

The desired pressure for the formation of the hydrate was 6 MPa. The average pressure over the time of the formation was 6.03 MPa, this value was used in the model. The room temperature (used in calculations of the overall gas density) was an averaged value of 294.7 K over the time of the formation, the maximum variation from this temperature was ± 2.8 K. A step size in the conversion of ice to hydrate was set by selecting an *f* value for eq (4.4) of 0.02.

4.5.2 Gas chromatography results and comparison to model

Figure 4.9 shows mole fraction of methane in the gas phase as a function of the volume pumped from the ISCO syringe pump both from experimental gas chromatography measurements and the constant pressure model. The flat regions of constant composition represent the points when samples were removed, and the change in the pump volume with no

change in the methane mole fraction represent the sample removal (or back pressure regulator leak for the widest flat region). The experimental and model data both display the same trends. The methane mole fraction in the gas phase increases with the conversion of ice to hydrate indicating that ethane was being preferentially enclathrated in the hydrate phase. The model increase of the methane mole fraction with the pump volume however is on average steeper. The final mole fraction of methane measured by GC was (92.5 ± 0.2) %, whereas the model predicted a value of 94.3 %, the percentage deviation of the model value from the GC measurement is thus +1.9 %. The total volume of gas pumped experimentally, 183.68 mL, was slightly larger than the model prediction of 183.12 mL.

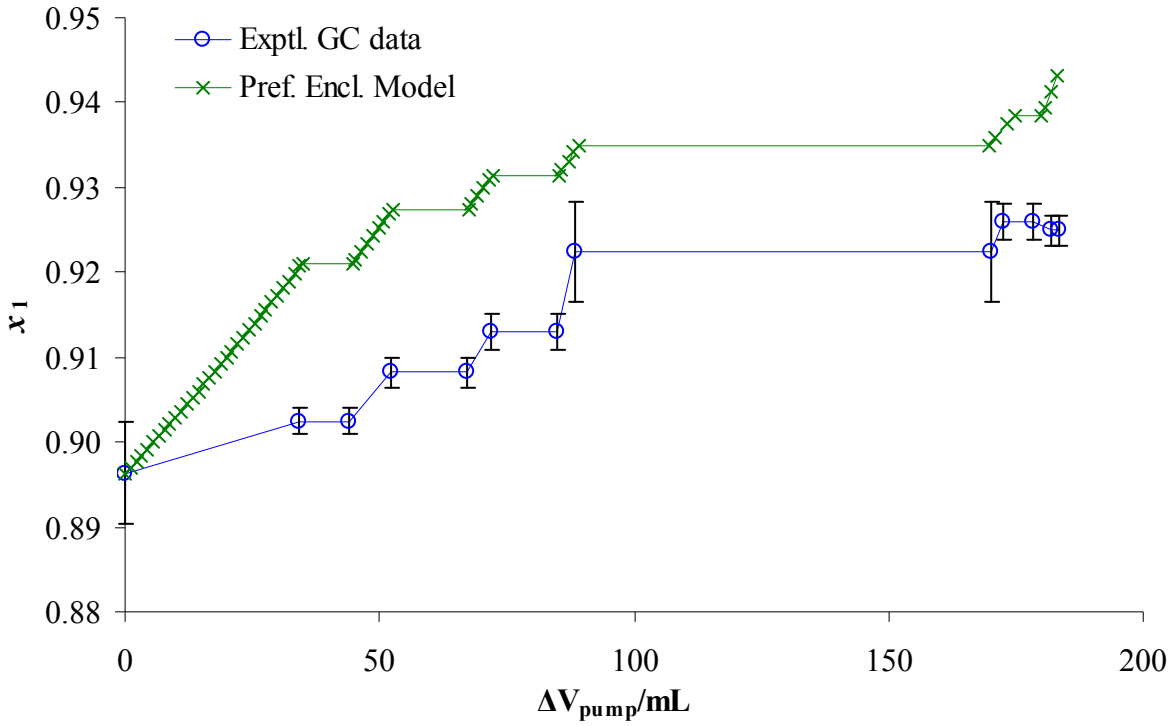

Figure 4.9 – Comparison of experimental and model preferential enclathration stripping of the gas phase.

While the prediction is not perfect the model could prove a useful tool to establish the direction and likely extent of stripping of the gas phase. The results suggest that the model is validated. The assumption that the equilibrium hydrate phase prediction can be used to determine the composition of the hydrate phase is probably the greatest source of discrepancy between the model and experimental results. The system is not at equilibrium during any of the steps in conversion. Once an initial layer of hydrate has grown on the outer surface of the ice particles the gases will begin to diffuse through fissures and cracks in the hydrate phase.

Diffusive separation of the gases is not likely to occur by mechanisms such as Knudsen diffusion however due to the elevated pressure reducing the mean free paths of the molecules. Once the hydrate has coated all the surfaces including the surfaces insides the fissures and cracks further conversion to hydrate occurs by diffusion through a layer of hydrate. Due to the size of methane it is believed that it will diffuse through the hydrate layer more easily than ethane. Ethane may have to be orientated longitudinally to pass through the hydrate layer. It might be expected for this reason that the hydrate phase would form with a higher proportion of methane than would be predicted by equilibrium thermodynamics. This could explain the discrepancy between the model predictions and experimental measurements observed in Figure 4.9.

The GC measured water free mole fraction of methane in the hydrate phase was (78.5 ± 0.7) % compared to a prediction of the model of 73.3 %. The difference of 5.2 % is larger in comparison to the difference for the final gas phase methane mole fraction. A possible cause was that the sampling method for the GC measurement was for a sample that was non-representative of the overall hydrate. In retrospect it may have been better to powder the entire hydrate sample and mix it (under the presence of liquid nitrogen in a mortar and pestle). On the other hand the model predicts greater stripping of ethane from the gas phase than the GC experimental results indicate, this should and does result in a lower methane mole fraction in the hydrate.

The sample of hydrate tested by X-ray diffraction indexed to a sII hydrate as expected. The gas phase mole fractions did not change enough to result in the formation of sI hydrate. If the amount of ice loaded initially into the cell was larger, or the amount of initial gas was less, then this might have been a possibility as both the experimental results and the model predicted that the gas phase methane mole fraction increased with the conversion of ice to hydrate, becoming closer to the structural transition value of approximately 99.3 % (as measured by Subramanian et al.[71]).

4.5.3 Constant volume model

The constant volume method was used to estimate the degree of stripping from the gas phase due to preferential enclathration for methane + ethane mixtures in Chapter 3. As the method

used in the constant volume method is similar to the constant pressure method it is possible to assume that this method is validated. Like the constant pressure model it should be noted that the constant volume model would not be expected to make perfect predictions (if implemented similarly to the prediction presented in Figure 4.9).

Figure 3.19 of Chapter 3 shows the predicted mole fraction of methane in the gas phase, x_1, as a function of the pressure (dashed curve) for a constant volume hydrate formation at 273.25 K from a mixture with a methane mole fraction of 98.8 % and an ethane mole fraction of 1.2 % initially at a pressure of 8.2 MPa. The curve indicates not much pressure drop would be needed under the conditions detailed to result in stripping of the gas phase from a sII forming region to a sI forming region.

Figure 3.24 of Chapter 3 shows the predicted mole fraction of methane in the gas phase, x_1, as a function of pressure (pressure/compositional tracking curve) for a constant volume hydrate formation at 273.25 K from a mixture with a methane mole fraction of 65.4 % and an ethane mole fraction of 34.6 % initially at a pressure of about 14.1 MPa. The gas composition used in this hydrate formation is close to the composition at which hydrate phase water free mole fractions of each component are predicted to be the same as the gas phase (see Figure 3.18). As a result of this the predicted stripping of the gas phase by the model was low (ethane fraction increased slightly in the gas phase). Crossing the sII to sII phase boundary due to too much pressure drop rather than gas phase component stripping was more of a concern for this formation. The cell was repressurized during the formation to prevent this from happening.

No direct measurements to determine the accuracy of the constant volume model were performed and the method has been assumed valid based on the results of the constant pressure method success. An experimental study further investigated the accuracy of the model.

4.5.4 Stepwise models for hydrate formation

The models for stepwise hydrate formation could potentially be adapted further. The temperature for example could be allowed to vary with each step, this would allow calculations of gas phase stripping and preferential enclathration for a gas mixture to be

performed for a constant volume system that is heated and/or cooled under hydrate forming conditions. The pressure may not drop for all steps if such adaptations were made however so they would have to also be fed in to the model at each step as well. The hydrate formation method described by Stern et al.[126] for the formation of hydrate from pure methane involved significant heating and cooling, the model could be applied to similar hydrate formations with gas mixtures.

The constant volume, (written before the constant pressure model) could potentially be rewritten in terms of conversion of a small fraction of ice to make it more like the constant pressure model. The current model is very slow to implement due to the two internal loops to, one, calculate the mole ratio of ice consumed per step to gas ($r_{\text{Ice-Gas}}$) and, two, calculate the molar density of the gas at the next step (ρ^{g}_{i+1}) (the fact that these loops interact certainly doesn't help either).

The models produced in this work could potentially be applied to situations other than laboratory hydrate plug formation. They may be useful in the modelling of separation processes utilising gas hydrates. The constant volume model could be applied to a batch separation process of a gas mixture. Hydrate could be formed from the mixture from an initial pressurisation in a closed vessel. The system could be cooled after sufficient conversion to low temperature so that the hydrate would be stable following removal of most of the gas phase. The gas phase could then be mostly removed by depressurising the vessel and the hydrate could be dissociated. Similarly the constant pressure syringe pump model could be used if the pressure was maintained constant in such a vessel by a syringe or piston pump (without flow of fresh gas in to the system).

Another potentially useful model would be one derived for an open-system at constant pressure where the gas pressure is regulated in the system by flow from a cylinder or other supply. This model was not generated in this work but could be by using similar assumptions and equations. Using this method with two different gas mixtures it may be possible to prevent changes in the gas phase composition during hydrate formation (see next subsection).

4.5.5 A proposed laboratory method to avoid changes in the gas phase composition during hydrate formation

A possible method to avoid changes in the gas phase composition during laboratory hydrate formation from melting ice particles would be to set up a system with two gas supplies that feed gas to the hydrate while keeping the pressure and temperature constant. At the initial pressurisation, the hydrate formation pressure cell containing the ice particles would be charged with the gas of interest for studies, this may be a gas with a typical pipeline natural gas composition. Once pressurisation is achieved this gas supply would be shut off. Figure 4.10 shows a general experimental setup. The gas of interest is labelled "initial gas supply" and has mole fractions y_1^{i} to y_J^{i} (for components 1 to *J*, where *J* is the total number of components). The second gas supply, labelled "formation gas supply" contains a gas mixture of mole fractions, y_1^{f} to y_J^{f}, that are equal to the hydrate phase mole fractions that would result if the initial gas was contacted with water at a high mole ratio of gas to water (these could be measured experimentally or estimated from CSMGem). During hydrate formation valve 1 would be shut and valve 2 open. The pressure regulator would be set to regulate the flow of gas in to the cell at the final pressure after filling with the initial gas supply. As hydrate formation begins the components that are stripped out of the gas phase should be replaced by gas from the formation gas supply and thus the gas phase composition should remain constant. This should also result in a uniform hydrate composition and a hydrate mass of only one structure independent of the initial gas supply. This method would have to be tested experimentally. It would be important to ensure that the formation gas supply composition was an accurate measure of the hydrate phase composition on a water free basis and good mixing of the gas would probably be required.

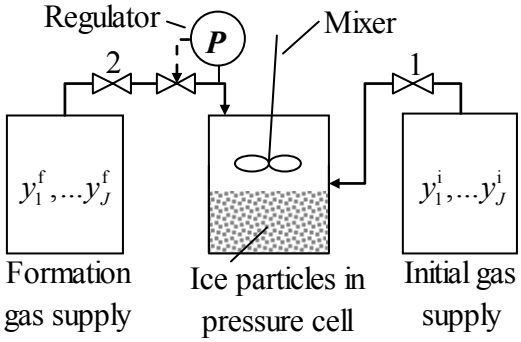

Figure 4.10 – Laboratory experimental set-up for hydrate formation from melting ice particles to avoid gas phase composition changes by the use of two gas supplies.

Chapter 5 TETRAISOPENTYLAMMONIUM FLUORIDE + METHANE SEMI-CLATHRATE HYDRATE PHASE MEASUREMENTS

5.1 Introduction

A general introduction to semi-clathrate hydrates (SCH) is presented in Chapter 1 of this work, including elements of their cage structures and stoichiometry. In brief, some host hydrate water lattice sites in a SCH are replaced by a peralkylonium cation central atom (such as the N atom of tetraisopentylammonium ion) and the anion. Typically SCH of peralkylonium salts with butyl or isopentyl alkyl chains are most stable, some have melting points as high as the mid 30 °Cs. As the water lattice is broken Davidson[11] suggested the term "semi-clathrate hydrate" rather than "clathrate hydrate". Structural studies reveal that these SCH contain vacant cages (see Davidson,[11] Dyadin and Udachin[3] and Jeffrey[4] for general reviews of SCH structures). At the end of the review of SCH in Chapter 1, gas storage in SCH was discussed with particular emphasis on optimising the gas storage capability, determined by the relative numbers of vacant cages per unit mass or volume of the SCH. The temperature stability of the SCH was also considered. An advantageous property for a SCH for gas storage would be if no refrigeration was required to keep the SCH stable and only slight heating or depressurisation was required to release the stored gas. From these consideration tetraisopentylammonium fluoride with the structural hydration number of 38 (TIPAF·38H_2O) appeared to be a good candidate.

This chapter focuses on the stability of TIPAF + water + methane at pressures higher than atmospheric and hence temperatures higher than the atmospheric pressure melting point. The measurements were performed for one concentration or hydration number of TIPAF and water. The TIPAF to water mole ratio was fixed by crystallizing the hydrate with structural hydration number of 38. This hydration number was measured by Karl Fischer titration to be 38.3. The *P*,*T* equilibria measured were semi-clathrate hydrate + aqueous solution + vapour (SCH + Aq + V) points, in the temperature range from about (309 to 320) K.

5.2 Enclathration of gases by semi-clathrate hydrates – literature review

As noted in the introduction the first observation of the ability of a SCH to enclathrate gas molecules was that of McMullan et al.[61] when they noted the release of gas as tetrabutylammonium fluoride crystals melted. They determined that this gas was air, by gas chromatography. Jeffrey[4], Davidson[11] and Shimada et al.[63] made similar observations.

The first specific investigation of the enclathration of gas molecules in a SCH was by Stupin and Stravitnaya.[65,66] They measured the adsorption of sulfur dioxide by the SCHs of tetraisopentylammonium and tetrabutylammonium phthalates as well as tetrabutylammonium bromide and acetate (TBAB and TBAAc). For their study with TBAB and TBAAc the stoichiometry of the SCHs were TBAB·24H2O and TBAAc·31.4H_2O respectively.[5] The sulfur dioxide was absorbed at low pressure (8 to 30) kPa and temperatures between (253 and 277) K, below the melting point of the SCH. The gas was adsorbed in to the SCHs in a pressure cell containing spherical PTFE beads that was mechanically shaken in an isothermal low temperature bath (Stupin and Stravitnaya note that this method was the same as used by Barrer and Edge[152] for the formation gas hydrates from ice and argon, krypton and xenon). The pressure at which adsorption occurred was kept constant by raising the level of mercury in a gas burette to reduce the volume of the system to compensate for the adsorbed gas. The volume of gas adsorbed could be calculated from the volume reduction (mercury level). The pressure was then slightly lowered in the pressure cell which resulted in the slow desorption over (2 to 3) h of gas from the SCH. The pressure was kept constant by lowering the level of mercury in the gas burette until desorption ended. The volume of gas released could then be calculated. The pressure reduction step was repeated several further times. A full set of measurements were then repeated at different bath temperatures. These measurements allowed the calculation of Langmuir isotherm adsorption constants. Interestingly Stupin and Stravitnaya suggest that methane or argon could not be adsorbed in to the TBAB·24H2O SCH "even at 195 K and 80 kPa".[5] More recent literature, outlined in paragraphs below, indicate methane can be enclathrated in at least some structures of TBAB SCH.

From observations that SCH formed from an aqueous solution of TBAB under atmospheric conditions released bubbles of gas, Shimada et al.[63] decided to investigate whether other gas molecules could be enclathrated. Mixtures of methane + ethane, methane + propane and pure

propane were investigated. In a pressure vessel the gas at a pressure of 1.0 MPa was sparged through a 10 % mass fraction solution of TBAB in water while cooling the solution from (20 to 1) °C. Crystals of SCH that formed were removed from the solution and heated in a small vessel, the released gas was then analysed by gas chromatography. Firstly the mixtures of methane + propane and methane + ethane where tested and it was shown that the gas released upon dissociation of the SCH was mainly methane. Experiments were then conducted with pure propane, however no gas bubbles were observed as the SCH dissociated. This lead Shimada et al. to believe that ethane and propane were only present in small amounts for the methane mixture experiments because the crystals that were dissociated where wetted with TBAB solution in which these components were dissolved. The structures of TBAB SCH were then investigated by X-ray crystallography and it was determined that the only vacant cages present were dodecahedral 5^{12} cages. One structure had already been presented in Davidson[11] the other structure found was unknown, this structure was later investigated by X-ray crystallography by Shimada et al.[62] and was found to be TBAB·38H_2O. The lack of vacant cages larger than the 5^{12} cage explained why propane was not enclathrated. Shimada et al. then suggest that TBAB SCH would provide a suitable method of separation of methane from ethane and propane. The separation of gases was further investigated in the paper by Kamata et al.[64] Five binary gas mixtures of methane + ethane, methane + propane, methane + hydrogen sulfide, methane + nitrogen and carbon dioxide + hydrogen sulfide were investigated (all at several different compositions) again using a 10 % mass fraction solution of TBAB. The gases were sparged through a prior evacuated pressure vessel at 1.0 MPa that was cooled from (20 to 0) °C. Samples of SCH were removed and wiped with hygroscopic paper and then placed in a 60 mL pressure vessel at -10 °C that was then evacuated. The pressure vessel was then heated to 25 °C to dissociate the SCH and the gas compositions were measured by gas chromatography. The TBAB SCH formed with the methane + ethane and methane + propane mixtures only enclathrated methane. For the methane + hydrogen sulfide mixtures over 95 % of the hydrogen sulfide was removed at all initial compositions (the hydrogen sulfide composition ranged from a mole fraction of (0.02 to 0.61) % in the initial vapour phase) This was explained by the fact that the solubility of H_2S is two orders of magnitude greater than CH_4 in water. The SCH formed from methane + nitrogen gas contained both components but the methane content of the SCH was between (10 and 30) % higher than the initial gas composition that was varied between a mole fraction of (10 and 80)

%. For the CO_2 + H_2S mixture it was found that the SCH enclathrates about 90 % of the initial vapour phase H_2S and it was concluded that CO_2 could probably not enter the vacant 5^{12} cage of the TBAB SCH as it is too large (note: more measurements with TBAB solutions and "biogas" mixtures methane and carbon dioxide containing less than 1 % mole fraction H_2S were published several years later by Kamata et al.[169] with similar results). Overall it was suggested that the size limits of molecules that can be enclathrated in the 5^{12} cages of the TBAB SCH are the same as the limits for the 5^{12} cages of gas hydrates.

The first measurements on the three phase SCH + aqueous solution + vapour (SCH + Aq + V) *P*,*T* equilibria system were those of Hashimoto et al.[46] for a mole fraction of 3.6 % TBAB in solution + hydrogen. This concentration of TBAB was selected to correspond to a 40 % mass fraction solution, that had been shown to be near the *T*,*x* phase diagram temperature maximum for TBAB + water by Shimada et al.[63] The solution of TBAB was introduced to an evacuated high pressure cell and pressurised with hydrogen. Agitation in the cell was provided using a mixing bar, driven by an exterior permanent magnetic ring. The high pressure cell contained a window from which the three phase condition could be observed visually. The three phase condition was established at constant temperature by adjusting the pressure of hydrogen. The window of the pressure cell also allowed in situ Raman measurements of all three phases present. Raman data from the SCH phase confirmed the occupation of the 5^{12} cages by hydrogen. The *P*,*T* three phase equilibria measurements were made in the temperature range from (285.4 to 287.3) K which resulted in equilibrium pressures between (0.13 and 13.6) MPa. In a recent paper Hashimoto et al.[46] repeated a similar set of measurements at TBAB mole fractions of 0.6 %, 2.0 % and 7.0 %, these measurements as well as those from the original paper are shown in Figure 5.1. From measurements on the *T*,*x* phase equilibrium of TBAB + water at atmospheric conditions it was assumed that the solution at the mole fraction of 0.6 % would form a different structure of SCH to that of the higher concentrations (and the 3.6 % mole fraction solution from the original paper). Raman measurements were again used to confirm that hydrogen had entered the cages of all SCH formed. The *P*,*T* phase measurements revealed similarly shaped three phase curves for each concentration of solution, each curve coincided with their respective points on the *T*,*x* phase equilibrium of TBAB + water at atmospheric pressure. In other words the TBAB solution at a composition near the temperature maximum on the TBAB + water at

atmospheric pressure *T*,*x* phase diagram also formed the most stable SCH containing hydrogen.

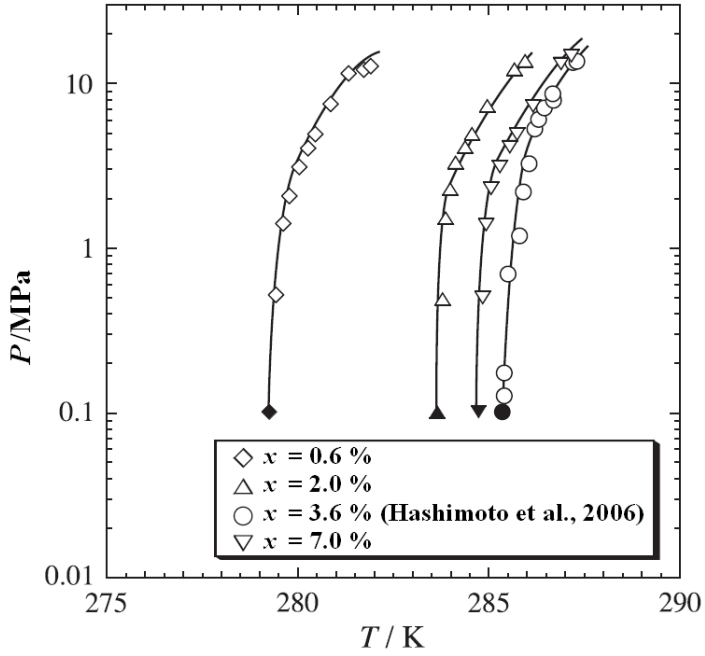

Figure 5.1 – *P*,*T* SCH + Aq + V phase measurements for the system hydrogen + TBAB aqueous solution at mole fraction of TBAB, *x*, in the solution. (Modified from Hashimoto et al.[47]).

Duc et al.[68] measured SCH + Aq + V *P*,*T* phase equilibria for pure carbon dioxide, pure nitrogen and mixtures of carbon dioxide and nitrogen with TBAB at mole fractions in water of 0.29 %, 0.61 %, 3.6 % and 9.4 %. Measurements were made in a high pressure autoclave with a cooling jacket, through which ethanol from a cryostatic temperature controller was circulated. The cell had two sapphire windows and the contents could be agitated with a blade turbine impeller. The autoclave was evacuated before the gas to be tested was introduced. After the gas had been allowed to cool for some time, TBAB solution was pumped in to the cell using an HPLC pump. The cell was maintained at a temperature above the formation pressure of the SCH at atmospheric conditions. The formation of SCH was observed after about four hours by a sudden sharp temperature increase (due to the exothermic crystallization process). Crystallization was assumed complete when the temperature no longer deviated from the coolant temperature, this was about 14 h after crystallization had begun. The cell was then heated at a rate of 1.5 $K \cdot h^{-1}$ and the onset and completion of SCH dissociation were noted as deviations in the heating rate, the SCH + Aq +

V points were noted as the temperature and pressure at the final point of deviation in the temperature versus time plot. During hydrate dissociation the vapour phase composition was measured by gas chromatography and the TBAB concentration in the liquid phase was measured by refractive index and ion exchange chromatography. The results showed that for the SCH formed with pure CO_2 and N_2 for all concentrations of TBAB the equilibria pressure reduction comparative to gas hydrates was lower by a factor of 10 to 50. For the mixtures of CO_2 + N_2 + TBAB solution at the 0.29 % mole fraction the equilibrium pressures were also lower than those of gas hydrates. The hydrate phase also showed evidence of preferentially enclathrating CO_2, the authors state "the CO_2 selectivity in the hydrate phase is at least four times higher than in the gas phase". [68] It was estimated that between (30 and 35) m^3 of gas at STP could be stored per m^3 of SCH. These measurements by Duc et al. suggest contrary to the indications of Kamata et al.[64] that CO_2 can be enclathrated by the SCHs of TBAB.

Tohidi's group at Heriot Watt University in Scotland have recently published extensive SCH + Aq + V *P*,*T* phase equilibria measurements for several aqueous concentrations of TBAB in water for the gases hydrogen, methane, nitrogen, carbon dioxide and a natural gas.[44] Measurements were also published in a slightly earlier paper for TBAB SCH + hydrogen and tetrabutylammonium fluoride (TBAF) SCH + hydrogen.[45] In this earlier paper by Chapoy et al.[45], SCH + Aq + V *P*,*T* phase equilibria measurements were made in the temperature range (280 to 310) K and at pressures up to 25 MPa. Solutions of both salts were prepared at the compositions that showed maximum thermal stability of the SCH at atmospheric conditions. The *P*,*T* measurements were determined by an isochoric step-heating technique described by Tohidi et al.[170] This method is non-visual and involves, as the name suggests, heating the constant volume pressure cell in a series of steps. After each heating step the system is allowed to equilibrate until the pressure remains constant, at this point the *P* and *T* are recorded. If dissociation of any of the hydrate occurs during the temperature step the recorded pressure points rise more rapidly with *T* due to release of gas from the hydrate. The increasing pressure in the vessel due to the dissociation and temperature increases acts to stabilise the remaining hydrate, however when all the hydrate is dissociated the *P* will no longer increase as steeply with the *T*. If several *P*,*T* points are recorded before and after complete dissociation the SCH + Aq + V *P*,*T* three phase point can be determined by the intercept of a line through the pre-dissociation data points and post-dissociation data points.

This can be visualised in a plot modified from Tohidi et al,[170] shown in Figure 5.2, where a dissociation point is found from the intercept of pre-dissociation *P,T* data point line and post-dissociation *P*,*T* data point line. The measurements of Chapoy et al.[45] show that the SCH + Aq + V three phase lines for both systems extend from their respective melting points under atmospheric conditions, their measurements are plotted in Figure 5.3, with data for sII H_2 hydrate from Mao et al.[171] and sII THF + H_2 hydrate from Florusse et al.[31] Chapoy et al. note that their quaternary ammonium salt SCH equilibria data with H_2 "demonstrate greatly increased thermal and low-pressure stability when compared with H_2 and H_2-THF clathrate hydrates".[45] They also noted that the hydrogen released from their SCHs was very pure containing only trace amounts of water from a chromatographic analysis, which they implied was not the case for H_2-THF clathrate hydrates. The more recent paper by Arjmandi et al.[44] includes SCH + Aq + V *P*,*T* phase equilibria measurements for H_2 + *w* = (0.1 and 0.4), CH_4 + *w* = (0.05, 0.1, 0.2 and 0.3), N_2 + *w* = 0.1, CO_2 + *w* = (0.10 and 0.427) and natural gas (of mole fractions 87.32 % methane + 5.67 % ethane + 1.68 % propane + 0.23 % 2-methylpropane + 0.4 % *n*-butane + 0.1 % 2-methylbutane + 3.24 % nitrogen + 1.36 % carbon dioxide) + *w* = (0.05, 0.1 and 0.43), where *w* is the mass fraction of TBAB in the aqueous solution. The measurements were completed in a pressure vessel with jacketed cooling, and a stirrer with a magnetic motor. Solutions of TBAB were introduced to the pre-evacuated vessel, followed by the gas. The gas pressure was increased after each measurement up to the highest pressure measurement. Several TBAB + water, SCH + Aq *P*,*T* phase equilibria measurements were also made in this study, in this case the cell was evacuated and then filled entirely with solution that was pressurised in to the cell using an HPLC pump. The SCH was formed by cooling the cell rapidly until a sharp pressure reduction confirmed their formation. To measure the dissociation point the temperature was "raised in steps of (3 to 5) K, with sufficient time being given following each temperature step for the system to reach equilibrium (stable pressure), until the point of complete hydrate dissociation was surpassed".[44] The dissociation point was then determined from a plot similar to that shown in Figure 5.2.

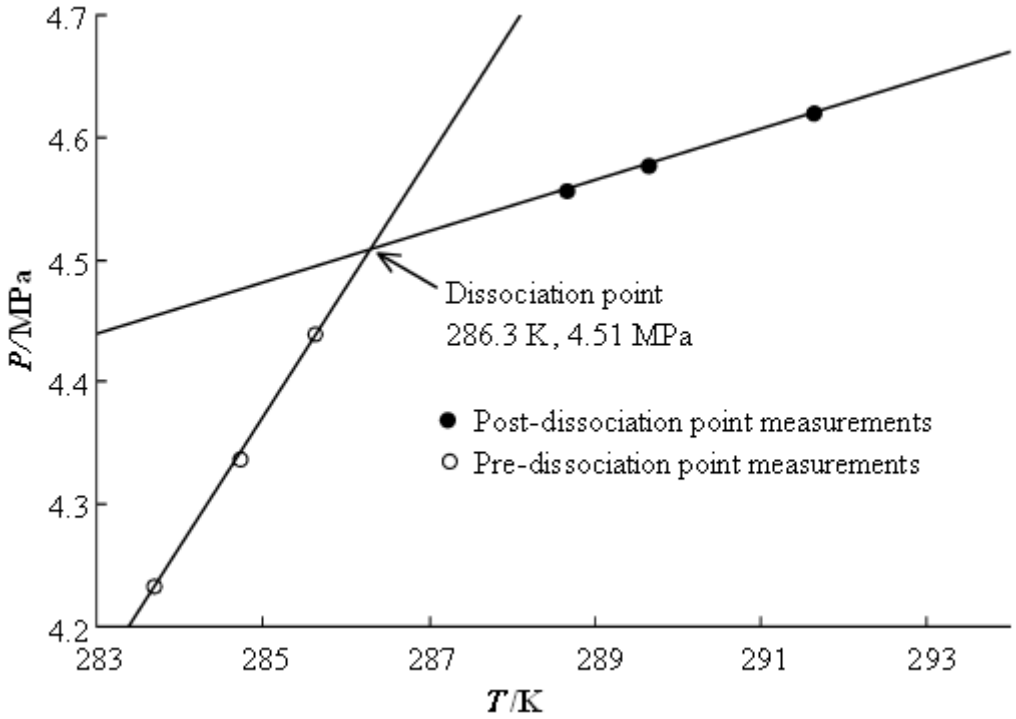

Figure 5.2 – Dissociation point determination from pre-dissociation point *P*,*T* measurements and post-dissociation point *P*,*T* measurements. (Modified from Tohidi et al.[170]).

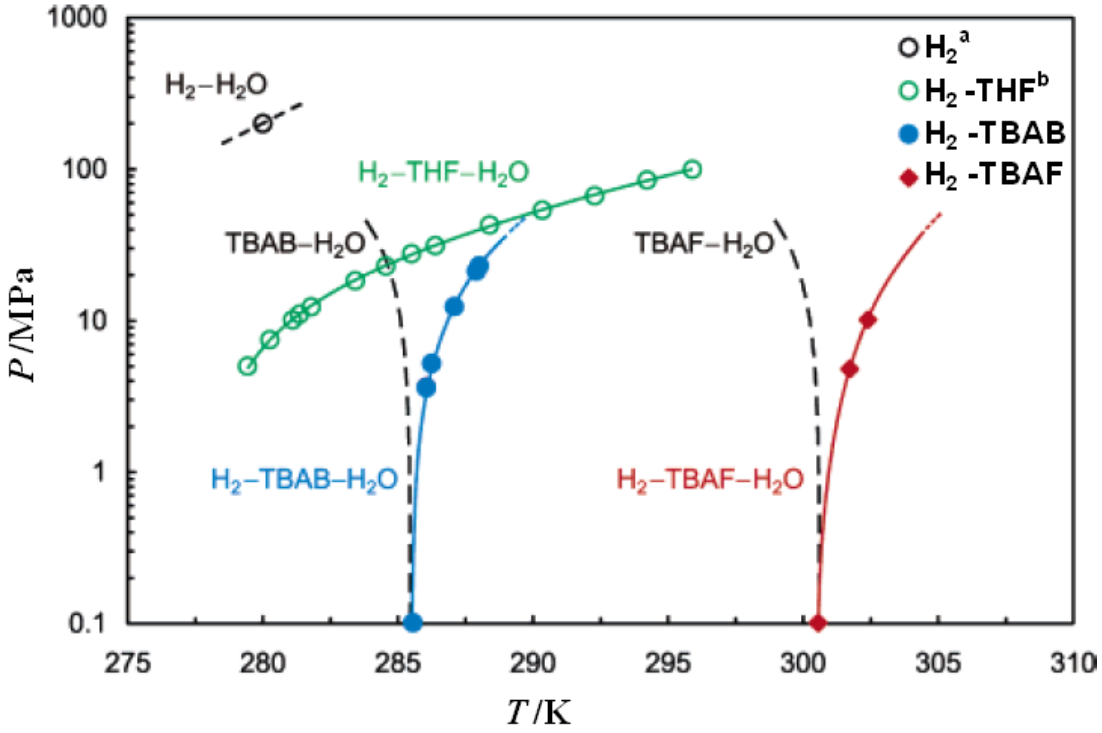

Figure 5.3 – Measurements of dissociation conditions of H_2+ TBAB SCH and H_2 + TBAF SCH, also plotted are data for pure H_2 sII hydrate and H_2 + THF sII hydrate. [a] H_2 sII hydrate data from Mao et al.[171] [b] H_2 + THF sII hydrate data from Florusse et al.[31] (Modified from Chapoy et al.[45]).

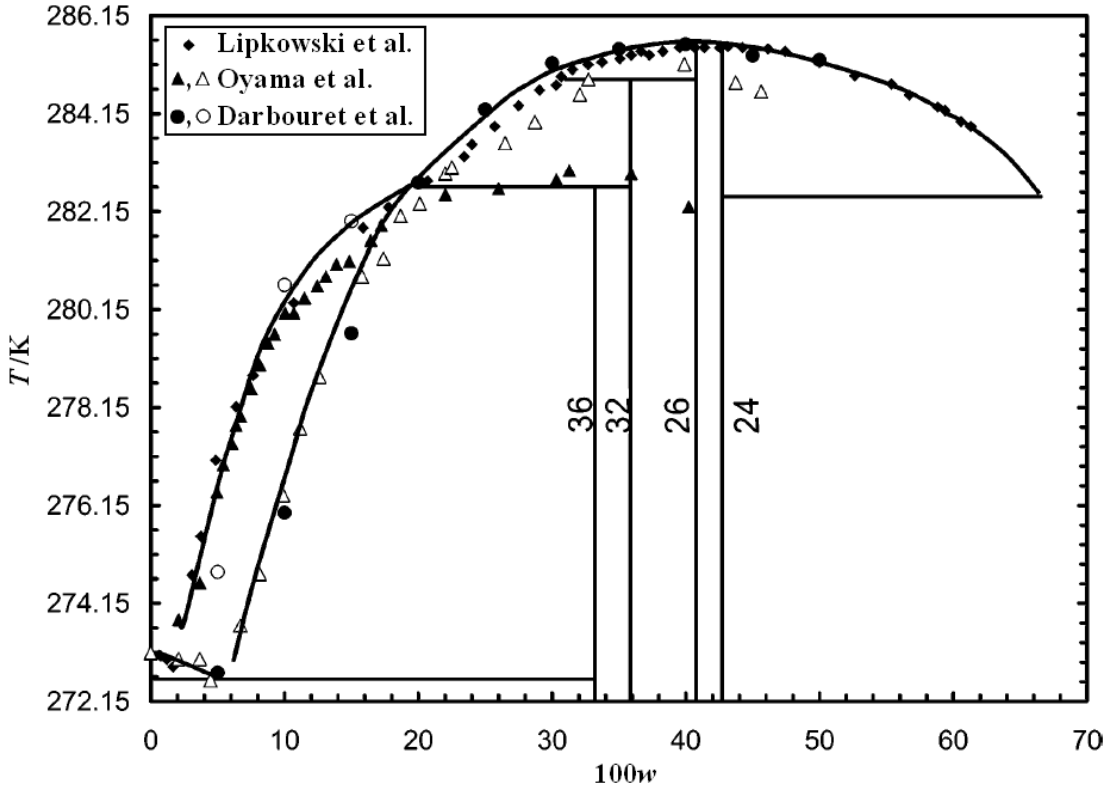

Figure 5.4 – *T*, *w* phase diagram for TBAB + water under atmospheric conditions, numbers along the vertical lines refer to hydration numbers. (Modified from Arjmandi et al.[44] data from Lipkowski et al.[172], Oyama et al.[69] Darbouret et al.[173]).

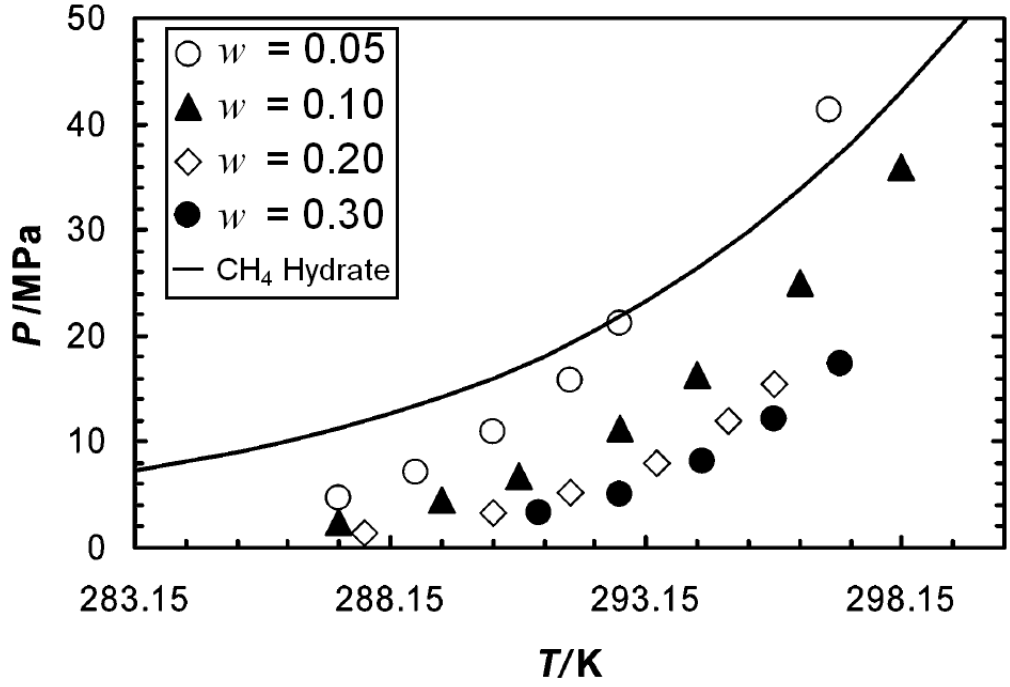

Figure 5.5 – Methane + TBAB + water phase boundaries, *w* = mass fraction of TBAB in solution. (Modified from Arjmandi et al.[44], note: methane hydrate line was calculated by Arjmandi et al. using the Heriot Watt Hydrate (HWHYD) model.[174,175]).

Figure 5.4 and Figure 5.5 from Arjmandi et al.[44] show a *T*,*w* phase diagram for TBAB + water and *P*,*T* phase diagram for SCH + Aq + V equilibria for TBAB + water + methane respectively. It is clear that the more stable the SCH is under atmospheric conditions the more stable the SCH is at higher pressures in the presence of methane. It is also clear that for most of the concentrations of TBAB in water the methane SCH is more stable than methane hydrate. At the lowest mass fraction of TBAB ($w = 0.05$) however at a temperature of greater than 292.15 K the methane SCH becomes less stable than methane hydrate, it is perhaps important to note that this mass fraction of TBAB is the most different from the mass fraction of TBAB associated with the SCH hydration numbers listed along the vertical lines in Figure 5.4.

5.3 Gas storage and semi-clathrate hydrates

5.3.1 Literature review

Strobel et al.[176] measured the hydrogen storage properties of several different clathrate hydrate materials including the SCHs of TBAB. Solutions of TBAB were prepared with a mole fraction between (1.0 and 5.9) % to account for the different structures of SCH that form in this system (see Figure 5.4). The SCH was formed by placing prepared solutions in a refrigerator for about 3 days. The SCH was then crushed to a powder under liquid nitrogen with a mortar and pestle to a particle size of 250 μm or less. About 5 g of the powdered SCH was weighed in to a 20 cm^3 pressure vessel and the vessel was sealed and placed in a 279.5 K temperature controlled bath. The cell was thrice purged with hydrogen and was then pressurized to 13.8 MPa. The cell was then left to equilibrate for 24 h. After this time the cell was quenched in liquid nitrogen and once the internal temperature had dropped below 130 K the cell was depressurised to atmospheric pressure. The cell was then placed in another temperature controlled bath that was just above the melting point of the TBAB SCH and a Ruska (model 2331) gasometer was attached to measure the volume flow of hydrogen from the dissociating SCH. Calibrations runs were used to account for the effects of the expansion of cold hydrogen and the internal cell volume. When gas evolution had ended the cell was weighed then dried. From the dry cell mass the final mass of solution was found to ensure it agreed with the initial mass of SCH loaded. The amount of hydrogen stored in the SCH was calculated from the corrected volume evolved and the final mass of solution after dissociation.

The results of the measurements are shown in Figure 5.6, where the bulk mass fraction of hydrogen stored ("not corrected for stoichiometry or contributions from multiple semi-clathrate phases present") is plotted as a function of the mole fraction of TBAB in the solution used to prepare the SCH. Strobel et al. noted the maximum hydrogen storage mass fraction of 0.241 % was at the mole fraction of TBAB in the solution of 2.71 %, which corresponds closely to the stoichiometry of the most recently discovered SCH of TBAB·38H_2O (by Shimada et al.[62]), in which the mole fraction of TBAB is 2.56 %. (note: the hydration number of this SCH is not shown on Figure 5.4).

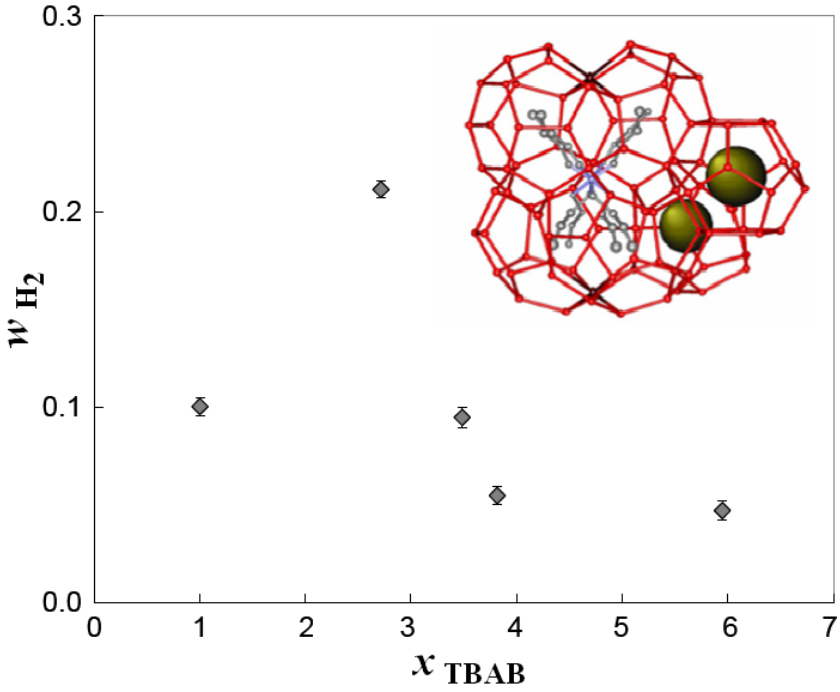

Figure 5.6 – Bulk mass fraction of hydrogen, w_{H_2}, stored as a function of the TBAB mole fraction, x_{TBAB}, in the solution used to prepare the SCH. (Modified from Strobel et al.[176]).

The work of Strobel et al.[176] suggests that the mass fraction of hydrogen stored in the SCH of TBAB was only as high as 0.214 %, just over a third of the calculated value assuming full occupation (by one hydrogen molecule) of 0.597 % in the TBAB·38H_2O structure. It is interesting to note however that McMullan et al.[61], Jeffrey[4], Davidson[11] and Shimada et al. [63] observed that air was enclathrated in their SCHs that they studied at atmospheric pressure. In the experiments of Strobel et al.[176] there were no apparent steps, such as evacuation, that would lead to the removal molecules of air (N_2, O_2, and Ar) from the SCH, this may have lead to an underestimation of the amount of hydrogen that could be stored in the TBAB SCH.

Also it is uncertain whether different results might have been obtained had the cell been depressurised to the atmosphere pressure at a temperature close (within (1 to 2) K) of the melting point of the SCH rather than at 130 K.

Recently Ahmadloo et al.[177] from Tohidi's group at Heriot Watt University presented measurements of the hydrate phase stability, hydrate gas composition and uptake of a natural gas in a TBAB SCH. The natural gas composition is listed below in Table 5.1. The apparatus used for measurements was the same as used by Arjmandi et al.[44] had used, consisting of a stirred 500 ml pressure cell with a jacket for temperature control. Phase stability measurements were made by the same method as Arjmandi et al. and are not considered further here (see Ahmadloo et al.[177] for details). Enclathrated gas compositions were measured for TBAB aqueous mass fractions of 0 to 0.43. The relative volumes or masses of solution and the gas used in these experiments were not listed. TBAB solution and the gas were introduced into the cell that had been previously evacuated. During filling the temperature and pressure was outside hydrate forming conditions. Following a period of equilibration of the gas and aqueous phase the cell was cooled to 4 °C to initiate hydrate formation. Hydrate formation was monitored by pressure drop and when the system had reached equilibrium samples of the vapour phase were taken. The vapour was then pumped out and the cell was heated to 30 °C to dissociate all the hydrate. Samples of the dissociated gas were taken and the composition of the vapour and hydrate gas were analysed by gas chromatography. The methane mole fraction in the gas released from the clathrate increased from 74.5 % to 96.75 % as the TBAB mass fraction was increased from 0 to 0.35. From a TBAB aqueous mass fraction of 0.35 to 0.43 the methane mole fraction was almost constant. The concentrations of the heavier hydrocarbons in the hydrate phase in contrast to methane decreased with increasing TBAB aqueous mass fraction. The carbon dioxide concentration increased in the hydrate phase with increasing TBAB mass fraction up to 0.33, but decreased sharply at higher TBAB mass fractions. These changes where explained by assumed changes in the structure and hence cages types and numbers with changing TBAB mass fraction (refer to Figure 5.4 presented as Figure 1 of Ahmadloo et al.[177]).

Table 5.1 – Mole fractions of the components in the natural gas used by Ahmadloo et al.[177]

Component	*x*
CH_4	0.898
C_2H_6	0.0651
C_3H_8	0.0181
i-C_4H_{10}	0.002
n-C_4H_{10}	0.0033
i-C_5H_{12}	0.0007
n-C_5H_{12}	0.0006
CO_2	0.0122

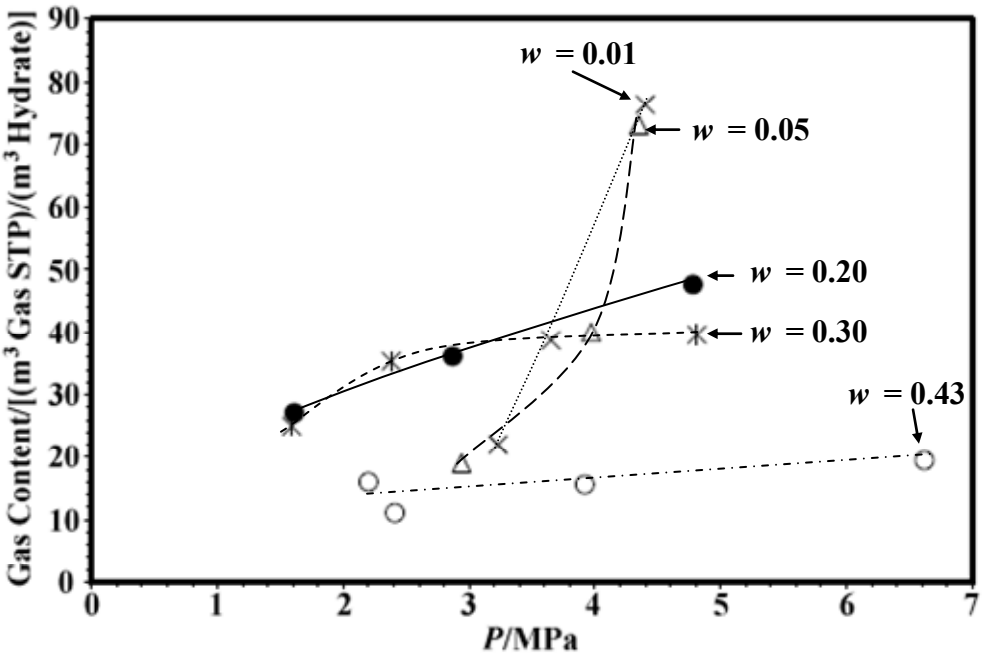

Figure 5.7 - Volume fraction of natural gas in SCH of TBAB. (Modified from Ahmadloo et al.[177]). (*w* = mass fraction of salt in aqueous solution)

The gas uptake in the hydrate phase as a volume of gas (assumed to be at STP) per volume of hydrate was calculated by pressure drop in the cell. Gas uptakes were presented for TBAB aqueous mass fractions of 0.01, 0.05, 0.2, 0.3 and 0.43 and are shown in Figure 5.7. The gas uptake varied between (11 and 76.3) m^3 of gas at STP per cubic metre of hydrate. The gas uptake is both a function of pressure and the concentration of the TBAB solution. Ahmadloo et al.[177] note that "as expected , gas consumed by hydrate formation increases with pressure. But, TBAB concentration has an inverse effect, and causes a reduction in the gas uptake in the hydrate. This is attributed to increased occupancy of the hydrate cages by TBAB molecules,

resulting in a reduction in empty cavities for capturing the gas molecules." This author suspects that the different shaped curves for the TBAB aqueous mass fraction of 0.01 and 0.05 may be a result of the formation of regular sI or sII hydrates in addition to any SCH.

5.3.2 Economics of gas storage in hydrates

The current method of transporting natural gas long distances involves liquefaction and shipping as a cryogenic liquid by LNG (liquefied natural gas) tanker. Gudmundsson and coworkers[41,178-183] have published economic comparisons on the use of natural gas hydrates (NGHs) as a storage and transportation medium for stranded natural gas reserves. Stranded natural gases are those that are too distant from markets to be transported by pipeline economically or too small to justify the costs of LNG plant. The economic feasibility of LNG technology is not considered viable for less than 4×10^9 m^3 STP per year of gas.[183] Following the discovery of hydrate self-preservation by Yakushev and Istomin,[184] Gudmundsson et al.[185] demonstrated that natural gas hydrates could remain practically stable at atmospheric pressure when refrigerated to -15 °C. Two types of hydrate technology have been studied; dry hydrate and slurry hydrate. The use of dry hydrate was proposed for long distance transportation[186] whereas the use of slurry hydrate was proposed for the capturing of associated gas (gas found within oil-wells) on floating production, storage and offloading (FPSO) vessels.[187] Børrehaug and Gudmundsson[186] compared the costs of 4×10^9 m^3 STP per year of gas NGH and LNG chains, including the capital cost of production, regasification plants and transport costs by ship. The cost was plotted as a function of the transport distance, this plot is reproduced in Figure 5.8. The cost to transport the gas via a pipeline and conversion and transportation of the gas as synthetic petroleum ("syncrude") were also compared. For distances greater than about 1000 km and 1800 km the capital cost of a pipeline was greater than the NGH and LNG chains respectively. At distances of over 6000 km the synthetic petroleum option was cheaper than the LNG option.

In situations where associated gas is available without a pipeline on a FSPO an investigation was made into the use of hydrate slurries made from hydrate particles in refrigerated crude oil.[187] The capital cost and operational and maintenance cost of such a process was estimated by Hove et al.[188] based on 580×10^6 m^3 STP per year of gas. The transport cost of the slurry based technology was based on a 20 year project life and 9 % per annum interest rate on capital. The operating cost was assumed 4 % of the capital cost and the fuel consumption in

transport was assumed to be 7 % of the natural gas converted to hydrate. The cost per GJ of gas is shown in Figure 5.9 reproduced from Gudmundsson et al.[183]

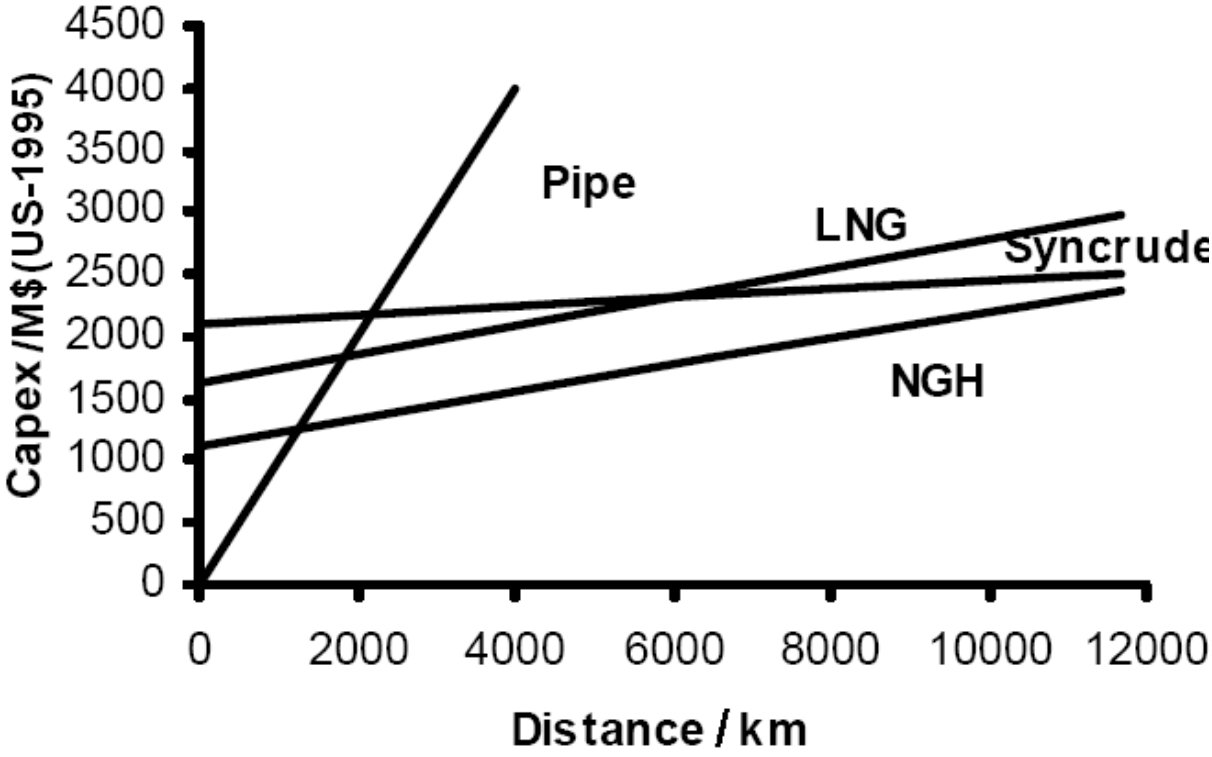

Figure 5.8 - Approximated capital cost of 4×10^9 m^3 STP per year of natural gas with distance transported. NGH = Natural gas hydrate. (Modified from Gudmundsson et al.[183])

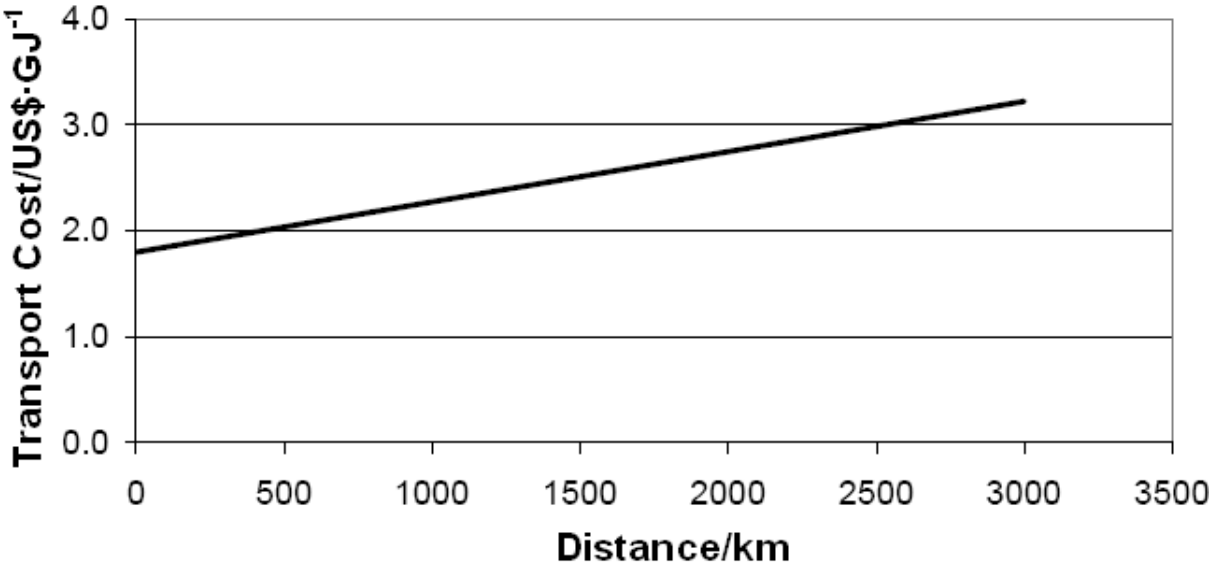

Figure 5.9 – Floating production, storage and offloading (FPSO) associated gas NGH slurry transport cost as a function of distance. (Modified from Gudmundsson et al.[183])

Gudmundsson et al.[183] also produced a figure to illustrate under what conditions of capacity and transport distance various gas transport technologies are likely to economically competitive. This figure is reproduced as Figure 5.10. Technologies compared include pipelines, LNG, compressed natural gas (CNG), gas to wire (GTW, using the gas to generate electricity and transporting energy electrically), and gas to liquids (GTL, the production of synthetic liquid fuels). The figure indicates that pipelines are most economical for transporting relatively large volumes of gas shorter distances (less than 1000 km). LNG technology is shown to be best for high capacity long distance transport. For lower capacities and short to moderate distances CNG, GTW and NGH technologies are competitive whereas for longer distances GTL was shown to be the better option. The area encompassed by the dashed box is a region where all of the technologies may be competitive.

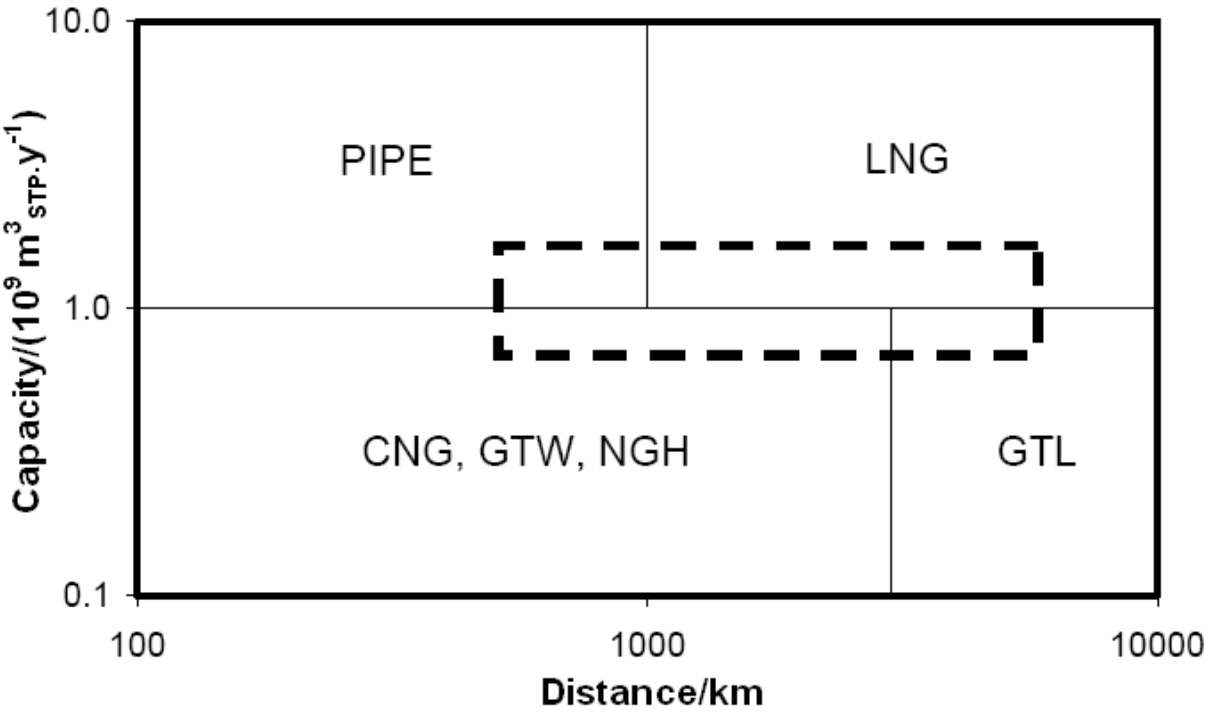

Figure 5.10 - Capacity-distance diagram for natural gas transport. (Modified from Gudmundsson et al.[183]). LNG = liquified natural gas, CNG = compressed natural gas, GTW = gas to wire, NGH = natural gas hydrate, GTL = gas to liquids.

The results of the studies by Gudmundsson et al. suggest that NGH transport may be an economically viable transportation method for relatively lower volumes of gas and short to moderate transportation distances. It is possible that gas storage in SCH may be economic

under these same constraints. Table 5.2 lists the methane mass fractions, methane storage densities as well as dissociation temperature for several hydrates.

Table 5.2 - Estimated methane mass fraction, mass density and dissociation temperature of several hydrates and LNG

Hydrate	w_{CH4}	ρ_{CH4} kg·m^{-3}	T_{dis} K
$CH_4 \cdot 5.75H_2O$[a]	13.4%	125	197.6
$CH_4 \cdot ½THF \cdot 8½H_2O$[b]	7.8%	82	277.3
$CH_4 \cdot 0.33TIPAF \cdot 12.7H_2O$[c]	4.6%	49	305.6
$CH_4 \cdot 0.29(C_4H_9)_3PO \cdot 9.9H_2O$[d]	6.3%	65	280.3
Self-preserved $CH_4 \cdot 6H_2O$[e]	6.5%	60	267
Liquid methane $CH_{4(l)}$[f]	100%	422	111.7

a. Density and dissociation temperature calculated from CSMGem.
b. Density estimated from the density of pure THF hydrate[189] with full occupation of small cages by methane molecules (lattice expansion neglected). Dissociation temperature from Handa et al.[144]
c. Density estimated from the density of pure TIPAF hydrate[5] with full occupation of 5^{12} cages by methane molecules (lattice expansion neglected). Dissociation temperature from Feil and Jeffrey.[5]
d. Density estimated from the density of pure tributylphosphine oxide hydrate[58] with full occupation of 5^{12} cages by methane molecules (lattice expansion neglected). Dissociation temperature from Dyadin and Udachin[3] (Figure 18b of their work).
e. Assumed methane hydrate composition and anomalous self-preservation temperature from Stern et al.[190] Mass fraction of methane estimated assuming 50 % dissociation given a 1 month transport time (refer Figure 1 of [190])
f. Liquefied methane density and boiling point (listed under T_{dis}) from NIST Refprop.[168]

If the self-preserved methane hydrate is estimated to have a methane storage capacity of 50 % after 1 month at 267 K (from Stern et al.[190]), then a THF + methane hydrate has a higher storage density and a tributylphosphine oxide SCH has a similar methane storage density assuming full occupancy of the empty 5^{12} cages in their structures. The methane storage density in the TIPAF + methane hydrate is slightly lower at 49 kg·m^{-3} versus 60 kg·m^{-3} for the self-preserved hydrate. As the THF + methane hydrate, tributylphosphine oxide + methane hydrate and the TIPAF + methane hydrate all dissociate at higher temperature they would require less or no refrigeration when being transported. This would need to be considered when making an economic analysis and comparison to NGH gas storage technology. The

more boil off or dissociation of gas from the hydrate the more recompression and cooling is needed. The chemical cost of the salt or promoter (THF) would need to be considered. For the THF + methane hydrate some THF might be lost to the gas phase during dissociation. For the SCH forming salts there should be no or negligible vaporisation of the salt. The salt chemical cost could thus be considered a capital cost. The THF cost would be both an initial capital cost and an operating cost for the fraction lost to vapour phase.

5.4 Experimental

Pressure-temperature measurements of SCH + Aq + V phase equilibria of the tetraisopentylammonium fluoride (TIPAF) + water + methane system were the primary focus of the experimental work. The salt TIPAF was selected as the SCH TIPAF·38H_2O has both a relatively high melting point (Feil and Jeffrey[5] give a melting point of 31.2 °C and Lipkowski et al.[67] give a value of 32.4 °C) as well as a high fraction of unoccupied cages comparable to other SCH (3 unoccupied cages per molecule of salt, see Chapter 1 section 1.6.2). TIPAF however was not available commercially and so was prepared from triisopentylamine, isopentyl bromide and silver fluoride, this preparation is described in the materials section below. The concentration of TIPAF was fixed for the phase equilibria measurements by the crystallisation of the SCH from an aqueous solution of the salt. The hydration number of the crystallised SCH was determined experimentally by Karl Fischer titration for the water content.

5.4.1 Materials

Methane was sourced from Linde Gas, U.K Ltd, with a purity of 99.975%, this was used without further purification.

Tetraisopentylammonium fluoride was prepared from triisopentylamine, isopentyl bromide and silver fluoride. The purities and sources of the chemicals used in the preparation and purification steps are listed in Table 5.3. The first step was the preparation of tetraisopentylammonium bromide (TIPAB). Lipkowski et al.[67] prepared TIPAB by refluxing triisopentylamine and isopentyl bromide in acetonitrile by the Menshutkin reaction, eq (5.1). The same method was used in this work, approximately 78.2 g (0.344 mol) of triisopentylamine, 86.4 g (0.572 mol) of isopentyl bromide and 97.6 g (2.38 mol) of

acetonitrile were weighed into a 1 L round bottom reaction flask. The mixture was refluxed under a nitrogen purge in the apparatus shown in Figure 5.11 for about 28 h. The brown liquid in the reaction flask at the completion of refluxing was poured into a vacuum flask and heated under vacuum to evaporate the solvent and remaining volatile components, this left crystals with a dark brown contaminant. Approximately equal volumes of benzene and deionized water were added to a fraction of the crystal/contaminant mixture. The contaminant appeared to partition to the benzene phase which was orange in colour however a microemulsion of benzene, TIPAB and water was the other stable phase. This was not expected, however after a literature search it was discovered that microemulsions had been observed in the TBAB + benzene + water system by Ohtani et al.[191] It was decided that a microemulsion phase would only complicate the separation so ethyl acetate was used to purify the remainder of the contaminated crystals (Aladko et al.[192] had used ethyl acetate to purify diisopentyldibutylammonium bromide). Pure ethyl acetate was added to the crystals in a conical flask, the flask was gently heated on an element until all the crystals dissolved in to the solution. The crystals were recrystallized overnight in a refrigerator at about 2 °C. The crystals were vacuum filtered and recrystallized a further two times from fresh ethyl acetate. The crystalline mass was then dried over several days in a vacuum oven (Towson and Mercer Ltd. 2 kW) at 40 °C until a constant mass was achieved. Further purification was performed on the TIPAB by thrice recrystallizing the semi-clathrate hydrate in deionized water, followed by drying in the vacuum oven at 40 °C until constant mass was achieved. The salt was then redissolved in deionized water in a vacuum flask and degassed under vacuum for a period of 30 min. Silver fluoride solution was freshly prepared in a clean brown chemical bottle from stoichiometric masses of barium fluoride and silver sulfate and degassed deionized water (vacuumed for 30 min). Water in slight excess of that required to fully dissolve the silver fluoride was used (note: the solubility of silver fluoride at 16 °C is 14 $mol \cdot L^{-1}$ [193]). The silver fluoride solution was then vacuum filtered of the precipitates of barium sulfate and silver bromide in a dark room and added to the solution of tetrabutylammonium bromide. This in turn was vacuum filtered to remove the precipitate of silver bromide. As a slight excess of silver fluoride was used to ensure all the bromide precipitated TIBAF SCH were recrystallized over several days in a refrigerator at 2 °C and were vacuum filtered. The salt was then redissolved in deionized water and again recrystallized over several days in a refrigerator. This salt could not be vacuumed dried as Sharma and Fry[194] showed that

tetraalkylammonium fluorides are unstable unless in the presence of at least three waters of hydration.

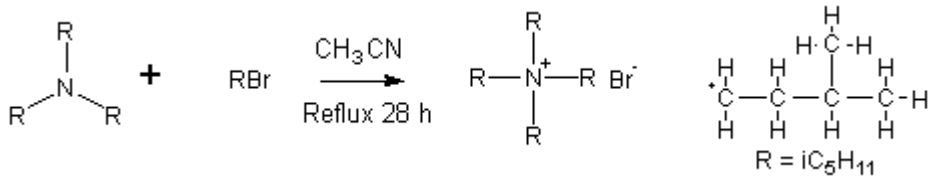

(5.1)

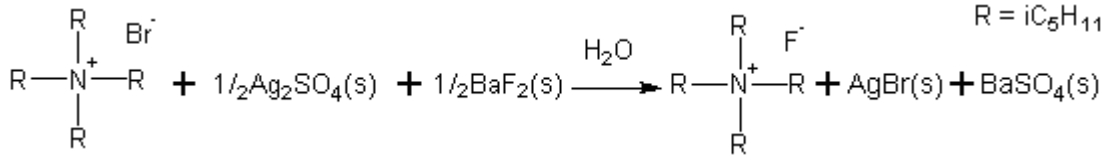

(5.2)

Table 5.3 – Chemical purities for preparation and purification of TIPAF.

Chemical	Supplier	Purity
Triisopentylamine	Fluka, technical grade	≥90 %
Isopentyl bromide	Aldrich	96 %
Acetonitrile	JT Baker, ACS reagent	99.5 %
Silver sulfate	Merck, Analysis grade ACS	98.5 %
Barium fluoride	Sigma Aldrich, <5 microns	98 %
Benzene	BDH, HPLC grade	99.8 %
Ethyl acetate	BDH, HPLC grade	99.8 %
Nitrogen	BOC gases, oxygen free	-

Samples of the TIPAF SCH were analysed by proton NMR in tetra-deuterated methanol (Cambridge isotope laboratories, 99.8%) to investigate the purity of the SCH. A sample of 11.8 mg of the TIPAF SCH was added to 267.5 mg of deuterated methanol (CD_3OD) in a 3 mm NMR tube. The spectrum was recorded on the University of Canterbury Chemistry departments' Varian VNMR 500 MHz spectrometer at an ambient temperature of 23 °C, and is shown in Figure 5.12. The chemical shifts of the TIPAF peaks are listed in Table 5.4, they are similar to those published by Harmon et al.[104] presented in Chapter 2 for tetraisopentylammonium iodide in D_2O (see Table 2.2). They are also similar to the comparable peaks for the tetrahexylammonium ion (see Figure 2.22), the chemical shift of the methylene hydrogens labelled 1 on both ions resonate within 0.07 ppm and the number 2 methylene hydrogens resonate within 0.02 ppm. If triisopentylamine was a contaminant in TIPAF the only distinguishable peak would be that on the first methylene group off the

nitrogen because all remaining alkyl chain hydrogen resonances are effectively the same as those of the alkyl chain of TIPAF (this concept can be visualised by comparing the spectra in Figure 2.22 and Figure 2.23). The data listed in Table 2.1 suggests that an amine resonance from the methylene group adjacent to the nitrogen atom (R_3-N^+-CH_2-R) would resonate at a chemical shift of (2.2 to 2.6) ppm, as no such shift is observed in the spectrum of Figure 5.12 it is assumed to be free of amine and pure.

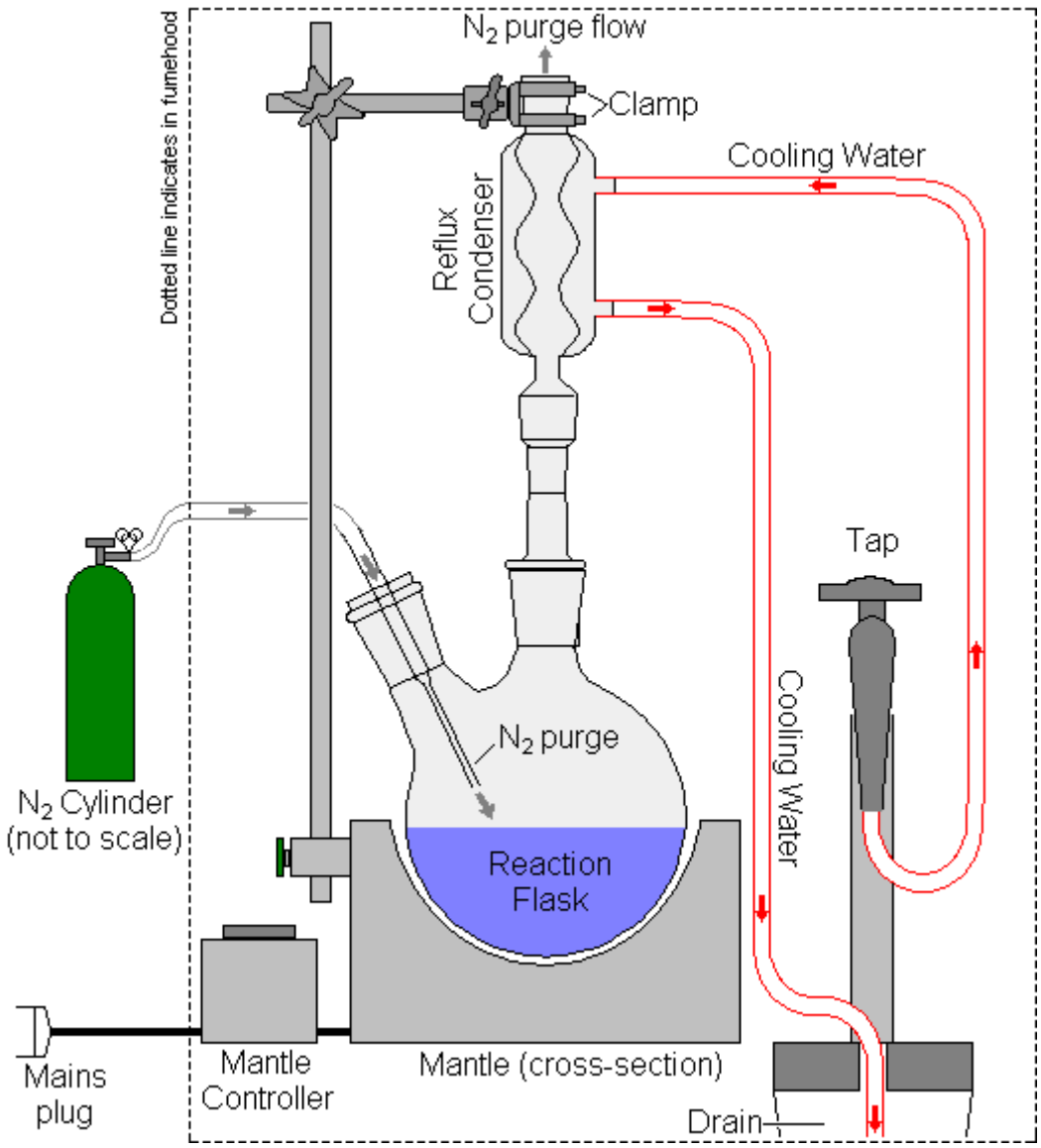

Figure 5.11 – Reflux apparatus for the preparation of tetraisopentylammonium bromide.

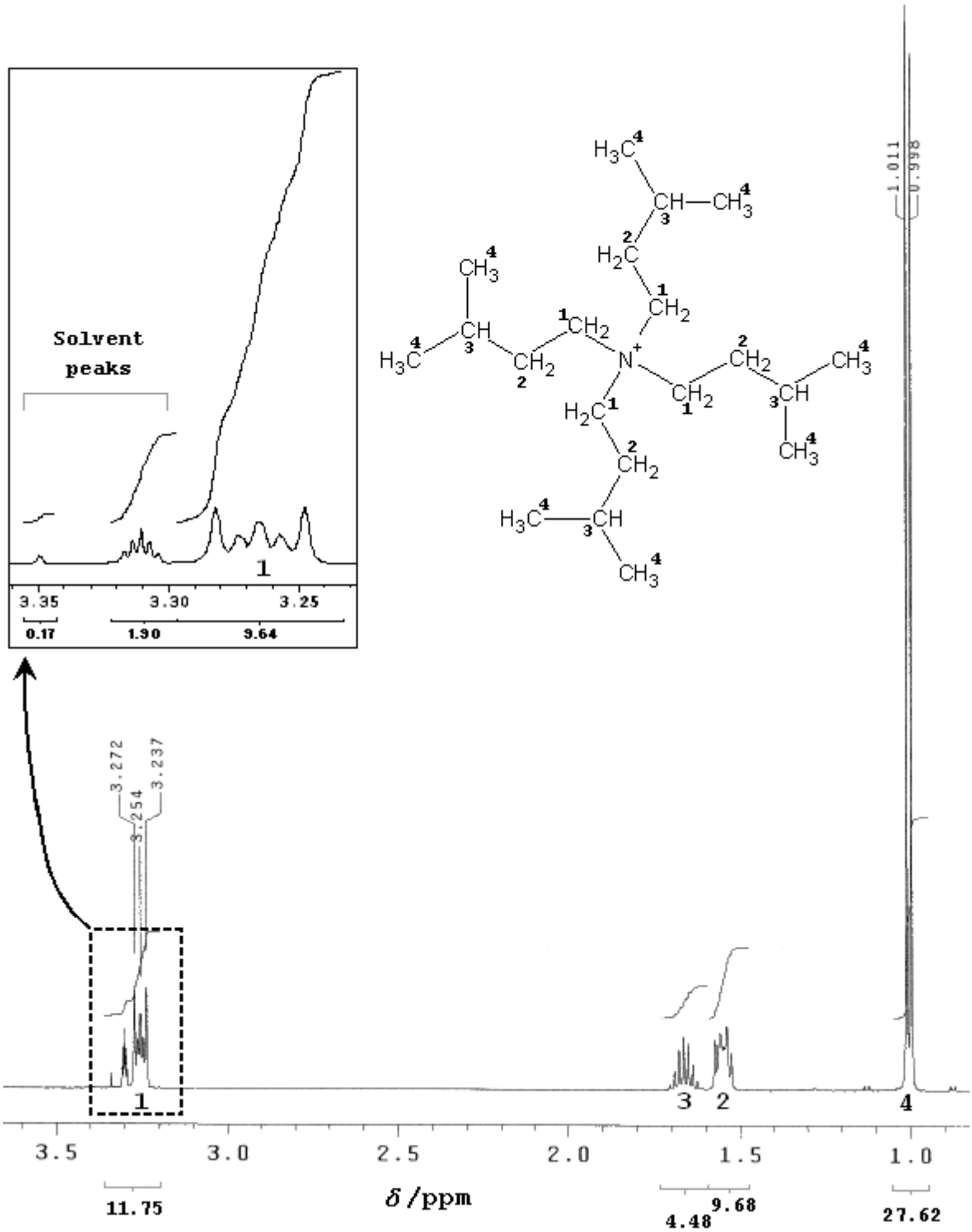

Figure 5.12 – Proton NMR spectrum of TIPAF in CD_3OD; TIPAF hydrogen peaks are labelled 1, 2, 3 or 4 with respect to the hydrogen of the molecule drawn, numerical values below the axis indicate relative peak areas, inset shows one sample peak and two peaks that were also present in a solvent only spectrum. Note: methanol and water peaks at higher chemical shift are not shown.

Table 5.4 – Proton NMR chemical shifts and calculated hydrogen atoms for each shift/peak

Resonating hydrogen (in bold)	Label in Figure 5.12	Chemical shift δ/ppm	Hydrogens from peak area*	Actual hydrogens
$N^+[C\mathbf{H_2}CH_2CH(CH_3)_2]_4$	1	3.25	8.2	8
$N^+[CH_2C\mathbf{H_2}CH(CH_3)_2]_4$	2	1.55	8.3	8
$N^+[CH_2CH_2C\mathbf{H}(CH_3)_2]_4$	3	1.67	3.8	4
$N^+[CH_2CH_2CH(C\mathbf{H_3})_2]_4$	4	1.00	23.6	24

* Calculated from fraction of total area for TIPAF peaks multiplied by 44 (the number of hydrogen atoms in a TIPAF molecule)

5.4.2 Preparation of tetraisopentylammonium fluoride + water at fixed concentration

The mole fraction of TIPAF in water for the *P*,*T* phase equilibria experiments was fixed by crystallizing a SCH of known hydration number. The TIPAF SCH with hydration number of 38 was desired as it has the highest melting point and the literature suggests that the SCH with the highest melting point forms the most stable SCH with gases. A dilute solution of TIPAF in water was prepared from crystals of TIPAF SCH by dissolving them in warm deionised water. A sample of this solution was analysed by Karl Fischer titration for water content using an automatic volumetric Karl Fischer (KF) titrator (Radiometer Analytical TIM550 Titralab). Methanol (BDH HPLC grade 99.8 %) was weighed on a balance (Mettler AE200, ± 0.0005 g half resolution) in to a septum bottle that had been prior flushed with dry nitrogen and the rubber bung cap was immediately placed on the bottle. A 1 mL syringe was tared on the balance and was then used to remove a methanol sample of between (0.2 and 0.4) mL from the septum bottle, this sample was then weighed on the balance. The sample was then injected in to the KF titrator and the start button was pressed to begin the titration. Before the titration began the KF titrator had been allowed to stabilize for several hours and was calibrated using a standard solution of mass fraction 1 % water (Merck Apura water standard 1 % for volumetric KF titration). The mass of methanol injected was entered at the prompting of the KF titrator's controller and the titrator calculated from the volume of titrant (Merck Combitrant 5) required the mass fraction of water in the sample. This analysis was repeated 10 times and an averaged value of the methanol water content was calculated as a mass fraction of (0.157 ± 0.006) % (where the uncertainty was calculated by a student-t 95 % confidence interval). The bottle of methanol was then reweighed and TIPAF solution was

injected by syringe in to the bottle on the balance, so that the mass of solution added was known. The bottle was shaken to mix the injected solution. Ten different samples of known mass (between (0.2 and 0.4)g) of the methanol + TIPAF + water solution were then analysed using the KF titrator. The concentration of water in the solution was calculated by considering the amount of water in the methanol and the relative masses of solution and methanol in the mixture. The mass fraction of TIPAF was calculated as (3.15 ± 0.12) % where the uncertainty was calculated by a student-t 95 % confidence interval. From Figure 1.6 this mass fraction of salt in solution should result in the crystallization of a SCH with a structural hydration number of 38. The dilute TIPAF solution was placed in a refrigerator at approximately 2 °C and crystallization of SCH was allowed to occur over 2 days. The solution containing SCH crystals was then vacuum filtered and the crystalline mass of about 25 g was gently squeezed between two large diameter (150 mm) sheets of absorbent filter paper. The procedure outlined above to measure the water content of methanol was then repeated with a different sample of methanol. A known mass of the SCH crystals (about 1 g) were added to known mass of methanol, dry nitrogen was flushed around the top of the septum bottle as soon as the crystals were added and the then septum bottle was resealed with the rubber bung. The SCH crystals were dissolved in the solution by gentle shaking and then 10 samples of the solution were tested using the KF titrator. The results indicate a mass fraction of TIPAF in the SCH crystals of (31.49 ± 0.38) %, which equates to a hydration number of 38.3 ± 0.7 (where the uncertainties were calculated by a student-t 95 % confidence interval).

5.4.3 *P,T* phase measurement technique

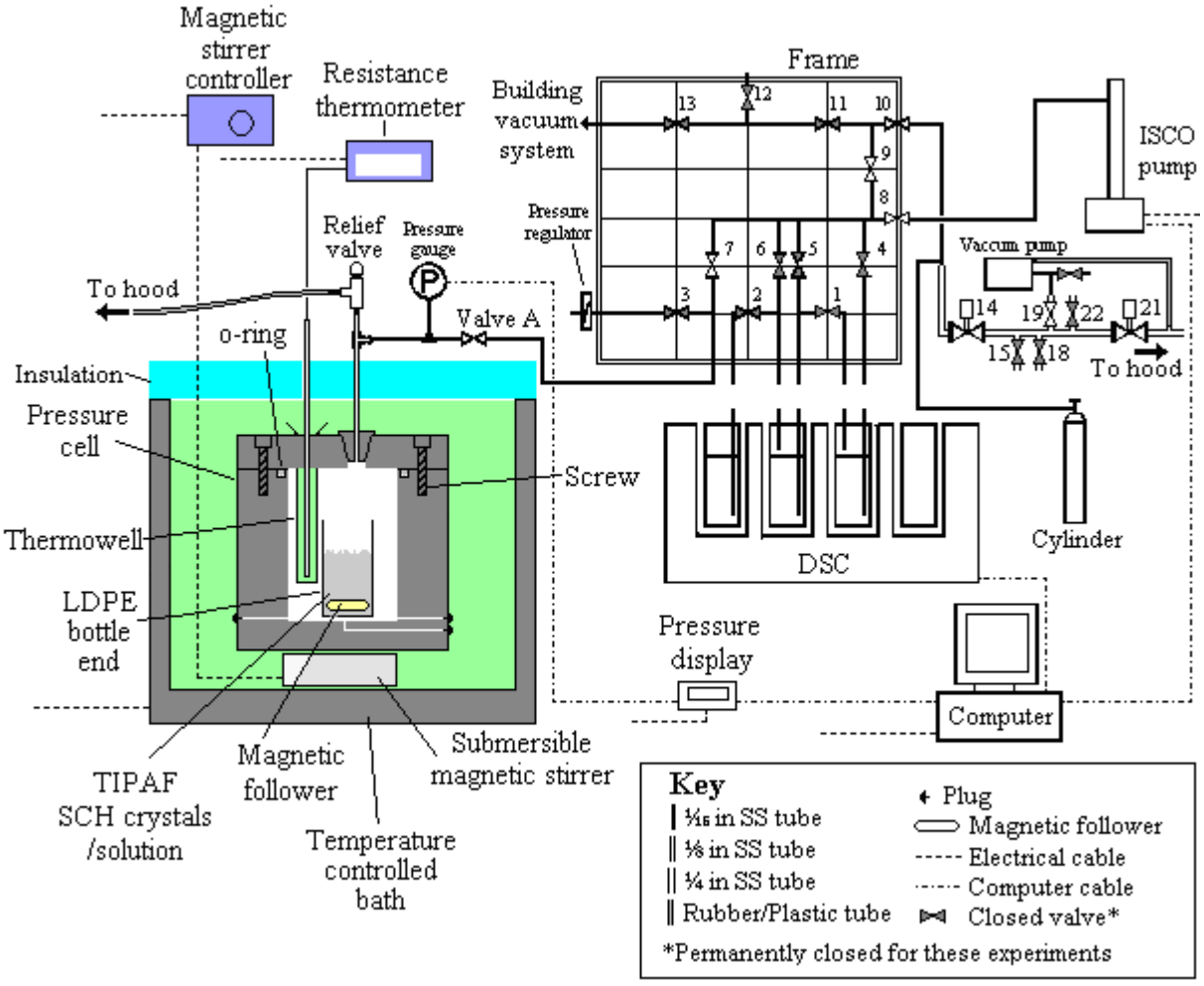

Figure 5.13 – Apparatus for *P,T* tetraisopentylammonium fluoride solution + methane semi-clathrate hydrate phase equilibria measurements.

The apparatus used for *P,T* phase measurements for the system methane + TIPAF, $w = 0.315$ is shown in Figure 5.13 (where w is the mass fraction of salt in the TIPAF solution/SCH, note: further mention of TIPAF solution or TIPAF SCH in this section will solely refer to this composition). Measurements were made by the isochoric method that was used by Arjmandi et al.[44] and Chapoy et al.[45] (described by Tohidi et al.[170]). Details of individual items of equipment shown in Figure 5.13 and others described below are listed with their specifications in Table 5.5. A magnetic follower was placed in a cut off end of a low density polyethylene bottle (about 25 mm in diameter and a cut height of 60 mm). A 19.3046 g mass of TIPAF SCH, weighed on a Mettler AE 200 balance (see Table 5.5) was then loaded in to the bottle. The bottle was used to contain the TIPAF SCH to protect against potential corrosion. The bottle was then carefully placed inside the pressure cell and the cell was

sealed by placement of an o-ring in the o-ring groove and by tightening the hexagon socket head cap screws to the required torque using a torque wrench (Norbar 200). The cell was then carefully placed in the temperature controlled bath (at 293.15 K) on top of a submersible magnetic stirrer (note: the magnetic stirrer had been tested to ensure it worked with the magnetic follower inside the cell before loading of the SCH and sealing of the cell). Methane was purged in to the system to a pressure of about 0.5 MPa from the cylinder with valves (7 to 10 and A) open and valves (11 and 14) closed. The gas was then vented to the hood to close to atmospheric pressure, by opening valve 14, valve 8 to the ISCO pump (model 260 D) was then closed (the ISCO pump is not designed for pressures below atmospheric, note the ISCO pump was empty (volume = 0.00 mL) for these steps) and valves (14 and 19) were then opened and the vacuum pump was switched on (see Table 5.5) which reduced the pressure to about 0.013 MPa. This process was repeated three times to purge air from the system. The cell was then filled with methane to a pressure of about 1 MPa and the temperature controlled bath was set to 313.15 K. By raising the temperature to 313.15 K all the SCH should have dissociated. The system was then cooled back to 273.15 K and the gas was vented to the hood to just above atmospheric pressure, followed by vacuuming using the vacuum pump (valve 8 to the ISCO pump was again closed and valves (14 and 19) were opened with the vacuum pump switched on). The purpose of this process was to remove potential air (nitrogen or oxygen) molecules from the 5^{12} cages of the SCH. The process was repeated once more. The bath temperature was then set to 283.15 K. Methane was introduced in to the ISCO pump from the cylinder with valves (8 to 10) open and valves (7 and A) closed. The methane was introduced at a pressure of about 12.5 MPa and the ISCO pump was reversed to a volume of about 200 ml. The cylinder valve was then closed and valves (7 and A) were slowly opened to gradually let methane in to the cell. The cell was monitored for leaks by checking for bubbles in the temperature controlled bath and by wetting connections with Swagelok Snoop® liquid leak detection liquid. When the system pressure had stabilised to a uniform value (about 8.5 MPa) the ISCO was set to pump at a constant flow rate of 10 mL/min until the pressure in the cell was about 20 MPa. At this point valves (7 to 10 and A) were closed.

Table 5.5 – Specifications of experimental equipment for *P*,*T* phase measurements.

Pressure cell	Pressure rated to 35 MPa Volume of (94.3 ± 0.5) mL	*
Pressure gauge	Paroscientific 9000-6K-101 Display model 715	0 MPa <*P* < 41.4 MPa Uncertainty ± 0.004 MPa
Temperature controlled bath	Polyscience model 9501 (filled with 50 % vol. fraction each of ethylene glycol and water)	Setability ± 0.01 K Stability ± 0.02 K
ISCO pump	Model 260 D	Total volume 266 mL Max. pressure 51.7 MPa
Magnetic stirrer	H+P Labortechnik AG Telemodul 20 C	Set at 350 rpm (Uncertainty ± 5 rpm)
Resistance thermometer	DSIR thermo RT200 Platinum resistance thermometer	Resolution ± 0.01 K Uncertainty ± 0.02 K
Valves	HIP 15-11AF1 (all valves except the relief valve). Relief valve: Swagelok SS-4R3A	Max. pressure 103 MPa (15000 psi) Set to relieve at 34.4 MPa with spring 177-R3A-K1-G
Mass comparator	Sartorius C 5000 type 1683	Tareable to 5 kg Resolution ± 1 mg
Balance	Mettler AE 2000	Resolution ± 1 mg
Vacuum pump	Edwards 8, two stage 240 V 1425 rpm AC motor	P_{min} = 0.013 MPa

*The volume of the pressure cell was measured by comparing the mass of the cell filled with water to the mass of the cell filled with air, these measurements utilized the mass comparator.

Initial experiments attempted to find whether all the 5^{12} cages of the assumed TIPAF·38H_2O crystal structure of SCH formed in the presence of methane molecules could be occupied, the pressure of methane was observed to drop very slowly. After 4 weeks the pressure drop had stopped (or was so slow it had appeared to stop) and estimations from the total pressure drop suggested that only 53 % of the 5^{12} cages were filled by methane (this calculation was based on the volume of the available for the gas to occupy calculated in Appendix I). Rather than continuing with these experiments it was decided to measure the *P*,*T* dissociation conditions of the SCH formed. An estimation of the likely dissociation point was made by considering the expected constant volume pressure rise on heating the cell, as well as the *P*,*T* dissociation conditions measured by Arjmandi et al.[44] for the system TBAB (w_{TBAB} = 0.3) + methane. From Figure 5.4 with w_{TBAB} = 0.3 the melting point of the SCH is approximately 285.15 K, from Figure 5.5 it was estimated that the dissociation temperature of methane + TBAB SCH at about 26 MPa would be roughly 298.15 K (by extrapolation). This equates to 13 K higher

than the melting point of the SCH under atmospheric conditions. It might be expected that TIPAF SCH would be stable to a similar degree over the melting point of the SCH under atmospheric conditions than TBAB SCH at the same pressure, therefore from the melting point of TIPAF·38H_2O of 305.6 K (using the value of Lipkowski et al.[67], see Table 1.2) it was estimated that the dissociation point at approximately 26 MPa would be roughly 317 K. However as this was only a rough estimate, temperature steps began at 309.15 K. The temperature was raised initially in steps of (1 to 2) K at a time. Approximately (20 to 28) h was allowed for the system to come to equilibrium after each temperature step, by this time the pressure (which was logged by computer, see Figure 5.13) had reached a new stable value. Smaller temperature steps of between (0.1 and 0.5) K were taken when there was a steeper rise in pressure between temperature steps indicating the start of dissociation of the SCH.

After the initial measurement was made the pressure was reduced in the cell by opening valves (7, 8 and A) and reversing the ISCO pump slowly until the desired pressure was achieved. The SCH was formed again by lowering the temperature of the bath to between (273 and 283) K and then reheating the SCH to a temperature of 309 K just greater than the melting point of the most stable SCH (TIPAF·27H_2O, MP 307.8 K [67]). The cycle of temperature was repeated several times and increased the rate of pressure drop and hence formation rate of methane enclathrated SCH. By heating to a temperature greater than that of the atmospheric melting point of the most stable SCH under atmospheric conditions it was figured that SCH structures that may not be able to enclathrate methane would also be removed. These steps were repeated for each new measurement.

5.5 Results and discussion

5.5.1 Dissociation point measurements

Figure 5.14 shows an example series of equilibrium point measurements for the TIPAF w = 0.315 solution/SCH + methane system for one dissociation point determination (note: all reference to TIPAF solution/SCH referred to in this section refers to that with a mass fraction of salt of w = 0.315 unless otherwise noted). Linear extrapolations were made from the points before and after complete dissociation and the SCH + Aq + V point (labelled in the Figure 5.14) that was found at the intersection point of these linear lines.

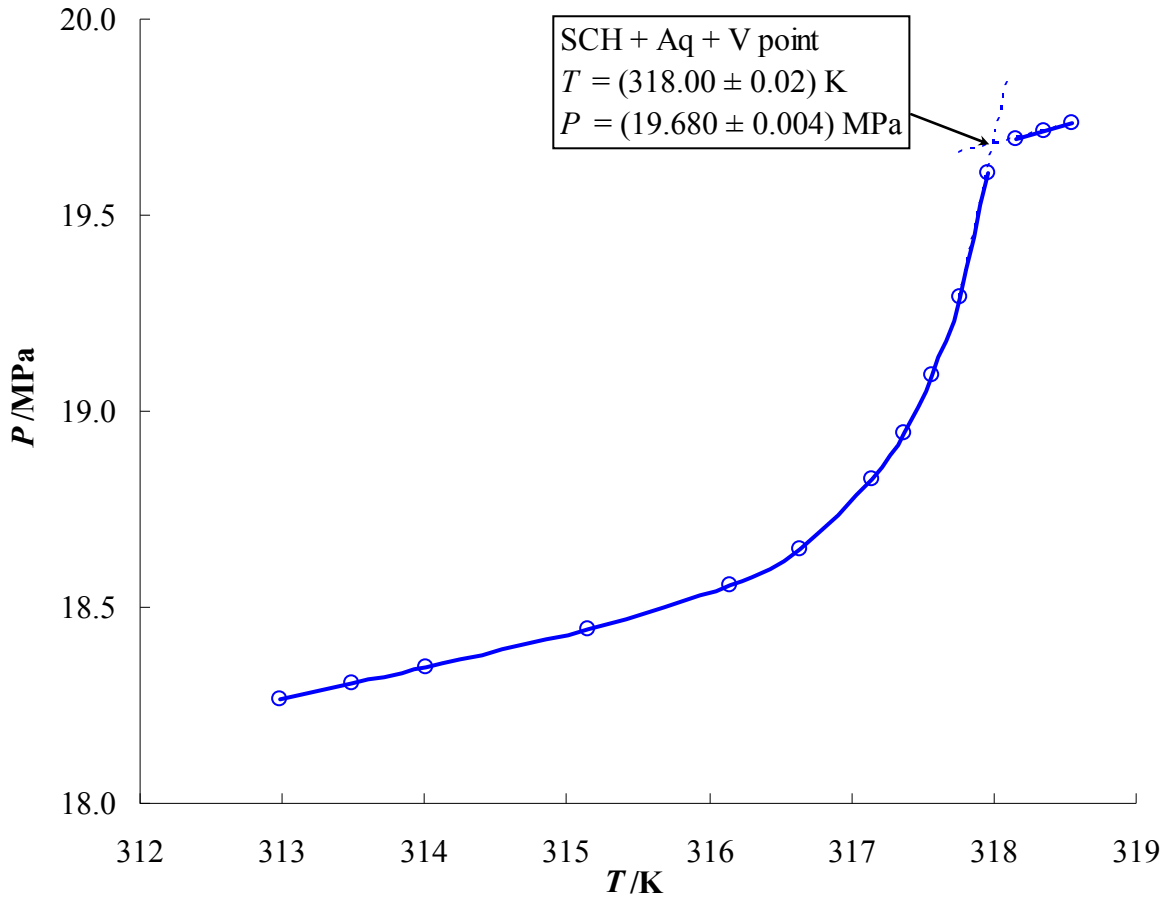

Figure 5.14 – Example of the equilibrium steps to determine a tetraisopentylammonium fluoride aqueous solution (TIPAF·38.3H_2O) + methane *P*,*T* SCH + Aq + V point.

Table 5.6 – *P*,*T* SCH + Aq + V equilibria points for TIPAF ($w = 0.315$) + methane.

T/K (± 0.02 K)	*P*/MPa (± 0.004 MPa)
309.53	2.029
313.90	7.343
318.00	19.680
319.67	26.653

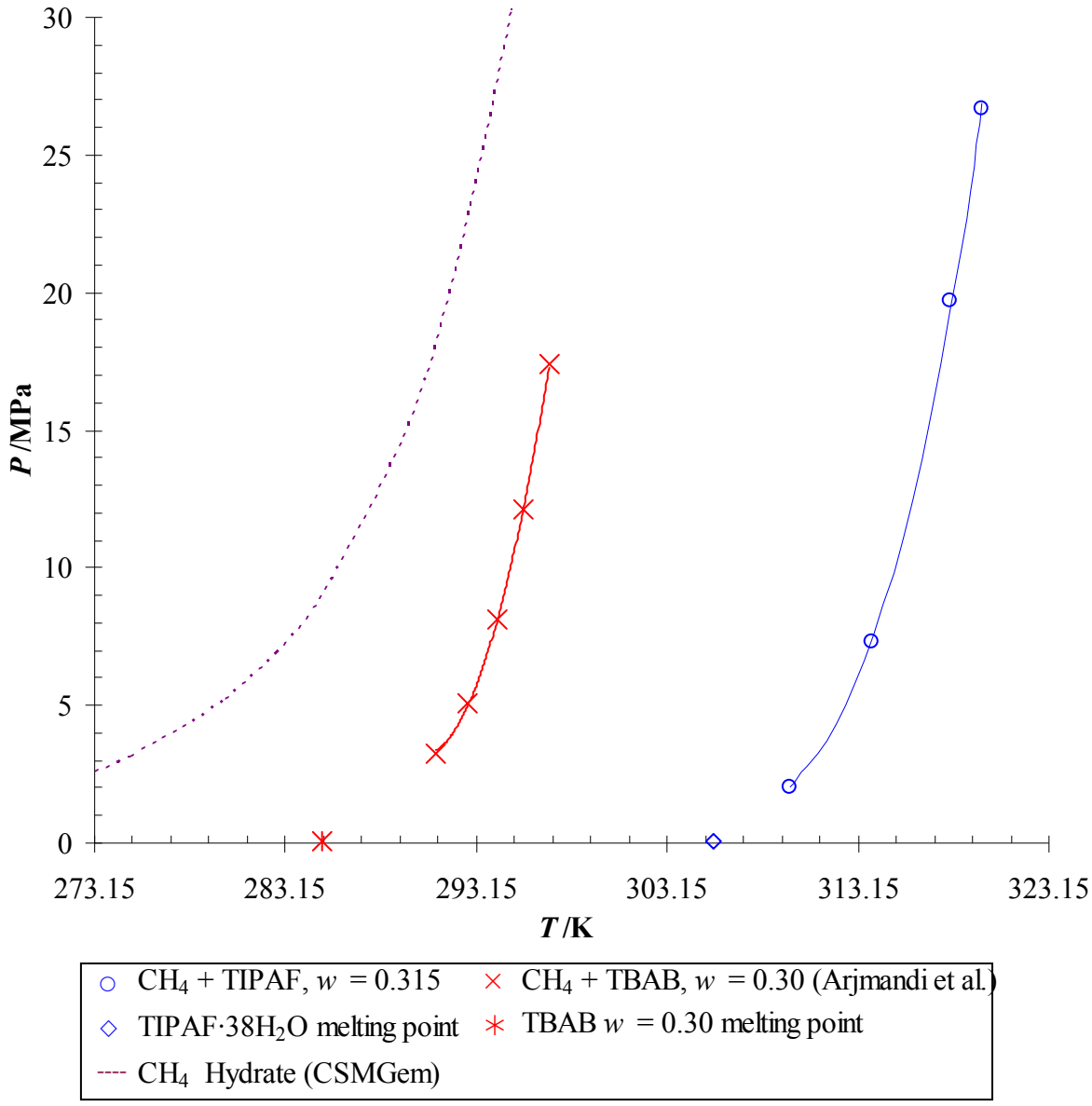

Figure 5.15 – *P*,*T* SCH + Aq + V equilibria points for TIPAF ($w = 0.315$) + methane compared to TBAB ($w = 0.3$) + methane from Arjmandi et al.[44] and methane hydrate data calculated using CSMGem the atmospheric melting point of each SCH is also shown (for TIPAF from Lipkowski et al.[67], for TBAB estimated from Figure 5.4).

Table 5.6 list the measured *P*,*T* SCH + Aq + V three phase equilibria points for methane + TIPAF SCH (w = 0.315). Figure 5.15 plots this data with that of Arjmandi et al.[44] for methane + TBAB (w = 0.3), the most stabilizing mass fraction of their measurements. It is clear that the shape and slope of the phase boundaries are similar for both sets of data, the major difference is that the TIPAF SCH curve is at temperatures higher by about 20 K at equivalent pressures. It is important to note however that the mass fraction of TBAB used Arjmandi et al.[44] of w = 0.30 is a little lower than the mass fraction corresponding to the stoichiometry of the SCH TBAB·38H_2O (for which w = 0.32). A SCH of methane + TBAB (w = 0.32) may be slightly more stable.

The melting points of both TIPAF and TBAB SCH under atmospheric conditions are included in Figure 5.15. It would appear that the *P*,*T* curves for SCH + Aq + V equilibria with methane would coincide with these values at atmospheric pressure, similar to what Chapoy et al.[45] and Hashimoto et al.[47] observed for hydrogen + SCH equilibria. This suggests that methane would be stable in these SCHs (TIPAF and TBAB) at atmospheric pressure; however the occupancy would be expected to be lower than at elevated pressure.

The data for methane hydrate calculated using CSMGem is also plotted in Figure 5.15. The dissociation temperature of the SCH is between (25 and 35) K higher at the same pressure. In terms of gas storage if it is assumed that the self-preserved hydrate only stores 50 % of the stable methane hydrate than SCHs may become viable as a gas storage matierals. SCH may be econmically competitive with NGH technologies at low gas capacities and short to moderate transport distances. The SCH have the advantage that they are stable to higher temperatures and would not require any or as much recompression and recooling of boiled off methane and less or no insulation for transport. These factors would have to be consided in the economic analysis.

Chapter 6 CONCLUSIONS AND RECOMMENDATIONS

6.1 Conclusions

6.1.1 Dissociation enthalpies and plug dissociation times of sI and sII gas hydrates prepared from methane + ethane mixtures

P,*T* hydrate phase diagrams prepared using CSMGem at a high gas to water mole ratio (N_g/N_w = 100) for a gas mixture of mole fractions 98.8 % methane + 1.2 % ethane reveal a similar diagram to that of a multi-component processed natural gas (PNG) mixture of Bollavaram.[54] A sII hydrate formation region occurs at low pressures and a sI region at high pressures separated by a sI+sII+V boundary line/region exhibiting a negative d*P*/d*T* slope. This indicates that a 98.8 % methane + 1.2 % ethane mixture can be representative of a PNG. A phase diagram prepared for a mixture of mole fractions 65.4 % methane + 34.6 % ethane on the other hand shows quite opposite behaviour with a sI region at lower pressures and a sII region at higher pressure separated by sI+sII+V boundary line/region exhibiting a positive d*P*/d*T* slope. This mixture was deemed to be non-representative of a PNG.

A further observation from the *P*,*T* hydrate phase diagrams was that a ln*P* versus 1/*T* plot of the phase data for the mixture of mole fractions 98.8 % methane + 1.2 % ethane under sI forming conditions aligned very closely with data plotted for pure methane hydrate. This suggests from the Clapeyron equation that the dissociation enthalpies of sI hydrate of this mixture would be almost identical to that of a pure methane sI hydrate.

Preferential enclathration was defined as the hydrate phase's preference to enclathrate a component or components of the gas thus stripping the gas phase of these components. An interesting phenomena observed from *P*,*T* phase calculations of methane + ethane mixtures was the existence of points were the water free composition of the hydrate is the same as that of the free gas. At these point there was no preferential enclathration or stripping of the gas phase. It was found however that these points where unstable, if a slight deviation in the composition of the mixture occurs preferential enclathration and stripping would result. An example of this was illustrated for a mixture of mole fractions 70 % methane + 30 % ethane at 15.77 MPa and 273.15 K. Predictions showed that if the feed gas was perturbed to a lower

mole fraction of methane the hydrate would preferentially enclathrate methane and the gas phase methane mole fraction would drop. On the other hand if the feed gas was perturbed to a higher mole fraction of methane the hydrate would preferentially enclathrate ethane and hence the gas phase methane mole fraction would increase. These points however could still be useful as the preferential enclathration is minimal and they could be used to form hydrates under conditions where the water to gas mole ratio is higher, i.e. typical laboratory conditions with minimal preferential enclathration or free gas stripping.

Structure I and structure II hydrate plugs were prepared from a mixture of mole fractions 65.4 % methane + 34.6 % ethane. The results showed that the dissociation time for the sII hydrate plug of this mixture was shorter than that of the sI hydrate plug. This was the opposite to the prediction made by the Peters' CSMPlug model[49] that the plug dissociation time of a sII plug would be 30 % longer than that of a sI plug. Estimates of the enthalpies of dissociation for each of these hydrates reveal that the dissociation enthalpy of sI hydrate is predicted to be higher than that of the sII hydrate which explains the poor prediction since the model assumes the enthalpy of dissociation of sII is greater than sI. The predicted enthalpies of dissociation for sI and sII hydrates prepared from a mixture of mole fractions of 98.8 % methane + 1.2 % ethane show the opposite, that the sII enthalpy of dissociation is higher than that of the sI hydrate. Plugs were prepared of sI hydrates from a mixture of mole fraction 98.8 % methane + 1.2 % ethane and sII hydrates from a mixture of mole fraction 80 % methane + 20 % ethane. Dissociation time measurements showed that on average the dissociation time for the sII hydrate plug was 25 % longer than for a sI hydrate plug. This agreed with the CSMPlug model prediction, probably as a result of the fact that the enthalpy of dissociation of the sII hydrate was greater than the sI hydrate, like the model assumes. An alternative hydrate dissociation model of Nguyen-Hong et al.[51] was shown to predict that the relative dissociation time of hydrate plugs of the same size, porosity and dissociation conditions was approximately equal to the ratio of the dissociation enthalpy multiplied by the hydrate density of each plug. This model and the experimental results both show that the dissociation enthalpy is probably the most important factor in the determination of the plug dissociation time.

Measurements of the dissociation enthalpy of sII hydrates with a mixture of mole fractions 98.8 % methane + 1.2 % ethane have been performed using a high pressure DSC at about 7 MPa. Two methods of formation were used, the first method involved forming the hydrate within the DSC's cell and second method involved cryogenically transferring hydrate formed in a pressure cell. The overall conversion of water to hydrate was 64.26 % and 98.16 % for these two methods respectively, and the enthalpies were (66.47 ± 0.50) kJ·mol^{-1} at 7.03 MPa and (63.15 ± 0.50) kJ·mol^{-1} at 6.92 MPa. Generally higher conversion are viewed to give better results,[143] this is one reason why these two differ to a greater extent then the uncertainty. Another possible reason is due to slightly different hydrate phase composition because of the different formation methods. The measured values were also compared to predictions provided from the Clapeyron equation using P,T phase data calculated in CSMGem. It was assumed in these calculations that the gases were not soluble in water and there was insignificant vaporisation of water into the vapour phase (however the volume of each phase was taken in account by use of eq (3.17) for the compressibility factor difference). Enthalpies of dissociation were calculated for sI and sII hydrate of the mixture of mole fractions 65.4 % methane + 34.6 % ethane, as well as sII hydrates of the mixture of mole fractions 98.8 % methane + 1.2 % ethane and sI pure methane hydrate. The measurement of the enthalpy of dissociation of (63.15 ± 0.50) kJ·mol^{-1} at 6.92 MPa for the sII hydrate of the mixture of mole fractions 98.8 % methane + 1.2 % ethane was within the uncertainty of the Clapeyron equation calculated enthalpy. The Clapeyron equation calculated enthalpies of dissociation for methane hydrate also compared within their uncertainty to published calorimetric measurements. These results indicate that the Clapeyron equation enthalpies of dissociation using the assumptions stated provides a good estimate of the true enthalpy.

Sloan and Fleyfel[154,155] suggested that enthalpy of dissociation varies as a function of the size of the guest for single guest hydrates. A comparison of the average guest diameter of each cage for both the sI and sII hydrates of the mixture of mole fractions 65.4 % methane + 34.6 % ethane reveal that for the sI hydrate the large cage guest diameter does not change much with pressure, however the guest average diameter for the small cages increases by about 1.4 Å in 10 MPa. For the sII hydrate the large cage average guest size remains almost constant with pressure and the small cage average guest size only increases by about 0.5 Å in 135 MPa. Comparing these results to the enthalpies of dissociation it clear to see that the sI

enthalpies for this mixture increases steeply with pressure, whereas the sII enthalpies remains approximately constantly over a wide pressure range. This indicates that Sloan and Fleyfel's suggestion is correct and can be applied to hydrates of mixed guests. This has implications on the plug dissociation time.

6.1.2 The modelling of preferential enclathration

In doing the plug dissociation studies in this work at high methane mole fractions a discontinuity was observed in the gas evolution rate and X-ray diffraction data indicated the possibility of the presence of both sI and sII hydrate structures in some plugs. Models were conceived for laboratory hydrate formations where there is typically a large mole ratio of gas to water during hydrate formation. Two stepwise models of hydrate formation were presented in Chapter 4 for the calculation of preferential enclathration of certain components in the hydrate phase and associated stripping of these components from the vapour phase. The first model was a constant pressure model whereby a gas is initially charged to a system containing a piston or syringe pump and a cell filled with ice or water. As hydrate formation proceeds the piston or syringe pump compresses the remaining gas to maintain constant pressure. This model takes small steps in conversion of ice to hydrate and uses equilibrium CSMGem predictions for the hydrate phase composition. The second model was a constant volume system where a cell containing ice or water was charged with gas at an initial pressure and the pressure was allowed to drop as hydrate formation proceeded. This model takes small steps in the pressure drop and again uses equilibrium CSMGem predictions for the hydrate phase composition.

A slightly modified constant pressure model was tested against experiments where the gas composition was monitored by gas chromatography (GC) as hydrate formation proceeded. A known amount of powdered ice was loaded into a pressure cell, the cell was pressurised with a mixture of mole fractions 89.7 % methane + 10.3 % ethane. The cell was then heated above the ice point to initiate hydrate formation and a syringe pump was used to maintain a constant pressure as hydrate formation proceeded. Before samples were removed for GC measurements the system was cooled to 258 K and mixing was achieved by cycling the syringe pump up and down in pressure. One of the model's assumptions was that there was no direct conversion of ice to hydrate. This was observed to be true as during a period where

the cell was held at 258 K for over 6 days there was negligible change in the volume of gas contained in the syringe pump at constant pressure. The GC measurements and the model predictions of the free gas methane mole fraction were plotted as a function of pumped gas volume (note the model had been modified to take in to account the removal of samples). The plot showed the model exhibited similar trends to the experimental measurements, in that the mole fraction of methane in the free gas increased with the volume of gas pumped. The percentage deviation of the final methane mole fraction was +1.9 %, (92.5 % from GC and 94.3 % from the model). The total gas pumped experimentally was 183.68 mL, whereas the model predicted a slightly lower 183.12 mL. From these results it was concluded that the model is validated. The model-experiment discrepancy was likely due to the use of equilibrium predictions of the hydrate phase composition. The phenomenological explanation of the discrepancy was that methane can diffuse more quickly thorough a layer of hydrate than ethane due to its smaller size. It was concluded therefore that it might be expected that the hydrate would form with a higher mole fraction of methane than predicted by equilibrium thermodynamics. As the constant volume model was similar in its assumptions and equations it was assumed to also be validated by these results. These results prove it is possible to form a hydrate plug containing both sI and sII hydrates if the typical laboratory formation conditions of a large initial mole ratio of ice or water to gas is used in experiments due to preferential enclathration and the accompanying stripping of components from the gas phase. The formation of both sI and sII hydrates is more likely to occur if the initial gas composition is close to a sI-sII boundary. In the experiments in this work the initial feed gas composition did not have a high enough methane mole fraction to result in the formation of both sI and sII hydrates.

6.1.3 Tetraisopentylammonium fluoride semi-clathrate hydrate (SCH) + methane *P*,*T* phase equilibria

Measurements of *P*,*T* SCH + Aq + V three phase equilibria points for methane + tetraisopentylammonium fluoride (TIPAF) in aqueous solution (w = 0.315) were made between temperatures of (309.53 and 319.67) K and between pressures of (2.029 and 26.653) MPa. The salt mass fraction was fixed by crystallisation of the SCH of structural hydration number 38 that was measured by Karl Fischer titration to be 38.3. This SCH was chosen as it has a melting point exceeding 30 °C as well as a relatively high number of cages

that could be filled by gas molecules. The phase boundary measured was similar in shape to one measured by Arjmandi et al.[44] for methane + tetrabutylammonium bromide (TBAB) in aqueous solution (w = 0.30) except that it was approximately 20 K higher in temperature. The results were also compared to the data of pure methane hydrate predicted using CSMGem. The phase boundary for methane + TIPAF solution (w = 0.315) was between (25 and 35) K higher at the same pressures. Comparison of the mass fraction of methane that could be stored in a self-preserved methane hydrate at 267 K after a month with the estimated maximum mass fraction of methane that could be stored in SCH indicate that SCH may be a useful gas storage material. The SCH may be useful for similar applications for which NGH technology has been shown to be economic, that is for lower gas field capacities and short to moderate transport distances. The advantage is no or little refrigeration and less or no insulation would be required for the storage of methane in this SCH.

6.2 Recommendations and future work

It is clear from a review of the calorimetric enthalpies of dissociation of natural gas hydrate constituents and mixtures that there is a general lack of data. Measurements of the enthalpies of dissociation of hydrates of CO_2, H_2S or another highly water soluble gaseous guest would be particularly useful for investigating assumptions associated with the use of the Clapeyron equation (such results for CO_2 hydrate may also prove useful for research on the sequestration of CO_2 in gas hydrates). Further measurement of the enthalpies of dissociation of hydrates with mixed guest would also be useful to further test the validity of the Clapeyron equation. (Note: more measurements might have been undertaken in this work had the DSC used been more reliable).

Modifications might be made to the CSMPlug program. It might be useful to include an option whereby the user may input an enthalpy of dissociation for their hydrate. Clapeyron equation predictions of the enthalpy of dissociation might also be added to the code of CSMGem. This would allow better predictions of the hydrate dissociation times.

For laboratory hydrate plug formation from gas mixtures that may either form sI or sII hydrates it is recommended that models such as those presented in Chapter 4 of this work be used to predict whether it is likely that more than one hydrate structure will form given an

initial amount of ice and gas. The use of the model may prevent unwanted mixtures of sI and sII hydrate being formed. It is recommended though that all phases be characterised as much as possible, preferably by structural analysis using X-ray diffraction, Raman spectroscopy or NMR on samples of hydrate, to confirm its structure. It is also useful to know the final composition of the gas used to form the hydrate plug as this may give an indication to whether it is likely that more than one structure of hydrate has formed. This can be easily measured by gas chromatography. The structural analysis of the hydrate may also reveal the composition of the hydrate phase. This can also be measured by gas chromatography and a comparison might prove useful and is not too difficult if hydrates samples are also required for structural analysis.

A method to prevent changes in the gas composition during laboratory hydrate formations from melting ice particles was proposed. This method relies upon the use of two gas mixtures. One mixture would be used to initially pressurise a cell containing the ice particles; this mixture might be at the composition of a typical pipeline natural gas. Once the initial pressurization is completed the supply would be switched to a gas mixture of the expected hydrate composition (on a water free basis) that would form from the initial gas mixture at a high mole ratio of gas to water. This "formation gas" supply would be regulated in to the cell at the pressure of the initial pressurisation. Thus as hydrate formation proceeds the initial gas composition is replaced by the "formation gas" in order to maintain the initial gas composition. This method is unproven and should be tested. The need for good mixing and accurate knowledge of the hydrate phase water free composition would probably be important.

There are only limited published measurements of phase equilibria of semi-clathrate hydrates (SCH) and gases. Most measurements so far have focussed on hydrogen semi-clathrates. The highest possible mass fraction of hydrogen able to be stored however is 0.83 % for the tributylphosphine oxide (TBPO) SCH $TBPO{\cdot}34.5H_2O$ assuming single occupancy of hydrogen in the 5^{12} cages. For the same assumption $TIPAF{\cdot}38H_2O$ SCH can only store 0.6 %. These low values are unlikely to be of commercial interest for gas storage purposes. The storage of gases such as methane may have more commercial applications. If SCHs such as that of tributylphosphine oxide can store as much methane as self preserved sI methane

hydrate it might be useful for the transportation of methane under similar conditions for which NGH has shown to be economic means of methane transportation. The economics of methane storage and transportation in SCHs under these conditions of low gas field capacity and short to moderate transport distance should be investigated. Given that some SCH are stable to greater than 30 °C they may require no or less refrigeration and insulation. The current method of transporting methane (or natural gas containing mostly methane) large distances is in the form of liquid as liquefied natural gas (LNG tankers). These tankers must be refrigerated as the boiling point of methane is only about 112 K (from NIST Refprop[168]). The extra mass of refrigeration systems, insulation and LNG plant should be assessed when making comparison of the storage capacities. A study could be made of these considerations to see if it would make sense to consider SCHs as methane storage materials at higher field capacities that are currently economic only for methane transportation by LNG.

The research of Shimada et al.[63] and Kamata et al.[64,195] have shown that it is possible to separate gas mixtures by the formation of SCH. Further research on gas separation using SCH should be considered. One possible SCH that could be studied is TIPAF·27H_2O; it contains the $5^4 4^4$ cage that only very small molecules such as hydrogen or helium could potentially fill (see Appendix B for a size estimate of this cage). The exclusion of large molecules by this SCH might be useful for purification of hydrogen.

REFERENCES

(1) Sloan, E. D. *Clathrate Hydrates of Natural Gases*. 2nd ed. ed.; Chemical Industries; Marcel Dekker: New York, 1998; Vol. 73, pp 705.

(2) Sloan, E. D.; Koh, C. A. *Clathrate Hydrates of Natural Gases*. 3rd ed.; Chemical Industries; Taylor & Francis CRC press: Boca Raton, FL, 2007.

(3) Dyadin, Y. A.; Udachin, K. A. Clathrate Polyhydrates of Peralkylonium Salts and Their Analogs. *J. Struct. Chem.* **1987,** *28*, 394-432

(4) Jeffrey, G. A. Hydrate Inclusion Compounds. In *Inclusion Compounds*, Atwood, J. L.; Davies, J. E. D.; MacNicol, D. D., Eds.; 1984; Vol. 1, pp 135-190.

(5) Feil, D.; Jeffrey, G. A. Polyhedral Clathrate Hydrates .II. Structure of Hydrate of Tetra Iso-Amyl Ammonium Fluoride. *J. Chem. Phys.* **1961,** *35*, 1863-1873.

(6) Nakayama, H.; Watanabe, K. Hydrates of Organic Compounds. II. The Effect of Alkyl Groups on the Formation of Quaternary Ammonium Fluoride Hydrates. *Bull. Chem. Soc. Jpn.* **1976,** *49*, 1254-6.

(7) Aladko, L. S.; Dyadin, Y. A.; Rodionova, T. V.; Terekhova, I. S. Clathrate Hydrates of Tetrabutylammonium and Tetraisoamylammonium Halides. *J. Struct. Chem.* **2002,** *43*, 990-994.

(8) Aladko, L. S.; Dyadin, Y. A.; Rodionova, T. V.; Terekhova, I. S. Effect of Size and Shape of Cations and Anions on Clathrate Formation in the System: Halogenides of Quaternary Ammonium Bases and Water. *J. Mol. Liq.* **2003,** *106*, 229-238.

(9) Priestly, J. Experiments and Observations of Different Kinds of Air and Other Branches of Natural Philosophy, Connected with the Subject. In *Observations on the Freezing of Water, impregnated with Fluor Acid Air, and with Vitriolic Acid Air*, Thomas Pearson: Birmingham, 1790; Vol. 2, pp 359-363.

(10) Prieto-Ballesteros, O.; Kargel, J. S.; Fernandez-Sampedro, M.; Selsis, F.; Martinez, E. S.; Hogenboom, D. L. Evaluation of the possible presence of clathrate hydrates in Europa's icy shell or seafloor. *Icarus* **2005,** *177*, 491-505.

(11) Davidson, D. W. Clathrate Hydrates. In *Water in Crystalline Hydrates; Aqueous Solutions of Simple Nonelectrolytes*, Franks, F., Ed. Water: A Comprehensive Treatise, Plenum: New York, 1973; Vol. 2, pp 115-234.

(12) Davy, H. The Bakerian Lecture. On some of the Combinations of Oxymuriatic gas and Oxygene, and on the chemical Relations of these Principles, to inflammable Bodies. *Philos. Trans. R. Soc. London* **1811,** *101*, 1-35.

(13) Faraday, M. On Fluid Chlorine. *Philos. Trans. R. Soc. London* **1823,** *113*, 160-165.

(14) Stuart, H. A.; Klemm, W.; Schmitz-Dumont, O.; von Stackelberg, M.; Nowotny, H. Structure of Inorganic Substances. *FIAT Rev. German Sci. 1939-46, Inorg. Chem., Pt. IV* **1948**, 1-109.

(15) von Stackelberg, M.; Gotzen, O.; Pietuchovsky, J.; Witscher, O.; Frühbuss, H.; Meinhold, W. Structure and Formula of Gas Hydrates. *Fortschritte der Mineralogie* **1947,** *26*, 122-124.

(16) von Stackelberg, M. Solid Gas Hydrates. *Naturwissenschaften* **1949,** *36*, 327-33,359-62.

(17) Claussen, W. F. Suggested Structures of Water in Inert Gas Hydrates. *J. Chem. Phys.* **1951,** *19*, 259-260.

(18) Claussen, W. F. Erratum: Suggested Structures of Water in Inert Gas Hydrates. *J. Chem. Phys.* **1951,** *19*, 662.

(19) von Stackelberg, M.; Müller, H. R. The Structure of Gas Hydrates. *Naturwissenschaften* **1951,** *38*, 456.

(20) von Stackelberg, M.; Müller, H. R. On the Structure of Gas Hydrates. *J. Chem. Phys.* **1951,** *19*, 1319-1320.

(21) Claussen, W. F. A 2nd Water Structure for Inert Gas Hydrates. *J. Chem. Phys.* **1951,** *19*, 1425-1426.

(22) Müller, H. R.; von Stackelberg, M. Structure of Gas Hydrates. *Naturwissenschaften* **1952,** *39*, 20-1.

(23) Pauling, L.; Marsh, R. E. The Structure of Chlorine Hydrate. *Proc. Natl. Acad. Sci. U. S. A.* **1952,** *38*, 112-118.

(24) McMullan, R. K.; Jeffrey, G. A. Polyhedral Clathrate Hydrates .IX. Structure of Ethylene Oxide Hydrate. *J. Chem. Phys.* **1965,** *42*, 2725-2732.

(25) Mak, T. C. W.; McMullan, R. K. Polyhedral Clathrate Hydrates .X. Structure of Double Hydrate of Tetrahydrofuran and Hydrogen Sulfide. *J. Chem. Phys.* **1965,** *42*, 2732-2737.

(26) Kirchner, M. T.; Boese, R.; Billups, W. E.; Norman, L. R. Gas Hydrate Single-Crystal Structure Analyses. *J. Am. Chem. Soc.* **2004,** *126*, 9407-9412.

(27) Sloan, E. D. Fundamental Principles and Applications of Natural Gas Hydrates. *Nature* **2003,** *426*, 353-359.

(28) Huo, Z. Hydrate Phase Equilibria Measurements by X-ray Diffraction and Raman Spectroscopy. Colorado School of Mines, Golden, CO, 2002.

(29) Dyadin, Y. A.; Larionov, E. G.; Manakov, A. Y.; Zhurko, F. V.; Aladko, E. Y.; Mikina, T. V.; Komarov, V. Y. Clathrate Hydrates of Hydrogen and Neon. *Mendeleev Commun.* **1999,** *9*, 209-210.

(30) von Stackelburg, M.; Meinhold, W. Solid Gas Hydrates. III. Mixed Hydrates. *Z. Elektrochem.* **1954,** *58*, 40-45.

(31) Florusse, L. J.; Peters, C. J.; Schoonman, J.; Hester, K. C.; Koh, C. A.; Dec, S. F.; Marsh, K. N.; Sloan, E. D. Stable Low-Pressure Hydrogen Clusters Stored in a Binary Clathrate Hydrate. *Science* **2004,** *306*, 469-71.

(32) van der Waals, J. H.; Platteeuw, J. C. Clathrate Solutions. In *Advances in Chem. Phys. I.* , Prigogine, Ed. Interscience Publishers, Inc.: 1959; Vol. 2, pp 1-57.

(33) Ballard, A. L. A Non-ideal Hydrate Solid Solution Model for a Multi-phase Equilibria Program. Colorado School of Mines, Golden, CO, 2002.

(34) Ballard, A. L. *CSMGem Hydrate Prediction Program*, Colorado School of Mines: 2001.

(35) Kini, R. A. NMR Studies of CH4, C2H6, and C3H8 Hydrates: Structure, Kinetics, and Thermodynamics. Colorado School of Mines, Golden, Co, 2003.

(36) Subramanian, S. Measurements of Clathrate Hydrates Containing Methane and Ethane using Raman Spectroscopy. Colorado School of Mines, Golden, Colorado, USA, 2000.

(37) Jager, M. D. High Pressure Studies of Hydrate Phase Inhibition using Raman Spectroscopy. Colorado School of Mines, Golden, CO, 2001.

(38) Sloan, E. D. *Hydrate Engineering*. SPE Monograph Series; Society of Petroleum Engineers: Richardson, Tx, 2000; Vol. 21.

(39) Hammerschmidt, E. G. Formation of Gas Hydrates in Natural Gas Transmission lines. *Ind. Eng. Chem.* **1934,** *26*, 851-5.

(40) Davies, S. R.; Selim, M. S.; Sloan, E. D.; Bollavaram, P.; Peters, D. J. Hydrate Plug Dissociation. *AIChE J.* **2006,** *52*, 4016-4027.

(41) Gudmundsson, J. S.; Børrehaug, A. In *A Frozen Hydrate for Transport of Natural Gas*, Proc. of the 2nd Int. Conf. on Natural Gas Hydrates, Toulouse, France, June 2-6, 1996; 1996; 415-422.

(42) Nakajima, Y.; Takaoki, T.; Ohgaki, K.; Ota, S. In *Use of Hydrate Pellets for Transportation of Natural Gas - II; Proposition of Natural Gas Transportation in Form of Hydrate Pellets*, Proc. of the 4th Int. Conf. on Gas Hydrates, Yokohama, Japan, May 19-23, 2002; 2002; 987-990.

(43) Shirota, H.; Aya, I.; Namie, S.; Bollavaram, P.; Turner, D. In *Measurement of Methane Hydrate Dissociation for Application to Natural Gas Storage and Transportation*, Proc. of the 4th Int. Conf. on Gas Hydrates, Yokohama, Japan, May 19-23, 2002; 2002.

(44) Arjmandi, M.; Chapoy, A.; Tohidi, B. Equilibrium Data of Hydrogen, Methane, Nitrogen, Carbon Dioxide, and Natural Gas in Semi-Clathrate Hydrates of Tetrabutyl Ammonium Bromide. *J. Chem. Eng. Data* **2007,** *52*, 2153-2158.

(45) Chapoy, A.; Anderson, R.; Tohidi, B. Low-Pressure Molecular Hydrogen Storage in Semi-clathrate Hydrates of Quaternary Ammonium Compounds. *J. Am. Chem. Soc.* **2007,** *129*, 746-747.

(46) Hashimoto, S.; Murayama, S.; Sugahara, T.; Sato, H.; Ohgaki, K. Thermodynamic and Raman spectroscopic studies on H_2 + tetrahydrofuran + water and H_2 + tetra-n-butyl ammonium bromide + water mixtures containing gas hydrates. *Chem. Eng. Sci.* **2006,** *61*, 7884-7888.

(47) Hashimoto, S.; Sugahara, T.; Moritoki, M.; Sato, H.; Ohgaki, K. Thermodynamic stability of hydrogen + tetra-n-butyl ammonium bromide mixed gas hydrate in nonstoichiometric aqueous solutions. *Chem. Eng. Sci.* **2008,** *63*, 1092-1097.

(48) Park, Y.; Kim, D.-Y.; Lee, J.-W.; Huh, D.-G.; Park, K.-P.; Lee, J.; Lee, H. Sequestering Carbon Dioxide into Complex Structures of Naturally Occurring Gas Hydrates. *Proc. Natl. Acad. Sci. U. S. A.* **2006,** *103*, 12690-12694.

(49) Peters, D. J. A Study of Hydrate Dissociation in Pipelines by the Method of Two-Sided Depressurisation: Experiment and Model. Colorado School of Mines, Golden, 1999.

(50) Gupta, A. Methane Hydrate Dissociation Measurements and Modeling: The Role of Heat Transfer and Reaction Kinetics. Colorado School of Mines, Golden, CO, 2007.

(51) Nguyen-Hong, D.; Gruy, F.; Herri, J. M. Experimental Data and Approximate Estimation for Dissociation Time of Hydrate Plugs. *Chem. Eng. Sci.* **2006,** *61*, 1846-1853.

(52) Moridis, G. J. In *Numerical Studies of Gas Production From Methane Hydrates*, Proc. SPE Gas Technology Symposium, Calgary, Canada April 30 - May 2nd, 2002; 2002; 75691.

(53) Hong, H.; Pooladi-Darvish, M.; Bishnoi, P. R. Analytical Modelling of Gas Production from Hydrates in Porous Media. *J. Can. Pet. Technol.* **2003,** *42*, 45-56.

(54) Bollavaram, P. Hydrate Plug Dissociation in Pipelines by Pressure Reduction: Experiment and Modeling. Colorado School of Mines, Golden, Colorado, 2003.

(55) Fowler, D. L.; Loebenstein, D. B.; Pall; Kraus, C. A. Some Unusual Hydrates of Quaternary Ammonium Salts. *J. Am. Chem. Soc.* **1940,** *62*, 1140-1142.

(56) Beurskens, G.; Jeffrey, G. A.; McMullan, R. K. Polyhedral Clathrate Hydrates .VI. Lattice Type and Ion Distribution in Some New Peralkyl Ammonium, Phosphonium, and Sulfonium Salt Hydrates. *J. Chem. Phys.* **1963,** *39*, 3311-3315.

(57) Jeffrey, G. A.; McMullan, R. K. Polyhedral Clathrate Hydrates .IV. Structure of Tri N-Butyl Sulfonium Fluoride Hydrate. *J. Chem. Phys.* **1962,** *37*, 2231-2239.

(58) Alekseev, V. I.; Gatilov, Y. V.; Polyanskaya, T. M.; Bakakin, V. V.; Dyadin, Y. A.; Gaponenko, L. A. Characteristic Features of the Production of the Hydrate Framework Around the Hydrophobic-Hydrophillic Unit in the Crystal Structure of the Clathrate Tri-n-butylphosphine Oxide 34.5-Hydrate. *J. Struct. Chem.* **1982,** *23*, 395-399.

(59) Bonamico, M.; McMullan, R. K.; Jeffrey, G. A. Polyhedral Clathrate Hydrates .III. Structure of Tetra N-Butyl Ammonium Benzoate Hydrate. *J. Chem. Phys.* **1962,** *37*, 2219-2231.

(60) McMullan, R.; Jeffrey, G. A. Hydrates of the Tetra n-Butyl and Tetra i-Amyl Quaternary Ammonium Salts. *J. Chem. Phys.* **1959,** *31*, 1231-1234.

(61) McMullan, R. K.; Jeffrey, G. A.; Bonamico, M. Polyhedral Clathrate Hydrates .V. Structure of Tetra-N-Butyl Ammonium Fluoride Hydrate. *J. Chem. Phys.* **1963,** *39*, 3295-3310.

(62) Shimada, W.; Shiro, M.; Kondo, H.; Takeya, S.; Oyama, H.; Ebinuma, T.; Narita, H. Tetra-n-butylammonium Bromide-Water (1/38) *Acta Crystallogr., Sect. C: Cryst. Struct. Commun.* **2005,** *61*, O65-O66

(63) Shimada, W.; Ebinuma, T.; Oyama, H.; Kamata, Y.; Takeya, S.; Uchida, T.; Nagao, J.; Narita, H. Separation of Gas Molecule using Tetra-n-butyl Ammonium Bromide Semi-Clathrate Hydrate Crystals. *Jpn. J. Appl. Phys., Part 2* **2003,** *42*, L129-L131.

(64) Kamata, Y.; Oyama, H.; Shimada, W.; Ebinuma, T.; Takeya, S.; Uchida, T.; Nagao, J.; Narita, H. Gas Separation Method Using Tetra-n-butylammonium Bromide Semi-Clathrate Hydrate. *Jpn. J. Appl. Phys., Part 1* **2004,** *43*, 362-365.

(65) Stupin, D. Y.; Stravitnaya, O. S. The Sorption of Sulphur Dioxide By the Clathrate Hydrates of Tetrabutylammonium Bromide and Acetate. *Russ. J. Phys. Chem.* **1991,** *65*, 672-675.

(66) Stupin, D. Y.; Stravitnaya, O. S. The Sorption of Sulphur Dioxide By the Clathrates of Tetrabutylammonium and Tetraisopentylammonium Phthalates. *Russ. J. Phys. Chem.* **1991,** *65*, 670-672.

(67) Lipkowski, J.; Suwinska, K.; Rodionova, T. V.; Udachin, K. A.; Dyadin, Y. A. Phase and X-ray Study of Clathrate Formation in the Tetraisoamylammonium Fluoride-Water System. *J. Inclusion Phenom.* **1994,** *17*, 137-48.

(68) Duc, N. H.; Chauvy, F.; Herri, J.-M. CO2 Capture By Hydrate Crystallization – A Potential Solution For Gas Emission of Steelmaking Industry. *Energy Convers. Manage.* **2007,** *48*, 1313-1322.

(69) Oyama, H.; Shimada, W.; Ebinuma, T.; Kamata, Y.; Takeya, S.; Uchida, T.; Nagao, J.; Narita, H. Phase diagram, latent heat, and specific heat of TBAB semiclathrate hydrate crystals. *Fluid Phase Equilib.* **2005,** *234*, 131-135.

(70) *ACD ChemSketch Freeware (Downloadable from www.acdlabs.com)*, Version 10.02; Advanced Chemistry Development: Toronto, Canada, 2006.

(71) Subramanian, S.; Ballard, A. L.; Kini, R. A.; Dec, S. F.; Sloan, E. D. Structural Transitions in Methane + Ethane Gas Hydrates. Part I: Upper Transition Point and Applications. *Chem. Eng. Sci.* **2000,** *55*, 5763-5771.

(72) Subramanian, S.; Kini, R. A.; Dec, S. F.; Sloan, E. D., Jr. Evidence of Structure II Hydrate Formation from Methane + Ethane Mixtures. *Chem. Eng. Sci.* **2000,** *55*, 1981-1999.

(73) Marsh, K. N.; O'Hare, P. A. G., Eds., *Solution Calorimetry*. Experimental thermodynamics; For IUPAC, Blackwell Scientific: Oxford, U.K., 1994; Vol. IV, p 576.

(74) Goodwin, A. R. H.; Marsh, K. N.; Wakeham, W. A. *Measurement of the Thermodynamic Properties of Single Phases*. Experimental Thermodynamics; For IUPAC, Elsevier: Amsterdam, 2003; Vol. VI.

(75) Claudy, P. M. Differential Scanning Calorimetry. In *Measurement of the Thermodynamic Properties of Single Phases*, Goodwin, A. R. H.; Marsh, K. N.; Wakeham, W. A., Eds.; Experimental thermodynamics, For IUPAC, Elsevier: Amsterdam, Netherlands, 2003; Vol. VI, pp 348-368.

(76) Boersma, S. L. A Theory of Differential Thermal Analysis and New Methods of Measurement and Interpretation. *J. Am. Ceram. Soc.* **1955,** *38*, 281-284.

(77) Mraw, S. C. Differential Scanning Calorimetry. In *Specific heat of solids*, Cezairliyan, A.; Ho, C. Y.; Anderson, A. C., Eds.; CINDAS Data Series on Material Properties. Group I, Theory, Estimation, and Measurement of Properties, Hemisphere: New York, 1988; Vol. 1-2, pp 395-433.

(78) Marsh, K. N. *Recommended Reference Materials for the Realization of Physicochemical Properties*. Blackwell Scientific Boston, MA, 1987.

(79) *Multi-cell Differential Scanning Calorimeter User's Manual*. 3rd ed.; Calorimetry Sciences Corporation: Lindon, UT, 1999.

(80) Nobelprize.org. The Nobel Prize in Physics 1901 Awarded to Wilhelm Roentgen "In Recognition of the Extraordinary Services He Has Rendered by the Discovery of the Remarkable Rays Subsequently Named after Him". http://nobelprize.org/nobel_prizes/physics/laureates/1901/ (accessed 31-Oct-07)

(81) Nobelprize.org. The Nobel Prize in Physics 1914 Awarded to Max von Laue "For His Discovery of the Diffraction of X-rays by Crystals". http://nobelprize.org/nobel_prizes/physics/laureates/1914/ (accessed 31-Oct-07)

(82) Nobelprize.org. The Nobel Prize in Physics 1915 Awarded to William H Bragg and William L Bragg "For Their Services in the Analysis of Crystal Structure by Means of X-rays". http://nobelprize.org/nobel_prizes/physics/laureates/1915/ (accessed 31-Oct-07)

(83) Ladd, M. F. C.; Palmer, R. A. *Structure Determination by X-ray Crystallography* 4th ed.; Kluwer Academic/Plenum: New York, 1993.

(84) Rietveld, H. M. A Profile Refinement Method for Nuclear and Magnetic Structures. *J. Appl. Crystallogr.* **1969,** *2*, 65-71.

(85) Cambridge Structural Database. http://www.ccdc.cam.ac.uk/products/csd/ (accessed 29-Oct-07); The Cambridge Crystallographic Data Centre

(86) Powder Diffraction File http://www.icdd.com/products/overview.htm (accessed 29-Oct-07); International Centre for Diffraction Data

(87) Kraus, W.; Nolze, G. *Powder Cell 2.4 for Windows (Downloadable from ftp://ftp.bam.de/Powder_Cell/pcw23.exe)*, Bundesanstalt für Materialfoschung und -prüfung: 2000.

(88) Owston, P. G. The Structure of Ice. *Q. Rev. Chem. Soc.* **1951,** *5*, 344-363.

(89) Jones, E. R.; Childers, R. L. *Contemporary College Physics* 2nd ed.; Addison-Wesley: Readings, Massachusetts, 1993.

(90) Skoog, D. A.; Holler, F. J.; Nieman, T. A. *Principles of Instrumental Analysis*. 5th edn ed.; Harcourt Brace College Publishers: Philadelphia, 1998.

(91) Nobelprize.org. The Nobel Prize in Physics 1930 Awarded to Venkata Raman "For His Work on the Scattering of Light and for the Discovery of the Effect Named After Him". http://nobelprize.org/nobel_prizes/physics/laureates/1901/ (accessed 31-Oct-07)

(92) Sum, A. K.; Burruss, R. C.; Sloan, E. D. Measurement of Clathrate Hydrates via Raman Spectroscopy. *J. Phys. Chem. B* **1997,** *101*, 7371-7377.

(93) Subramanian, S.; Kini, R. A.; Dec, S. F.; Sloan, E. D. Structural Transition Studies in Methane + Ethane Hydrates using Raman and NMR. *Ann. N. Y. Acad. Sci.* **2000,** *912*, 873-886.

(94) Subramanian, S.; Sloan, E. D. Trends in Vibrational Frequencies of Guests Trapped in Clathrate Hydrate Cages *J. Phys. Chem. B* **2002,** *106*, 4348-4355.

(95) Martin, A. J. P.; Synge, R. L. M. A New Form of Chromatogram Employing Two Liquid Phases. *Biochem. J.* **1941,** *35*, 1358-1368.

(96) James, A. T.; Martin, A. J. P. Gas-Liquid Partition Chromatography: The Separation and Micro-Estimation of Volatile Fatty Acids from Formic Acid to Dodecanoic Acid *Biochem. J.* **1952,** *50*, 679-690.

(97) Martin, A. J. P. The Development of Partition Chromatography, Nobel Lecture. http://nobelprize.org/nobel_prizes/chemistry/laureates/1952/martin-lecture.pdf (accessed 23-Jan-08)

(98) Nobelprize.org. The Nobel Prize in Chemistry 1952 Awarded to Archer Martin and Richard Synge "For Their Invention of Partition Chromatography". http://nobelprize.org/nobel_prizes/chemistry/laureates/1952/ (accessed 31-Oct-07)

(99) Fischer, K. New Method for the Volumetric Determination of Water Contents in Liquids and Solids. *Angew. Chem.* **1935,** *48*, 394-396.

(100) Wieland, G. *Water Determination by Karl Fischer Titration*. GIT VERLAG: Beerfelden, Germany, 1987.

(101) McDowell, C. A.; Raghunathan, P. A Nuclear Magnetic Resonance Study of Molecular Motion and "Guest" Structure in the Clathrate Hydrates of (i-C5H11)4NF and (n-C4H9)4NF. *Mol. Phys.* **1968,** *15*, 259-270.

(102) Nobelprize.org. The Nobel Prize in Physics 1952 Awarded to Felix Bloch and Edward Purcell "For Their Development of New Methods for Nuclear Magnetic Precision Measurements and Discoveries in Connection Therewith". http://nobelprize.org/nobel_prizes/physics/laureates/1952/ (accessed 28-Oct-07)

(103) Brown, W. H. *Organic Chemistry*. 1st ed.; Saunders College Publishing: Fort Worth, TX, 1995.

(104) Harmon, K. M.; Bulgarella, J. A. Hydrogen Bonding Part 59. NMR Study of N,N,N-Trimethyl-1-adamantylammonium, Trimethyl-i-pentylammonium, and Tetra-i-pentylammonium Ions; an Explanation for the Anomalous Hydration Behavior of N,N,N-Trimethyl-1-adamantylammonium Ion Salts. *J. Mol. Struct.* **1994,** *326*, 157-162.

(105) Sigma Aldrich Online Catalog, F-T NMR of Triethylamine. http://www.sigmaaldrich.com/spectra/fnmr/FNMR003893.PDF (accessed 04-May-07)

(106) Sigma Aldrich Online Catalog, F-T NMR of Tripropylamine. http://www.sigmaaldrich.com/spectra/fnmr/FNMR003898.PDF (accessed 04-May-07)

(107) Sigma Aldrich Online Catalog, F-T NMR of Trihexylamine. http://www.sigmaaldrich.com/spectra/fnmr/FNMR002298.PDF (accessed 04-May-07)

(108) Heinsen, M. J.; Pochapsky, T. C. Site-Selective Deuterium Labeling of the Tetrabutylammonium Cation. *J. Labelled Compd. Radiopharm.* **2000,** *43*, 473-480.

(109) Sigma Aldrich Online Catalog, F-T NMR of Tetrahexylammonium Hydrogensulfate http://www.sigmaaldrich.com/spectra/fnmr/FNMR008426.PDF (accessed 04-May-07)

(110) de Avellar, I. G. J.; Godoy, K.; Magalhães, d. New Quaternary Ammonium Salts Derived from Cardanol and Their Use as Phase Transfer Catalyst. *J. Braz. Chem. Soc.* **2000,** *11*, 22-26.

(111) Marsh, K. N.; Hughes, T. J.; Sloan, E. D. *Gas Hydrate Dissociation Kinetics and Calorimetry Measurements of Hydrate Enthalpies of Dissociation*; RR-194; Gas Processors Association: Tulsa, OK, 2008.

(112) Hafemann, D. R.; Miller, S. L. Clathrate Hydrates of Cyclopropane. *J. Phys. Chem.* **1969,** *73*, 1392-1397.

(113) Hawkins, R. E.; Davidson, D. W. Dielectric Relaxation in the Clathrate Hydrates of Some Cyclic Ethers. *J. Phys. Chem.* **1966,** *70*, 1889-1894.

(114) von Stackelberg, M.; Jahns, W. Solid Gas Hydrates. VI. The Work of Lattice Expansion. *Z. Elektrochem.* **1954,** *58*, 162-4.

(115) Hendriks, E. M.; Edmonds, B.; Moorwood, R. A. S.; Szczepanski, R. Hydrate structure stability in simple and mixed hydrates. *Fluid Phase Equilib.* **1996,** *117*, 193-200.

(116) Chou, I. M.; Sharma, A.; Burruss, R. C.; Hemley, R. J.; Goncharov, A. F.; Stern, L. A.; Kirby, S. H. Diamond-Anvil Cell Observations of a New Methane Hydrate Phase in the 100-MPa Pressure Range. *J. Phys. Chem. A* **2001,** *105*, 4664-4668.

(117) Chou, I. M.; Sharma, A.; Burruss, R. C.; Shu, J.; Mao, H.-k.; Hemley, R. J.; Goncharov, A. F.; Stern, L. A.; Kirby, S. H. Transformations in Methane Hydrates. *Proc. Natl. Acad. Sci. U. S. A.* **2000,** *97*, 13484-13487.

(118) Hirai, H.; Tanaka, T.; Kawamura, T.; Yamamoto, Y.; Yagi, T. Structural Changes in Gas Hydrates and Existence of a Filled Ice Structure of Methane Hydrate Above 40 GPa. *J. Phys. Chem. Solids* **2004,** *65*, 1555-1559.

(119) Ripmeester, J. A. Hydrate Research—From Correlations to a Knowledge-based Discipline: The Importance of Structure. *Ann. N. Y. Acad. Sci.* **2000,** *912*, 1-16.

(120) Deaton, W. M.; Frost, E. M. *Gas Hydrates and Their Relation to the Operation of Natural-Gas Pipe Lines*. U.S Bureau of Mines Monograph; 1946; Vol. 8, pp 101.

(121) Hester, K. C. Probing Hydrate Stability and Structural Characterization of Both Natural and Synthetic Clathrate Hydrates. Colorado School of Mines, Golden, CO, 2007.

(122) Hester, K. C.; Sloan, E. D. sII Structural Transitions from Binary Mixtures of Simple sI Formers. *Int. J. Thermophys.* **2005,** *26*, 95-106.

(123) Sugahara, T.; Makino, T.; Ohgaki, K. Isothermal Phase Equilibria for the Methane + Ethylene Mixed Gas Hydrate System. *Fluid Phase Equilib.* **2003,** *206*, 117-126.

(124) OLGA VERSION 5: The next generation dynamic multiphase flow simulator. http://www.sptgroup.com/olga/olga.html (accessed 09-Feb-2008)

(125) Jager, M.; Sloan, E. D. In *Structural Transition of Clathrate Hydrate Formed from a Natural Gas*, Proc. 4th International Conference on Gas Hydrates, Yokohama, Japan, 2002, May 19-23; Mori, Y. H., Ed. 2002, May 19-23; 575-579.

(126) Stern, L. A.; Kirby, S. H.; Durham, W. B. Peculiarities of Methane Clathrate Hydrate Formation and Solid-State Deformation, Including Possible Superheating of Water Ice. *Science* **1996,** *273*, 1843-1848.

(127) Hwang, M. J.; Wright, D. A.; Kapur, A.; Holder, G. D. An Experimental Study of Crystallization and Crystal Growth of Methane Hydrates from Melting Ice. *J. Inclusion Phenom. Macrocyclic Chem.* **1990,** *8*, 103-116.

(128) Stern, L. A.; Kirby, S. H.; Durham, W. B. Polycrystalline Methane Hydrate: Synthesis from Superheated Ice, and Low-Temperature Mechanical Properties. *Energy Fuels* **1998,** *12*, 201-211.

(129) Ivanic, J. Hydrate Plug Dissociation: Investigations of Two-Sided Depressurization. Colorado School of Mines Golden, CO, 2005.

(130) Lysne, D.; Saeter, G.; Lund, A. In *Evaluation of Potential Hydrate Problems for Tordis Field Development*, NPF Conference Multiphase Transportation III-Present Application and Future Trends, Roros, Norway, Sept, 1992; 1992; 1-18.

(131) Berge, L.; Gjertsen, L.; Lysne, D. In *The Importance of Porosity and Permeability for Dissociation of Hydrate Plugs in Pipes*, Proceedings of the 2nd International Conference on Natural Gas Hydrates, Toulouse, France, June 2-6, 1996; Monfort, J. P., Ed. Association PROGEP: Toulouse, France, 1996; 533-540.

(132) Kelkar, S. K.; Selim, M. S.; Sloan, E. D. Hydrate Dissociation Rates in Pipelines. *Fluid Phase Equilib.* **1998,** *150-151*, 371-382.

(133) Lysne, D. An Experimental Study of Hydrate Plug Dissociation by Pressure Reduction. University of Trondheim, Trondheim, Norway, 1995.

(134) Austvik, T.; Hustvedt, E.; Meland, B.; Berge, L. I.; Lysne, D. In *Tommeliten Gamma Field Hydrate Experiments*, 7th International Conference on Multiphase Flow, Cannes, France, 1996; Wilson, A., Ed. Mechanical Engineering Publications: London, 1996; 539-552.

(135) Handa, Y. P. Compositions, Enthalpies of Dissociation, and Heat Capacities in the Range 85 to 270 K for Clathrate Hydrates of Methane, Ethane, and Propane, and Enthalpy of Dissociation of Isobutane Hydrate, as Determined by a Heat-Flow Calorimeter. *J. Chem. Thermodyn.* **1986,** *18*, 915-21.

(136) Handa, Y. P. Calorimetric Determinations of the Compositions, Enthalpies of Dissociation, and Heat Capacities in the Range 85 to 270 K for Clathrate Hydrates of Xenon and Krypton. *J. Chem. Thermodyn.* **1986,** *18*, 891-902.

(137) Handa, Y. P. A Calorimetric Study of Naturally Occurring Gas Hydrates. *Ind. Eng. Chem. Res.* **1988,** *27*, 872-874.

(138) Lievois, J. S.; Perkins, R.; Martin, R. J.; Kobayashi, R. Development of an Automated, High Pressure Heat Flux Calorimeter and it Application to Measure the Heat of Dissociation and Hydrate Numbers of Methane Hydrate. *Fluid Phase Equilib.* **1990,** *59*, 73-97.

(139) Rueff, R. M.; Sloan, E. D.; Yesavage, V. F. Heat Capacity and Heat of Dissociation of Methane Hydrates. *AIChE J.* **1988,** *34*, 1468-76.

(140) Nagayev, V. B.; Gritsenko, A. I.; Murin, V. I. In *Determination of Heat of CO2 Hydrate Formation*, Transactions of the 8th All-Union Conference on Calorimetry and Chemical Thermodynamics, Ivanovo, U.S.S.R, 1979; 1979; 58.

(141) Cherskii, N. V.; Groisman, A. G.; Nikitina, L. M.; Tsarev, V. P. Results of the First Experimental Determination of Heats of Decomposition of Natural Gas Hydrates. *Dokl. Akad. Nauk SSSR* **1982,** *265*, 185-9 [Geochem.].

(142) Kang, S. P.; Lee, H.; Ryu, B. J. Enthalpies of Dissociation of Clathrate Hydrates of Carbon Dioxide, Nitrogen, (Carbon Dioxide + Nitrogen), and (Carbon Dioxide + Nitrogen + Tetrahydrofuran). *J. Chem. Thermodyn.* **2001,** *33*, 513-521.

(143) Marsh, K. N.; Gao, J. Enthalpies of Formation of Gas Hydrates. *Annual Convention Proceedings - Gas Processors Association* **2004,** *83*, 1-10.

(144) Handa, Y. P.; Hawkins, R. E.; Murray, J. J. Calibration and Testing of a Tian-Calvet Heat-Flow Calorimeter. Enthalpies of Fusion and Heat Capacities for Ice and Tetrahydrofuran Hydrate in the Range 85 to 270 K. *J. Chem. Thermodyn.* **1984,** *16*, 623-32.

(145) Levik, O. I. Thermophysical and Composition Properties of Natural Gas Hydrates. Norwegian University of Science and Technology, Trondheim, Norway, 2000.

(146) Rydzy, M. B.; Schicks, J. M.; Naumann, R.; Erzinger, J. Dissociation Enthalpies of Synthesized Multicomponent Gas Hydrates with Respect to the Guest Composition and Cage Occupancy. *J. Phys. Chem. B* **2007,** *111*, 9539-9545.

(147) Anderson, G. K. Enthalpy of Dissociation and Hydration Number of Carbon Dioxide Hydrate from the Clapeyron Equation. *J. Chem. Thermodyn.* **2003,** *35*, 1171-1183.

(148) van der Waals, J. H.; Platteeuw, J. C. Validity of Clapeyrons Equation for Phase Equilibria Involving Clathrates. *Nature* **1959,** *183*, 462-462.

(149) Barrer, R. M.; Stuart, W. I. Non-Stoicheiometric Clathrate Compounds of Water. *Proc. R. Soc. London, A* **1957,** *243*, 172-189.

(150) Glew, D. N. Some Stocheiometric Gas Hydrates. *Nature* **1959,** *184*, 545-546.

(151) Roberts, O. L.; Brownscombe, E. R.; Howe, L. S. Methane and Ethane Hydrates. *Oil Gas J.* **1940,** *39*, 37-42.

(152) Barrer, R. M.; Edge, A. V. J. Gas Hydrates Containing Argon, Krypton and Xenon: Kinetics and Energetics of Formation and Equilibria. *Proc. R. Soc. London, A* **1967,** *300*, 1-24.

(153) Skovborg, P.; Rasmussen, P. Comments on: Hydrate dissociation enthalpy and guest size. *Fluid Phase Equilib.* **1994,** *96*, 223-231.

(154) Sloan, E. D.; Fleyfel, F. Hydrate Dissociation Enthalpy and Guest Size. *Fluid Phase Equilib.* **1992,** *76*, 123-40.

(155) Sloan, E. D.; Fleyfel, F. Reply to "Comments on: Hydrate Dissociation Enthalpy and Guest Size". *Fluid Phase Equilib.* **1994,** *96*, 233-5.

(156) Anderson, G. K. Enthalpy of Dissociation and Hydration Number of Methane Hydrate from the Clapeyron Equation. *J. Chem. Thermodyn.* **2004,** *36*, 1119-1127.

(157) Glew, D. N. Aqueous Nonelectrolyte Solutions. Part XVIII. Equilibrium Pressures of Two Methane Hydrates With Water. Formulae and Dissociation Thermodynamic Functions for the Structures I and II Methane Hydrates. *Can. J. Chem.* **2002,** *80*, 418-439.

(158) Yoon, J.-H.; Yamamoto, Y.; Komai, T.; Haneda, H.; Kawamura, T. Rigorous Approach to the Prediction of the Heat of Dissociation of Gas Hydrates. *Ind. Eng. Chem. Res.* **2003,** *42*, 1111-1114.

(159) Bollavaram, P.; Sloan, E. D. In *Pipeline Hydrate Dissociation: Effects of Crystal Structure*, Proc. 4th International Conference on Gas Hydrates, Yokohama, Japan, May 19-23, 2002; Mori, Y. H., Ed. 2002; 947-951.

(160) Wilcox, W. I.; Carson, D. B.; Katz, D. L. Natural Gas Hydrates. *Ind. Eng. Chem.* **1941,** *33*, 662-665.

(161) Carson, D. B.; Katz, D. L. Natural Gas Hydrates. *Trans. AIME* **1942,** *146*, 150-158.

(162) Happel, J.; Hnatow, M. A.; Meyer, H. The Study of Separation of Nitrogen from Methane by Hydrate Formation Using a Novel Apparatus. *Ann. N. Y. Acad. Sci.* **1994,** *715*, 412-424.

(163) Kini, R. A. NMR Studies of CH_4, C_2H_6, and C_3H_8 Hydrates: Structure, Kinetics, and Thermodynamics. Colorado School of Mines, Golden, Co, 2002.

(164) Fleyfel, F.; Devlin, J. P. Carbon Dioxide Clathrate Hydrate Epitaxial Growth: Spectroscopic Evidence for Formation of the Simple Type-II Carbon Dioxide Hydrate. *J. Phys. Chem.* **1991,** *95*, 3811-3815.

(165) Staykova, D. K.; Kuhs, W. F.; Salamatin, A. N.; Hansen, T. Formation of Porous Gas Hydrates from Ice Powders: Diffraction Experiments and Multistage Model *J. Phys. Chem. B* **2003,** *107*, 10299-10311.

(166) Schicks, J. M.; Ripmeester John, A. The Coexistence of Two Different Methane Hydrate Phases under Moderate Pressure and Temperature Conditions: Kinetic versus Thermodynamic Products. *Angew. Chem., Int. Ed.* **2004,** *43*, 3310-3313.

(167) Schicks, J. M.; Naumann, R.; Erzinger, J.; Hester, K. C.; Koh, C. A.; Sloan, E. D. Phase Transitions in Mixed Gas Hydrates: Experimental Observations versus Calculated Data *J. Phys. Chem. B* **2006,** *110*, 11468-11474.

(168) Lemmon, E. W.; Huber, M. L.; McLinden, M. O. *NIST Standard Reference Database 23: Reference Fluid Thermodynamic and Transport Properties-REFPROP*, 7.1; National Institute of Standards and Technology: Gaithersburg, MD, 2003.

(169) Kamata, Y.; Yamakoshi, Y.; Ebinuma, T.; Oyama, H.; Shimada, W.; Narita, H. Hydrogen Sulfide Separation Using Tetra-n-butyl Ammonium Bromide Semi-clathrate (TBAB) Hydrate. *Energy Fuels* **2008,** *19*, 1717-1722.

(170) Tohidi, B.; Burgass, R. W.; Danesh, A.; Østergaard, K. K.; Todd, A. C. Improving the Accuracy of Gas Hydrate Dissociation Point Measurements. *Ann. N. Y. Acad. Sci.* **2000,** *912*, 924-931.

(171) Mao, W. L.; Mao, H.-K.; Goncharov, A. F.; Struzhkin, V. V.; Guo, Q.; Hu, J.; Shu, J.; Hemley, R. J.; Somayazulu, M.; Zhao, Y. Hydrogen Clusters in Clathrate Hydrate. *Science* **2002,** *297*, 2247-9.

(172) Lipkowski, J.; Komarov, V. Y.; Rodionova, T. V.; Dyadin, Y. A.; Aladko, L. S. The Structure of Tetra-Butyl-Ammonium Bromide Hydrate $(C_4H_9)_4NBr \cdot 2^1/_3H_2O$. *J. Supramol. Chem.* **2002,** *2*, 435-439.

(173) Darbouret, M.; Cournil, M.; Herri, J. M. In *Rheological Study of a Hydrate Slurry for Air Condtioning Applications*, Proceedings of the Fifth International Conference on Gas Hydrates, Trondheim, Norway, Jun 12-16, 2005; 2005.

(174) Tohidi, B.; Danesh, A.; Todd, A. C. Modelling Single and Mixed Electrolyte Solutions and its Applications to Gas Hydrates. *Chem. Eng. Res. Des.* **1995,** *73A*, 464-472.

(175) Tohidi-Kalorazi, B. Gas Hydrate Equilibria in the Presence of Electrolyte Solutions. Herriot-Watt University, Edinburgh, U.K, 1995.

(176) Strobel, T. A.; Koh, C. A.; Sloan, E. D. Hydrogen Storage Properties of Clathrate Hydrate Materials. *Fluid Phase Equilib.* **2007,** *261*, 382-389.

(177) Ahmadloo, F.; Mali, G.; Chapoy, A.; Tohidi, B. In *Gas Separation and Storage Using Semi-Clathrate Hydrates*, Proceedings of the 6th International Conference on Gas Hydrates, Vancouver, Canada, July 6-10, 2008; University of British Columbia Information Repository (circle.ubc.ca), 2008.

(178) Gudmundsson, J. S.; Andersson, V.; Dugut, I.; Levik, O. I.; Mork, M. In *NGH on FPSO - Slurry Process and Cost Estimate*, Proceedings of the SPE Annual Technical Conference, Houston, Tx, October 3-6, 1999; 1999.

(179) Gudmundsson, J. S.; Andersson, V.; Levik, O. I. In *Gas Storage and Transport Using Hydrates*, Proceedings of the Offshore Mediterranean Conference, Ravenna, Italy, Mar 19-21, 1997; 1997.

(180) Gudmundsson, J. S.; Børrehaug, A. Natural Gas Hydrate - An Alternative to Liquefied Natural gas. *Petrol. Rev.* **1996,** *50*, 232-235.

(181) Gudmundsson, J. S.; Graff, O. F. In *Hydrate Non-Pipeline Technology for Transport of Natural Gas*, Proceedings of the 22nd World Gas Conference, Tokyo, Japan, June 1-5, 2003; 2003.

(182) Gudmundsson, J. S.; Mork, M. In *Stranded Gas to Hydrate for Storage and Transport*, 2001 International Gas Research Conference, Amsterdam, Netherlands, November 5-8, 2001; 2001.

(183) Gudmundsson, J. S.; Mork, M.; Graff, O. F. In *Hydrate Non-Pipeline Technology*, Proceedings of the 4th International Conference on Gas Hydrates, Yokohama, Japan, May 19-23, 2002; 2002.

(184) Yakushev, V. S.; Istomin, V. A. Gas-Hydrates Self-Preservation Effect. In *Physics and Chemistry of Ice*, Maeno, N.; Hondoh, T., Eds.; Hokkaido Univ. Press: Sapporo, Japan, 1992; pp 136-139.

(185) Gudmundsson, J. S.; Parlaktuna, M.; Khokar, A. A. Storing Natural Gas as Frozen Hydrate. *SPE Prod. Facil.* **1994,** *9*, 69-73.

(186) Børrehaug, A.; Gudmundsson, J. S. In *Gas Transportation in Hydrate Form*, EUROGAS 96, Trondheim, Norway, 3-5 Jun, 1996; 1996; 35-41.

(187) Gudmundsson, J. S.; Andersson, V.; Levik, O. I.; Mork, M. Hydrate Technology for Capturing Stranded Gas. *Ann. N. Y. Acad. Sci.* **1999,** *912*, 403-410.

(188) Hove, A. M.; G, L.; Gudmundsson, J. S. In *NGT Technology - A Promising Concept for Gas Storage and Transport*, Proceedings of Gas to Liquids II, London, UK, Sep 22-23, 1999; 1999.

(189) Tse, J. S. Thermal Expansion of the Clathrate Hydrates of Ethylene Oxide and Tetrahydrofuran. *J. Phys. Colloques* **1987,** *48*, C1-543-C1-549.

(190) Stern, L. A.; Circone, S.; Kirby, K. B.; Durham, W. B. Temperature, Pressure, and Compositional Effects on Anomalous or "Self" Preservation of Gas Hydrates. *Can. J. Phys.* **2003,** *81*, 271-283.

(191) Ohtani, N.; Yamashita, T.; Hosoda, Y. Phase Behavior of Tetrabutylammonium Salt/Oil/Water/Inorganic Salt Four-Component Systems. *Bull. Chem. Soc. Jpn.* **2000,** *73*, 2269-2277.

(192) Aladko, L. S.; Dyadin, Y. A.; Mikina, T. V. Diisoamyldibutylammonium Bromide Clathrate Hydrates. *Russ. J. Gen. Chem.* **2002,** *72*, 364-367.

(193) Owe Berg, T. G. Liquid Structure and Solubility of Sparingly Soluble Salts in Water. *Acta Chem. Scand.* **1953,** *7*, 1313-1322.

(194) Sharma, R. K.; Fry, J. L. Instability of Anhydrous Tetra-n-alkylammonium Fluorides. *J. Org. Chem.* **1983,** *48*, 2112-2114.

(195) Kamata, Y.; Yamakoshi, Y.; Ebinuma, T.; Oyama, H.; Shimada, W.; Narita, H. Hydrogen Sulfide Separation Using Tetra-n-butyl Ammonium Bromide Semi-clathrate (TBAB) Hydrate. *Energy Fuels* **2005,** *19*, 1717-1722.

(196) Huheey, J.; Keiter, E. A.; Keiter, R. L. *Inorganic Chemistry, Principles of Structure and Reactivity*. 4th ed.; Harper Collins: New York, 1993.

(197) Wells, A. F. *Structural Inorganic Chemistry*. 5th ed.; Oxford University Press: Oxford, U.K., 1984.

(198) Ferraro, J. R.; Nakamoto, K.; Brown, C. W. *Introductory Raman Spectroscopy*. 2nd ed.; Academic Press: Amsterdam, 2003.

(199) Laugier, J.; Bochu, B. *GRETEP v2: Grenoble Thermal Ellipsoids Plot Program (Downloadable from http://www.ccp14.ac.uk/ccp/web-mirrors/lmgp-laugier-bochu/gretep.zip)*, Laboratoire des Matériaux et du Génie Physique, Ecole Nationale Supérieure de Physique de Grenoble (INPG): 2003.

(200) Macrae, C. F.; Edgington, P. R.; McCabe, P.; Pidcock, E.; Shields, G. P.; Taylor, R.; Towler, M.; van de Streek, J. *Mercury 1.4.2 (build 2) (Downloadable from http://www.ccdc.cam.ac.uk/free_services/mercury/downloads/Mercury_1.4.2/mercury_1_4_2.exe)*, The Cambridge Crystallographic Data Centre: 2007.

(201) Schuster, C. E. ExxonMobil High-Pressure Process Technology for LDPE. In *Handbook of Petrochemicals Production Processes*, 1st ed.; Meyers, R. A., Ed. McGraw Hill: New York, 2005; pp 14.45-14.58.

APPENDICES

Appendix A Crystal structures and space groups

Solid crystals are composed of atoms arranged in a repetitive pattern in three dimensions. The three dimensional arrays are referred to as a lattice which Ladd and Palmer[83] define as "a regular, infinite arrangement of points in which every point has the same environment as any other point". The "unit cell" as "the simplest array of points from which a crystal can be created".[196] Unit cells have one of seven basic shapes or crystal systems, refer to Table A.1, these are cubic, tetragonal, orthorhombic, trigonal (or rhombohedral), hexagonal, monoclinic or triclinic. There are only fourteen possible lattices, referred to as Bravais lattices (named after the French scientist Auguste Bravais), for the seven crystal systems. Bravais lattice centerings may be primitive (P), body-centred (I), face-centred (F), face centred on one set of faces (C), or rhombohedral (R). Figure A.1 shows the fourteen Bravais lattices.

Table A.1 – The seven crystal systems. (Modified from Wells[197]).

System	**Relations between edges and angles of unit cell**	**Lengths and angles to be specified**
Cubic	$a = b = c$ $\alpha = \beta = \gamma = 90°$	a
Tetragonal	$a = b \neq c$ $\alpha = \beta = \gamma = 90°$	a, c
Orthorhombic	$a \neq b \neq c$ $\alpha = \beta = \gamma = 90°$	a, b, c
Monoclinic	$a \neq b \neq c$ $\alpha = \gamma = 90° \neq \beta$	a, b, c β
Triclinic	$a \neq b \neq c$ $\alpha \neq \beta \neq \gamma \neq 90°$	a, b, c α, β, γ
Hexagonal	$a = b \neq c$ $\alpha = \beta = 90°$ $\gamma = 90°$	a, c
Trigonal (Rhombohedral)	$a = b = c$ $\alpha = \beta = \gamma \neq 90°$	a α

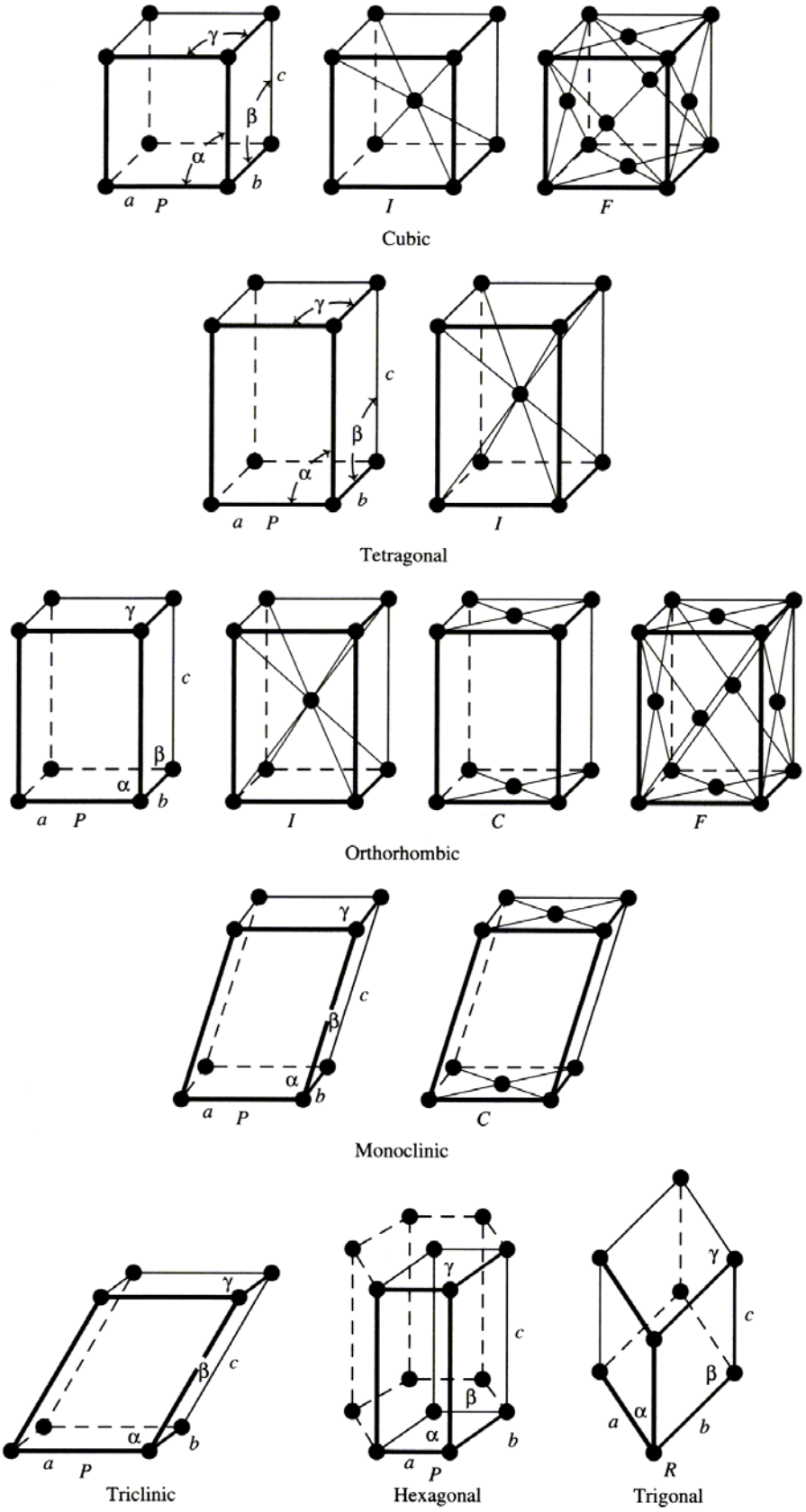

Figure A.1 – The fourteen Bravais lattices groups according to the seven crystal systems. (Reproduced from Huheey et al.[196]).

The unit cell can be defined as the smallest unit that can generate the crystal structure with only translation operations. The asymmetric unit on the other hand is the smallest unit upon which symmetry operations will allow the unit cell to be generated. Space groups in the commonly used Hermann-Mauguin notation describe both the centrings of the lattice in terms of P, I, F, C or R as well as the symmetry operations that are required to generate the unit cell from the asymmetric unit. The space group symbolism is described in Table A.2 the first symbol is the lattice centring, the second the principal axis, further symbols may describe axes of rotation, screw axes, mirror planes or glide planes. A detailed description of these symmetry operations may be found in Ladd and Palmer,[83] Huheey et al.[196] or Ferraro et al.[198]

Table A.2 – Hermann-Manguin space group symbolism. (Modified from Ferraro et al.[198]).

First symbol refers to the Bravais lattice
P = primitive
C = centred lattice
F = face centred
I = body centred
R = rhombohedral
Principal axis of ration given number *n* = order
e.g., 2 = twofold axis of rotation
For screw axis, n_p: n = order of axis, *p/n* = fraction of primitive lattice over which translation parallel to screw axis occurs
e.g., $P2_1$ = primitive lattice with a twofold axis of rotation, translation, one-half unit cell
Mirror plane = *m*
Glide planes = symbols *a*, *b*, *c* along (*a*), (*b*), (*c*) axes
symbol *n* = (*b* + *c*)/2 or (*a* + *b*)/2
symbol *d* = (*a* + *b*)/4 or (*b* + *c*)/4 or (*a* + *c*)/4
e.g. $P2_1$/m; = mirror plane perpendicular to the principal axis*
C2/c; = glide plane axis perpendicular to principal axis*

* The slash indicates the glide plane is perpendicular to the principal axis (if a slash is not present the glide plane is parallel to the principal axis)

The specification of the coordinates of atoms of the asymmetric unit, the space group and the unit cell parameters (*a*, *b* and *c*) fully define the crystal structure. If the asymmetric unit coordinates are expressed in fractions of the unit cell parameters, *x*, *y* and *z*, then space groups allow the generation of a set of positions based on the asymmetric unit coordinates generally described by $(\pm x \pm f_x, \pm y \pm f_y, \pm z \pm f_z)$, where f_x, f_y, f_z are a fraction of the unit cell parameter in the parameters and may differ for each generated set of position (and may be equal to zero). Some example of these can be seen in the sixth column of Table B.1.

Appendix B Size calculation of $4^4 5^4$ cage of tetraisopentylammonium fluoride, TIPAF·27H_2O

The size of a $4^4 5^4$ cage was calculated from Lipkowski et al.'s[67] crystallographic data for tetraisopentylammonium fluoride with 27 waters of hydration (TIPAF·27H_2O). The data was initially entered into the computer program GRETEP v2 [199] and was then exported via a CIF (crystallographic information file) to Mercury 1.4.2 [200] for visualisation, a partially visible $5^4 4^4$ cage was expanded and its twelve vertices (oxygen atoms) were selected. A centroid was produced at the centre of the twelve oxygen atoms (at fractional coordinates x_{fr} = 0.5, y_{fr} = 0.25, z_{fr} = 0.875). The generated atoms were then exported to Microsoft Excel where the distance between each atom and the centroid was calculated. The distance of each oxygen atom from the centroid was calculated using the formula $d = \sqrt{(a\Delta x_{fr})^2 + (b\Delta y_{fr})^2 + (c\Delta z_{fr})^2}$, where d is the distance, a, b and c are the lattice parameters, and Δx_{fr}, Δy_{fr}, and Δz_{fr} are the deviations of the fractional coordinates of each oxygen atom from the centroid. The distances to the centre of the cage (or centroid) are listed in Table B.1, giving a mean value of 3.331 Å. Using the van der Waals radius of oxygen of 1.4 Å that Davidson[11] used to calculate the mean "free diameters" of the 5^{12}, $5^{12}6^2$ and $5^{12}6^4$ cages of sI and sII hydrate the mean "free diameter" of the $5^4 4^4$ cage is 3.9 Å (2×3.331 - 2×1.4). This indicates that molecules the size of Argon (largest van der Waals diameter = 3.8 Å)[11] and smaller molecules such as hydrogen, helium and neon could fit inside the cage. Slightly larger molecules on the other hand such as krypton and oxygen both with a largest van der Waals diameter of 4.0 Å [11] as well as methane, nitrogen, hydrogen sulfide, each with a largest van der Waals diameter of 4.1 Å [11] could probably not fit unless the cage was able to expand slightly to accommodate these larger molecules. The non-spherical nature of the cage may also mean that only appropriately shaped molecules may fit, however this is probably only important when the molecule's largest van der Waals diameter approaches 3.9 Å. One way to quantify the non-sphericity of a cage is to compare the maximum and minimum distances of atoms that make up the vertices of a cage to the mean value for all the atoms. Deviations of the maximum and minimum distances from the cage centre to the cage atoms relative to the mean distance from the cage centre to cage atoms are presented in Table B.2. Data for sI 5^{12}, sII 5^{12}, sI $5^{12}6^2$ and sII $5^{12}6^4$ are compared to that for the $4^4 5^4$ cage. It is clear that the $4^4 5^4$ is the most non-spherical cage by a large margin, with distance to the centre of the cage deviating from the mean value by

approximately ± 15 %, compared to the next value of greatest magnitude of 7.3 % for the sII $5^{12}6^2$ cage.

Table B.1 – Generated atoms making up a $5^4 4^4$ cage.[a]

Label[b]	x_{fr}	y_{fr}	z_{fr}	d/Å	Symm. op.[b]
O1	0.3672	0.1741	0.8075	2.830	1.25-y,-1/4+x,3/4+z
O1	0.4241	0.3828	0.9425	2.830	x,-1/2+y,1-z
O1	0.5759	0.1172	0.9425	2.830	1-x,1-y,1-z
O1	0.6328	0.3259	0.8075	2.830	-1/4+y,3/4-x,3/4+z
O2	0.4171	0.2628	1.0513	3.333	1-x,1/2-y,1+z
O2	0.4872	0.1671	0.6987	3.333	1/4+y,3/4-x,3/4-z
O2	0.5128	0.3329	0.6987	3.333	3/4-y,-1/4+x,3/4-z
O2	0.5829	0.2372	1.0513	3.333	x,y,1+z
O4	0.378	0.3398	0.7086	3.828	1/4+y,3/4-x,3/4-z
O4	0.4102	0.128	1.0414	3.828	x,y,1+z
O4	0.5898	0.372	1.0414	3.828	1-x,1/2-y,1+z
O4	0.622	0.1602	0.7086	3.828	3/4-y,-1/4+x,3/4-z

[a] Atoms generated from data of Lipkowski et al.[67] for TIPAF·27H_2O, all values/entries except distances, d, are from Mercury 1.4.2.[200] Fractional coordinates of the atoms in the unit cell, x_{fr}, y_{fr} and z_{fr} ($x_{fr} = x/a, y_{fr} = y/b, z_{fr} = z/c$, where a, b and c are the lattice parameters) are listed for the atoms generated from the labelled oxygen atom in the first column generated using the symmetry operation in the "Symm. Op." column. For Lipkowski et al.'s[67] TIPAF·27H_2O structure the lattice parameters at -50 °C where used: $a = b$ = 16.894 Å, c = 17.111 Å. (tetragonal), using the parameters at 0 °C generated d values of 2.838 Å, 3.342 Å and 3.839 Å and a mean free cage diameter that was 0.02 Å larger (3.88 Å versus 3.86 Å)

[b] Labelled oxygen atoms using the numbering of Lipkowski et al.[67], the symmetry operations to generate the positions listed are in the sixth column of the table labelled "Symm. Op.".

Table B.2 – Comparison of sphericity of cages.[a]

	Distances from cage centre /Å				
	sI 5^{12}	sII 5^{12}	sI $5^{12}6^2$	sII $5^{12}6^4$	4^45^4
max.	3.96	3.748	4.645	4.729	3.828
min.	3.83	3.956	4.06	4.635	2.830
mean	3.91	3.902	4.33	4.683	3.331
	Percentage deviations from mean value				
	sI 5^{12}	sII 5^{12}	sI $5^{12}6^2$	sII $5^{12}6^4$	4^45^4
max dev.	1.3%	-3.9%	7.3%	1.0%	14.9%
min dev.	-2.0%	1.4%	-6.2%	-1.0%	-15.0%

[a] Data for cages other than 4^45^4 from table II of Davidson.[11]

Appendix C The electrical circuit-thermal analogy

In the electrical circuit thermal analogy the thermal properties listed on the left hand side of Table C.1 are compared to the electrical properties on the right hand side. Electrical laws represented on the left at the bottom of Table C.1 can be applied analogously. Kirchhoff's current law, the last equation at the bottom right of Table C.1, can be applied to junctions/nodes to generate equations in terms of heat (thermal equivalent) that describe the behaviour of the circuit.

Table C.1 – Electrical equivalents of thermal properties for the electrical circuit analogy. (Adapted from Claudy[75]).

Thermal	symbol	unit		Electrical	symbol	unit
Temperature	T	K	↔	Voltage/Electrical Potential	E	V
Heat	q	J	↔	Quantity of charge	Q	C
Heat flow rate	Φ	W	↔	Current	I	A
Thermal resistance	R	$\mathrm{K \cdot W^{-1}}$	↔	Electrical resistance	R_{elec}	Ω
Heat capacity at constant pressure*	C_p	$\mathrm{J \cdot K^{-1}}$	↔	Electrical capacitance	C_{elec}	F
			Equations			
$\Phi = \mathrm{d}q/\mathrm{d}t$			↔	$I = \mathrm{d}Q/\mathrm{d}t$		
$\Phi = \Delta T/R$			↔	$I = \Delta E/R_{\mathrm{elec}}$		
$\mathrm{d}q = C_p \mathrm{d}T$			↔	$\mathrm{d}Q = C_{\mathrm{elec}} \mathrm{d}E$		
$\Phi = C_p \, \mathrm{d}T/\mathrm{d}t$			↔	$I = C_{\mathrm{elec}} \, \mathrm{d}E/\mathrm{d}t$		
$\sum_{\mathrm{node}} \Phi = 0$			↔	$\sum_{\mathrm{node}} I = 0$		

*Note: The specific heat capacity at constant pressure, c_p (in units of Joules per Kelvin per kilogram), is defined as: $c_p = C_p/m$.

Appendix D Mole balance on hydrate dissociation

Hydrate dissociation can be represented by the equation:

$$\mathrm{G}\cdot n\mathrm{H_2O} \rightarrow N_\mathrm{V}\mathrm{V} + N_\mathrm{Aq}\mathrm{Aq}\,, \tag{A.1}$$

where G represents the hydrate guest, n the hydrate number (moles of water per mole of guest), V represents the vapour phase, N_V represents the moles of vapour phase (subscript V = vapour phase), Aq represents the aqueous phase and N_Aq represents the moles of aqueous phase (subscript Aq = aqueous phase).

If a mole balance is performed based on eq (A.1) then for the guest:

$$1 = x_\mathrm{V}^\mathrm{G} N_\mathrm{V} + x_\mathrm{Aq}^\mathrm{G} N_\mathrm{Aq}\,, \tag{A.2}$$

where x_V^G is the mole fraction of the guest in the vapour phase and x_Aq^G is the mole fraction of the guest in the aqueous phase. A similar mole balance may be performed on the water:

$$n = x_\mathrm{V}^{\mathrm{H_2O}} N_\mathrm{V} + x_\mathrm{Aq}^{\mathrm{H_2O}} N_\mathrm{Aq}\,, \tag{A.3}$$

where $x_\mathrm{V}^{\mathrm{H_2O}}$ is the mole fraction of water in the vapour phase and $x_\mathrm{Aq}^{\mathrm{H_2O}}$ is the mole fraction of water in the aqueous phase.

Solving eqs (A.2) and (A.3) simultaneously leads to:

$$N_\mathrm{Aq} = \frac{n - (n+1)\, x_\mathrm{V}^{\mathrm{H_2O}}}{1 - x_\mathrm{V}^{\mathrm{H_2O}} - x_\mathrm{Aq}^\mathrm{G}}\,, \tag{A.4}$$

and

$$N_{\mathrm{V}} = \frac{1-(n+1)x_{\mathrm{Aq}}^{\mathrm{G}}}{1-x_{\mathrm{V}}^{\mathrm{H2O}}-x_{\mathrm{Aq}}^{\mathrm{G}}}. \tag{A.5}$$

These equations have been defined in terms of the mole fractions that tend towards zero under the "idealised conditions" of no solubility of the guest in water and no vaporisation of the water in to the vapour phase. So by setting $x_{\mathrm{V}}^{\mathrm{H_2O}} = 0$ and $x_{\mathrm{Aq}}^{\mathrm{G}} = 0$ the result is:

$$N_{\mathrm{Aq}} = n, \tag{A.6}$$

and

$$N_{\mathrm{V}} = 1. \tag{A.7}$$

Using eqs (A.6) and (A.7) in eq (A.1) the following is obtained:

$$\mathrm{G}{\cdot}n\mathrm{H_2O} \rightarrow \mathrm{G} + n\mathrm{H_2O}, \tag{A.8}$$

otherwise for non-idealised conditions:

$$\mathrm{M}{\cdot}n\mathrm{H_2O} \rightarrow \left[\frac{1-(n+1)x_{\mathrm{Aq}}^{\mathrm{G}}}{1-x_{\mathrm{V}}^{\mathrm{H2O}}-x_{\mathrm{Aq}}^{\mathrm{G}}}\right]\mathrm{V} + \left[\frac{n-(n+1)x_{\mathrm{V}}^{\mathrm{H_2O}}}{1-x_{\mathrm{V}}^{\mathrm{H_2O}}-x_{\mathrm{Aq}}^{\mathrm{G}}}\right]\mathrm{Aq}. \tag{A.9}$$

Anderson (eq 6, p1175),[147] uses the following equation for the volume difference:

$$\Delta V = \left[1-\frac{nx_{\mathrm{Aq}}^{\mathrm{G}}}{1-x_{\mathrm{Aq}}^{\mathrm{G}}}\right]V_V + nV_{\mathrm{Aq}} - V_{\mathrm{H}}. \tag{A.10}$$

From eq (A.5) for the moles of vapour if it is assumed that $x_{\mathrm{V}}^{\mathrm{H_2O}} = 0$ (no vaporisation of water) then:

$$N_{\mathrm{V}} = \frac{1-\left(n+1\right)x_{\mathrm{Aq}}^{\mathrm{G}}}{1-x_{\mathrm{V}}^{\mathrm{H2O}}-x_{\mathrm{Aq}}^{\mathrm{G}}} = \frac{1-\left(n+1\right)x_{\mathrm{Aq}}^{\mathrm{G}}}{1-x_{\mathrm{Aq}}^{\mathrm{G}}} = \frac{1-x_{\mathrm{Aq}}^{\mathrm{M}}-nx_{\mathrm{Aq}}^{\mathrm{G}}}{1-x_{\mathrm{Aq}}^{\mathrm{G}}} = 1-\frac{nx_{\mathrm{Aq}}^{\mathrm{G}}}{1-x_{\mathrm{Aq}}^{\mathrm{G}}}, \tag{A.11}$$

which is the same as what Anderson has used in eq (A.10).

From eq (A.4) for the mole of aqueous solution if it is assumed that $x_{\mathrm{V}}^{\mathrm{H_2O}} = 0$ then:

$$N_{\mathrm{Aq}} = \frac{n-\left(n+1\right)x_{\mathrm{V}}^{\mathrm{H_2O}}}{1-x_{\mathrm{V}}^{\mathrm{H_2O}}-x_{\mathrm{Aq}}^{\mathrm{G}}} = \frac{n}{1-x_{\mathrm{Aq}}^{\mathrm{G}}}, \tag{A.12}$$

Anderson neglects the $x_{\mathrm{Aq}}^{\mathrm{G}}$ in the denominator for the aqueous volume and gives eq (A.6).

Appendix E Gas mixture preparation mixing concerns (methane + ethane mixtures)

Figure E.1 below shows a density temperature phase diagram for ethane. If the amount of ethane added to the mixture cylinder before the methane results in a density exceeding 86.4 kg·m^{-3} at assumed ambient conditions of 20 °C, then some liquid ethane will be present.

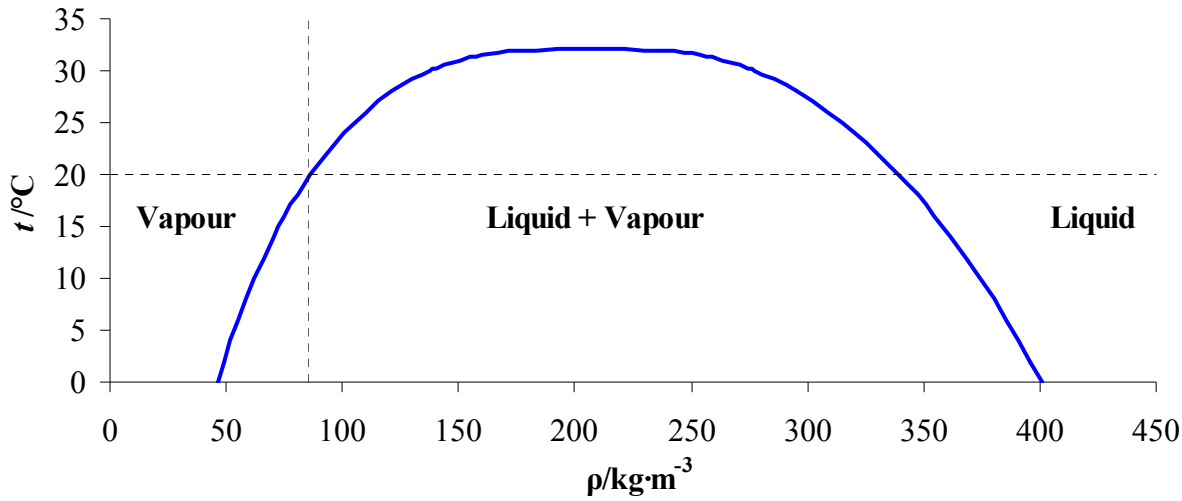

Figure E.1 – Density – temperature phase diagram for ethane calculated using NIST REFPROP.[168]

Figure E.2 shows a density composition phase diagram for the methane + ethane mixture at 20 °C. At a mole fraction of ethane less than 0.81 no liquid should be present if there is sufficient mixing.

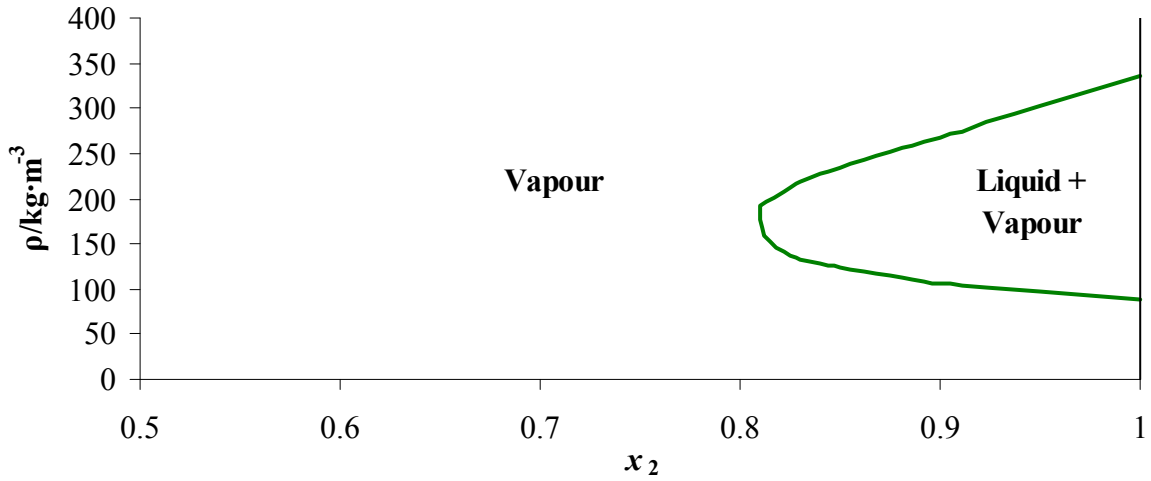

Figure E.2 – Phase diagram for methane (1) + ethane (2) mixture at 20 °C where x_2 is the mole fraction of ethane, calculated using NIST REFPROP.[168]

Appendix F ISCO pump gas mixture calculations

The initial molar density, $\rho_{mix,i}$, of the mixture of methane (1) + ethane (2) was calculated in NIST Refprop[168] from the known initial mole fractions of each component of the gas ($x_{1,i}$, $x_{2,i}$), P and T, the moles of methane and ethane were then individually calculated using eq (A.13), where j represents the component number, by guessing an initial volume of gas to charge the ISCO pump with, V_i:

$$n_{j,i} = x_{j,i}\rho_{mix,i}V_i \,. \tag{A.13}$$

Then using the final desired gas composition ($x_{1,f}$, $x_{2,f}$), P and T, it was possibly to work out the final molar density of the mixture, $\rho_{mix,f}$, in NIST Refprop. Using this molar density and the ISCO pump maximum volume of 266 ml as the final mixture volume, V_f, it was possible to calculate the final moles of methane, $n_{1,f}$ using eq (A.14). The initial volume, V_i, was then iterated until the final calculated composition of methane in the gas, $x_{1,f}$, from eq (A.15) matched the final desired composition.

$$n_{1,f} = x_{1,f}\rho_{mix,f}V_f \,. \tag{A.14}$$

$$x_{1,f} = \frac{n_{1,f}}{n_{1,f} + n_{2,i}} \,. \tag{A.15}$$

Appendix G Hydraulic pressure testing of constructed cells

Hydraulic pressure testing was carried out on the long cell and short cell that were constructed for plug dissociation measurements at the University of Canterbury. Water was used as the test fluid and a screw piston pump type pressure generator with a maximum operating pressure of 103.4 MPa (15000 psi) obtained from HiP (High Pressure Equipment Company model number 50-6-15) was used to pressurise the cells. The system is shown in Figure G.1. The system was initially started with both valves 1 and 2 closed. The cell was attached to the system then held in an upright position by clamping it to a retort stand. A plug fitting at the top of the cell was removed and the cell was filled completely with water. The system was gently rocked and allowed to stand for half an hour so that any air bubbles would rise to the top. The system was then topped up with water again and the plug fitting was replaced and tightened. Water was then drawn in to the screw piston pump by opening valve 1 and rotating the handle counter clockwise until fully extended. Valve 1 was then closed and valve 2 opened. The pumps handle was then rotated in a clockwise direction and the rising pressure was monitored on the pressure gauge (Heise CM-18357). When the handle reached zero extension the system pressure was noted, valve 2 was closed, and valve 1 opened. The pump was refilled with water by rotating the handle counter clockwise to maximum extension. Valve 1 was then closed. The pump handle was then rotated clockwise until the pressure reached approximately the same pressure as before the pump was refilled, then valve 2 was opened. This was done to minimize the pressure shock on the cell. When the pressure reached 70 MPa (10150 psi) pumping was stopped and the system was allowed to rest for 1 hour. To depressurize the system the handle was wound back. When the handle reached full extension the pressure in the system was noted valve 2 was shut and valve 1 opened. The pump handle was then rotated clockwise to about half extension then valve 1 was shut. The system up to valve 2 was then repressurized to the approximate pressure in the cell and valve 2 was opened. Depressurization then continued by rotating the handle counter clockwise until the pressure in the cell dropped to atmospheric.

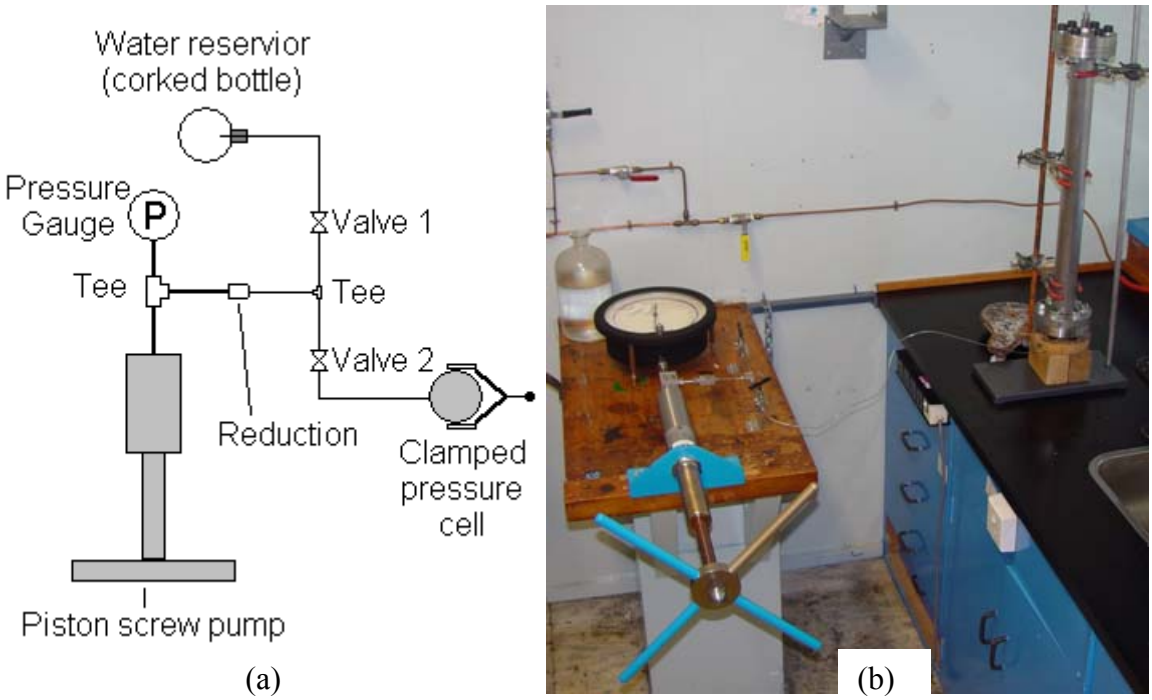

Figure G.1 – Pressure testing of the cells. (a) Apparatus diagram. (b) Photograph with long cell in place.

Appendix H Comparison of Clapeyron slopes calculated from experimental *P,T* phase data and CSMGEM predicted *P,T* phase data

Deaton and Frost (1946)

x_1 =	56.4%		CSMGEM		CSMGEM
T / K	1000 K/*T*	*P*/MPa	*P*/MPa	ln(*P*/Pa)	ln(*P*/Pa)
274.8	3.639	0.945	8.98E-01	13.76	13.71
277.6	3.602	1.289	1.2293	14.07	14.02
280.4	3.566	1.758	1.6881	14.38	14.34
283.2	3.531	2.434	2.3366	14.71	14.66
278.96	3.585		Clapeyron slope	-8750.0	-8852.2
				difference	1.2%

x_1 = mole fraction of methane

Clapeyron Slope: $\frac{\mathrm{d}\ln P}{\mathrm{d}(1/T)}$

x_1 =	90.4%		CSMGEM		CSMGEM
T / K	1000 K/*T*	*P*/MPa	*P*/MPa	ln(*P*/Pa)	ln(*P*/Pa)
274.8	3.639	1.524	1.58E+00	14.24	14.27
277.6	3.602	2.096	2.1556	14.56	14.58
280.4	3.566	2.889	2.9468	14.88	14.90
283.2	3.531	3.965	4.0549	15.19	15.22
278.96	3.585		Clapeyron slope	-8864.2	-8727.8
				difference	-1.5%

x_1 =	95.0%		CSMGEM		CSMGEM
T / K	1000 K/*T*	*P*/MPa	*P*/MPa	ln(*P*/Pa)	ln(*P*/Pa)
274.8	3.639	1.841	1.9131	14.43	14.46
277.6	3.602	2.53	2.6009	14.74	14.77
280.4	3.566	3.447	3.5508	15.05	15.08
283.2	3.531	4.771	4.8941	15.38	15.40
278.96	3.585		Clapeyron slope	-8798.7	-8696.1
				difference	-1.2%

x_1 =	97.1%		CSMGEM		CSMGEM
T / K	1000 K/*T*	*P*/MPa	*P*/MPa	ln(*P*/Pa)	ln(*P*/Pa)
274.8	3.639	2.158	2.2132	14.58	14.61
277.6	3.602	2.958	3.0026	14.90	14.91
280.4	3.566	4.034	4.0978	15.21	15.23
277.58	3.603		Clapeyron slope	-8607.6	-8475.5
				difference	-1.5%

x_1 =	97.8%		CSMGEM		CSMGEM
T / K	1000 K/*T*	*P*/MPa	*P*/MPa	ln(*P*/Pa)	ln(*P*/Pa)
274.8	3.639	2.365	2.3642	14.68	14.68
277.6	3.602	3.227	3.2042	14.99	14.98
280.4	3.566	4.413	4.3718	15.30	15.29
282.6	3.539	5.668	5.6288	15.55	15.54
283.2	3.531	6.088	6.042	15.62	15.61
279.68	3.575		Clapeyron slope	-8754.9	-8697.8
				difference	-0.7%

Deaton and Frost (1946) continued

x_1 =	98.8%		CSMGEM		CSMGEM		Metastable sl*	
T / K	1000 K/T	P/MPa	P/MPa	ln(P/Pa)	ln(P/Pa)	CSMGEM	CSMGEM P/MPa	CSMGEM ln(P/Pa)
274.8	3.639	2.861	2.6706	14.87	14.80	sII	2.8893	14.88
277.6	3.602	3.806	3.6108	15.15	15.10	sII	3.8448	15.16
280.4	3.566	5.088	4.9213	15.44	15.41	sII	5.1474	15.45
277.58	3.603		Clapeyron slope	-7921.1	-8410.2			-7945.326
				difference	6.2%			0.3%

* Measurements appear to be all for sI hydrate as the P-T data CSMGEM predicts for sI matches much better than that of sII. CSMGEM predicts that sI is metastable compared to sII for these P-T conditions and composition.

McCleod & Campbell (1961)

x_1 =	80.9%		CSMGEM		CSMGEM
T / K	1000 K/T	P/MPa	P/MPa	ln(P/Pa)	ln(P/Pa)
304.1	3.288	68.57	63.927	18.04	17.97
303.1	3.299	61.95	56.784	17.94	17.85
301.3	3.319	48.64	45.168	17.70	17.63
299	3.344	35.61	32.662	17.39	17.30
296.4	3.374	23.48	21.687	16.97	16.89
293.3	3.409	13.89	12.922	16.45	16.37
291.7	3.428	10.45	10.045	16.16	16.12
288.8	3.463	7.00	6.6829	15.76	15.72
297.12	3.366		Clapeyron slope	-13460.9	-13259.4
				difference	-1.5%

x_1 =	94.6%		CSMGEM		CSMGEM		sI and metastable sI**		
T / K	1000 K/T	P/MPa	P/MPa	ln(P/Pa)	ln(P/Pa)		CSMGEM P/MPa	CSMGEM ln(P/Pa)	
302	3.311	68.43	67.619	18.04	18.03	sI	67.619	18.03	sI
301.2	3.320	62.23	61.732	17.95	17.94	sI	61.732	17.94	sI
299.1	3.343	48.23	48.079	17.69	17.69	sI	48.079	17.69	sI
296.6	3.372	34.44	33.432	17.35	17.33	sII	34.95	17.37	m sI
293.6	3.406	24.42	20.422	17.01	16.83	sII	23.196	16.96	m sI
289.7	3.452	13.89	11.041	16.45	16.22	sII	13.427	16.41	m sI
287.9	3.473	10.45	8.5862	16.16	15.97	sII	10.549	16.17	m sI
284.9	3.510	6.93	5.863	15.75	15.58	sII	7.2447	15.80	m sI
294.25	3.398		Clapeyron slope sI	-10903.9	-10643.3		-11543.1	-11415.6	
				difference	-2.4%		difference	-1.1%	

** Measurements appear to be all for sI hydrate as there is no change in slope of the P-T data. CSMGEM predicts that for the points where T > 299.1 K sI is metastable compared to sII.

The comparison of the Clapeyron slopes calculated from experimental versus CSMGEM P,T phase data shows that the CSMGEM prediction is within ± 1.5%. The experimental methane + ethane + water L_W-H-V P,T phase data of Deaton & Frost and McCleod & Campbell for the predictions was obtained from Sloan.[1]

Appendix I Estimation of the volume available for the gas phase in the *P*,*T* equilibria measurements pressure cell

Table I.1 contains an estimate of the volume of the system of Figure 5.13 that can be occupied by gas.

Table I.1 – Estimations of volumes of the cell and constant volume system (between valve A and relief valve of Figure 5.13).

Volume		Calculation, estimation method or source
V_{cell}/mL (Volume of the pressure cell).	94.3	Measured from comparison of the mass of the cell filled with water to the mass of the cell filled with air using mass comparator detailed in Table 5.5
$V_{connections}$/mL (Volume of connection to pressure cell).	0.54	Calculated from length of various tubes and tubing inner diameters as well as estimates of fitting volumes (including relief valve).
$V_{pressure\ gauge}$/mL (Internal volume of pressure transducer).	0.26	From a personal email to Paroscientific.
$V_{LDPE\ bottle}$/mL (Annular and base volume of LDPE bottle).	6.3	Calculated from the mass and a typical density of 0.92 g·cm^{-3} (from Schuster[201]).
$V_{magnetic\ follower}$/mL (Volume of magnetic follower).	1.2	Estimated from water displacement in a measuring tube.
V_{SCH}/mL (Volume of SCH crystals loaded into cell).	18.9	Calculated from the mass of SCH loaded in to the cell and the density of 1.019 g·cm^{-3} given by Lipkowski et al.[67]
$V_{free\ gas}$/mL (Volume of the free gas phase).	68.7	$V_{free\ gas} = V_{cell} + V_{connections} + V_{pressure\ gauge} - V_{LDPE\ bottle} - V_{magnetic\ follower} - V_{SCH}$